New evaluation of delayed-neutron data and associated covariances

Daniela Foligno

AIX-MARSEILLE UNIVERSITY
Particle Physics and Astrophysics
Commissariat aux Energies Alternatives
CEA/CAD/DEN/DER/SPRC/LEPh

A thesis submitted in fulfillment of the requirements for the degree of Doctor of Particle Physics and Astroparticles

Discipline: Physics and Materials Science ED352
Specialty: Particle Physics and Astrophysics

Daniela FOLIGNO

New evaluation of delayed-neutron data and associated covariances

Defended the 10/10/2019 in front of the following jury:

C. MOREL	AMU	President
P. DESSAGNE	IPHC	Reviewer
A. PAUTZ	EPFL	Reviewer
V.P. DIMITRIOU	IAEA	Invited
D. DORE	CEA/DRF	Examiner
J. BUSTO	AMU	Ph.D. Director
P. LECONTE	CEA/DER	Ph.D. Supervisor

"A lot of people want a shortcut.
I find the best shortcut is the long way,
which is basically two words: work hard."
Randy Pausch

Acknowledgements

A Ph.D. is a long journey, a journey that is impossible to embark alone.

The first thanks go to my guide, my counselor, and my colleague: my supervisor Pierre Leconte. He saw in me qualities I was not aware of having, and pushed me at the limits of my skills to show me that limits do not exist. I want to thank him for his scientific support, his brilliant ideas and his immeasurable trust.

Then, I want to thank the ALDEN team for the experimental campaign. It was a big project and everyone's contribution has been essential to its success.

A huge thanks go to the people who made my working day so enjoyable: the CEA SPRC service and in particular the LEPh laboratory. The time spent at the coffee machine put me in a good mode and helped me to overcome difficult moments. In particular, I want to thank Abdhelaziz Cheboubbi and Pierre Tamagno for their continuous help, given without judgment.

A special thanks go to the Ph.D. students team, and in particular to Giorgio and Martin, which I spent all my working breaks and some after-works with. We shared pain and frustration and laughed over it.

I also want to thank the Italian team, which welcomed me from the very first day. It is a wonderful group of people, and I hope it will continue making new students feel at home.

After that, I want to thank my family for attending my Ph.D. defense in a language they did not speak on a subject they did not understand. I was moved when I saw all of them standing in the room, nervous almost as much as me. A special thanks go to my mother, my father, and my sister. They followed me wherever I went and supported me in the most difficult and the happiest moments of my life. Finally, I want to thank my boyfriend Alexis, for the love and attention in my regards.

Thank you all, without you, it would not have been the same.

Daniela

Contents

List of Figures **XII**

List of Tables **XVI**

Abstract **XVII**

Résumé **XVIII**

Résumé Étendu **XIX**

I Bibliography **1**

1 Introduction to Delayed Neutrons **2**
1.1 Energy from Fission . . . 3
1.2 The Importance of Delayed Neutrons in Reactor Physics . . . 5
1.2.1 Basic Quantities . . . 5
1.2.2 The Effect of Delayed Neutrons . . . 5
1.2.3 The Inhour Equation . . . 7
1.2.4 The Decay Heat . . . 10
1.3 Quantities of Interest . . . 10
1.3.1 Microscopic nuclear parameters . . . 11
1.3.2 Macroscopic nuclear parameters . . . 12
1.3.3 Reactor parameters . . . 13
1.4 A Bit of History . . . 14
1.4.1 The International Databases . . . 14
1.4.2 "Dear Old Keepin" . . . 15
1.4.3 Tuttle's evaluation of ν_d . . . 17
1.4.4 Brady & England's summation calculation . . . 18
1.4.5 The NEA/WPEC-SG6 . . . 19
1.4.6 The IAEA/CRP . . . 22
1.5 Scientific challenges of this Ph.D. . . . 22

2 Uncertainty Estimation Methodologies **25**
2.1 Statistics and Treatment of Experimental Data . . . 25
2.1.1 Characterizing a Probability Distribution . . . 26
2.1.2 Some Known Probability Distributions . . . 28
2.2 Bayes and The Learning Process . . . 29
2.2.1 Bayes' theorem . . . 30
2.2.2 Bayes theorem applied to an experiment . . . 31

2.2.3 Analytical Method . . . 31
2.2.4 Monte Carlo Method . . . 32
2.3 Uncertainty Propagation Methodologies . . . 32
2.3.1 Bayesian Marginalization . . . 32
2.3.2 Types of Marginalization . . . 33
2.4 CONRAD® . . . 34

II Microscopic Approach 36

3 Average Delayed-Neutron Yield 37
3.1 Merging Fission Yields and Radioactive Decay Data . . . 38
3.2 Libraries comparison . . . 39
3.2.1 The concept of precursor's importance . . . 40
3.2.2 Libraries . . . 40
3.2.3 Recommended values . . . 41
3.2.4 Neutron-induced fission of ^{235}U . . . 41
3.2.5 Neutron-induced fission of ^{238}U and ^{239}Pu . . . 50
3.3 Sensitivity of the ν_d to the CY and to the P_n . . . 53
3.4 Alternative method to compute the ν_d . . . 55
3.5 Results with the optimal FY-RDD combination . . . 56
3.6 Energy dependence . . . 58
3.6.1 State of the art . . . 58
3.6.2 Summation calculation . . . 59

4 Kinetic Parameters 62
4.1 Development and validation of the *Bateman solver* . . . 63
4.1.1 Development . . . 63
4.1.2 Validation with DARWIN . . . 66
4.2 Estimation of the abundances by direct summation . . . 68
4.2.1 Simple equivalence . . . 69
4.2.2 Exponential equivalence . . . 70
4.3 Estimation of the abundances by fit of the decay curve . . . 72
4.3.1 Analytical marginalization . . . 72
4.3.2 Monte Carlo marginalization . . . 74
4.4 Methods comparison . . . 77
4.5 Other fissioning systems . . . 81
4.6 Energy dependence . . . 84
4.7 Delayed-neutron spectra . . . 90

III Macroscopic Approach 92

5 Basics of neutron detection 93
5.1 Interaction of radiation with matter . . . 93
5.1.1 Heavy Particles . . . 94
5.1.2 Gamma Rays . . . 94
5.1.3 Neutrons . . . 95
5.2 Neutron detectors . . . 99
5.2.1 ^{3}He proportional counters . . . 100

5.2.2 Fission chambers . . . 102

6 ALDEN set-up 103
6.1 Principles of the ALDEN experiment . . . 104
6.2 LOENIE long counter . . . 106
6.2.1 LOENIE-V1 . . . 106
6.2.2 Purpose and Design of LOENIE-V2 . . . 106
6.2.3 Detectors' arrangement . . . 109
6.2.4 Efficiency as a function of the position . . . 110
6.3 The fissile target . . . 111
6.4 The fast-shutter . . . 112
6.5 Acquisition System and Pulse Processing . . . 114
6.5.1 Traditional analog chain . . . 114
6.5.2 Caen DPP firmware . . . 115
6.5.3 Acquisition system in the ALDEN experiment . . . 117
6.6 Description of the first experimental campaign . . . 119

7 Data regression analysis 121
7.1 From a binary file to a proper decay curve . . . 122
7.1.1 Nomad output files . . . 122
7.1.2 Analysis types . . . 122
7.1.3 Energy Range Of Interest . . . 123
7.1.4 Reference Bin . . . 124
7.1.5 C++ Procedure . . . 125
7.1.6 Average background estimation . . . 125
7.1.7 Optimizing the mesh . . . 126
7.2 Loss of counts correction . . . 126
7.2.1 Detector dead time in proportional counters . . . 127
7.2.2 Estimation of the electronic dead time with the distribution of arrival times . . . 128
7.2.3 Loss of counts estimation with a pulser . . . 129
7.2.4 Check on the quality of the correction: ring ratio test . . . 131
7.3 Absolute efficiency calibration at NPL . . . 133
7.4 Irradiation duration . . . 135
7.5 Analysis of the decay curve . . . 136
7.5.1 F from the spectroscopy of the fission chamber and of a dosimeter 137
7.5.2 F from the fission chamber signal . . . 138
7.5.3 F from the irradiation phase . . . 139
7.5.4 From F to ν_d . . . 140
7.5.5 Adopted procedure . . . 141
7.6 Results from the ALDEN experiment . . . 142

IV Evaluation and Benchmarking 145

8 Evaluation and Benchmarking 146
8.1 Bayesian assimilation of experimental data . . . 147
8.2 Neutron reactor noise analysis . . . 150
8.3 Validation of the average DN yield . . . 151
8.3.1 MISTRAL1 . . . 151

8.3.2 IPEN/MB-01 . . . 154
8.3.3 SNEAK7B . . . 156
8.4 Validation of the kinetic parameters . . . 158
8.5 Uncertainty propagation on the reactivity for a PWR-type reactor . . . 161

Conclusions and Perspectives **163**

Bibliography **169**

Appendices **173**

A WPEC-SG6 Recommendations **174**

B Error Propagation **175**
B.1 Error propagation for the $\nu_{\mathbf{d}}$ . . . 175
B.1.1 Analytical method - Error propagation . . . 175
B.1.2 Stochastic method - Monte Carlo . . . 176
B.2 Analytical error propagation for the $\mathbf{a_i}$: simple equivalence . . . 176
B.3 Analytical error propagation for the $\mathbf{a_i}$: exponential equivalence . . . 177
B.4 Analytical error propagation for the $\overline{\mathbf{T_{1/2}}}$ . . . 178
B.4.1 Direct summation . . . 178
B.4.2 Group model with correlations . . . 178
B.5 Analytical error propagation for the ρ . . . 179

C Complete tables nud **180**
C.1 ^{235}U thermal fission - Complete $\overline{\nu_d}$-table . . . 180
C.2 Precursors' Importance - $^{235}\mathrm{U}_{\mathrm{thermal}}$ . . . 180
C.3 Precursors' Importance - $^{235}\mathrm{U}_{\mathrm{fast}}$ . . . 183
C.4 Precursors' Importance - $^{238}\mathrm{U}_{\mathrm{fast}}$ . . . 185
C.5 Precursors' Importance - $^{239}\mathrm{Pu}_{\mathrm{thermal}}$ . . . 187
C.6 Precursors' Importance - $^{239}\mathrm{Pu}_{\mathrm{fast}}$ . . . 190

D Bateman-solver validation with DARWIN **193**
D.1 Analytical method . . . 193
D.2 Numerical method . . . 194
D.2.1 DARWIN analytical resolution . . . 195

List of Figures

1.1 Illustration of Neutron Induced Nuclear Fission (taken from [2]). 3
1.2 General fission products' decay scheme. 4
1.3 delayed-neutron emission from ^{137}I, scheme and illustration. 4
1.4 Illustration of the delayed neutron effect on the mean neutron lifetime. . . 6
1.5 Illustration of the G+1 solutions of the Inhour Equation [53]. 8
1.6 Part of the nuclide chart containing the P_n of the different fission products, taken from [31]. 12
1.7 Experimental set-up used by Keepin in 1957 [41]. 16

3.1 Cumulative vs independent yields taken from ENDF/B-VII.0 (upper plot) and JEFF-3.1.1 (lower plot). 44
3.2 Cumulative yields for $^{235}U_t$ taken from JEFF-3.1.1 and from ENDF/B-VII.0. The first plot shows the cumulative fission yields while the second one shows the ratio of the *CY* of the two libraries, taking JEFF-3.1.1 as a reference. 45
3.3 Energy dependence of the cumulative yields. The figures show the evolution of the *CY* from thermal to fast incident energy according to JEFF-3.1.1 (upper plot) and ENDF/B-VII.0 (lower plot). The arrows refer to the isotopes for which the increase/decrease by at least a factor of 1.5. . . 46
3.4 Energy dependence of the precursors' contribution to the ν_d of ^{235}U. In both figures the *CY* from JEFF-3.1.1 and ENDF/B-VII.0 are compared. The *FY* library is coupled with JEFF-3.1.1 (upper plot) or with ENDF/B-VII.1 (lower plot). 47
3.5 Delayed-neutron emission probability for the main precursors in two versions of RIPL-3 library. 48
3.6 Delayed-neutron emission probability comparison. 49
3.7 Precursors' contribution to the recommended $\overline{\nu_d}$ [in %] of $^{235}U_t$. In both plots the *RDD* libraries JEFF-3.1.1, ENDF/B-VII.0 and Pfeiffer are compared. The upper plot uses the *CY* from JEFF-3.1.1 while the lower plot takes them from ENDF/B-VII.0. 49
3.8 Precursors' contribution to the recommended ν_d[in %] of $^{238}U_f$. In both plots the *RDD* libraries JEFF-3.1.1, ENDF/B-VII.0 and Pfeiffer are compared. The upper plot uses the *CY* from JEFF-3.1.1 while the lower plot takes them from ENDF/B-VII.0. 51
3.9 Cumulative yields for the thermal (upper plot) and fast (lower plot) fission of ^{239}Pu according to JEFF-3.1.1 and ENDF/B-VII.0. 52
3.10 Correlations among the ν_d of several fissioning systems computed using JEFF-3.1.1 fission yields and ENDF/B-VIII.0 radiactive decay data. The values are represented in logarithmic scale. 57

3.11 Library comparison of the average delayed-neutron yield as a function of energy for ^{235}U. Fig. 3.11a contains all the versions of JEFF library from the 2.2 to the 3.3. Fig. 3.11b contains all the versions of ENDF/B library from the V.0 to the VIII.0. Both figures show experimental data for comparison. . . . 59
3.12 Summation calculation performed with JEFF-3.1.1 fission yields and with JEFF-3.1.1 and ENDF/B-VII.1 radioactive decay data for ^{235}U. Experimental data and evaluated libraries are shown for comparison. . . . 60
3.13 Energy dependence of average delayed-neutron yield computed with GEF-6.1 *FY* and with JEFF-3.1.1 *FY* modified with GEF-6.1 energy dependence. Experimental values are reported for comparison. . . . 61

4.1 Neutron flux as a function of time used to simulate the irradiation and the decay phase of a sample. The duration of the phases as well as the intensity of the flux are arbitrary and have been chosen for illustrative purposes. . . . 64
4.2 General decay scheme. . . . 64
4.3 Complete decay scheme for ^{87}Br. It shows all the ways ^{87}Br can be created apart from direct fission. . . . 65
4.4 Time evolution of the most relevant precursors' concentration after an irradiation of 600 s. . . . 67
4.5 Time evolution of the most relevant precursors' concentration after an irradiation of 10 s. . . . 67
4.6 Time evolution of the most relevant precursors' concentration after an irradiation of 0.001 s. . . . 67
4.7 *Simple equivalence* scheme. . . . 69
4.8 Importance of the eight delayed-neutron groups during the decay phase following a long irradiation. Long means that all the precursors reached their equilibrium concentration. . . . 70
4.9 *Exponential equivalence* scheme. . . . 70
4.10 Correlation matrix associated with the abundances computed by *analytical marginalization* with the *two-experiences normalization* technique. . . . 73
4.11 Correlation matrix associated with the abundances computed by *analytical marginalization* with the *self-normalization* technique. . . . 74
4.12 Correlation matrix associated with the abundances computed by *Monte Carlo marginalization*. . . . 77
4.13 Mean precursors' half-life for the thermal fission of ^{235}U calculated using the abundances derived by summation method using different techniques and compared with the recommended values from the WPEC-SG6. . . . 78
4.14 Eight-group abundances for the thermal fission of ^{235}U calculated by summation method using different techniques and compared with the recommended values from the WPEC-SG6. . . . 79
4.15 Figure (a) shows the ratio between the activity computed using the 8-group model and the one calculated by summation method. Figure (b) is the analogous ratio, but for the reactivity. . . . 80
4.16 Energy dependence of the first abundance computed with the original JEFF-3.1.1 *FY* and with the with JEFF-3.1.1 *FY* modified with GEF-6.1 energy dependence. Experimental values are reported for comparison. 85

4.17 Energy dependence of the second abundance computed with the original JEFF-3.1.1 *FY* and with the with JEFF-3.1.1 *FY* modified with GEF-6.1 energy dependence. Experimental values are reported for comparison. For the legend please refer to Fig. 4.16. 85
4.18 Energy dependence of the third abundance computed with the original JEFF-3.1.1 *FY* and with the with JEFF-3.1.1 *FY* modified with GEF-6.1 energy dependence. Experimental values are reported for comparison. For the legend please refer to Fig. 4.16. 86
4.19 Energy dependence of the fourth abundance computed with the original JEFF-3.1.1 *FY* and with the with JEFF-3.1.1 *FY* modified with GEF-6.1 energy dependence. Experimental values are reported for comparison. For the legend please refer to Fig. 4.16. 86
4.20 Energy dependence of the fifth abundance computed with the original JEFF-3.1.1 *FY* and with the with JEFF-3.1.1 *FY* modified with GEF-6.1 energy dependence. Experimental values are reported for comparison. For the legend please refer to Fig. 4.16. 87
4.21 Energy dependence of the sixth abundance computed with the original JEFF-3.1.1 *FY* and with the with JEFF-3.1.1 *FY* modified with GEF-6.1 energy dependence. Experimental values are reported for comparison. For the legend please refer to Fig. 4.16. 87
4.22 Energy dependence of the seventh abundance computed with the original JEFF-3.1.1 *FY* and with the with JEFF-3.1.1 *FY* modified with GEF-6.1 energy dependence. Experimental values are reported for comparison. For the legend please refer to Fig. 4.16. 88
4.23 Energy dependence of the eigth abundance computed with the original JEFF-3.1.1 *FY* and with the with JEFF-3.1.1 *FY* modified with GEF-6.1 energy dependence. Experimental values are reported for comparison. For the legend please refer to Fig. 4.16. 88
4.24 Energy dependence of the mean precursors' half-life computed with the original JEFF-3.1.1 *FY* and with the with JEFF-3.1.1 *FY* modified with GEF-6.1 energy dependence. Experimental values are reported for comparison. For the legend please refer to Fig. 4.16. 89
4.25 Group and equilibrium spectra for the thermal fission of ^{235}U computed by summation method using ENDF/B-VIII.0's individual precursors' spectra. 91

5.1 Simplified scheme of the neutron interaction with matter. n represents the number of neutrons and the indices *in*, *out*, *c*, *s*, and *f* represent the neutrons entering, exiting, being captured, being scattered and causing fission, respectively. S is the surface of the bulk material while d represents its thickness. 97
5.2 Total, elastic scattering and fission cross section for the fissile isotope ^{235}U according to JEFF-3.1.1. 98
5.3 Scheme of a gas-filled ionization detector [48]. 100
5.4 Operating conditions of gas-filled ionization detectors [48]. 100
5.5 Pulse Height Amplitude of a typical ^{3}He detector [57]. Note that gamma rays indirectly ionize the gas and appear as a low energy peak in the PHA. 101

6.1 Simplified scheme of the experimental set-up during the two phases of the ALDEN experiment. 104
6.2 Typical irradiation run of the ALDEN experiment. 105

6.3 ALDEN experimental set-up. . . . 105
6.4 LOENIE-V1 long counter and efficiency of its 17 ^{3}He tubes. . . . 107
6.5 LOENIE-V2 detector. . . . 107
6.6 Detection efficiency associated with the ^{3}He(n,p)^{3}H reaction of a ^{3}He tube as a function of the incident neutron energy and of the distance from the center. . . . 108
6.7 TRIPOLI4® simulation of LOENIE-V2 long counter. . . . 108
6.8 Nomenclature of holes (H), detectors (H), quadrants (G) and channels (CH). . . . 109
6.9 Counting rate of the 16 ^{3}He tubes sorted by their ring. . . . 110
6.10 Pulse Height Amplitude of the 16 ^{3}He, together with their sum. . . . 111
6.11 CFP12 n. 2328, produced at the Laboratory of Dosimetry, Sensors, and Instrumentation at CEA. . . . 111
6.12 Fast shutter designed at CEA Cadarache. . . . 112
6.13 Opening and closing steps of the fast shutter. . . . 113
6.14 One of the frames used for the estimation of the fast-shutter speed. . . . 113
6.15 Elements of the acquisition system. . . . 114
6.16 Signal transformation in the analog chain, taken from [9]. . . . 115
6.17 CAEN V1724 digitizer, taken from [1]. . . . 115
6.18 Block diagram of the DPP-PHA, taken from [9]. . . . 116
6.19 DPP filters, taken from [67] The TT filter transforms the tail pulse into a bipolar pulse. When the latter crosses the zero, the time stamp is registered and the trigger is sent to the TF, which starts the trapezoidal shaping of the pulse. . . . 116
6.20 Details of the DPP filters, taken from [67]. . . . 117
6.21 Pile-up treatment in the DPP, taken from [67]. . . . 118
6.22 Acquisition system scheme. . . . 118
6.23 Pictures of the acquisition system. . . . 119

7.1 Pulse Height Amplitude of one of the four inner counters. The three spectra are shown, corresponding to irradiation, decay, and background phases. . . . 123
7.2 Iterative procedure to find the index corresponding to the end of the irradiation. . . . 124
7.3 Decay curve in the original and in the optimized mesh. . . . 126
7.4 Idealized dead time models for a τ of 10 μs. . . . 127
7.5 Distribution of arrival times for a Poissonian process, taken from [48]. . . . 128
7.6 Distribution of arrival time in one of the inner tubes. . . . 129
7.7 Pulser PHA in response to a 1 V signal. . . . 130
7.8 Effect of the channel 0 on the background of Cycle 1. . . . 131
7.9 Dead-time correction. . . . 131
7.10 Ring ratio test. . . . 132
7.11 Ring ratio. . . . 132
7.12 Anisotropy of NPL sources. . . . 134
7.13 Comparison between simulation and measurement of the efficiency and of the ring ratio for NPL sources. . . . 135
7.14 Distribution of the starting and ending point of the irradiation phase. . . . 136
7.15 Distribution of the average counting rate during the irradiation phase of the 168 runs of cycle 1. . . . 139
7.16 PHA of the CFP12 during the irradiation phase. . . . 139

7.17 Uncertainty components as a function of the length of the fitted decay curve. . . . 141
7.18 Correlation matrix associated with the abundances derived from the fit of the ALDEN experimental decay curve through *analytical marginalization*. 142
7.19 Experimentally measured ν_d for $^{235}U_t$ as a function of the year in which the experiment took place. The red band represents the values recommended by Tuttle in his evaluation of 1979. . . . 143
7.20 Experimentally measured $\overline{T_{1/2}}$ for $^{235}U_t$ as a function of the year in which the experiment took place. The red band represents the values recommended by Tuttle in his evaluation of 1979. . . . 144

8.1 Correlation matrix associated with the abundances derived from the Bayesian assimilation of the ALDEN experiment through *analytical marginalization*. 147
8.2 Reactor transfer function scheme [25]. . . . 150
8.3 MISTRAL1 core scheme. . . . 152
8.4 Picture of the IPEN/MB-01 core, taken from [32]. . . . 154
8.5 Decomposition of the reactivity in the IPEN/MB-01 core. . . . 155
8.6 Scheme of the SNEAK7B core, taken from [22]. . . . 156
8.7 Reactivity comparison. . . . 160
8.8 Reactivity simulation comparison for the IPEN/MB-01 core. Note that the uncertainties associated with the (C-E)/E are nothing but the uncertainties on the experiment (E). . . . 160
8.9 Effect of the input data on the uncertainty in the simulated reactivity. . . . 162
8.10 Ratio between the inner ring (4 counters) and the other rings (12 counters). 166

D.1 Example of a closed decay-chain treatment. . . . 194

List of Tables

1.1 Best fit of the kinetic parameters for the thermal fission of ^{235}U (99.9% ^{235}U) and ^{239}Pu (99.8% ^{239}Pu) and the fast fission of ^{238}U (99.98% ^{238}U) from Keepin's experiment [41]. . . . 16

1.2 Delayed-neutron yields recommended by Tuttle in his critical review [56]. The values with a star (*) are partially or wholly determined by analytical prediction. . . . 17

1.3 Results of the summation calculation performed by Brady and England in 1989 using ENDF/B-V library [49]. . . . 19

1.4 Set of half-lives recommended by the WPEC-SG6 [40]. . . . 20

1.5 Origin of the kinetic parameters recommended by WPEC-SG6. The sets being in the six-group model have been expanded into the eight-group model before being recommended. . . . 20

1.6 Delayed-neutron yields and kinetic parameters recommended by the WPEC-SG6 in 2002 [38]. σ_{a_i} represents the uncertainty associated with the abundances a_i. No uncertainty is recommended for the average delayed-neutron yields. . . . 21

1.7 Mean precursors' half-life computed using the kinetic parameters recommended by the European and the American international libraries. . . . 23

3.1 Average delayed-neutron yield recommended by the WPEC-SG6. . . . 42

3.2 ν_d calculation by summation method - $^{235}U_t$. . . . 42

3.3 ν_d calculation by summation method - $^{235}U_f$. . . . 43

3.4 Cumulative vs independent yield ratio for some precursors. . . . 44

3.5 ν_d calculation by summation method - other fissioning systems. . . . 50

3.6 Delayed-neutron emission probability of ^{98}Y in the last three versions of ENDF/B. The author highlighted the mistake in 2017 and the P_n-value has been corrected before the release of ENDF/B-VIII.0. . . . 53

3.7 Uncertainty components for the ν_d associated with the thermal fission of ^{235}U. . . . 53

3.8 Methods comparison for the estimation of the ν_d by summation calculation. The results refer to the thermal fission of ^{235}U, computed using JEFF-3.1.1's *FY* and ENDF/B-VIII.0's *RDD*. . . . 55

3.9 ν_d computed by summation method using JEFF-3.1.1 cumulative fission yields (CY) and ENDF/B-VIII.0 radiactive decay data (*RDD*) as microscopic input data, and compared with Tuttle's evaluation and with JEFF-3.1.1 library. . . . 56

3.10 Correlation matrix among ν_d of different fissioning systems at different energies, computed by CONRAD® using JEFF-3.1.1 fission yields and ENDF/B-VIII.0 radiactive decay data as microscopic input data. Correlations are reported in logarithmic scale. . . . 57
3.11 Experimental energy dependence of the delayed-neutron yield. The values in the table represent the relative variation of the ν_d with the incident neutron energy, in the specified energy range. . . . 58
3.12 Calculated energy dependence of the delayed-neutron yield. The values in the table represent the relative variation of the ν_d with the incident neutron energy, from thermal to fast. . . . 59

4.1 Discrepancies in the concentration at the end of the irradiation. [1], [2] and [3] refer to an irradiation length of 0.001 s, 10 s and 600 s, respectively. The precursors are shown in order of importance with respect to the delayed-neutron emission. . . . 68
4.2 Results of the *simple equivalence* method for the thermal fission of ^{235}U using JEFF-3.1.1 fission yields and ENDF/B-VIII.0 radioactive decay data. σ_{a_i} are given in percentage of a_i. . . . 70
4.3 Half-lives associated with the 8 delayed-neutron groups according to the WPEC-6. . . . 71
4.4 Results of the *exponential equivalence* method for the thermal fission of ^{235}U using JEFF-3.1.1 fission yields and ENDF/B-VIII.0 radioactive decay data. The group decay constants have been taken from WPEC-6 [40] except for λ_1, replaced by the λ of ^{87}Br according to ENDF/B-VIII.0. σ_{a_i} are given in percentage of a_i. . . . 72
4.5 Results of the *analytical marginalization* method with *two-experiences normalization* for the thermal fission of ^{235}U using JEFF-3.1.1 fission yields and ENDF/B-VIII.0 radioactive decay data. The group decay constants have been taken from WPEC-6 [40] except for λ_1, replaced by the λ of ^{87}Br according to ENDF/B-VIII.0. σ_{a_i} are given in percentage of a_i. 73
4.6 Results of the *analytical marginalization* method with *self-normalization* for the thermal fission of ^{235}U using JEFF-3.1.1 fission yields and ENDF/B-VIII.0 radioactive decay data. The group decay constants have been taken from WPEC-6 [40] except for λ_1, replaced by the λ of ^{87}Br according to ENDF/B-VIII.0. σ_{a_i} are given in percentage of a_i. . . . 74
4.7 Original and perturbed parameters. . . . 75
4.8 Results of the *Monte Carlo marginalization* method for the thermal fission of ^{235}U using JEFF-3.1.1 fission yields and ENDF/B-VIII.0 radioactive decay data. The group decay constants have been taken from WPEC-6 [40] except for λ_1, replaced by the λ of ^{87}Br according to ENDF/B-VIII.0. The computation has been done considering $K = 10000$. σ_{a_i} are given in percentage of a_i. . . . 76
4.9 Eight-group abundances for the thermal fission of ^{235}U calculated by summation method using different techniques and compared with the recommended values from the WPEC-SG6. The uncertainties are given in percentage of a_i. . . . 77
4.10 Average mean precursors' half-life for the main fissioning systems. The *direct summation* is an average of the individual precursors' half-lives weighted on the isotope's contribution to the ν_d. The $\overline{T_{1/2}}$ under the other two columns are computed using the respective abundances sets. . . . 81

4.11 Energy evolution of the ^{239}Pu cumulative yields according to JEFF-3.1.1. 82
4.12 Results of the *Exponential Equivalence* method using JEFF-3.1.1 fission yields and ENDF/B-VIII.0 radioactive decay data. The group decay constants have been taken from WPEC-6 [40] except for λ_1, replaced by the λ of ^{87}Br according to ENDF/B-VIII.0. Note that the uncertainties are given in percentage of the a_i value. 83
4.13 Average energy computed by summation method using JEFF-3.1.1's *FY* and ENDF/B-VIII.0's *RDD*. 90

6.1 Detectors configuration. 109
6.2 Features of the two fission chambers produced in 2019 for the ALDEN experiment, and expected counting rates. 112
6.3 Nomad parameters common to all experiments. 119
6.4 List of the experimental campaigns. 120
6.5 Long cycles. 120

7.1 Pulser test. For each run, the frequency of the pulser is reported, as well as the response of the acquisition system. 129
7.2 Slope and loss estimation before and after correction channel by channel. 133
7.3 NPL sources' characteristics. 134
7.4 Efficiency and ring ratio for the different NPL sources. 135
7.5 Estimated cycle duration. 136
7.6 Efficiency of the group with respect to the global efficiency. 137
7.7 Results of the fit of the decay curve using a fission rate estimated through different methods. 140
7.8 Results of the ALDEN experiment. *Prior* are the guessed values given to CONRAD® in order not to constrain the fit, while *Posterior* are the results of the fit. 143

8.1 Results of the Bayesian assimilation of the ALDEN experiment. *Prior* are the guessed values given to the CONRAD® code and taken from the summation calculation, while *Posterior* are the results of the fit. 147
8.2 Summary of the abundances and average yields obtained in the different steps of this work: summation calculation, experiment, and Bayesian combination of the two. 148
8.3 Input data comparison. As far as *Foligno*'s parameters are concerned, ^{238}U$_f$'s are the results of the summation calculation while ^{235}U$_t$'s come from the Bayesian assimilation of calculation and experiment. 149
8.4 Effect of the DN input data on the simulated β - MISTRAL1. 153
8.5 Contribution of the different fissioning systems to the β_{eff} of the MISTRAL1 core. f_x is the contribution of x to the β_{eff} of the mix. 153
8.6 β_{eff} simulation comparison for the MISTRAL1 core. Note that the uncertainties associated with the (C-E)/E are nothing but the uncertainties on the experiment (E). 154
8.7 Effect of the DN input data on the simulated β - IPEN/MB-01. 155
8.8 Contribution of the different fissioning systems to the β_{eff} of the IPEN/MB-01 core. f_x is the contribution of x to the β_{eff} of the mix. 155
8.9 TRIPOLI4® β_{eff} simulation comparison for the IPEN/MB-01 core. Note that the uncertainties associated with the (C-E)/E are nothing but the uncertainties on the experiment (E). 156

8.10 Contribution of the different fissioning systems to the β_{eff} of the SNEAK7B core. f_x is the contribution of x to the β_{eff} of the mix. 157
8.11 Effect of the DN input data on the simulated β - SNEAK7B. 157
8.12 β_{eff} simulation comparison for the SNEAK7B core. Note that the uncertainties associated with the (C-E)/E are nothing but the uncertainties on the experiment (E). 158
8.13 TRIPOLI4® abundances simulation comparison for the IPEN/MB-01 core. Within brackets, the relative uncertainty of the abundances is reported. Note that the uncertainties associated with the (C-E)/E are nothing but the uncertainties on the experiment (E). 158
8.14 Reactivity simulation comparison for the IPEN/MB-01 core. Note that the uncertainties associated with the (C-E)/E are nothing but the uncertainties on the experiment (E). 159

A.1 Origin of the kinetic parameters recommended by the WPEC. 174

C.1 $\overline{\nu_d}$ calculation by Summation Method - $^{235}U_{th}$. 180
C.2 Precursors' importance for the thermal fission of ^{235}U. 183
C.3 Precursors' importance for the fast fission of ^{235}U. 185
C.4 Precursors' importance for the fast fission of ^{238}U. 187
C.5 Precursors' importance for the thermal fission of ^{239}Pu. 190
C.6 Precursors' importance for the fast fission of ^{239}Pu. 192

Abstract

In the context of nuclear reactor physics, one of the main issues is the control of the chain reaction. After a fission event has occurred, around three prompt neutrons are *immediately* emitted. Luckily, a small fraction of neutrons - less than 1% - appears with a certain *delay* with respect to the fission event. *Delayed neutrons* (DN) are an easy way out from the uncontrollable prompt-neutron driven chain reaction because they slow down the response of the reactor to a change in reactivity.

Quantifying the fraction of such neutrons as well as their kinetic behavior is essential to design a safe reactor. In particular, in order to determine the safety margins, a rigorous estimation of uncertainties and covariances is necessary. The main consequence of a lack of accurate DN data is the conservatism in the design of a reactor. Nowadays, the discrepancy between the reactivity simulated using different international databases, rises up to 16% for LWRs, and the uncertainties associated with the currently recommended parameters are still too large for the needs of the industry. In addition to that, the covariance matrix associated with the abundances has never been produced. The DN parameters are generally estimated through a calculation or an integral measurement.

This Ph.D. aims at producing a new set of DN parameters by performing both calculations and measurements, and by exploiting the two through the Bayesian inference, with the aim of reducing the uncertainties and creating the associated covariance matrices.

The results for ^{235}U, together with the calculated values for ^{238}U, have been tested in three benchmarks, giving satisfying solutions with respect to the effective delayed neutron fraction. The main achievement of this work is the great improvement in the predicted reactivity, especially for negative periods, which is accompanied by an extremely good precision, never exceeding 2.2%.

Résumé

Dans le domaine de la physique des réacteurs, une des principales préoccupation est la maîtrise de la réaction en chaîne. Lorsqu'un noyau fissionne, environ trois neutrons prompts sont émis immédiatement. Toutefois, une faible fraction de neutrons supplémentaires - moins d'1% de la population totale - apparaît un certain temps après la fission. Les neutrons retardés (NR) contre-balancent le caractère incontrôlable d'une réaction en chaîne pilotée uniquement par des neutrons prompts en ralentissant la réponse d'un réacteur à une variation de réactivité.

Quantifier la fraction de NR ainsi que leur cinétique est essentiel pour concevoir des réacteurs sûrs. La principale conséquence d'un manque de précision sur les données des NR est l'augmentation du conservatisme à la conception du réacteur au regard des marges de sûreté imposées par l'Autorité de Sûreté. Aujourd'hui, la dispersion entre les réactivités simulées avec différentes bibliothèques de données internationales atteint jusqu'à 16% pour les réacteurs à eau légère et les incertitudes associées aux paramètres recommandés restent trop importante pour les besoins de l'industrie. A cela s'ajoute le fait que les matrices de covariance associées aux abondances des NR dans les différentes familles de NR n'ont jamais été évaluées. Jusqu'à présent, les paramètres associés aux NR ont été estimés soit par calculs soit par mesures intégrales.

Cette thèse a pour but de produire un nouveau jeu de paramètres pour les NR en conduisant à la fois des calculs et des mesures puis en exploitant ces deux sources grâce à l'assimilation Bayesienne. Cela permettrait de réduire les incertitudes sur les données des NR et de créer les matrices de covariance qui leurs sont associées.

Les résultats pour l'^{235}U et les paramètres calculés pour l'^{238}U, ont été testés dans trois benchmarks, en donnant des solutions satisfaisantes par rapport à la fraction effective de neutrons retardés. La réussite principale de ce travail est la grande amélioration de la réactivité prédite, spécialement pour des périodes négatives. De plus, elle est accompagnée par une précision extrêmement bonne, qui ne dépasse jamais 2.2%.

Résumé Étendu

Introduction sur les neutrons retardés

Dans le domaine de la physique des réacteurs, une des principales préoccupation est la maîtrise de la réaction en chaîne. Lorsqu'un noyau fissionne, environ trois neutrons prompts sont émis immédiatement. Après l'évaporation des neutrons, les fragments de fission sont appelés *produits de fission*. Les produits de fission, en étant riches en neutrons, sont naturellement instables. Pour atteindre la stabilité, ils subissent une série de décroissance β^-. Une fraction de ces décroissances donne lieu à un fils avec une énergie d'excitation plus élevée que l'énergie de séparation du dernier neutron, ce qui laisse à l'isotope la possibilité d'atteindre la stabilité à travers l'émission d'un rayon gamma ou d'un neutron. Les neutrons créés par la désexcitation des produits de fission - moins d'1% de la population totale - sont appelé retardés car ils apparaissent avec un certain retard par rapport à l'événement de fission (entre une fraction de seconde et quelque minutes). Les neutrons retardés (NR) contre-balancent le caractère incontrôlable d'une réaction en chaîne pilotée uniquement par des neutrons prompts en ralentissant la réponse d'un réacteur à une variation de réactivité.

En conditions normales, les réacteurs nucléaires se trouvent à l'état critique, une condition favorable dans laquelle la population neutronique est à l'équilibre. Les neutrons sont émis par fission et ils disparaissent par absorption, capture ou fuite. Pour contrôler la population de neutrons, les physiciens des réacteurs ont introduit une nouvelle quantité, la *réactivité* (ρ), qui quantifie l'écart à la criticité. En conditions critiques, $\rho = 0$, et la réaction en chaîne est stable. Le taux de changement de la population neutronique après une insertion de réactivité dépend de la réactivité insérée, ainsi que de la durée de vie moyenne des neutrons (ℓ). L'effet principale des neutrons retardés est d'augmenter ℓ de 10^{-5} s à environ 0.085 s, ce qui veut dire que pour une insertion de réactivité de 10 pcm, le temps nécessaire à augmenter la puissance d'un facteur 2.718 serait 1 s sans neutrons retardés et 850 s en présence de ces derniers, rendant le réacteur plus facilement contrôlable.

La principale conséquence d'un manque de précision sur les données des NR est l'augmentation du conservatisme à la conception du réacteur au regard des marges de sûreté imposées par l'Autorité de Sûreté. Les quantités d'intérêt pour les neutrons retardés sont :

- ν_d : le nombre moyen de neutrons retardés émis par fission, en fiss/s
- β_{eff} : la fraction effective de neutrons retardés, en pcm où en \$
- a_i : les abondances par famille des neutrons retardés

- λ_i : les constantes de décroissance des familles de neutrons retardés, en s^{-1}
- $\overline{T_{1/2}}$: le temps de vie moyenne des neutrons retardés, en s.

Les données nucléaires évaluées sont distribuées par la Nuclear Data Organization , qui recommande les valeurs de plus haute qualité et les publie dans des bibliothèques internationales de données. La bibliothèque Européenne s'appelle JEFF, alors que celle Américaine s'appelle ENDF/B. Elles contiennent les données associées aux systèmes fissionants ainsi qu'à leurs produits de fission.

Il y a environ 300 précurseurs de neutrons retardés. Par le passé, il était impossible de traiter autant de données dans les calculs cinétiques des réacteurs. Pour cette raison, G.R. Keepin eu l'idée de regrouper les précurseurs en familles, selon leur constante de décroissance, en faisant l'hypothèse que l'activité en neutrons retardés puisse être décrite avec une somme de six exponentiels. En 1957 il a réalisé une expérience intégrale pour estimer ν_d, a_i et λ_i. Keepin a été pendant longtemps la référence incontestée pour les données de neutrons retardés. In 1989, M.C. Brady et T.R. England ont fait un effort considérable pour produire un set complet de données évaluées pour 43 systèmes fissionants. L'innovation de leur travail consistait à obtenir toutes les quantités d'intérêt par un calcul de sommation plutôt que par la réalisation d'une expérience. En 1990, la NEA a lancé un WPEC sur les neutrons retardés pour ameliorer les données et reduire les écarts entre valeurs mesurées et calculées. En conclusion du WPEC, il a été établi que le modèle à six familles était désormais obsolète et que un nouveau modèle à huit familles était nécessaire. De plus, ce nouveau modèle devait avoir un seul set de constants de décroissance, dont les trois premières devaient correspondre au précurseurs à vie longue les plus dominants (^{87}Br, ^{137}I, ^{88}Br), et les cinq derniers à une moyenne pondérée des constantes de décroissance relatives au précurseurs les plus dominants dans la famille respective. Les données recommandées par le WPEC ont remplacé les données de Keepin dans la bibliothèque JEFF-3.1.1, alors que la bibliothèque ENDF/B-VIII.0 continue à recommander les données de Brady & England.

Cette thèse a pour but de produire un nouveau jeu de paramètres pour les neutrons retardés en conduisant à la fois des calculs et des mesures puis en exploitant ces deux sources grâce à l'assimilation Bayesienne. Cela permettrait de réduire les incertitudes sur les données des NR et de créer les matrices de covariance qui leurs sont associées.

Méthode d'estimation des incertitudes

Une erreur n'est pas une faute. L'erreur associé à une mesure est l'incertitude intrinsèque de l'expérience elle même. L'incertitude est une quantité qui ne peut pas être évitée mais qui peut être quantifiée. Il y a deux types d'erreurs :

- *Erreurs aléatoires* : elles sont dues aux fluctuations statistiques de la mesure
- *Erreurs systématiques* : elles sont dues à quelque chose qui biaise la mesure.

L'inférence Bayesienne est la traduction de la logique en mathématique et permet d'exploiter au mieux les informations à disposition. Elle est utilisé en générale pour mettre à jour des valeurs de certains paramètres lorsqu'une nouvelle expérience est disponible. Le théorème de Bayes peut être résolu à travers une méthode analytique ou une méthode Monte Carlo. Pour ce qui concerne la propagation des incertitudes, il

faut faire attention aux paramètres de nuisance, paramètres qui ne font pas partie du modèle théorique mais qui ont un effet non négligeable sur l'incertitude des résultats. Ces paramètres peuvent être pris en considération à travers la marginalisation Bayesienne, qui consiste à les considérer comme des variables aléatoires ayant une distribution Gaussienne. Encore une fois, la marginalisation peut être estimée soit à travers une méthode analytique ou une méthode Monte Carlo.

Approche microscopique

Les codes neutroniques utilisent comme données d'entrée des bibliothèques applicatives qui ne sont pas adaptés à la comparaison de ces dernières. Étant donné que la flexibilité était un prérequis de l'étude à mener, un code a été développé en C++ pour traduire les rendements de fission (FY) et les données de décroissance radioactive (RDD) du format ENDF-6 et les fusionner en une seule bibliothèque mixte. Une des façons de calculer le rendement moyen en neutrons retardés est la méthode par sommation, qui consiste à sommer les contributions de tous les précurseurs

$$\nu_d = \sum_{i=1}^{N} CY_i P_{n,i} x_i \tag{1}$$

où CY_i est le rendement cumulé, P_{n_i} la probabilité de décroître par β_n^- et x_i le nombre moyen de neutrons émis par décroissance du précurseur i. Dans le cadre de cette thèse, plusieurs bibliothèques de FY et de RDD ont été prises en compte. Une étude approfondie de comparaison a mené à la conclusion que la meilleure combinaison est celle qui utilise les FY de JEFF-3.1.1 et les RDD de ENDF/B-VIII.0. De plus, cette étude a permis d'identifier des erreurs dans certaines des bibliothèques, comme le CY de l'^{86}As dans ENDF/B-VII.0 ou la P_n du ^{98m}Y dans ENDF/B-VII.1. Ces erreurs ont été communiquées aux évaluateurs de la bibliothèque ENDF/B et corrigées. Les rendements moyens en neutrons retardés calculés avec la combinaison choisie ainsi que les valeurs recommandées par JEFF-3.1.1 sont comparées dans le Tableau 1. Le calcul a été répété pour plusieurs systèmes fissionants. Il est important de rappeler que JEFF-3.1.1 ne fournit pas les incertitudes associées aux valeurs recommandées. Globalement, la méthode par sommation marche plutôt bien pour la plupart des isotopes fissionants. Par contre, comme dans tous les calculs, la qualité du résultat dépend des données d'entrée. Les écarts montrés dans le Tableau 1 pour certains isotopes indiquent des pistes vers des données méritant d'être améliorées. Une recherche plus approfondie serait nécessaire pour investiguer les rendements de fission de ces systèmes fissionants.

Un code qui suit l'évolution des concentrations des précurseurs dans un système physique pendant et après une phase d'irradiation a été développé pour l'estimation des paramètres cinétiques. Ce code, dont la validation a été faite par comparaison avec le code de calcul DARWIN, reconstruit l'arbre généalogique de chaque précurseur et calcule sa concentration dans le temps. Les abondances par famille de neutrons retardés ont été estimées avec quatre techniques différentes, dont deux consistent à assigner une famille à chaque précurseurs et à en estimer la contribution et les autres deux à reconstruire l'activité en neutrons retardés et à l'ajuster avec huit exponentiels. Enfin, il a été possible d'estimer à partir des paramètres cinétiques, le temps de vie moyen des neutrons retardés, et de le comparer avec la littérature (Tableau 2).
Les différentes méthodes ne reproduisent pas l'activité et la réactivité de la même façon. Les deux méthodes d'ajustement permettent de reconstruire fidèlement l'activité en neu-

Table 1: ν_d calculés par méthode de sommation en utilisant les CY de JEFF-3.1.1 et les P_n de ENDF/B-VIII.0, comparés avec la bibliothèque JEFF-3.1.1.

Fissioning System	**This work**	**JEFF-3.1.1**
$^{232}\mathrm{Th_f}$	6.11E-02 (4.5%)	5.27E-02
$^{233}\mathrm{U_t}$	7.82E-03 (7.5%)	6.73E-03
$^{233}\mathrm{U_f}$	1.12E-02 (7.6%)	7.40E-03
$^{235}\mathrm{U_t}$	1.61E-02 (5.2%)	1.62E-02
$^{235}\mathrm{U_f}$	1.80E-02 (5.1%)	1.63E-02
$^{236}\mathrm{U_f}$	2.60E-02 (6.2%)	2.24E-02
$^{237}\mathrm{Np_f}$	1.26E-02 (5.4%)	1.20E-02
$^{238}\mathrm{U_f}$	4.49E-02 (3.4%)	4.78E-02
$^{239}\mathrm{Pu_t}$	6.56E-03 (6.9%)	6.50E-03
$^{239}\mathrm{Pu_f}$	7.22E-03 (6.8%)	6.50E-03
$^{241}\mathrm{Pu_t}$	1.37E-02 (4.5%)	1.60E-02
$^{241}\mathrm{Pu_f}$	1.41E-02 (5.1%)	1.60E-02
$^{241}\mathrm{Am_f}$	4.44E-03 (12.9%)	4.30E-03

Table 2: Temps de vie moyen associé à l'$^{235}\mathrm{U_t}$ calculé en utilisant différentes techniques de sommation et comparé avec la valeur recommandée par le WPEC-SG6. Les incertitudes sont données en pourcentage du $\overline{T_{1/2}}$.

	WPEC-6	Simple Eq.	Exponential Eq.	MC Margi.	AN Margi.
$\overline{T_{1/2}}$	9.02 (3.0%)	9.24 (3.2%)	9.27 (6.6%)	9.45 (6.1%)	9.43 (6.4%)

trons retardés, avec un écart maximale de 0.3%. Cependant, la réactivité est surestimée d'environ 2.2%. Bien au contraire, les deux méthodes de sommation directe sous-estiment l'activité de 2.5 à 4%, mais reproduisent parfaitement la réactivité. La raison est que la réactivité associée à des longues périodes dépend fortement du temps de vie moyen, qui est mieux estimé par des calculs directs plutôt que par des ajustements. Les $\overline{T_{1/2}}$ calculés avec la méthode exponentielle ainsi que les valeurs recommandées par le WPEC-6 sont comparés dans le Tableau 3.

Table 3: Temps de vie moyen pour les principaux systèmes fissionants.

Fiss. Syst.	$\overline{T_{1/2}}$ [s]	
	Exp. Eq.	WPEC-6
$^{232}Th_f$	6.11 (6.0%)	6.99 (2.7%)
$^{233}U_t$	11.88 (8.9%)	12.78 (4.0%)
$^{233}U_f$	10.63 (9.4%)	12.39 (3.4%)
$^{235}U_t$	9.27 (6.6%)	9.02 (3.0%)
$^{235}U_f$	8.44 (6.6%)	9.11 (1.0%)
$^{236}U_f$	7.01 (8.3%)	7.34 (8.5%)
$^{237}Np_f$	8.77 (7.7%)	8.87 (0.8%)
$^{238}U_f$	5.11 (4.8%)	5.32 (2.0%)
$^{239}Pu_t$	10.49 (9.0%)	10.69 (8.1%)
$^{239}Pu_f$	9.14 (9.8%)	10.35 (10.0%)
$^{241}Pu_t$	9.14 (6.2%)	7.78 (4.9%)
$^{241}Pu_f$	8.59 (6.7%)	7.85 (6.8%)
$^{241}Am_f$	10.42 (16.6%)	9.99 (11.5%)

Approche macroscopique

Le projet ALDEN a été lancé pour procéder à une nouvelle évaluation des données des neutrons retardés associées à la fission thermique de l'^{235}U. L'objective principale était de réduire les incertitudes par rapport aux données de Keepin. De plus, cela aurait permis à la communauté internationale d'avoir accès à des courbes expérimentales pour tester des éventuelles modifications du modèle à huit familles. Finalement, ce projet visait aussi à produire une matrice de corrélations associée aux huit abondances, absente dans la plupart des mesures. Dans cette thèse, un détecteur a été développé et une expérience mise en place pour mesurer l'activité en neutrons retardés et dériver les quantités d'intérêt et les incertitudes associées.

Pour mesurer l'activité en neutrons retardés, la première étape consiste à irradier la cible fissile pour un certain temps t_{irr}. Les neutrons, frappant la cible, causent des fissions. Pour chaque fission, des produits de fission sont émis, et avec eux 2 ou 3 neutrons prompt. La deuxième étape consiste à interrompre le faisceau de neutrons avec un beam-shutter. Le processus de fission s'interrompt et avec lui l'émission de neutrons prompts. A ce moment ci, seuls le neutrons retardés sont présents et leurs activité, qui suit la décroissance des précurseurs, peut être mesurée et utilisée pour estimer le rendement en neutrons retardés ainsi que les abondances à huit familles. Le détecteur LOENIE-V2 a été spécialement conçu pour l'expérience ALDEN.

La cible utilisée dans l'expérience ALDEN est une chambre a fission miniaturisée avec un dépôt de matériel fissile électrodeposé sur un support en titanium de 8 mm de diamètre. La quantité de matière fissile a été choisie pour ne pas dépasser 10 kHz sur chaque tube à ^{3}He pendant la phase d'irradiation sous un flux équivalent de neutrons de $4 \cdot 10^8$ cm^{-2}s^{-1}. Cette limite a comme objective de préserver l'intégrité des détecteurs et éviter les effets de temps mort. En 2018 trois cibles ont été fabriquées : ^{235}U (210 μg), ^{239}Pu (140 μg), et une cible témoin sans dépôt.

Pour interrompre le faisceau assez rapidement et de manière programmée, un nouveau

système a été conçu. Il s'agit d'un moteur brushless tournant supportant une plaquette en aluminium avec deux écrans neutroniques. Les matériaux absorbants ont été choisis pour réduire le taux de fission dans la cible d'un facteur 10^8.

Le système d'acquisition comprends le DDP (Digital Pulse Processing), implémenté dans la carte CAEN V1724, utilisé pour passer du signal analogique au signal numérique. Chaque signal passe à travers deux filtres : un en temps et un en énergie. Le logiciel utilisé pour accéder à la mémoire de la carte et transférer les données sur le disque, a été fourni par l'ILL et il s'appelle *Nomade*.

Dans le cadre de l'expérience ALDEN, plusieurs campagnes expérimentales ont été réalisées. La plus importante a eu lieu auprès du réacteur de l'ILL en Septembre 2018 pour la mesure de l'activité ainsi que du bruit de fond et du temps mort. En Janvier 2019, LOENIE-V2 a été envoyé en Angleterre pour une mesure d'efficacité absolue avec des sources de neutrons. En Mars, l'efficacité relative a été mesurée auprès de l'accélérateur de l'IRSN AMANDE. De plus, un test avec un pulser a eu lieu à Cadarache pour l'estimation du temps mort et du pile-up du système d'acquisition.

Nomad transfère les données sous forme de fichiers binaires contenant, pour chaque événement, le temps d'arrivée, l'énergie et le détecteur dans lequel le signal a été détecté. Un logiciel, nommé *Alproc* a été codé en C++ pour traduire les fichiers binaires en fichiers texte et pour corriger les éventuels bugs de codage. Pour l'analyse des données, un autre logiciel, appelé *Alden*, a été créé, ayant pour objectif de transformer toutes les acquisitions réalisées en une courbe moyenne de décroissance, corrigée du temps mort et du bruit de fond. La perte de comptage due au pile-up du système d'acquisition a été estimée avec un pulser à environ 5% et elle a été corrigée, pour chaque voie de chaque acquisition, avec un polynôme empirique. Les équations décrivant le comptage des neutrons pendant la phase d'irradiation et la phase de décroissance sont décrites en Eq. 2 et Eq. 3.

$$\overline{n_{irr}} = F(\nu_p\epsilon_p + \nu_d\epsilon_d) + b_{irr}, \tag{2}$$

$$n_{dec}(t) = F\nu_d\epsilon_d \sum_{i=1}^{8} f_i a_i (1 - e^{-\lambda_i t_{irr}})(1 + e^{-\lambda_i t_m})e^{-\lambda_i t_0} e^{-\lambda_i t} + b_{dec} \tag{3}$$

En exploitant les deux équations, il est possible d'obtenir une expression de l'activité qui ne nécessite pas l'estimation explicite du taux de fission (F). La première étape de l'analyse consiste à ajuster le ν_d en utilisant les 500 premières ms de la courbe après la fin de l'irradiation. Touts les paramètres apparaissant dans le modèle sont marginalisés de façon à transférer leurs incertitudes à la variable ajustée. La deuxième étape consiste à ajuster les huit abondances sur la courbe de décroissance entière, en marginalisant cette fois seulement le ν_d obtenu dans l'étape précédente. Il est important de souligner que les paramètres d'intérêt sont laissés complètement libres dans l'ajustement, en ayant des prior improbables et très incertains. Les résultats de cette procédure sont comparés avec la littérature en Fig. 1 et 2. L'accord des mesures ALDEN avec les évaluations les plus récentes, ainsi que la grande réduction des incertitudess sont évidents.

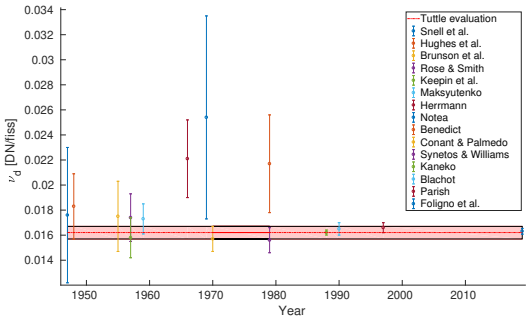

Figure 1: ν_d mesuré expérimentalement pour l'$^{235}U_t$. La bande rouge représente la valeur recommandée par Tuttle en 1979.

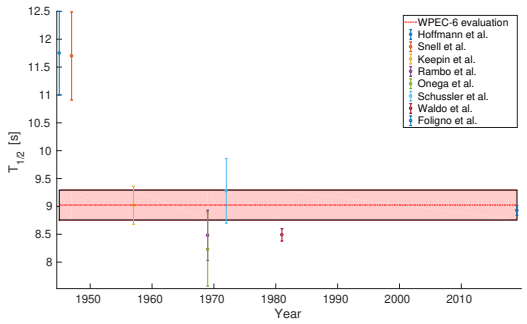

Figure 2: ν_d mesuré expérimentalement pour l'$^{235}U_t$. La bande rouge représente la valeur recommandée par le WPEC-6 en 2002.

Évaluation et benchmarking

L'inférence Bayesienne permet d'améliorer l'estimation des paramètres à partir d'expériences en faisant des hypothèses sur le résultat. Ce théorème a été utilisé pour l'estimation des paramètres des neutrons retardés en utilisant un modèle théorique, des données expérimentales et une connaissance préalable des paramètres (prior) calculés par sommation. De cette façon, les approches microscopique et macroscopique ont été combinées et exploitées au mieux. Le fait de donner un prior bien défini contraint l'ajustement. Le rendement en neutron retardés et les abondances à huit familles estimées à travers les différentes étapes de ce travail sont reportés dans le Tab. 4. La Figure 3 montre la matrice de corrélation associée aux abondances obtenues à travers l'assimilation Bayesienne .
La première chose à remarquer est que rien n'a changé pour le ν_d, ni en valeur ni en incertitude, ce qui veut dire que le calcul n'a pas apporté d'informations supplémentaires, ce qui n'est pas le cas pour les abondances. Les familles à vie plus courte ont subi une forte réduction des incertitudes. L'amélioration globale des abondances peut être aperçue à travers la comparaison des temps de vie moyen. La combinaison des deux méthodes donne une valeur plus proche de celle recommandée par le WPEC-6. De plus, l'incertitude est réduite de 3% à 0.5%.

Pour tester les nouvelles données de rendement moyen de neutrons retardés (l'$^{235}U_t$ calculé et mesuré et l'$^{238}U_f$ calculé), trois benchmarks ont été choisis. Le trois visent à mesurer la fraction effective des données en neutrons retardés (β_{eff}) du cœur à

Table 4: Données des neutrons retardés obtenues dans les différentes étapes de ce travail.

Quantité	**WPEC-6**	**Foligno et al.**		
		Sommation	**Expérience**	**Inférence Bayesienne**
ν_d [DN/fiss]	1.620E-02 (-)	1.609E-02 (5.2%)	1.631E-02 (1.4%)	1.645E-02 (1.6%)
a_1	3.28E-02 (12.8%)	3.50E-02 (14.6%)	3.64E-02 (2.7%)	3.55E-02 (1.8%)
a_2	1.54E-01 (4.4%)	1.61E-01 (14.9%)	1.31E-01 (3.3%)	1.38E-01 (2.4%)
a_3	9.14E-02 (9.8%)	9.48E-02 (17.2%)	1.15E-01 (4.9%)	1.08E-01 (3.8%)
a_4	1.97E-01 (11.7%)	1.72E-01 (15.4%)	1.66E-01 (4.8%)	1.78E-01 (3.5%)
a_5	3.31E-02 (2.0%)	3.16E-01 (9.11%)	3.55E-01 (5.2%)	3.37E-01 (3.4%)
a_6	9.03E-02 (5.0%)	1.35E-01 (11.9%)	6.92E-02 (40.8%)	9.51E-02 (15.0%)
a_7	8.12E-02 (2.0%)	6.09E-02 (41.2%)	8.15E-02 (49.3%)	7.32E-02 (16.0%)
a_8	2.29E-02 (41.5%)	2.35E-02 (12.7%)	4.58E-02 (66.3%)	3.51E-02 (25.3%)
$\overline{T_{1/2}}$ [s]	9.02 (3.0%)	9.27 (6.6%)	8.93 (5.7%)	8.98 (2.2%)
$\overline{T_{1/2}}$ avec corr [s]	9.02 (3.0%)	9.27 (6.6%)	8.93 (1.0%)	8.98 (0.6%)

$$\begin{bmatrix} 1 & -0.696 & 0.693 & -0.303 & 0.226 & -0.07 & 0.003 & -0.102 \\ -0.696 & 1 & -0.876 & 0.686 & -0.387 & 0.322 & -0.131 & -0.246 \\ 0.693 & -0.876 & 1 & -0.751 & 0.554 & -0.306 & 0.093 & -0.004 \\ -0.303 & 0.686 & -0.751 & 1 & -0.848 & 0.651 & -0.26 & -0.191 \\ 0.226 & -0.387 & 0.554 & -0.848 & 1 & -0.823 & 0.384 & -0.021 \\ -0.07 & 0.322 & -0.306 & 0.651 & -0.823 & 1 & -0.705 & -0.025 \\ 0.003 & -0.131 & 0.093 & -0.26 & 0.384 & -0.705 & 1 & -0.519 \\ -0.102 & -0.246 & -0.004 & -0.191 & -0.021 & -0.025 & -0.519 & 1 \end{bmatrix}$$

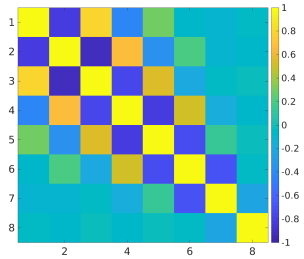

Figure 3: Matrice de corrélation associée aux abondances à huit familles dérivées par assimilation Bayesienne de la manip ALDEN.

travers la technique du bruit neutronique. Pour les deux premiers, MISTRAL1 et IPEN/MB-01, principalement sensibles à l'$^{235}U_t$, les résultats montrent qu'il y a une compensation entre l'augmentation du ν_d de l'$^{235}U_t$ et la réduction du ν_d de l'$^{238}U_f$. Globalement, la simulation donne un C/E de +1.3% ± 1.5% pour MISTRAL1 et de +4.12% ± 0.67% pour IPEN/MB-01, un peu plus écartés que les simulations faites avec JEFF-3.1.1. Le troisième benchmark, SNEAK7B, étant plus sensible à l'$^{238}U_f$, donne un C/E de -2.30% ± 5.0%.

Une partie du benchmark IPEN/MB-01 était dédiée à la mesure de la réactivité, qui peut être utilisé pour tester les paramètres cinétiques. La réactivité dépend du β_{eff} mais aussi du temps de vie moyen. L'amélioration apportée par l'expérience ALDEN (*Foligno et al.*) par rapport aux bases de données internationales, est soulignée en Fig. 4. Pour conclure, un dernier test a été mené pour évaluer les effets liés à la réduction importante des incertitudes sur les données des neutrons retardés. Le test consiste à calculer, pour un vecteur de périodes du réacteur donné, la réactivité associée et son incertitude, en utilisant les données de neutrons retardés recommandées par JEFF-3.1.1 et évaluées au cours de ce travail. L'incertitude en fonction de la réactivité elle même est montrée en Fig. 5.

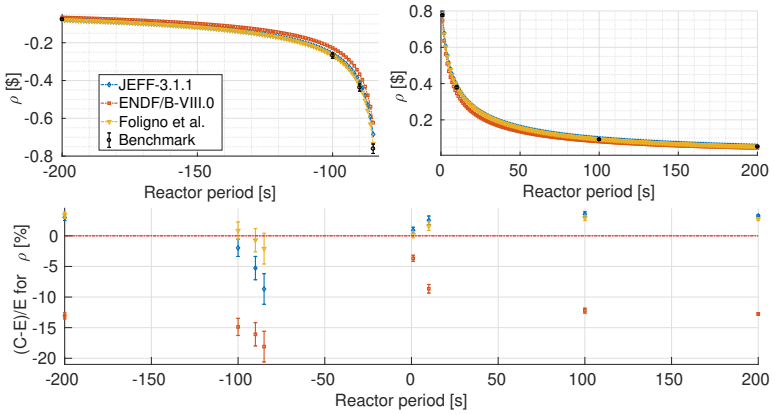

Figure 4: Comparaison des simulations de la réactivité pour le cœur IPEN/MB-01. Il est important de remarquer que les incertitudes associées aux (C-E)/E sont les incertitudes de l'expérience. t (E).

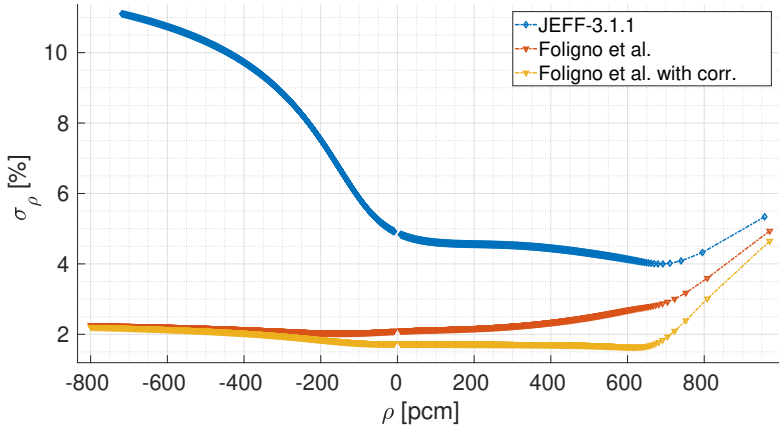

Figure 5: Effet des données d'entrée sur l'incertitude de la reactivité simulée.

Conclusions et perspectives

L'innovation principale de ce travail était d'appliquer aux neutrons retardés la même procédure généralement utilisée pour l'évaluation des sections efficaces. Cette technique consiste à calculer des quantités par sommation et à ajouter, au modèle théorique, une ou plusieurs observables expérimentales. Elle a été testée pour la fission thermique de l'^{235}U. Les quantités d'intérêt ont été calculées par sommation pour les systèmes fissionants les plus importants. En ce qui concerne la partie expérimentale, le projet ALDEN a été lancé et l'activité des neutrons retardés a été mesurée pour différents cycles d'irradiation (de 0.25 à 50 s) et de décroissance. Malheureusement, le seuil de détection des neutrons a été mal choisi pour les cycles courts, qui n'ont pas pu être exploités. En perspective, il serait intéressant de réaliser de nouvelles mesures avec des cycles courts. En particulier, étant donné que pour l'estimation du ν_d seulement le premiers 500 ms sont nécessaires, il serait interessant d'optimiser les cycles d'irradiation et décroissance. De plus, il faudrait répéter toute l'expérience avec des nouvelles cibles fissiles. Trois sets de résultats ont été obtenus : le résultat du calcul, le résultat de l'expérience et le résultat venant de la combinaison Bayesienne des deux premiers. Ce dernier set a été testé avec trois benchmarks : MISTRAL1, IPEN et SNEAK7B. La réussite principale de ce travail est l'

amélioration importante de la réactivité prédite, plus particulièrement pour des périodes négatives. De plus, elle est accompagné par une précision extrêmement bonne, qui ne dépasse jamais 2.2%. Il est important de souligner que l'industrie associe aujourd'hui au β_{eff} une incertitude de 5%, qui uni aux 3% du $\overline{T_{1/2}}$ donne une incertitude sur la réactivité de 6%! Ce travail a donc permis de produire des données de NR avec une justesse et une précision très nettement améliorées.

Part I

Bibliography

Chapter 1

Introduction to Delayed Neutrons

> You've got to get the fundamentals down, because otherwise the fancy stuff is not going to work.
>
> Randy Pausch

Contents

1.1 Energy from Fission . . . 3
1.2 The Importance of Delayed Neutrons in Reactor Physics . . 5
1.2.1 Basic Quantities . . . 5
1.2.2 The Effect of Delayed Neutrons . . . 5
1.2.3 The Inhour Equation . . . 7
1.2.4 The Decay Heat . . . 10
1.3 Quantities of Interest . . . 10
1.3.1 Microscopic nuclear parameters . . . 11
1.3.2 Macroscopic nuclear parameters . . . 12
1.3.3 Reactor parameters . . . 13
1.4 A Bit of History . . . 14
1.4.1 The International Databases . . . 14
1.4.2 "Dear Old Keepin" . . . 15
1.4.3 Tuttle's evaluation of ν_d . . . 17
1.4.4 Brady & England's summation calculation . . . 18
1.4.5 The NEA/WPEC-SG6 . . . 19
1.4.6 The IAEA/CRP . . . 22
1.5 Scientific challenges of this Ph.D. . . . 22

The objective of this chapter is to make the reader understand the importance of having a good knowledge of the delayed-neutron data. Section 1.1 describes the fission process and the origin of delayed neutrons. Section 1.2 focuses on the importance of such neutrons while Section 1.3 introduces the quantities of interest for reactor physics applications. The bibliography on the state of the art is done in Section 1.4, where the main works performed so far are mentioned and quickly described. Finally, Section 1.5 illustrates the scientific challenges of this Ph.D.

1.1 Energy from Fission

The Energy Transformations If you can read your emails every day and you managed to download this thesis from your laptop is because physicists and engineers worked together to transform heat into electricity and to bring it right into your home. If you live in France, there is a strong probability that the energy you are using comes from nuclear power. Nuclear fission reactors are a clean and sustainable way of producing electricity. From the nucleus of a fuel atom to our homes, the energy undergoes several transformations. The mass difference between fission fragments and the fissioning nucleus mainly appears as kinetic energy of the fragments[1]. The kinetic energy is lost in the structures as heat. The thermal energy is then extracted by a coolant and transferred to a secondary circuit where it is transformed into the mechanical work of a turbine. Finally, an electric generator transforms mechanical energy into electricity.

The Fission Process The most common fuel used in current nuclear reactors is made of ^{235}U and ^{239}Pu. Both of them are called *fissile* because they can undergo fission if hit by a neutron of any energy. Let's take the example of the ^{235}U. In the uranium nucleus, the nucleons are bound together by an average binding energy of 7.6 MeV per nucleon[2]. In the fission fragment nuclei, the medium binding energy per nucleon amounts to approximately 8.5 MeV. The difference in binding energy (0.9 MeV per nucleon, thus about 200 MeV per ^{235}U nucleus) is the ancestor of the electricity we use to charge our mobile phones [4]. Right after the fission process (10^{-18} to 10^{-14} s), 2 or 3 neutrons are emitted from the excited fission fragments (*neutron evaporation and prompt-gamma emission*). Those neutrons are called *prompt* because they can be considered as if they were created *during* fission. The number of prompt neutrons emitted by a fragment partly depends on the mass of the fragment itself. After the neutron evaporation, fission fragments are called *fission products*. Figure 1.1 illustrates the fission process and the chain reaction. Fission products, being neutron-rich isotopes, are naturally unstable. To

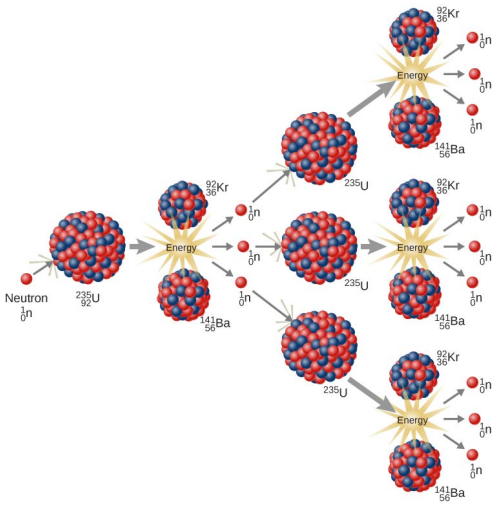

Figure 1.1: Illustration of Neutron Induced Nuclear Fission (taken from [2]).

[1] Note that about 85% of the mass difference is transformed into kinetic energy, while the remaining 15% appears as excitation energy of the fragments.

[2] The binding energy is the energy required to separate particles which are bound by electromagnetic or nuclear forces.

reach stability, they undergo a series of β^- decays. A fraction of those decays ends up with the daughter having an excitation energy (Q_β) larger than the separation energy of the last neutron (S_n), leaving to the isotope the possibility of reaching stability through either gamma- or neutron-emission (P_n).

Figure 1.2 shows the ways through which a fission fragment can reach stability. This neutron is emitted instantaneously at the moment of the β^--decay and it is a common practice to consider it to be emitted by the father, called *delayed-neutron precursor* rather than by the daughter, called *delayed-neutron emitter*. Neutrons arising from the de-excitation of fission products are called *delayed* because they appear with a certain delay with respect to fission (from a fraction of a second to some minutes).

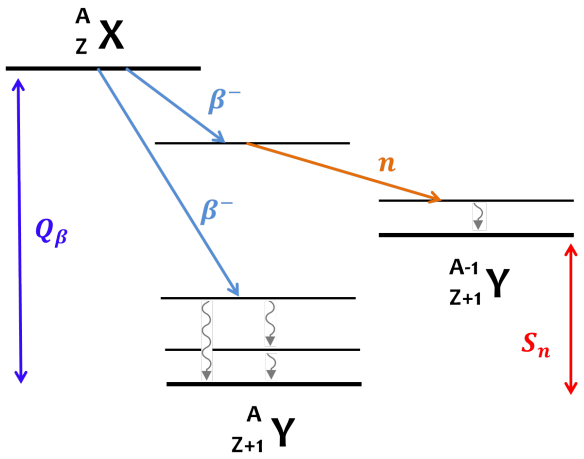

Figure 1.2: General fission products' decay scheme.

Figure 1.3 illustrates the decay scheme for ^{137}I, one of the most important precursors. The delay in the appearance of the neutron with respect to the fission event is only due to the half-life of the precursor. Delayed neutrons account for less than 1% of the total neutron emission.

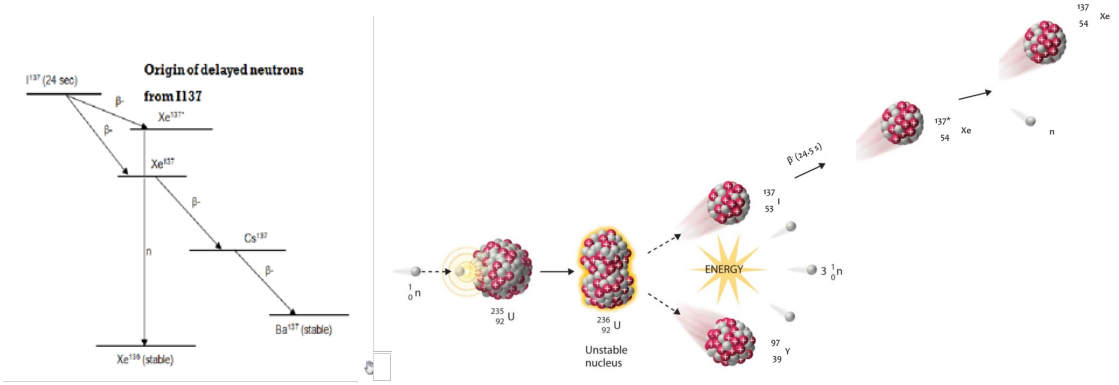

(a) ^{137}I decay scheme. (b) Illustration of the process.

Figure 1.3: delayed-neutron emission from ^{137}I, scheme and illustration.

1.2 The Importance of Delayed Neutrons in Reactor Physics

1.2.1 Basic Quantities

In order to understand why delayed neutrons are so important in reactor physics, some quantities need to be introduced. It has been already mentioned that, for each fission event, most of the neutrons are promptly emitted while less than 1% arrives with a certain delay. To distinguish the two types of neutrons, reactor physicists introduced the following variables

- ν_p - *prompt-neutron yield*
- ν_d - *delayed-neutron yield*
- ν_t or ν - *total-neutron yield* ($\nu = \nu_p + \nu_d$)

which represent the prompt, delayed and total number of neutrons emitted per fission. To have an order of magnitude, the neutron-induced fission of a nucleus of ^{235}U is followed by the emission of about 2.425 neutrons (ν_t), of which 0.0162 are born delayed (ν_d). The fraction of the two (β) is called *total delayed-neutron fraction* and is defined as

$$\beta = \frac{\nu_d}{\nu_t} \approx 0.7\%. \tag{1.1}$$

In steady state operations, nuclear reactors operate near what is called *critical state*, a favorable condition in which the neutron population is at equilibrium. Neutrons are produced by fission and disappear by absorption, capture or leakage. To monitor the neutron balance, reactor physicists introduced the *reactivity* (ρ), a quantity that measures how far a reactor is from criticality

$$\rho = \frac{\delta k}{k} = \frac{k-1}{k}. \tag{1.2}$$

In Eq. 1.2, k is the neutron multiplication factor and it characterizes the chain reaction since it represents the ratio between two generations of neutrons[3]. In critical conditions, $k = 1$ and $\rho = 0$, meaning that the chain reaction is self-sustaining (one of the neutrons produced per each fission survives capture, absorption, and leakage and causes further fission). In order for a reactor to be under control, the system must be subcritical ($k < 1$) with prompt neutrons and critical ($k = 1$) with delayed neutrons.

1.2.2 The Effect of Delayed Neutrons

Delayed neutrons are very important from the point of view of reactor kinetics and safety [26]. The delay introduced by such a small fraction of neutrons in the dynamic time response of a reactor allows the control of the neutron population by mechanical systems. The rate of change of the neutron population due to a step reactivity insertion depends on the inserted reactivity (ρ) and on the mean neutron lifetime (ℓ), the average time a neutron spends in the system before leaking or being absorbed. To describe the rate of change of the neutron population, the *point-kinetics equation*[4] is used

$$\frac{\mathrm{d}n}{\mathrm{d}t} = \frac{kn - n}{\ell} = \frac{n}{\ell}\delta k, \tag{1.3}$$

[3]Note that in the whole thesis, k stands for k_{eff}, the *effective multiplication factor*, which differs from k_∞ since it takes into account the thermal and fast neutron leakage probabilities.

[4]The hypothesis behind this formulation is that only the amplitude of the neutron flux changes, while the shape does not. The reactor is considered as a point, as the name of the equation suggests.

whose solution is[5]

$$n(t) = n_0\, e^{\frac{\delta k}{\ell} t}, \tag{1.4}$$

where n is the neutron density and n_0 is its value at $t = 0$. Equation 1.4 shows that the reactor power will exponentially increase at a rate which depends on the ratio $\delta k/\ell$. The *reactor period* (τ) is the time needed for the system to raise the neutron flux by a factor e

$$n(\tau) = n_0\, e^{\frac{\delta k}{\ell}\tau} = n_0\, e \Rightarrow e = e^{\frac{\delta k}{\ell}\tau} \Rightarrow \frac{\delta k}{\ell}\tau = 1 \tag{1.5}$$

$$\tau = \frac{\ell}{\delta k} \tag{1.6}$$

Substituting Eq. 1.6 in Eq. 1.4 one has

$$n(t) = n_0\, e^{\frac{t}{\tau}}. \tag{1.7}$$

In absence of delayed neutrons, the mean neutron lifetime corresponds to the prompt neutron lifetime ($\ell = \ell_p = 10^{-5}$ s). The main effect of the delayed neutrons is to increase the average lifetime from about 10^{-5} s to about 0.085 s.
Figure 1.4 shows this effect. For each fission, $(1 - \beta_{eff})\nu_t$ prompt neutrons are immediately created and remain in the system for a time ℓ_p. After a certain average time $\overline{T}$ (delayed-neutron lifetime), $\beta_{eff}\nu_t$ delayed neutrons are emitted and, like all neutrons, absorbed after a time ℓ_p.

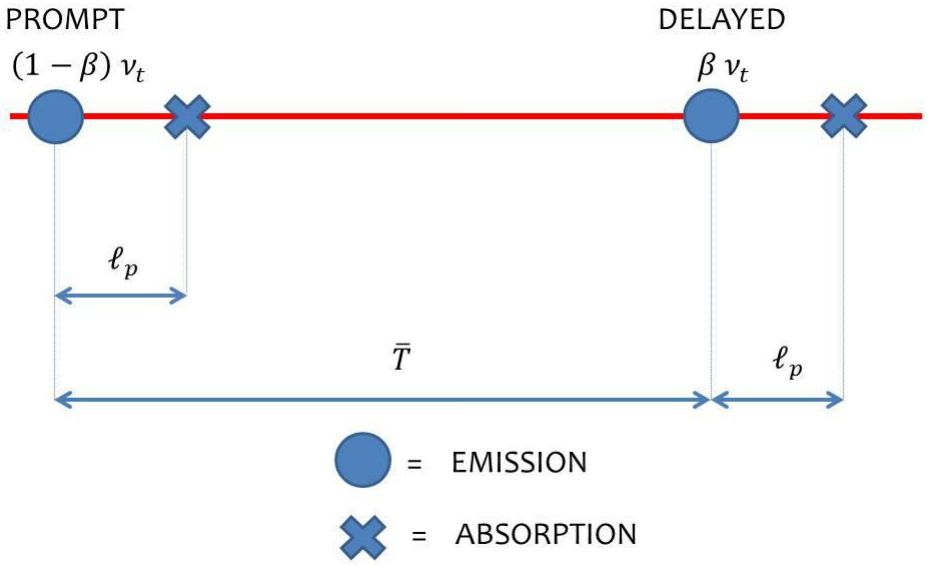

Figure 1.4: Illustration of the delayed neutron effect on the mean neutron lifetime.

From the system's point of view, a fraction $(1 - \beta_{eff})$[6] of all neutrons lives ℓ_p and a fraction β_{eff} lives $\overline{T} + \ell_p$. Therefore, the weighted average of the mean neutron lifetime can be written as

$$\ell = (1 - \beta_{eff})\ell_p + \beta_{eff}(\overline{T} + \ell_p) = \ell_p + \beta_{eff}\overline{T} \approx \beta_{eff}\overline{T}. \tag{1.8}$$

[5]The solution is obtained assuming the mean lifetime and the reactivity to be constant during the transient.

[6]β is a *nuclear* parameter and must be distinguished from the *Total Effective Delayed–Neutron Fraction*, β_{eff}, which is a *reactor* parameter. The reader who needs further clarification can go to Subsection 1.3.3.

This means that for a step reactivity insertion of 10 pcm (from k=1.0000 to k=1.0001) the time needed to increase the power by a factor 2.718 would be $\tau = 10^{-5}/0.0001 = 1$ s without delayed neutrons and $\tau = 0.085/0.0001 = 850$ s with delayed neutrons, much easier to control. The reactor period is a *measurable* quantity which can be used to *estimate* the inserted reactivity if delayed neutron parameters are known.

1.2.3 The Inhour Equation

Equation 1.3 is only an approximation and is not valid for large reactivity insertions. The *exact point kinetic equations* are the following

$$\begin{cases} \frac{dn}{dt} & = \frac{\rho-\beta_{eff}}{\Lambda} n(t) + \sum_{i=1}^{G} \lambda_i C_i(t) \\ \frac{\mathrm{d}C_i(t)}{\mathrm{d}t} & = \frac{\beta_{eff,i}}{\Lambda} n(t) - \lambda_i C_i(t). \end{cases} \tag{1.9}$$

The first equation describes the change of the neutron density in time, while the others are the precursor-balance equations. Λ is the *effective generation time*. In principle, G should be the number of precursors in the system. In reality, it is common practice to sort the precursors in 6 or 8 groups, each of which is characterized by a specific decay constant λ_i. $C_i(t)$ is the concentration of the precursor (or of the group) at a certain time, and the second equation represents its evolution.

Solution in case of constant parameters In the case of a steady-state subcritical reactor in presence of a step-reactivity insertion, the parameters ρ, β_{eff} and Λ are time independent. Equation 1.9 is a system of $G+1$ first-order linear differential equations, whose solution is a linear combination of exponential solutions [53] of the type

$$\begin{bmatrix} n(t) \\ C_1(t) \\ \vdots \\ C_G(t) \end{bmatrix} = \begin{bmatrix} n \\ C_1 \\ \vdots \\ C_G \end{bmatrix} e^{\omega t}. \tag{1.10}$$

The final solution is therefore of the form

$$\begin{bmatrix} n(t) \\ C_1(t) \\ \vdots \\ C_G(t) \end{bmatrix} = \sum_{j=0}^{G} \begin{bmatrix} n_j \\ C_{1,j} \\ \vdots \\ C_{G,j} \end{bmatrix} e^{\omega_j t}. \tag{1.11}$$

Substituting Eq. 1.10 into Eq. 1.9 one has

$$\begin{cases} n_0 \omega e^{\omega t} & = \frac{\rho-\beta_{eff}}{\Lambda} n_0 e^{\omega t} + \sum_{i=1}^{G} \lambda_i C_{1,0} e^{\omega t} \\ C_{1,0} \omega e^{\omega t} & = \frac{\beta_{eff,i}}{\Lambda} n_0 e^{\omega t} - \lambda_i C_{1,0} e^{\omega t} \end{cases} \tag{1.12}$$

and, after the simplification of the terms $e^{\omega t}$,

$$\begin{cases} n_0 \omega & = \frac{\rho-\beta_{eff}}{\Lambda} n_0 v + \sum_{i=1}^{G} \lambda_i C_{1,0} \\ C_{1,0} \omega & = \frac{\beta_{eff,i}}{\Lambda} n_0 - \lambda_i C_{1,0}. \end{cases} \tag{1.13}$$

Extracting C_i from the second equation of the system 1.13

$$C_{1,0} = \frac{\beta_{eff,i}}{\Lambda(\lambda_i + \omega)} n_0, \tag{1.14}$$

substituting it into the first one

$$\cancel{n_0}\omega = \frac{\rho - \beta_{eff}}{\Lambda}\cancel{n_0} + \sum_{i=1}^{G} \lambda_i \frac{\beta_{eff,i}}{\Lambda(\lambda_i + \omega)}\cancel{n_0} \tag{1.15}$$

and rearranging the terms, one obtains what is called *Inhour Equation* or *Nordheim Equation*

$$\begin{aligned} \rho &= \Lambda\omega + \beta_{eff} - \sum_{i=1}^{G} \frac{\lambda_i \beta_{eff,i}}{(\lambda_i+\omega)} \\ &= \Lambda\omega + \sum_{i=1}^{G} \beta_{eff,i} - \frac{\lambda_i \beta_{eff,i}}{(\lambda_i+\omega)} \\ &= \Lambda\omega + \sum_{i=1}^{G} \frac{\beta_{eff,i}(\lambda_i+\omega) - \lambda_i \beta_{eff,i}}{(\lambda_i+\omega)} \\ &= \Lambda\omega + \sum_{i=1}^{G} \frac{\beta_{eff,i}\omega}{(\lambda_i+\omega)} \end{aligned} \tag{1.16}$$

$$\boxed{\rho = \omega\left(\Lambda + \sum_{i=1}^{G} \frac{\beta_{eff,i}}{\lambda_i + \omega}\right)} \tag{1.17}$$

For a step reactivity insertion ρ, Eq. 1.17 has $G+1$ roots, the exponents ω of the $G+1$ fundamental solutions. The RHS (*Right-Hand-Side*) of Eq. 1.17 is plotted as a function of ω in Figure 1.5 for six delayed-neutron groups ($G = 6$).

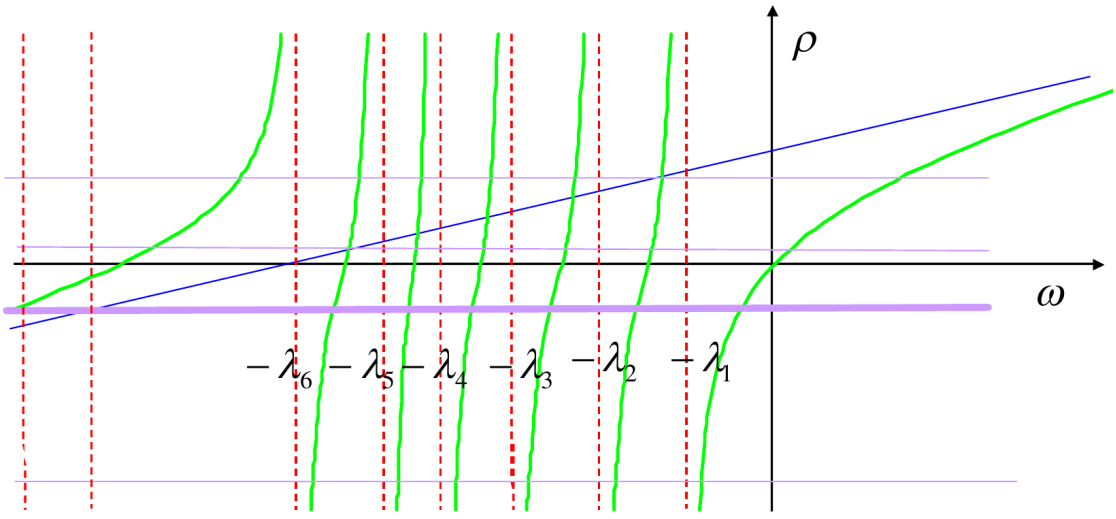

Figure 1.5: Illustration of the G+1 solutions of the Inhour Equation [53].

The solutions of the equation are the points of intersection between the RHS and the horizontal line $y = \rho$ (constant reactivity). G solutions are always negative while the one at the right of $-\lambda_1$ depends on the sign of the reactivity and is usually referred to as ω_0 or ω_{max}. Correspondingly, ω_{min} is situated at the left of $-\lambda_G$ (in this case $-\lambda_6$).

The solution 1.11 can be factorized in order to isolate the first and largest exponential term $e^{\omega_0 t}$, the only one that can survive for $t \to \infty$ since $(\omega_j - \omega_0) < 0$.

$$\begin{aligned}
\begin{bmatrix} n(t) \\ C_1(t) \\ \vdots \\ C_G(t) \end{bmatrix} &= \sum_{j=0}^{G} \begin{bmatrix} n_j \\ C_{1,j} \\ \vdots \\ C_{G,j} \end{bmatrix} e^{\omega_j t} = \begin{bmatrix} n_0 \\ C_{1,0} \\ \vdots \\ C_{G,0} \end{bmatrix} e^{\omega_0 t} + \cdots + \begin{bmatrix} n_G \\ C_{1,G} \\ \vdots \\ C_{G,G} \end{bmatrix} e^{\omega_G t} \\
&= e^{\omega_0 t} \left(\begin{bmatrix} n_0 \\ C_{1,0} \\ \vdots \\ C_{G,0} \end{bmatrix} + \sum_{j=1}^{G} \begin{bmatrix} n_j \\ C_{1,j} \\ \vdots \\ C_{G,j} \end{bmatrix} e^{(\omega_j - \omega_0)t} \right) \\
&\underset{=}{t \to \infty} e^{\omega_0 t} \begin{bmatrix} n_0 \\ C_{1,0} \\ \vdots \\ C_{G,0} \end{bmatrix},
\end{aligned} \tag{1.18}$$

The last line of Eq. 1.18 describes the asymptotic behaviour of the system after the transition phenomena have died out, and the inverse of ω_0 is called *asymptotic period*

$$\tau = \frac{1}{\omega_0}. \tag{1.19}$$

For a negative reactivity insertion, all exponents of 1.11 die out and, after a certain time, all the terms drop to zero. For a positive reactivity insertion, all exponents except the first one are negative and, after a long time, both the neutron populations and the precursor concentrations exponentially increase according to $e^{\frac{t}{\tau}}$. Finally, if $\rho = 0$, G solutions die out while $\omega_0 = 0$. Neutrons and precursors stabilize at a constant value. From the measurement of the asymptotic period it is possible to infer the reactivity inserted in the system.

Low reactivity insertion If the inserted reactivity is very small ($\rho \ll \beta_{eff}$), ω_0 is also very small ($\omega_0 \ll \lambda_G$) and Eq. 1.17 becomes

$$\rho \approx \omega \left(\Lambda + \sum_{i=1}^{G} \frac{\beta_{eff,i}}{\lambda_i} \right) \tag{1.20}$$

Considering that $T_i = \frac{1}{\lambda_i}$ and remembering Eq. 1.19, the reactor period can be found as

$$\tau \approx \frac{1}{\rho} \left(\Lambda + \sum_{i=1}^{G} \beta_{eff,i} T_i \right) \approx \frac{\beta_{eff} \overline{T}}{\rho} \tag{1.21}$$

Less than one prompt neutron is produced per generation and there must be delayed neutrons to keep the system supercritical [43].

Large reactivity insertion If, on the other hand, the inserted reactivity is larger than the effective delayed-neutron fraction $\rho \geq \beta_{eff}$, prompt neutrons compensate by themselves the neutron loss and the first root of the Inhour Equation is large with respect to the delayed-neutron decay constants ($\omega_0 \gg \lambda_G$). In that case Eq. 1.17 becomes

$$\rho \approx \omega \left(\Lambda + \sum_{i=1}^{G} \frac{\beta_{eff,i}}{\omega} \right) = \omega \Lambda + \beta_{eff} \tag{1.22}$$

and

$$\tau \approx \frac{\Lambda}{\rho - \beta_{eff}}. \tag{1.23}$$

Comparing Eq. 1.20 and Eq. 1.22 one can conclude that for small reactivity insertions the kinetic of the reactor is dominated by delayed neutrons ($\overline{T}$), while for large reactivities, the exponential increase is driven by prompt neutrons only (Λ).

1.2.4 The Decay Heat

As mentioned in the very first paragraph of the thesis, the energy we use every day as electricity was at the beginning nothing but heat. What changes from a source of energy to another is the way of producing that heat. Nuclear power exploits the transformation of mass into energy. This energy comes in several forms [52]:

- kinetic energy of fission products and neutrons
- prompt γ-radiation from highly-excited fission fragments
- delayed radiation released through the natural decay of the radioactive isotopes

The last item of the list is commonly called *decay heat* and its main feature is that it does not disappear with the reactor shutdown. Even though the chain reaction can be easily controlled and stopped, there are various radioactive species in the system which are capable of generating heat. The main sources of decay heat are [68]:

- Heavy elements and actinides: mainly generated by the neutron-induced transmutation of the fuel during reactor operation. They can emit α, β or γ rays
- Fission products: largest component of the decay heat
- Structural and cladding materials: activated by the neutron irradiation during operations. The majority of them decays directly to stable isotopes
- Delayed-neutron-induced fission: emitted by some fission products. They can cause further fissions and are particularly important in the first few minutes following a shutdown
- Spontaneous-fission: actinides created during operation can also undergo spontaneous fission but their contribution is very small

The residual power has to be removed by a coolant and reliable decay-heat calculations are needed. One way to compute the decay heat is the *summation calculation*, described in Chapter 3. Both the qualitative evaluation of the nuclear data and the methods developed in this thesis are of use for decay-heat-related purposes.

1.3 Quantities of Interest

The reactivity of a reactor changes for several reasons: fuel burnup, poisons, temperature, etc. In normal reactor operations, those changes fall into the category *small reactivity insertions* and the kinetics of the system is driven by Eq. 1.21. To estimate the ***reactivity (ρ)*** from the measurement of the ***reactor period (τ)***, reactor physicists must know, with a sufficient degree of confidence, the parameters appearing in the equation

$$\rho \approx \frac{\beta_{eff}\overline{T}}{\tau}. \tag{1.24}$$

Let's look into details at those parameters and at what is needed to estimate them.

1.3.1 Microscopic nuclear parameters

Microscopic parameters are at the scale of the fission products. Each precursor is characterized by the following quantities: FY, λ, and $\overline{P_n}$.

Precursor's fission yield (FY): Each precursor has a defined probability of being created during the fission event. The average number of atoms of a certain isotope created by one fission, after the prompt neutron emission, and before any radioactive decay, is called ***Independent Fission Yield (IFY, or simply IY)*** [50]. As an example, ^{89}Br, one of the most important delayed-neutron precursor, has an IY of 0.012944 (according to the JEFF-3.1.1 library), meaning that for each fission, 0.012944 atoms of ^{89}Br will be formed. The ***Cumulative Fission Yield (CFY, or simply CY)*** instead, is the number of atoms of a certain isotope produced over all time after fission [50], taking into account the decay of the radioactive isotope under consideration as well as its production by the decay of other fission products. For infinite irradiations, at a fission rate of 1 fiss/s, the CY represents the decay rate of a radioactive nuclide or the production rate of a stable one [50].

Precursor's decay constant (λ): Some years after the discovery of radioactivity it was noted that the decay rate of a radioactive nucleus decreases with time following an exponential law and that the decay is purely statistical in nature [47]. The ***Decay Constant (λ)*** represents the probability for an atom to decay per unit time and it is constant. An atom has and will always have the same probability of decaying in time, independently on its age! Therefore, the rate of decay ($\mathrm{d}N/\mathrm{d}t$) of a certain number of atoms (N) is proportional to the number of radioactive nuclei (N) present at time t

$$\lambda = -\frac{\mathrm{d}N/\mathrm{d}t}{N} \qquad [\mathrm{s}^{-1}]. \tag{1.25}$$

Precursor's effective delayed-neutron emission probability ($\overline{P_n}$): If the excitation energy of the parent nucleus (Q_β) is larger than the separation energy of the last neutron (S_n) there is a probability of neutron emission after the β-decay. If $Q_\beta > S_{xn}$ with $x > 2$ there is also the possibility of multiple neutron emission [61]. The effective delayed-neutron emission probability measures the fraction of β-strength above the neutron separation energy and represents the probability that the β-decay is followed by at least one neutron emission. It is defined as

$$\overline{P_n} = \sum_{x=1}^{X} xP_{xn} = 1P_{1n} + 2P_{2n} + \cdots XP_{Xn} \tag{1.26}$$

where P_{xn} is the probability of having a β-decay followed by the emission of x neutrons. Fig. 1.6 shows part of the nuclide chart together with the P_n of the different neutron-rich nuclei.

Precursor's delayed-neutron spectrum (χ): Each delayed-neutron precursor has its own **Spectrum (χ)**, which describes the energy distribution of the emitted neutrons. In principle, the spectral data of an isotope can be measured, but experiments are very thorny, due to the counting statistics. Indeed, it is not easy to isolate delayed-neutron precursors and at the same time to determine its spectrum; especially due to their radioactive decay constants. Nowadays, there are only 34 evaluated experimental spectra, while the others are determined through theoretical QRPA calculations [12].

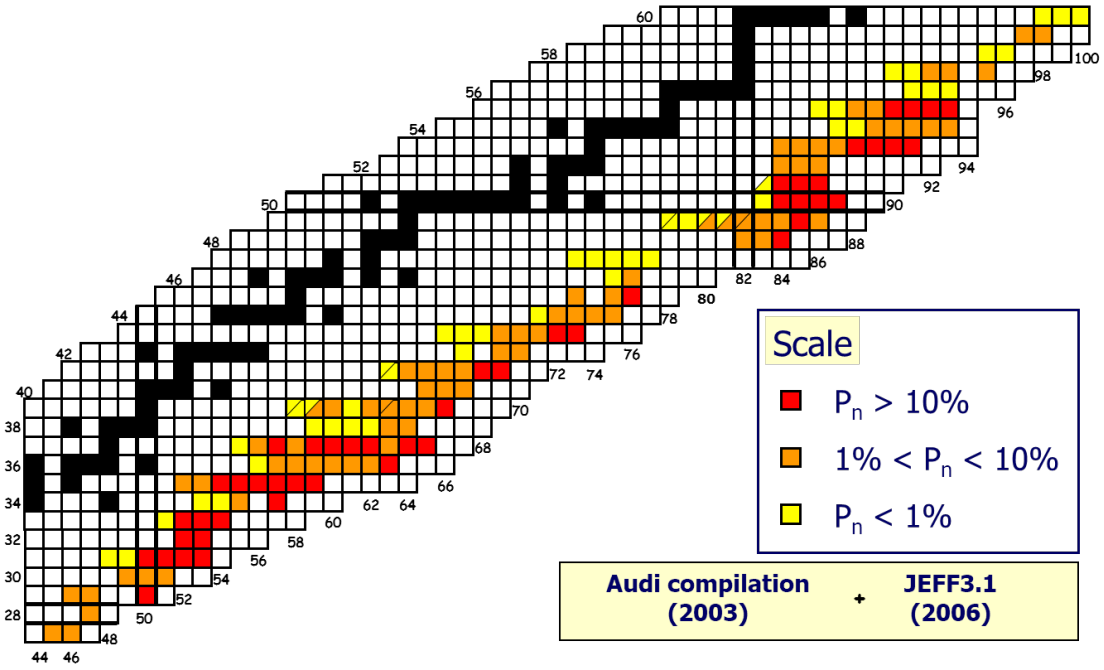

Figure 1.6: Part of the nuclide chart containing the P_n of the different fission products, taken from [31].

1.3.2 Macroscopic nuclear parameters

Macroscopic parameters are at the scale of the fuel. For each fissioning system, the following quantities can be defined: ν_d, the set (a_i, λ_i), $\chi_{d,i}$, $\overline{T_{1/2}}$ and β.

Average delayed-neutron yield ν_d The ***average delayed-neutron yield (ν_d)*** is the average number of delayed neutrons emitted per fission. It can be either computed through a microscopic calculation (see Eq. 1.27, where N is the number of precursors) or measured by an integral method. According to JEFF-3.1.1, it is energy independent up to 4 MeV, after which it decreases.

$$\nu_d = \sum_{j}^{N} CY_j \, \overline{P_{n,j}} \tag{1.27}$$

For more information about how to compute this quantity, go to Section 3.2 of Chapter 3, while to know more about the experimental technique go to Section 6.1 of Chapter 6.

Kinetic parameters a_i, λ_i In the group approximation, delayed-neutron precursors are sorted in 6 or 8 groups characterized by a decay constant (λ_i) and a relative abundance (a_i). Like the ν_d, those parameters can either be computed or measured. While the abundances depend on the fissioning system, the decay constants are fixed (see Subsection 1.4.5). For more information on the kinetic parameters go to Chapter 4 or to Section 6.1 of Chapter 6.

delayed-neutron spectra $\chi_{d,i}$ delayed-neutron groups replace hundreds of fission products, each of which, according to its excitation energy, might emit a different energy spectrum of delayed neutrons. When using the group approximation, apart from an

average abundance and an average decay constant, one should also estimate an average ***delayed-neutron spectrum*** ($\boldsymbol{\chi_{d,i}}$).

Mean precursors' half-life ($\overline{T_{1/2}}$) The ***mean precursors' lifetime*** ($\overline{T}$) is defined, in the delayed-neutron-group approximation, as

$$\overline{T} = \frac{\sum_{i=1}^{G} a_i T_i}{\sum_{i=1}^{G} a_i}, \tag{1.28}$$

where T_i is the delayed-neutron group lifetime ($T_i = 1/\lambda_i$) and G is the number of groups. If, instead of the lifetime, one uses the half-life ($T_{1/2} = \ln 2/\lambda_i$), the quantity of interest becomes the ***mean precursors' half-life*** ($\overline{T_{1/2}}$)

$$\overline{T_{1/2}} = \frac{\sum_{i=1}^{G} a_i T_{1/2,i}}{\sum_{i=1}^{G} a_i}. \tag{1.29}$$

In any case, the two formulations are equivalent and only differ by a factor $\ln 2$.

Total delayed-neutron fraction (β) Great attention has to be put in dealing with β and β_{eff}. Apart from the name, the two parameters are very different. The ***total delayed-neutron fraction*** (β) is a nuclear parameter and represents the fraction of delayed neutrons produced by the fission process. It is the ratio between the delayed neutrons and the total number of neutrons emitted per fission. This quantity depends on the fuel under considerations as well as on the incident neutron energy.

$$\beta(E) = \frac{\nu_d}{\nu_t} \tag{1.30}$$

On the other hand, β_{eff} is a reactor parameter and will be described in Subsection 1.3.3.

1.3.3 Reactor parameters

In a reactor, a mix of fissioning systems is used as fuel, each one giving its own set of fission products. In order to study the behavior of the system at the reactor level, other factors have to be taken into account.

Effective delayed-neutron fraction (β_{eff}) The ***effective delayed-neutron fraction*** (β_{eff}) is a reactor parameter and represents the fraction of fission caused by delayed neutrons. It is β weighted by the neutron importance, which represents the neutron's effectiveness in causing fission.

$$\begin{aligned} \beta_{eff} &= \beta I \\ &= \frac{\int \mathrm{d}\vec{r} \int \mathrm{d}E \Phi^{+}(E,\vec{r}) \Sigma_i \chi_{d,i}(E) \int \mathrm{d}E' \nu_{d,i} \Sigma_{f,i}(E') \Phi(E',\vec{r})}{\int \mathrm{d}\vec{r} \int \mathrm{d}E \Phi^{+}(E,\vec{r}) \Sigma_i \chi_i(E) \int \mathrm{d}E' \nu_{t,i} \Sigma_{f,i}(E') \Phi(E',\vec{r})} \end{aligned} \tag{1.31}$$

The importance (I) depends on the position and on the energy of the neutron when it is born. As illustrated in Eq. 1.31, I depends on both the prompt and the delayed-neutron spectra (χ), on the neutron flux (Φ), on the adjoint flux (Φ^{+}) and on the fission cross

section (Σ_f), most of which are time-dependent. It follows that β_{eff} is time-dependent and the reactivity of the system in dollars (giving an estimation of the safety margin) changes in time. Nevertheless, in reactor applications, it is often assumed that β_{eff} is constant during a particular transient. It is worth mentioning that β_{eff} strongly depends on the chosen set of delayed-neutron data.

Recap: Quantities of Interest

Reactor parameters: characteristic of the reactor

- ρ: reactivity
- τ: reactor period
- β_{eff}: effective delayed-neutron fraction

Macroscopic nuclear parameters: characteristic of the fissioning system

- ν_d: average delayed-neutron yield
- a_i, λ_i: kinetic parameters
- $\chi_{d,i}$: delayed-neutron spectra
- $\overline{T_{1/2}}$: mean precursors' half-life
- β: total delayed-neutron fraction

Microscopic nuclear parameters: characteristic of the precursor

- FY: precursor's fission yield
- λ: precursor's decay constant
- $\overline{P_n}$: precursor's effective delayed-neutron emission probability
- χ: precursor's delayed-neutron spectrum

1.4 A Bit of History

1.4.1 The International Databases

Nuclear data are occasionally evaluated by a Nuclear Data Organization, which recommends the highest-quality values and publishes them in standard nuclear data libraries. The standard format for the storage of nuclear data is the ENDF-6 (*Evaluated Nuclear Data File*) format [42].

JEFF (*Joint Evaluated Fission and Fusion File*) is the European library, created by the members of the NEA[7], in the framework of the OECD[8].

ENDF/B (*Evaluated Nuclear Data File / B*) is the American library and is created by the CSEWG[9] thanks to the cooperation of national laboratories, industry, and universities.

[7] *Nuclear Energy Agency.*
[8] *Organisation for Economic Co-operation and Development.*
[9] *Cross Section Evaluation Working Group.*

JENDL (*Japanese Evaluated Nuclear Data Library*) is the Japanese library and it is handled by the JNDC[10] at the JAEA[11].

The international databases contain both the macroscopic nuclear parameters associated with the fissioning isotopes and the microscopic nuclear data associated with their fission products. Unfortunately, the libraries have different origins and do not always agree with each other. Moreover, uncertainties and covariances are not always reported in the databases, meaning that a consistent evaluation of the error brought by the data itself in the reactor-parameters estimation cannot be performed. The main consequence is an excessive conservatism in both the design and the operation of a reactor. For example, EDF considers a conservative uncertainty of 10% for the β_{eff} of UO_2-fuelled reactors.

1.4.2 "Dear Old Keepin"

According to the (American) library ENDF/B-VII.1, there are about 300 neutron emitters. In the past, dealing with such amount of data was not feasible for reactor kinetic calculations. For that reason, G.R. Keepin had the idea of sorting the precursors into groups according to their half-lives, under the assumption that the delayed-neutron emission rate could be represented as a sum of exponentials. In 1957 he performed an experiment to measure periods, relative abundances and absolute yields of delayed neutrons from fast fission of ^{233,235,238}U, ^{239,240}Pu, ^{232}Th and thermal fission of ^{233,235}U and ^{239}Pu [41]. Keepin used the Godiva bare sphere of ^{235}U to irradiate a sample at Los Alamos. He performed both *infinite* and *instantaneous* irradiations, in order to emphasize the long- and the short-lived precursors, respectively. For fast irradiation he used the bare Godiva, which had a slightly degraded fission-neutron spectrum [41]. Instead, to obtain thermal neutrons, the sphere was surrounded by a block of polyethylene and a screen of Cd. Figure 1.7 shows the experimental set-up used by Keepin for his fast-irradiation experiment. After the irradiation, the fissile sample (2-5 g) was transported to the detector by a pneumatic system in approximately 50 ms. The delayed-neutron activity measurement lasted 500 s and was performed by a $^{10}BF_3$ proportional counter optimized to have an approximately flat efficiency as a function of energy in the range 23 keV - 1.5 MeV (5% of deviation) [41]. The dead-time was estimated to be roughly 1 μs. The sum of exponentials has been linearized by Taylor's expansion and coded for iterative least-square analysis (LSF) on the IBM 704 computer at Los Alamos [41]. The number of groups is arbitrary but in 1957 he proposed a six-group representation, affirming that six was a sufficient number of groups to properly fit the experimentally measured delayed-neutron activity. In the first step, the four long period groups were fitted from the infinite irradiation experiment. Then, the four short period groups were fitted from the burst irradiation experiment. Finally, the two sets were normalized to provide a six-group set of kinetic parameters. Note that both the abundances and the decay-constants were free parameters of the fit. Ten cycles of irradiations were performed, which allowed computing the spread of the derived abundances. The final set was obtained from a LSF of the 10 runs, and not from an average of the 10 sets of kinetic parameters derived by fitting the individual decay curves.
As far as the delayed-neutron yield is concerned, two techniques were possible: either computing the *integral* of the decay curve following a burst of irradiation, or extrapolating the *counting rate* at t=0 after an infinite irradiation. The first method appeared

[10] *Japanese Nuclear Data Committee.*
[11] *Japan Atomic Energy Agency.*

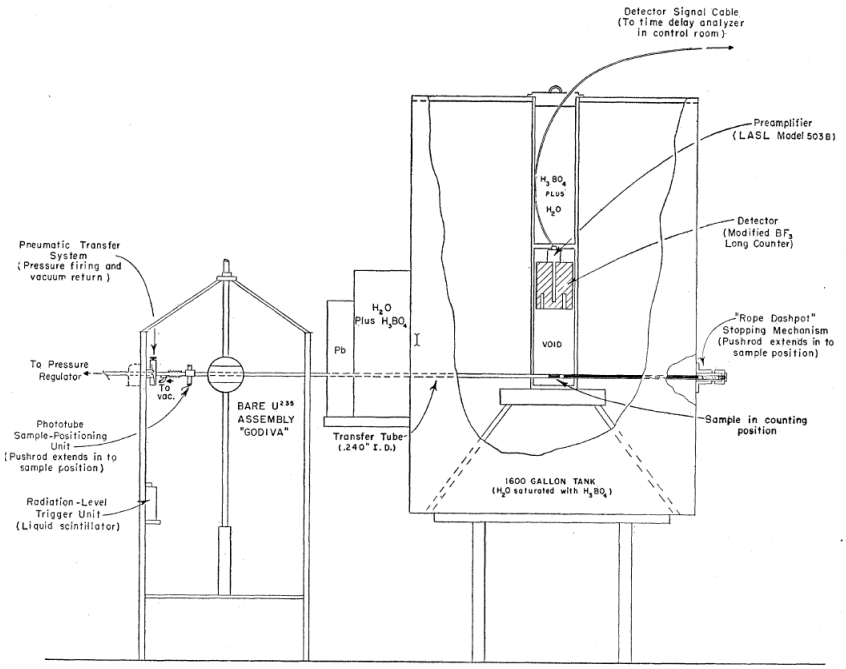

Figure 1.7: Experimental set-up used by Keepin in 1957 [41].

Table 1.1: Best fit of the kinetic parameters for the thermal fission of ^{235}U (99.9% ^{235}U) and ^{239}Pu (99.8% ^{239}Pu) and the fast fission of ^{238}U (99.98% ^{238}U) from Keepin's experiment [41].

Sample	Param.	1	2	3	4	5	6
$^{235}U_t$	$T_{1/2,i}$	55.72(128)	22.72(71)	6.22(23)	2.30(9)	0.610(83)	0.230(25)
	a_i	0.033(3)	0.219(9)	0.196(22)	0.395(11)	0.115(9)	0.042(8)
	ν_d			0.0158 ± 0.0005			
$^{238}U_f$	$T_{1/2,i}$	52.38(129)	21.58(39)	5.00(19)	1.93(7)	0.490(23)	0.172(9)
	a_i	0.013(1)	0.137(2)	0.162(20)	0.388(12)	0.225(13)	0.075(5)
	ν_d			0.0412 ± 0.0017			
$^{239}Pu_t$	$T_{1/2,i}$	54.28(234)	23.04(167)	5.60(40)	2.13(24)	0.618(213)	0.257(45)
	a_i	0.035(9)	0.298(35)	0.211(48)	0.326(33)	0.086(29)	0.044(2)
	ν_d			0.0061 ± 0.0003			

to be more accurate. For an instantaneous irradiation, the integral of the decay curve is given by

$$I = F\epsilon \int_0^\infty \nu_{d,i}\lambda_i e^{-\lambda_i t}\mathrm{d}t = F\epsilon \sum_{i=1}^{6} \nu_{d,i} = F\epsilon\nu_d \tag{1.32}$$

where t is the time starting from the end of the irradiation, $\nu_{d,i}$ and λ_i are the partial yield and the decay constant of group i, respectively. To obtain the ν_d, it is sufficient to divide the total number of counts (I) by the efficiency of the detector (ϵ) and by the fission rate (F), estimated with a ^{99}Mo dosimeter

$$\nu_d = \frac{I}{F\epsilon}. \tag{1.33}$$

Corrections have been applied for self-multiplication (1%) and for the impurity of the sample. Keepin has been for a long time, and still is, the uncontested reference for delayed-neutron data (see Tab. 1.1).

1.4.3 Tuttle's evaluation of ν_d

In 1979 R.J. Tuttle performed an extensive critical review of all delayed-neutron yields measurements available at the time [56]. For each one, he studied the experimental procedure and identified eventual flaws or systematic errors in the analysis. Next, he conducted an evaluation, and he recommended a set of yields with associated uncertainties weighing the experiments by their reliability. Table 1.2 shows the average delayed-neutron yields recommended by Tuttle in his evaluation of 1979.

Table 1.2: Delayed-neutron yields recommended by Tuttle in his critical review [56]. The values with a star (*) are partially or wholly determined by analytical prediction.

Fiss. Sys.	Thermal	Fast	High
^{232}Th	-	5.31E-02 (4.2%)	2.85E-02 (4.6%)
^{233}U	6.67E-03 (4.3%)	7.31E-03 (4.9%)	4.22E-03 (5.2%)
^{235}U	1.62E-02 (3.1%)	1.67E-02 (2.1%)	9.27E-03 (3.1%)
^{236}U	-	2.21E-02 (10.7%)*	1.30E-02 (13.3%)*
^{238}U	-	4.39E-02 (2.3%)	2.73E-02 (2.9%)
^{239}Pu	6.28E-03 (6.0%)	6.30E-03 (2.5%)	4.17E-03 (3.7%)
^{241}Pu	1.52E-02 (7.3%)	1.52E-02 (7.3%)	8.34E-03 (8.4%)

He considered all incident neutron energies up to 15 MeV. The ratio between yields at high energy to those at low energy has been used to estimate the yield at high energy for isotopes for which there were no measurements (^{234}U, ^{236}U, ^{238}Pu and ^{242}Pu) [56]. It was impossible at the time to estimate the energy dependence below 4 MeV using the available experiments, due to the fact that it might be overshadowed by the combination of broad-spectrum and monoenergetic neutron experiments. Tuttle stated that there were significant gaps in the energy-dependent yield measurements. In particular, (he said) no information was available between 4 and 14 MeV for ^{239}Pu and between 7 and 14 MeV for all other nuclides. Finally, he suggested a list of experiments to be performed in order of priority.

1.4.4 Brady & England's summation calculation

Ten years after Tuttle's review, M.C. Brady and T.R. England made an extensive effort to provide a complete set of evaluated data for 43 fissioning systems [49]. The objective of their work was to complement the measured data for individual precursors with models, in order to produce a database to be incorporated in ENDF/B-VI. They focused on the calculation of average delayed-neutron yields, half-lives and aggregate spectra. The innovation of their work consisted in trying to derive, for the first time, the kinetic parameters associated with delayed neutrons by performing a summation calculation rather than a measurement. The same is true for the spectra. In their paper, they highlighted the advantage of performing a summation calculation: the fact that a single radioactive decay data and spectra database could be used to estimate delayed-neutron data for any fissioning system. In 1989, measured values of P_n were available for only 83 ground-state and 6 isomeric-state precursors. Brady and England exploited these probabilities to fit the parameters a and b of the Kratz-Hermann equation (Eq. 1.34)

$$P_n = a\left[\frac{Q_\beta - S_n}{Q_\beta - K}\right]^b, \tag{1.34}$$

where Q_β is the Q-value of the β^--decay, S_n the last-neutron binding energy in the daughter and K is a parameter that is equal to 0 for an even-even nucleus, $13\sqrt{A}$ for an odd nucleus and $26\sqrt{A}$ for an odd-odd nucleus. Then, they used the equation with the fitted parameters to predict unmeasured P_n. As they stated in their document [49], the 89 measured probabilities belong to the precursors accounting for more than 80% of the total delayed-neutron emission. As far as the temporal behavior is concerned, they performed a summation calculation using the CINDER code and fitted the delayed-neutron curve with 12 free parameters (6 abundances and 6 decay constants). They took into account the possibility of fixing a set of decay constants for all fissioning systems but finally they considered it to be unnecessary. Ultimately, the computed parameters have been tested with the Godiva benchmark, but their uncertainty has never been estimated. Concerning the average delayed-neutron yields, Brady and England performed the calculation using ENDF/B-V library, but in the end, they recommended the computed ν_d only in absence of experiments. Table 1.3 shows the delayed-neutron data they recommended for the main fissioning systems. It is worth emphasizing that, even if the calculated ν_d have not been recommended, the American library adopted[12] and still adopts[13], the kinetic parameters computed by Brady and England, even though several authors highlighted some inconsistencies regarding ^{235}U [39] [60]. Uncertainties, as well as correlations, are not provided.

Brady and England performed an extensive analysis of the precursors' spectra as well. At the time of their publication (1989), only 34 precursors had a measured spectrum. Furthermore, 30 of them had to be extended with nuclear models because they were considered inadequate in the measured energy range [49]. Brady and England performed the mentioned expansion and predicted the delayed-neutron spectrum of 237 other precursors using a modified evaporation model [49]. Comparison with the measured spectra led to the conclusion that such a model did not allow the estimation of the measured spectra variations. Furthermore, it never managed to converge to the measured values in the low energy part of the spectra. Brady and England sorted the precursors in 6

[12] From the version ENDF/B-VI.
[13] At the time of writing, the latest version is ENDF/B-VIII.0.

Table 1.3: Results of the summation calculation performed by Brady and England in 1989 using ENDF/B-V library [49].

Sample	Param.	1	2	3	4	5	6
$^{235}U_t$	$T_{1/2}$	52.1	21.3	5.69	2.19	0.701	0.235
	a_i	0.0380	0.1918	0.1638	0.3431	0.1744	0.0890
	ν_d	0.0167					
$^{235}U_f$	$T_{1/2}$	52.1	21.2	5.74	2.29	0.816	0.243
	a_i	0.0350	0.1807	0.1725	0.3868	0.1586	0.0664
	ν_d	0.0167					
$^{238}U_f$	$T_{1/2}$	51.0	22.1	5.62	2.14	0.765	0.227
	a_i	0.0139	0.1128	0.1310	0.3851	0.2540	0.1031
	ν_d	0.0400					
$^{239}Pu_t$	$T_{1/2}$	52.1	23.0	6.11	2.35	0.812	0.264
	a_i	0.0306	0.2623	0.1828	0.3283	0.1482	0.0479
	ν_d	0.0065					
$^{239}Pu_f$	$T_{1/2}$	52.1	22.4	6.11	2.37	0.808	0.254
	a_i	0.0363	0.2364	0.1789	0.3267	0.1702	0.0515
	ν_d	0.0065					

groups, using previously defined half-life boundaries, and produced aggregate spectra by weighting the individual spectra by the contribution of the precursor to the $\nu_{d,i}$ of its group. Nothing has changed since then. The (European) library JEFF-3.1.1 contains only the 34 measured spectra, while the (American) database ENDF/B-VI included the results of their calculation. It has to be noted though, that the 34 measured spectra account to about 67% of the aggregate one.

1.4.5 The NEA/WPEC-SG6

In 1990 the NEA[14] sponsored a WPEC[15] Sub-group activity on delayed neutrons. The goals were to review the state of the art and to propose a program to improve delayed-neutron data. In particular, the SG6 (*SubGroup 6*) aimed at "reducing the discrepancies between calculated and measured values of the reactivity scale based on reactor kinetics by reducing the uncertainties in the delayed-neutron data for ^{235}U, ^{238}U, and ^{239}Pu" [38]. One of the conclusions of the 12-years effort was that the 6-group model was obsolete and that a new 8-group model was needed. In addition, this new model had to come with specific characteristics:

- a single set of 8 decay constants had to be used for all fissioning systems and at all energies
- the decay constants of the first three groups had to be the ones of the most dominant precursor in the respective group (^{87}Br, ^{137}I, and ^{88}Br), as shown in Tab. 1.4
- the decay constants of the remaining groups had to take into account the three or four most dominant precursors belonging to the group.

[14] *Nuclear Energy Agency.*
[15] *Working Party on International Nuclear Data Evaluation Co-operation.*

Table 1.4: Set of half-lives recommended by the WPEC-SG6 [40].

Group	Prec.	Prec. $T_{1/2}$ [s]	Group $T_{1/2}$ [s]
1	^{87}Br	55.6	55.6
2	^{137}I	24.5	24.5
3	^{88}Br	16.3	16.3
4	^{138}I	6.46	5.21
	^{93}Rb	5.93	
	^{89}Br	4.38	
5	^{94}Rb	2.76	2.37
	^{139}I	2.30	
	^{85}As	2.08	
	^{98m}Y	2.00	
6	^{93}Kr	1.29	1.04
	^{144}Cs	1.00	
	^{140}I	0.86	
7	^{91}Br	0.542	0.424
	^{95}Rb	0.384	
8	^{96}Rb	0.203	0.195
	^{97}Rb	0.170	

The set of half-lives was provided by Piksaikin in 1998 [40] and remains the same today. It would have been very easy to take the experimentally measured data and to repeat the fitting procedure with the new constraints. However, the original data had been lost and what was left were 245 sets of abundances and decay constants for 20 fissioning systems derived in different experimental conditions. The sets had between 4 and 7 groups. In the framework of the WPEC-SG6, these 245 sets have been expanded through what is called *the expansion technique*. The principle was to use the collection of recommended kinetic parameters to derive the missing decay curve and then to use the latter to perform a new fit. Adjustments had to be done, together with a thorough bibliographic study, to identify the most reliable sets of data. Table 1.5 reports a short list of what the WPEC-SG6 has considered the most reliable sets of measurements. The complete list can be found in Appendix A.

Table 1.5: Origin of the kinetic parameters recommended by WPEC-SG6. The sets being in the six-group model have been expanded into the eight-group model before being recommended.

Fiss. Sys.	Energy	Original Nb. Groups	Reference	Year
^{235}U	thermal	6	Keepin *et al.* [41]	1957
^{235}U	fast	8	Piksaikin *et al.* [69]	1997
^{238}U	fast	6	Keepin *et al.* [41]	1957
^{239}Pu	thermal	6	Keepin *et al.* [41]	1957
^{239}Pu	fast	6	Besant *et al.* [17]	1977

Finally, the working party suggested a new set of abundances for the main fissioning systems at thermal (0.025 eV), fast (400 keV) and high (14 MeV) energy, reported in Tab. 1.6. As far as the uncertainty was concerned, the uncertainty in both the decay constants and the abundances was transferred to the abundances only. The process was done in such a way as to preserve the uncertainty on the computed reactivity. JEFF-

Table 1.6: Delayed-neutron yields and kinetic parameters recommended by the WPEC-SG6 in 2002 [38]. σ_{a_i} represents the uncertainty associated with the abundances a_i. No uncertainty is recommended for the average delayed-neutron yields.

Sample	Param.	1	2	3	4	5	6	7	8
All	$T_{1/2,i}$	55.6	24.5	16.3	5.21	2.37	1.04	0.424	0.195
$^{235}U_t$	a_i	0.0328	0.154	0.0914	0.197	0.331	0.0903	0.0812	0.0229
	σ_{a_i}	0.0042	0.0068	0.009	0.023	0.0066	0.0045	0.0016	0.0095
	ν_d	0.0162							
$^{235}U_f$	a_i	0.0340	0.150	0.0991	0.200	0.312	0.0931	0.0871	0.0240
	σ_{a_i}	0.0007	0.003	0.003	0.004	0.007	0.004	0.004	0.001
	ν_d	0.0163							
$^{238}U_f$	a_i	0.0840	0.104	0.0375	0.137	0.294	0.198	0.128	0.0931
	σ_{a_i}	0.0013	0.0022	0.00075	0.020	0.012	0.0023	0.013	0.0034
	ν_d	0.0465							
$^{239}Pu_t$	a_i	0.0319	0.237	0.0826	0.182	0.294	0.0816	0.0722	0.0185
	σ_{a_i}	0.0120	0.034	0.0016	0.052	0.029	0.0016	0.0310	0.00037
	ν_d	0.00650							
$^{239}Pu_f$	a_i	0.0288	0.2250	0.0951	0.149	0.351	0.0370	0.0974	0.0168
	σ_{a_i}	0.0021	0.0045	0.0098	0.043	0.007	0.019	0.0910	0.0390
	ν_d	0.00651							

3.1.1 has adopted the data from the WPEC-SG6 report published in 2002 [38], where the eight-group a_i come from the expansion of a six-group set that Keepin obtained in 1957 through an integral measurement [41]. The uncertainties on the 8-group abundances have been estimated in such a way to preserve the 6-group set estimation of the uncertainty in the reactivity. It is interesting to see that those results are still used today in the JEFF-3.1.1 library and that there has not been any new measurement to either confirm or contest the correctness of the data. Correlations are not provided in any of the international databases.

1.4.6 The IAEA/CRP

The IAEA[16] encourages and assists research on atomic energy and on its application for peaceful purposes by fostering the exchange of information and of scientists. The IAEA's CRPs[17] bring together scientists from the IAEA Member States to focus on defined areas or research. In 2012 a CRP was approved with the aim of producing a *Reference Database for Beta-Delayed Neutron Emission Data* including

- compiled and evaluated microscopic precursor data (λ, P_n, χ_d)
- recommended macroscopic quantities (ν_d, set of (a_i, λ_i), $\chi_{d,i}$) for fissile materials of interest.

The objective was to enhance knowledge and calculational capabilities in the field of nuclear energy, safeguards, used fuel, waste management, and nuclear science. This CRP began in 2013 and ended in 2019. It started with a compilation of experimental data on half-lives, P_n and spectra for all precursors. It included the production of a list of P_n for the precursors of different mass regions. It continued with a compilation of measurements of average yields, spectra and kinetic parameters. Finally, after a study on the systematics of the mean half-life, the CRP ended with recommendations of unconstrained 6- and constrained 8- group kinetic parameters for thermal and fast fission of the major actinides. I had the possibility to join the project in 2017, to take part in the 3rd CRP Meeting which took place in June at IAEA Headquarters, and to contribute to the redaction of the final document. I compared the set of data recommended by the CRP to the one reported in the international databases and assessed its effect on the delayed-neutron activity prediction. I considered the microscopic-data differences as well as their effects on the calculation of quantities of interest. The method used in all my computations is described in Chapter 4. At the time of writing this PhD the CRP final document was not yet published and the recommended data could not be used for comparison.

1.5 Scientific challenges of this Ph.D.

A reliable prediction of the system's kinetic response following a reactivity insertion is the main goal of all works on delayed-neutron data. Inaccurate delayed-neutron data leads to an excessive conservatism in both the design and the definition of the safety margins of a reactor. The uncertainty on the reactivity, obtained through the uncertainty propagation of the delayed-neutron data, is about 6% when using the WPEC-6 recommendations [10], the main contribution coming from the mean precursors' half-life. A. Santamarina, in his proceeding for the PHYSOR 2018 conference [10], highlighted the discrepancies between JEFF-3.3.1 and ENDF/B-VII.0 in simulating specific benchmarks, which rises up to 16% for the reactivity associated with a given doubling time in a typical LWR. Such a strong inconsistency is mainly due to the differences in the mean precursors' half-life, as shown in Tab. 1.7.
The delayed-neutron parameters can be both measured or computed. As far as the experiments are concerned, the principles, as well as the procedure to exploit the raw data, are by now consolidated. In the same way, the method to derive the parameters by computation is today mature. To date, the classical approach consists in measuring the quantities associated with the major isotopes and computing, using models,

[16] *International Atomic Energy Agency.*
[17] *Coordinated Research Projects.*

Table 1.7: Mean precursors' half-life computed using the kinetic parameters recommended by the European and the American international libraries.

Database	$^{235}U_t$	$^{235}U_f$	$^{238}U_f$	$^{239}Pu_t$	$^{239}Pu_f$
JEFF-3.1.1	9.02 (3.0%)	9.11 (1.0%)	5.32 (2.1%)	10.69 (8.0%)	10.35 (10.5%)
ENDF/B-VII.0	7.67 (-)	7.67 (-)	3.05 (-)	9.21 (-)	9.21 (-)

the ones that had poor or missing experimental data. In addition, the covariance matrix associated with the abundances has never been produced because all the studies in the field focused more on the values than on the uncertainties. The reduction of the uncertainties associated with those quantities and the estimation of their correlations has never been given enough importance to launch a program on the subject.

This Ph.D., which started in 2016, aimed at producing a new set of DN parameters by performing both calculations and measurements and by exploiting the two through the Bayesian inference with the aim of reducing the uncertainties and creating the associated covariance matrices. The innovation of this work lies in the application, for delayed-neutron data, of the same procedure generally used for cross section evaluation. The technique consists in carrying out a calculation using microscopic data for the estimation of the quantities of interest together with their uncertainties and covariances. The second step consists in adding information through the Bayesian assimilation of integral experiments. Finally, the last step consists in the evaluation of the produced set of data through consistent benchmarks. This technique, more rigorous than just a simple experiment or calculation, has been tested on the delayed-neutron data associated with the thermal fission of ^{235}U.

Following a bibliographic study of the state of the art and of the existing methods used to produce the parameters associated with delayed neutrons, two approaches have been adopted and coupled: microscopic and macroscopic.

Microscopic approach The microscopic approach consisted in reconstructing macroscopic quantities by summing up the contributions of the different delayed-neutron precursors. The success of this method depends on the quality of nuclear data and therefore on the international database the microscopic data is taken from. The first step has therefore been to compare fission yields and radioactive decay data from different libraries to establish the most reliable combination. Then, it was necessary to develop a program to compute, by summation method, the following quantities: ν_d, a_i, λ_i, $\overline{T_{1/2}}$ and $\chi_{d,i}$. Note that for the estimation of the kinetic parameters, the delayed-neutron activity curve had to be reconstructed. Uncertainties and covariances among parameters and/or among nuclides have been estimated through different methods. The calculation was repeated for the main fissioning systems: : $^{232}Th_f$, $^{233}U_f$, $^{235}U_t$, $^{235}U_f$, $^{236}U_f$, $^{237}Np_f$, $^{238}U_f$, $^{239}Pu_t$, $^{239}Pu_f$, $^{241}Pu_t$, $^{241}Pu_f$, $^{241}Am_f$. A parallel study focused on the energy dependence of delayed-neutron quantities, due to the dependence of fission yields on the incident neutron energy.

Macroscopic approach The macroscopic approach consisted in the measurement of the delayed-neutron activity following the irradiation of a fissile sample. For this purpose, a specific detector has been designed. The experiment took place at the cold-neutron

beam PF1B at the Institute-Laue-Longevin (ILL). For the purpose, a miniaturized fission chamber, which acted as a fissile target, has been designed and manufactured. In the framework of this Ph.D., two CFP12 were built: one with ^{235}U, and one without fissile deposit (dummy chamber), used for the background estimation. A special fast shutter had to be designed to stop the neutron beam according to the requirements. The detector has been calibrated at NPL and at the AMANDE accelerator. The data regression analysis aimed at reconstructing the neutron activity evolution in time, starting from the arrival time of all the neutron-interactions in the detectors. The fit of the decay curve has been performed with the CONRAD code, to extract the kinetic parameters of $^{235}\mathrm{U_t}$.

Evaluation and Benchmark The last step was the Bayesian assimilation of the experimental data into the theoretical model. The procedure consisted in using the calculated kinetic parameters as guessed input to fit the experimental curve with the theoretical model. The uncertainty and the covariance matrix have also been produced and compared with the recommended values. Three benchmarks have also been tested on thermal and fast reactors to assess the quality of the produced set of parameters and its impact on reactor analysis.

Chapter 2

Uncertainty Estimation Methodologies

> It ain't what you don't know that gets you into trouble. It's what you know for sure that just ain't so.
>
> *Mark Twain*

Contents

2.1 Statistics and Treatment of Experimental Data 25
2.1.1 Characterizing a Probability Distribution 26
2.1.2 Some Known Probability Distributions 28
2.2 Bayes and The Learning Process 29
2.2.1 Bayes' theorem 30
2.2.2 Bayes theorem applied to an experiment 31
2.2.3 Analytical Method 31
2.2.4 Monte Carlo Method 32
2.3 Uncertainty Propagation Methodologies 32
2.3.1 Bayesian Marginalization 32
2.3.2 Types of Marginalization 33
2.4 CONRAD® 34

The objective of this chapter to introduce the concept of uncertainty associated with an experiment. The first section (Section 2.1) focuses on the types of error and on the probability distributions. Section 2.2 introduces the Bayes theorem and the concept of Bayesian inference, to obtain the maximum of information from a given measurement. Section 2.3 describes several ways of propagating the uncertainties in the input data on the wanted parameters. Finally, Section 2.4 introduces the CONRAD® code.

2.1 Statistics and Treatment of Experimental Data

Experience has shown that no measurement, however carefully made, is completely free of uncertainties [55]. In his book, *Introduction to error analysis*, J.R. Taylor underlines

that *errors* are not *mistakes*. The error associated with a measurement is nothing but the inherent uncertainty of the experiment. It is something that cannot be avoided but can be quantified. Errors can be divided into two types:

- *Random errors:* due to the statistical fluctuations in the measurement, coming from either the instrument or the environmental conditions. They can be determined through statistical analysis and usually follow the Gaussian normal distribution. The only way to reduce this component of the uncertainty is to take more data by increasing the sample size, the duration of the measurement, the efficiency of the detector and so on
- *Systematic errors:* due to something that biases the measurement. They are reproducible and always go in the same direction. It is much more difficult to detect this type of error and the procedure must be adapted to the case under consideration.

The *precision* of a measurement concerns the dispersion of the measured values. It deals with the statistical uncertainty of the experiment. The *accuracy* of a measurement, on the other hand, concerns how far the measured and the true value are. It deals with the systematic uncertainty of the experiment.

Statistics is a form of mathematical analysis that deals with random processes, processes that are impossible to predict with certainty due to their fluctuations. Random events are described by probability density functions, giving the expected frequency of occurrence of each possible outcome [48]. Those outcomes are called *random variables (x)* and might have a continuous or a discrete distribution $P(x)$. For a discrete distribution, $P(x_i)$ represents the frequency of occurrence of each possible outcome x_i. On the other hand, for a continuous distribution, $P(x)$ represents a density function and the probability of obtaining x in the interval $(x, x + \mathrm{d}x)$ is given by $P(x)\mathrm{d}x$ [48]. To simplify this chapter, only the continuous distributions will be considered[1].

2.1.1 Characterizing a Probability Distribution

Theoretical mean, variance and covariance

If the probability distribution $P(x)$ is known, mean and variance are its first two moments. The first moment around zero is the *mean* (μ) of x,

$$\mu = \int xP(x)\mathrm{d}x \tag{2.1}$$

and represent the average value. The second moment around the mean is known as *variance* (σ^2) and is the average (squared) deviation of x from the mean μ

$$\sigma^2 = \int (x-\mu)^2 P(x)\mathrm{d}x. \tag{2.2}$$

Its square root σ is called *standard deviation* and represents the dispersion of the distribution $P(x)$. In the case the process is driven by several random variables $x, y, z...$, the probability distribution becomes *multivariate* $P(x, y, z...)$ and a new quantity can be introduced: the *covariance*

$$cov(x, y) = \int (x-\mu_x)(y-\mu_y)P(x, y)\mathrm{d}x\mathrm{d}y, \tag{2.3}$$

which describes the relationship between x and y.

[1] Note that to pass from continuous to discrete it is sufficient to replace the integrals by sums.

Sample mean, variance and covariance

Sampling is a way to determine the parameters of an unknown distribution [48]. Let's assume there is a sample $x_1, x_2, \cdots, x_n$ of n elements and that we want to estimate the best value of the parameters under investigation as well as their uncertainty. The *sample mean* (also called *expected value*) is the arithmetic average of the sample

$$\overline{x} = E[x] = \frac{1}{n}\sum_{i=1}^{n} x_i. \tag{2.4}$$

In the same fashion, the *sample variance* is the average of the squared deviations[2] [48]. The problem is that the only way to know μ is to collect an infinite number of data points. In order to use the experimental mean ($\overline{x}$), the square of the *residuals* must replace the square of the *deviations* and $N-1$ must replace N [46]. For a large set of experimental data, the two expressions are equivalent

$$s^2 = E[(x-\mu)^2] = \frac{1}{n}\sum_{i=1}^{n}(x_i-\mu)^2 = \frac{1}{n-1}\sum_{i=1}^{n}(x_i-\overline{x})^2, \tag{2.5}$$

and the *sample covariance* is computed as

$$cov(x,y) = E[(x-\mu_x)(y-\mu_y)] = \frac{1}{n}\sum_{i=1}^{n}(x_i-\overline{x})(y_i-\overline{y}). \tag{2.6}$$

Remember

Note that, by convention, μ is the **theoretical mean** obtained from a theoretical distribution, while $\overline{x}$ is the **sample mean** computed from a sample. In the same fashion σ^2 is the **theoretical variance** to be distinguished from the **sample variance** s^2. In the limit of an infinite sample ($n \to \infty$), the sample quantities approach the theoretical ones

$$\mu = \lim_{n\to\infty}\overline{x} = \lim_{n\to\infty}\frac{1}{n}\sum_{i=1}^{n} x_i \tag{2.7}$$

$$\sigma^2 = \lim_{n\to\infty} s^2 = \lim_{n\to\infty}\frac{1}{n-1}\sum_{i=1}^{n}(x_i-\overline{x})^2 \tag{2.8}$$

The error associated with estimation of the mean (μ), called σ_μ, can be computed by dividing the *standard deviation of the sample* (σ) by the square root of the sample size n, under the assumption that the samples are independent of each other and that they are not affected by systematic uncertainty

$$\sigma_\mu = \frac{\sigma}{\sqrt{n}}. \tag{2.9}$$

It is important to stress that, for an experiment, the uncertainty associated with the value μ is σ_μ and not σ!

$$\mu \pm \sigma_\mu \tag{2.10}$$

[2] The *deviation* of a given data point x_i is the difference from the point itself and the true mean value μ. On the other hand, the *residual* is the difference from the point itself and the experimental mean $\overline{x}$ [46]

2.1.2 Some Known Probability Distributions

The Binomial distribution

The Binomial distribution describes a phenomenon in which only two outcomes are possible for each trial [48]; let's say A and B. If N is the number of trials and p the probability of getting A (constant independently of the trial), then the probability of getting r times A is described by the Binomial distribution $P(r)$

$$P(r) = \frac{N!}{r!(N-r)!} p^r (1-p)^{N-r}. \tag{2.11}$$

The theoretical mean and variance can be computed as

$$\mu = \sum_r rP(r) = Np \tag{2.12}$$

$$\sigma^2 = \sum_r (r-\mu)^2 P(r) = Np(1-p). \tag{2.13}$$

The Poisson distribution

As mentioned in the Introduction, radioactivity is a random process and the only way to describe the phenomenon is through statistics and probabilities. The Poisson distribution is the particular case of the more general Binomial distribution, for $p \to 0$ and $N \to \infty$. It is particularly suitable to describe the stochastic decay of a radioactive nucleus since decays are independent events (p is constant) with a very small probability of occurring (small p) and a large rate of trials/atoms (large N) [48]. The probability of observing r decays is given by

$$P(r) = \frac{\mu^r e^{-\mu}}{r!}. \tag{2.14}$$

were $\mu = Np$ is the mean rate of events (decay/s) occurring in the sample. The standard deviation can be computed as the square root of the mean value

$$\sigma = \sqrt{\sigma^2} = \sqrt{\mu}. \tag{2.15}$$

The Gaussian distribution

The Gaussian or Normal distribution is a continuous function approximating the exact Binomial distribution. It is a bell-shaped curve and σ represents the width of the peak at 68.3% of the full height. Using the Gaussian distribution, therefore, gives a probability of 0.683 of obtaining a result within one σ from the mean μ.

$$P(x) = \frac{1}{\sigma\sqrt{2\pi}} \exp\left(-\frac{(x-y)^2}{2\sigma^2}\right) \tag{2.16}$$

The Chi-Squared distribution

The Chi-Squared distribution is generally used as a criterion to determine the quality of a fit. It is particularly used for the fitting of experimental data with a theoretical model [48]. If n is the number of independent random variables x_i normally distributed,

then u (also known as χ^2) is the sum of the squared deviates[3] and represents the fluctuations with respect to the Gaussian distribution. The chi-square u follows the distribution $P(u)$, shown in Eq. 2.17

$$P(u) = \frac{(u/2)^{(\nu/2)-1} e^{-u/2}}{2\Gamma(\nu/2)}, \tag{2.17}$$

where ν is the degree of freedom of the distribution. In statistics, ν reflects the balance between the amount of data you have (m) and the number of parameters you want to determine with the analysis (p)

$$\nu = m - p. \tag{2.18}$$

As a consequence, it represents the number of *independent* variables that you can use to estimate your parameters. Mean and standard deviation of the distribution are given by

$$\mu = \nu \tag{2.19}$$

$$\sigma^2 = 2\mu. \tag{2.20}$$

2.2 Bayes and The Learning Process

The Bayesian inference is the translation of logic into mathematics. I like the vision of Brandon Rohrer[4] who says that *inference* is nothing but *educated guessing*. In everyday life, our brain draws conclusions in a very short time, sometimes using very little input data. Any additional input information shrinks the range of output possibilities. Brandon Rohrer makes the following example. You are in the hall of a cinema and someone in front of you drops a ticket. You pick it up to return and, seeing the person from behind, you don't know if it is a man or a woman. The question is: do you say "Excuse me, sir" or "Excuse me, ma'am"? Let's assume that the person has long hair. Your intuition suggests you that it is a woman, even though you know that men can have long hair too. Why is that? While you think that it was your sixth sense to guess, in reality, your brain performed a quick Bayesian inference, since, in your experience, the percentage of women having long hair is larger than the respective percentage for men. Now assume that this person was in line for the men's restroom. You have one additional piece of information and suddenly your answer adjusts to better fit the set of inputs you got. The probabilities of having long hair did not change but you know that it is rare for a woman to stand in line for the men's restroom. The additional information (long hair, in line for the men's restroom) made you change the *prior* answer, that would have been 50-50. This is the heart of the Bayesian learning process; a method capable of extracting the maximum amount of knowledge from the available input data and of adjusting when a piece of additional information is at hand.

Marginal Probability The marginal probability is the likelihood of something to occur. In mathematical terms, it is the ratio between the number of ways that something can occur over the number of things that can occur. In probability theory, it is sometimes called *unconditional probability* or simply *probability* and it is usually represented as $P(A)$ (*probability of the event* A).

[3] A deviate is the ratio between the distance of a data point from the mean and the standard deviation of the distribution.

[4] Instructor on data science who explains complex concepts in a very easy way on the network. For this purpose I suggest his website `https://brohrer.github.io/how_bayesian_inference_works.html`.

Joint probability The joint probability is the likelihood of two separate events occurring simultaneously. It is expressed as $P(A \cap B)$ (*probability of A and B*) and, if the two events are independent of each other, it is calculated by multiplying the probabilities of A and B

$$P(A \cap B) = P(A) \cdot P(B) = P(B) \cdot P(A) = P(B \cap A). \tag{2.21}$$

Note that the order of occurrence of the events is not important.

Conditional probability The conditional probability is the probability of something to occur, given that something else has already occurred. It is written as $P(A \mid B)$ (*probability of the event A given B*) and it is the ratio between the joint probability of A and B divided by the probability of B alone

$$P(A \mid B) = \frac{P(A \cap B)}{P(B)}. \tag{2.22}$$

An important feature of the conditional probability is that it is not commutative

$$P(A \mid B) \neq P(B \mid A). \tag{2.23}$$

2.2.1 Bayes' theorem

Thomas Bayes was an English statistician and Presbyterian minister of the eighteenth century who studied logic and theology at the University of Edinburgh. His findings on probability theory were published by his friend Richard Price. The problem can be formulated in the following way: if the conditional probability $P(B \mid A)$ is known, is there a way to derive the reverse conditional probability $P(A \mid B)$? Bayes had an intuition. From Eq. 2.22 one can derive

$$P(A \cap B) = P(A \mid B) \cdot P(B) \tag{2.24}$$

but also

$$P(B \cap A) = P(B \mid A) \cdot P(A). \tag{2.25}$$

Bayes knew that the conditional probabilities were not commutative (Eq. 2.23), but he noticed that the same could not be said for the joint probabilities (Eq. 2.21). Equations 2.24 and 2.25 are therefore equivalent and the two conditional probabilities are linked by the Bayes' theorem

$$\boxed{P(A \mid B) = \frac{P(B \mid A) \cdot P(A)}{P(B)}} \tag{2.26}$$

In probability theory nomenclature

- $P(A)$ is called *prior* and represents our prior knowledge of A, before any additional information
- $P(B \mid A)$ is called *likelihood* of the data and shows the probability that B occurs given A. It represents our additional information about the answer
- $P(B)$ is called *marginal likelihood* and represents the probability of B
- $P(A \mid B)$ is called *posterior* and it is what we are interested in.

Bayesian inference is very useful because it allows improving the estimate of some measurements by making assumptions about the answer.

2.2.2 Bayes theorem applied to an experiment

Bayes theorem is particularly used to update the values of some parameters of a model when new experiments are performed. Let's assume we have a theoretical model able to simulate an experiment. This model contains several parameters:

- $\vec{y}$ is the vector containing the quantities that can be measured and that can be computed by the model (e.g. the delayed neutron emission rate)
- $\vec{x}$ is the vector containing the parameters to be estimated from the model once $\vec{y}$ is given (in this work the abundances a_i)
- U is the prior knowledge of $\vec{x}$ (e.g. JEFF-3.1.1 abundances a_i)

For the moment, any other variable that might describe the model is not considered. The idea is to measure $\vec{y}$ and to estimate $\vec{x}$ using the model. The continuous form of Eq. 2.26 is [15]

$$p(\vec{x} \mid \vec{y}, U) = \frac{p(\vec{x} \mid U) \cdot p(\vec{y} \mid \vec{x}, U)}{\int \mathrm{d}\vec{x} \cdot p(\vec{x} \mid U) \cdot p(\vec{y} \mid \vec{x}, U)} \tag{2.27}$$

where $p(\vec{x} \mid \vec{y}, U)$ is the posterior distribution, $p(\vec{x} \mid U)$ is the prior distribution, $p(\vec{y} \mid \vec{x}, U)$ is the likelihood function, sometimes written as $\mathcal{L}(\vec{y} \mid \vec{x}, U)$, and the denominator is just a normalization factor. In the nuclear field it is common practice to estimate the parameters $\vec{x}$ by computing the first two moments of the posterior probability distribution [15].

2.2.3 Analytical Method

To analytically solve Eq. 2.27 one has to make assumptions on both the prior and the likelihood distributions. According to the *Maximum Entropy Theorem*, the distribution that maximizes the entropy is the multivariate Gaussian [15]. Therefore the prior distributions becomes

$$p(\vec{x} \mid U) \propto e^{-\frac{1}{2}(\vec{x}-\vec{x_m})^T M_x^{-1} (\vec{x}-\vec{x_m})} \tag{2.28}$$

given that its mean $(\vec{x_m})$ and its covariance matrix (M_x) are known, while the likelihood distribution becomes

$$p(\vec{y} \mid \vec{x}, U) \propto e^{-\frac{1}{2}(\vec{y}-\vec{t})^T M_y^{-1} (\vec{y}-\vec{t})} \tag{2.29}$$

where $\vec{t}$ is the set of theoretical calculations to be compared with $\vec{y}$, and M_y is the experimental covariance matrix. Neglecting the normalization factor of Eq. 2.27 it is evident that the posterior probability distribution is proportional to the product of the prior and the likelihood probability distributions. Taking into account Eq. 2.28 and 2.29 the posterior probability distribution becomes

$$p(\vec{x} \mid \vec{y}, U) \propto e^{-\frac{1}{2}[(\vec{x}-\vec{x_m})^T M_x^{-1} (\vec{x}-\vec{x_m}) + (\vec{y}-\vec{t})^T M_y^{-1} (\vec{y}-\vec{t})]} \tag{2.30}$$

and the problem is reduced to finding its first two moments. Here another approximation must be added: that the posterior distribution is itself a multivariate Gaussian with the same characteristics of the right-hand-side of Eq. 2.30 (Laplace approximation [16]). To solve the problem then it is sufficient to use the Generalized Least Squares Method (GLS), which consists in finding the minimum of the cost function

$$\chi^2_{GLS} = (\vec{x} - \vec{x_m})^T M_x^{-1} (\vec{x} - \vec{x_m}) + (\vec{y} - \vec{t})^T M_y^{-1} (\vec{y} - \vec{t}). \tag{2.31}$$

2.2.4 Monte Carlo Method

The Bayesian Monte Carlo (BMC) allows solving the Bayesian inference without resorting to any approximation. In particular, the Monte Carlo sampling is used to compute integrals, as shown in Eq. 2.32

$$\int p(\vec{x}) \cdot f(\vec{x}) \mathrm{d}\vec{x} = \lim_{n\to\infty} \left(\frac{1}{n} \sum_{k=1}^{n} f(\vec{x_k}) \right). \tag{2.32}$$

One example of application could be the first moment of the posterior probability distribution, also called *mean*, which in continuous form is calculated as

$$\begin{aligned} \langle \vec{x} \rangle &= \int \vec{x} \cdot p(\vec{x}) \mathrm{d}x \\ &= \int \vec{x} \cdot \frac{p(\vec{x}|U) \cdot p(\vec{y}|\vec{x},U)}{\int p(\vec{x}|U) \cdot p(\vec{y}|\vec{x},U) \mathrm{d}\vec{x}} \mathrm{d}\vec{x}. \end{aligned} \tag{2.33}$$

To solve the integral, the prior probability distribution $p(\vec{x} \mid U)$ is sampled and for each $\vec{x_k}$, the likelihood $\mathcal{L}_k = p(\vec{y_k} \mid \vec{x_k}, U)$ is computed [16]. Then, after N_x samples, the mean becomes

$$\langle \vec{x} \rangle_{N_x} = \frac{\sum_{k=1}^{N_x} x_{i,k} \mathcal{L}_k}{\sum_{k=1}^{N_x} \mathcal{L}_k}. \tag{2.34}$$

2.3 Uncertainty Propagation Methodologies

The purpose of any uncertainty analysis is to identify and quantify all sources of uncertainty and to assess their effect on the estimated quantities. Errors can be statistical or systematic, and can be due to the input data (microscopic data uncertainties), to the experimental procedure (sample composition, alignment of the beam, calibration) or to the data reduction process (normalization, background, definition of the exact end of the irradiation).

2.3.1 Bayesian Marginalization

Systematic uncertainties come from parameters that do not belong to the theoretical model under consideration but which have a significant effect on the final parameters' uncertainty. They are usually called *nuisance* parameters and one way to deal with them is to consider them as random variables ($\vec{\theta}$) having a specific probability distribution and to include them in the Bayesian inference. The difference between the parameters $\vec{x}$ and $\vec{\theta}$ is that the latter is assumed to be known with a certain prior covariance matrix, while the former has to be fitted. The problem consists in propagating the uncertainty of $\vec{\theta}$ during the fitting of $\vec{x}$ [16] and the procedure is called *Bayesian marginalization*. The posterior probability density function (Eq. 2.27) when adding nuisance parameters becomes

$$p(\vec{x} \mid \vec{y}, \vec{\theta}, U) = \frac{p(\vec{x} \mid \vec{\theta}, U) \cdot p(\vec{y} \mid \vec{x}, \vec{\theta}, U)}{\int \mathrm{d}\vec{x} \cdot p(\vec{x} \mid \vec{\theta}, U) \cdot p(\vec{y} \mid \vec{x}, \vec{\theta}, U)} \tag{2.35}$$

One common assumption is that the prior knowledge of $\vec{x}$ is independent of $\vec{\theta}$ so that $p(\vec{x} \mid \vec{\theta}, U)$ can be replaced by $p(\vec{x} \mid U)$ [16]. The last step is to integrate over the

nuisance parameters and to compute the first two moments of the resulting *marginal distribution*[5]

$$\begin{aligned} p_{\vec{\theta}}(\vec{x} \mid \vec{y}, U) &= \int \mathrm{d}\vec{\theta} \cdot p(\vec{x} \mid \vec{y}, \vec{\theta}, U) \\ &= \int \mathrm{d}\vec{\theta} \cdot p(\vec{\theta} \mid U) \cdot p(\vec{x} \mid \vec{y}, \vec{\theta}, U) \\ &= \int \mathrm{d}\vec{\theta} \cdot p(\vec{\theta} \mid U) \cdot \frac{p(\vec{x}|U) \cdot p(\vec{y}|\vec{x}, \vec{\theta}, U)}{\int \mathrm{d}\vec{x} \cdot p(\vec{x}|U) \cdot p(\vec{y}|\vec{x}, \vec{\theta}, U)}. \end{aligned} \tag{2.36}$$

Again, even if nuisance parameters have been added, one can choose to use either a stochastic treatment or an analytical formalism to solve the problem.

2.3.2 Types of Marginalization

Marginalization is a procedure used to propagate the effect (uncertainties and correlations) of non-adjusted parameters. It can either be estimated by an Analytical or a Monte Carlo method.

Analytical Marginalization (M-GLS)

This technique can be used under the assumption that all probability density distributions are Gaussian [11]. In that case, all the parameters, both the ones to be fitted and the nuisance, must be put in the same vector $\vec{X}$

$$\vec{X} = \begin{pmatrix} \vec{x} \\ \vec{\theta} \end{pmatrix} \tag{2.37}$$

and all their covariances must be put in the associated matrix M_X

$$M_X = \begin{pmatrix} M_x & M_{x,\theta} \\ M_{\theta,x} & M_{\theta}. \end{pmatrix} \tag{2.38}$$

Then, the partial derivatives of the theoretical results $\vec{t}$ with respect to the model parameters $\vec{x}$ and $\vec{\theta}$ have to be computed and put in the derivative matrix G

$$G^x = \begin{pmatrix} \frac{\mathrm{d}t_1}{\mathrm{d}x_1} & \cdots & \frac{\mathrm{d}t_1}{\mathrm{d}x_n} \\ \vdots & & \vdots \\ \frac{\mathrm{d}t_k}{\mathrm{d}x_1} & \cdots & \frac{\mathrm{d}t_k}{\mathrm{d}x_n} \end{pmatrix} \qquad G^\theta = \begin{pmatrix} \frac{\mathrm{d}\theta_1}{\mathrm{d}x_1} & \cdots & \frac{\mathrm{d}t_1}{\mathrm{d}\theta_n} \\ \vdots & & \vdots \\ \frac{\mathrm{d}t_k}{\mathrm{d}\theta_1} & \cdots & \frac{\mathrm{d}t_k}{\mathrm{d}\theta_n} \end{pmatrix} \tag{2.39}$$

to obtain the covariance matrix for the theoretical parameters M_t

$$G = (G^x \; G^\theta) \tag{2.40}$$

$$M_t = G \; M_X \; G^T. \tag{2.41}$$

The following step is to transfer all the uncertainties and covariances to the fitted parameters and to its covariance matrix M_x^{margi}, as if all the uncertainties come from the vector $\vec{x}$ (note that G^x is used instead of G)

$$G^x \; M_x^{margi} \; G^{x^T} = G \; M_X \; G^T. \tag{2.42}$$

[5] Note that we want the results independently of $\vec{\theta}$ so to get rid of it we need to integrate over the nuisance parameters. This is the marginal distribution $p_{\vec{\theta}}(\vec{x} \mid \vec{y}, U)$.

Monte Carlo Marginalization

The Monte Carlo method consists in simulating N sets of nuisance parameters $\vec{\theta}$ and for each of them ($k = 1 \cdots N$) fitting the parameters $\vec{x}$ with the distribution [16]

$$p_{\vec{\theta}=\vec{\theta}^{(k)}}(\vec{x} \mid \vec{y}, U) \propto p(\vec{x} \mid U) \cdot p(\vec{y} \mid \vec{x}, \vec{\theta} = \vec{\theta}^{(k)}, U), \tag{2.43}$$

which is the same marginal distribution of Eq. 2.36, but instead of integrating over θ we fix $\vec{\theta}$ to be $\vec{\theta}^{(k)}$. After the fitting, there are N sets of fitted parameters $\vec{x}^{(k)}$, each with an associated covariance matrix $X^{(k)}$ which can be seen as a *conditional* covariance matrix since it is the covariance matrix that we would get *given* the nuisance parameters vector $\vec{\theta}^{(k)}$

$$X^{(k)} = cov(x_i, x_j \mid \vec{\theta} = \vec{\theta}^{(k)}). \tag{2.44}$$

The *total covariance theorem*

$$cov(x_i, y_i) = cov(x_i^{(k)}, y_i^{(k)}) + \mathbb{E}(X^{(k)}) \tag{2.45}$$

affirms that the covariance matrix of the fitted parameters $cov(x_i, x_j)$ can be found by adding two terms:

- $cov(x_i^{(k)}, y_i^{(k)})$: the covariance matrix calculated by using the N sets of n fitted parameters (see Eq. 2.46)

$$cov(x_i^{(k)}, y_i^{(k)}) = \frac{1}{N-1} \begin{bmatrix} \sum_{k=0}^{N} (x_{k,1} - \mu_1)^2 & \cdots & \sum_{k=0}^{N} (x_{k,1} - \mu_1)(x_{k,n} - \mu_n) \\ \vdots & \ddots & \vdots \\ \sum_{k=0}^{N} (x_{k,n} - \mu_n)(x_{k,1} - \mu_1) & \cdots & \sum_{k=0}^{N} (x_{k,N} - \mu_n)^2 \end{bmatrix} \tag{2.46}$$

- $\mathbb{E}(X^{(k)})$: the average of the N covariance matrices associated with each fit.

The Bayesian Monte Carlo allows propagating the systematic uncertainties on the fitted parameters, without any assumption on the distribution of the nuisance parameters.

2.4 CONRAD®

CONRAD® (*COde for Nuclear Reaction Analysis and Data assimilation*) is an object-oriented code developed in C++ at CEA Cadarache in the LEPh (*Laboratoir d'Etudes de PHysique*) laboratory which belongs to the SPRC (*Service de Physique des Réacteurs et du Cycle*) service [14]. The code is intended to help nuclear physicists in the nuclear data evaluation process. It contains [62]:

- *Analysis classes* providing statistical tools for data evaluation methodologies and covariance generation
- *Theoretical models* for the treatment of cross sections and fission observables
- *Experimental classes* for the treatment of microscopic measurements or the assimilation of integral information
- *Interface classes* for the communication among classes and the choice of output format.

In the framework of the thesis, CONRAD® has been extensively used for fitting, for the uncertainty and covariances estimation as well as for the assimilation of integral measurements. Both the Analytical and the Monte Carlo marginalization are implemented in the CONRAD® code. The user can choose which calculation scheme to use by specifying it in the input file. Special thanks go to Pierre Tamagno for his help in using the CONRAD® code.

Part II

Microscopic Approach

Chapter 3

Average Delayed-Neutron Yield

> It doesn't matter which side of the fence you get off on sometimes. What matters most is getting off. You cannot make progress without making decisions.
>
> Jim Rohn

Contents

3.1 Merging Fission Yields and Radioactive Decay Data 38
3.2 Libraries comparison 39
3.2.1 The concept of precursor's importance 40
3.2.2 Libraries 40
3.2.3 Recommended values 41
3.2.4 Neutron-induced fission of ^{235}U 41
3.2.5 Neutron-induced fission of ^{238}U and ^{239}Pu 50
3.3 Sensitivity of the ν_d to the *CY* and to the P_n 53
3.4 Alternative method to compute the ν_d 55
3.5 Results with the optimal *FY*-*RDD* combination 56
3.6 Energy dependence 58
3.6.1 State of the art 58
3.6.2 Summation calculation 59

THE objective of this chapter is to compute the ν_d for the major fissioning systems at several energies using different combinations of nuclear data libraries. Section 3.1 describes the solver created to merge the FY and the RDD in a single practical file to be able to combine FY and RDD coming from different libraries and to easily use them. Section 3.2 deals with the computation of the ν_d for several fissioning systems in order to identify which combination of libraries gave the closest ν_d to the one recommended by the WPEC. The procedure has been repeated for several fissioning systems and energies and with different input libraries. Section 3.4 describes an alternative method to compute the ν_d. In Section 3.3, the sensitivity of the ν_d to the input data is shown. In Section 3.5, the combination of FY and RDD giving the best ν_d is identified and used for the main

fissioning systems. Finally, Section 3.6 focuses on the energy dependence of the average delayed-neutron yield.

3.1 Merging Fission Yields and Radioactive Decay Data

One way to assess the quality of certain data from a given library is to compare it with the same data coming from other libraries, in the same conditions. Neutronics codes usually take as input a whole database and are not suited for library comparison. Since flexibility in the choice of the input data was an essential requirement of the study, a code has been developed in C++ to extract Fission Yields (FY) and Radioactive Decay Data (RDD) from the ENDF-6 format and to merge them in a single library. Note that both the Independent Yields (IY) and the Cumulative Yields (CY) are taken from the same FY-database, even though the CY in principle depend on the branching ratios and therefore on the RDD. Changing the family tree of an isotope could lead to small differences in the CY. This phenomenon has been studied in Section 3.4. The conclusion is that the discrepancies are negligible and the libraries can be merged without any problem of consistency. For each isotope, the FY library contains

- Z: atomic number of the isotope
- A: atomic mass of the isotope
- I: flag for the isomeric state of the isotope[1]
- IY: independent yield of the isotope
- σ_{IY}: uncertainty in the independent yield of the isotope
- CY: cumulative yield of the isotope
- σ_{CY}: uncertainty in the cumulative yield of the isotope

while the RDD contains

- Z: atomic number of the isotope
- A: atomic mass of the isotope
- I: flag for the isomeric state of the isotope.
- *type*: radioactive decay mode of the isotope[2]
- RFS: flag for the isomeric state of the daughter nuclide after the decay of the isotope. It is equivalent to I but for the daughter isotope
- BR: branching ratio of the isotope for a certain decay mode. It represents the fraction of nuclide which undergoes the corresponding decay[3].
- σ_{BR}: uncertainty in the branching ratio
- HL: half-life of the isotope
- σ_{HL}: uncertainty in the half-life

Note that very often the uncertainties in the FY or in the BR are not reported in the libraries. This happens when the quantities have been computed by models rather than measured. In the absence of any uncertainty, it is possible to impose it as percentage

[1]The isomeric states in the ENDF-6 format are: 0 (ground state), 1 (first metastable state), and 2 (second metastable state).

[2]Types of radioactive decay in the ENDF-6 format: 1.0 for β^- decay, 1.5 for β_n^- decay (one emitted neutron), 1.55 for β_{2n}^- decay (two emitted neutrons), 1.555 for β_{3n}^- decay (three emitted neutrons), and 1.5555 β_{4n}^- decay (four emitted neutrons).

[3]Note that the sum of all the branching ratios of an isotope must be equal to 1.

of the quantity of interest. So for example, if the quantity A has no uncertainty, it is possible to define f so that

$$A \pm fA. \tag{3.1}$$

The program is written in such a way that two values of f can be set: one for the FY and one for the BR. Playing with those quantities is one method of deriving the sensitivity of the uncertainty of a parameter of interest (e.g. σ_{ν_d}) to the uncertainties of the variables used to compute it (σ_{FY}, σ_{BR}). When an isotope is present in both libraries (same Z, A, and I), it is added to the merged database.

3.2 Libraries comparison

There are several ways to compute the ν_d. Among them, one consists in using the cumulative yields and considering all the precursors at equilibrium

$$\nu_d = \sum_{i}^{N} CY_i \; P_{n,i} \; x_i \qquad \text{[DN/fiss]}, \tag{3.2}$$

while another one consists in using the independent yields and letting the system reach the equilibrium state, meaning that each nuclide decays at the same rate at which it is produced.

$$\begin{aligned} \nu_d &= \lim_{t_{irr}\to t_\infty} n_d(t_{irr}) \\ &= \lim_{t_{irr}\to t_\infty} \left(\sum_{i}^{N} x_i \; \lambda \; N_i(t_{irr}) \; P_{n,i} \right) \qquad \text{[DN/fiss]}. \end{aligned} \tag{3.3}$$

N_i is the precursor i's concentration in at or $at \cdot cm^3$, and depends on IY_i. In both the equations, $P_{n,i}$ is the probability for delayed-neutron emission after the β^--decay of the precursor i, and x_i is the number of delayed neutrons emitted during the decay. The use of this formulation implies that all the isotopes under consideration only undergo β^--decay. This is true for the delayed-neutron precursors as well as for all the fission products. However, in a more general case, one should rather use the BR, which takes into account *first* the probability of undergoing β^--decay and *then* the probability to emit a neutron after the β^--decay. Depending on the library under consideration, either the P_n or the BR are given. The evaluated libraries (JEFF, ENDF/B, JENDL $\cdots$) provide directly the branching ratios. Other databases (Pfeiffer, CRP...) give the Pn values and in that case, the branching ratio for delayed-neutron emission has to be derived from the P_n. For example, for $P_n = 63\%$, $P_{2n} = 12\%$ and $P_{3n} = 3.5\%$, the BR are calculated as follows

$$BR_{\beta_n^-} = BR_{\beta^-} \cdot P_n \tag{3.4}$$

where $BR_{\beta^-} = 1$. The BR for the β^- decay without delayed-neutron emission is therefore

$$BR_{\beta^-} = 1 - BR_{\beta_n^-} - BR_{\beta_{2n}^-} - BR_{\beta_{3n}^-} \tag{3.5}$$

In order to evaluate the quality of the nuclear data libraries and to identify the most reliable ones for reactor physics applications, a comparison between predicted and experimental results is essential. From Eq. 3.2 it is evident that the delayed-neutron yield is particularly suited for the library comparison because it is a quantity that only depends on the FY and on the BR. The two methods (Eq. 3.2 and Eq. 3.3) give approximately the same result, but the uncertainty is larger when using the second method, due to

the fact that the independent yields are used, which are characterized by larger uncertainties than the corresponding cumulative yields. Furthermore, more input parameters are needed to compute the activity, which introduces further uncertainties, as shown in Section 3.4.

3.2.1 The concept of precursor's importance

Nuclear data libraries do not always agree on nuclear data. The differences for any data type (e.g. FY or P_n) vary from isotope to isotope. It is possible to state *how different* a library is, with respect to another one. However, the difference is more or less relevant for our purpose depending on the **importance** of the isotope. As shown in Eq. 3.2, the delayed-neutron yield can be calculated as the sum of the product $CY_i \cdot P_{n,i}$ over the whole range of precursors. To state *how important* a precursor is, it is useful to define a new quantity: the importance (I_i), giving the contribution of the precursor i to the ν_d.

$$I_i = \frac{CY_i \cdot P_{n,i}}{\nu_d} \tag{3.6}$$

This 'importance' depends on the couples ($P_{n,i}$, CY_i) and therefore on the chosen libraries. Nevertheless, the 20 major precursors are common to all the libraries, accounting for more than 90% of the global delayed-neutron yield.

3.2.2 Libraries

Nuclear data libraries have different origins and each one includes data coming from either experiments, models or a mixture of the two and completed with further adjustments. It is therefore essential to understand where the data comes from. Here is a list of the libraries considered in this work:

Fission Yields (FY) Libraries:

- **JEFF-3.1.1 (2009)** [8]
- **ENDF/B-VII.0 (2009)** [6]
- **FIFRELIN** [24][4]
- **GEFY-5.3** [7][5]

Radioactive Decay Data (*RDD*) Libraries:

- **RIPL-3** [66]
- **RIPL-3-2015 (2015)**

[4]FIFRELIN (*FIssion Fragments Evaporation Leading to an Investigation of Nuclear data* is a Monte Carlo code developed to model fission fragments de-excitation through neutron emission, γ emission and internal conversion [24]. It employs both nuclear models and empirical hypothesis. Simulations cannot be performed without having a pre-emission mass yield distribution and a kinetic energy distribution per mass as input. The observables (e.g. mean neutron multiplicity) are reproduced leaving five free parameters. The main objective of the FIFRELIN code is to improve the predictive power of nuclear models by estimating more obsevables simultaneously.

[5]GEF (*a General description of Fission Observables* is a model developed with the aim to provide dedicated nuclear data for applications in nuclear technology and engineering. The code considers spontaneous fission and fission up to an excitation energy of about 100 MeV (including multi-chance fission) for a wide range of heavy nuclei from polonium to seaborgium. The development of GEF has been supported by the European Union in the framework of the EFNUDAT project, of the ERINDA project, of the CHANDA project and, during the years 2010 - 2016, by the OECD Nuclear Energy Agency.

- **ENDF/B-VII.1 (2011)** [33]
- **ENDF/B-VIII.0 (2018)** [27]
- **JEFF-3.1.1 (2009)** [8]
- **JENDL-FPDD2000 (2001)** [65]
- **NNDC** [3]
- **Audi (2003)** [64]
- **Pfeiffer and Kratz (2002)** [63]

Among the *FY*-libraries it is important to highlight that JEFF and ENDF/B are evaluated data libraries, while FIFRELIN and GEFY-5.3 data are the results of calculations. Note that both individual and cumulative fission yields were available in the JEFF-3.1.1, ENDF/B-VII.0, and GEFY-5.3 libraries, while only individual yields were present in FIFRELIN. Regarding the P_n-libraries RIPL-3, RIPL-3-2015, ENDF/B-VII.1, ENDF/B-VIII.0 and JEFF-3.1.1, the data has been directly taken from the original databases, while for the other libraries (JENDL-FPDD2000, NNDC, Audi and Pfeiffer[6]) it has been retrieved from the work of L. Mathieu [31]. While RIPL-databases contained both β_n^- and β_{2n}^- probabilities (without any associated uncertainty), the others only had the β_n^- probabilities (including the uncertainty for some specific isotopes). Being *FY* and P_n independent from each other (no covariances), it has been possible to freely combine them and to compute the associated uncertainty.

3.2.3 Recommended values

Table 3.1 reports the recommended ν_d-values for three fissioning systems (^{235}U, ^{238}U and ^{239}Pu) at two different energies: *thermal* ($\sim$ 0.025 eV) and *fast* ($\sim$ 400 keV). It is worth noticing that while the average delayed-neutron yield strongly depends on the fissioning system, it is almost insensitive to the energy-change below 4 MeV. At high energies, the average delayed-neutron yield is supposed to decrease due to the second- and third-chance fissions which are linked to the strengthening of the odd-even effect [70]. Protons, as well as neutrons, are paired-up, and a nucleus with an even number of protons is more stable than one with an odd number. As a consequence, the fission yields of odd-proton nuclei are in general smaller than the ones of even-proton nuclei. Moreover, it is well known that odd-charge nuclei are responsible for more than 90% of the delayed-neutron emission (even-charge nuclei are more stable and rarely decay). The odd-even effect, therefore, tends to reduce the ν_d. However, at higher incident neutron energies, the protons pairing energy becomes negligible when compared to the fissioning nucleus excitation energy. As a consequence, the odd-even effect weakens with energy, meaning that, the higher the energy, the larger the delayed-neutron emission is (see the small increase with energy in Tab.3.1). This is true until the second-chance fission threshold ($\sim$ 4 MeV). The second-chance fissioning system (A) has a smaller excitation energy than the first-chance fissioning system (A+1), and therefore it is characterized by a large odd-even effect that strongly reduces the delayed-neutron emission. A second drop of the ν_d is expected after 12 MeV, when the third-chance fission becomes possible.

3.2.4 Neutron-induced fission of ^{235}U

Given the number of library-combinations, performing the same calculation and comparison for all the possible cases would lead to a large amount of unreadable and often

[6]Note that Audi and Pfeiffer are evaluations of the delayed-neutron emission probabilities, and only contain the precursors' branching ratios.

Table 3.1: Average delayed-neutron yield recommended by the WPEC-SG6.

Fissioning System	**WPEC-6** [38]
$^{235}U_t$	1.62E-02
$^{235}U_f$	1.66E-02
$^{238}U_f$	4.65E-02
$^{239}Pu_t$	6.50E-03
$^{239}Pu_f$	6.55E-03

useless results. At the same time, the more the cases, the easiest is to note particular trends. This is the reason why these calculations have actually been performed. However, for the sake of clarity and to facilitate the interpretation of the results, only the relevant results have been reported, while an example of the complete table can be found in the Appendix C. Tables 3.2 and 3.3 show the average delayed-neutron yield for the thermal and fast fission of ^{235}U. It is important to clarify that the uncertainties shown in the ν_d-tables have been calculated assuming that the error was zero when missing[7].

Table 3.2: ν_d calculation by summation method - $^{235}U_t$.

$^{235}U_t$		**FY**		
		FIFRELIN	**JEFF-3.1.1**	
		IY	**IY**	**CY**
P_n	**RIPL-3**	1.54E-02 (-)	1.36E-02	1.47E-02 (-)
	RIPL-3-2015	1.68E-02 (-)	1.49E-02 (-)	1.63E-02 (-)
	ENDF/B-VII.1	1.68E-02 (1.2%)	1.43E-02 (7.2%)	1.57E-02 (5.2%)
	JENDL FPDD2000	1.66E-02 (2.6%)	1.45E-02 (7.5%)	1.58E-02 (5.6%)
	JEFF-3.1.1	1.53E-02 (1.3%)	1.35E-02 (7.4%)	1.48E-02 (5.4%)
	NNDC	1.69E-02 (2.6%)	1.49E-02 (7.5%)	1.63E-02 (5.6%)
	Audi	1.66E-02 (2.6%)	1.41E-02 (7.7%)	1.55E-02 (5.8%)
	Pfeiffer	1.69E-02 (2.5%)	1.48E-02 (7.3%)	1.62E-02 (5.5%)
		GEFY-5.2	**ENDF/B-VII.0**	
		CY	**IY**	**CY**
	RIPL-3	1.67E-02 (-)	1.40E-02 (-)	1.56E-02 (-)
	RIPL-3-2015	1.82E-02 (-)	1.54E-02 (-)	1.87E-02 (-)
	ENDF/B-VII.1	1.80E-02 (1.2%)	1.65E-02 (4.9%)	1.90E-02 (5.5%)
	JENDL FPDD2000	1.80E-02 (2.6%)	1.60E-02 (4.3%)	1.85E-02 (5.4%)
	JEFF-3.1.1	1.69E-02 (1.4%)	1.41E-02 (3.1%)	1.73E-02 (3.4%)
	NNDC	1.84E-02 (2.6%)	1.54E-02 (4.6%)	1.90E-02 (6.0%)
	Audi	1.79E-02 (2.6%)	1.49E-02 (4.6%)	1.86E-02 (6.0%)
	Pfeiffer	1.86E-02 (2.5%)	1.51E-02 (4.2%)	1.84E-02 (5.7%)

[7]The same calculations have been performed assuming an uncertainty of 100% when missing, and will be reported in the following together with the sensitivity of the ν_d to the CY and to the P_n.

Table 3.3: ν_d calculation by summation method - $^{235}U_f$.

$^{235}U_f$		FY	
		JEFF-3.1.1	**ENDF/B-VII.0**
		CY	**CY**
P_n	**ENDF/B-VII.1**	1.72E-02 (5.0%)	1.76E-02 (6.6%)
	JEFF-3.1.1	1.70E-02 (5.2%)	1.66E-02 (5.5%)
	NNDC	1.83E-02 (5.5%)	1.83E-02 (7.0%)
	Pfeiffer	1.81E-02 (5.5%)	1.81E-02 (7.2%)

Fission Yields Library

1. **Cumulative vs Independent Yields**

Observation:
The difference between the ν_d obtained with IYs and the one obtained with CYs is of the order of 7-9% for JEFF-3.1.1 and 10-20% for ENDF/B-VII.0 thermal-fission yields libraries, IYs always giving the smallest value. On the contrary, at higher energies, the difference becomes 4-5% for JEFF-3.1.1 and 6-7% for ENDF/B-VII.0.

$$thermal = \begin{cases} \nu_d(CY)_{JEFF} > \nu_d(IY)_{JEFF} & [\sim 7\text{-}9\%] \\ \nu_d(CY)_{ENDF/B} > \nu_d(IY)_{ENDF/B} & [\sim 10\text{-}20\%] \end{cases}$$

$$fast = \begin{cases} \nu_d(CY)_{JEFF} > \nu_d(IY)_{JEFF} & [\sim 4\text{-}5\%] \\ \nu_d(CY)_{ENDF/B} > \nu_d(IY)_{ENDF/B} & [\sim 6\text{-}7\%] \end{cases}$$

As mentioned before, independent and cumulative yields are not exactly the same physical quantity, except if the precursor's decay-chain only contains β^--decays. Since the cumulative yields allow to take into account the whole decay chain leading to a precursor, it is easy to imagine they give a larger ν_d value than independent yields. On the other hand, while the 7-9%-difference of JEFF-3.1.1 is reasonable, the 10-20% of ENDF/B-VII.0 seems to be excessive (see the complete Table in Appendix C.1). To investigate the reason for this large inconsistency, both the IYs and CYs from JEFF-3.1.1 and ENDF/B-VII.0 have been plotted, as shown in Fig. 3.1.

While in JEFF-3.1.1 the cumulative yield can be 1 (^{98m}Y) to 1.5 (^{87}Br) larger than the independent yield, in ENDF/B-VII.0 this difference can go from 1 (^{98m}Y) to 1.8 (^{85}As) for all the considered precursors except for ^{86}As, characterized by an unphysical difference of 27.8 times. This would mean that for each fission, a number IY of ^{86}As atoms will be directly produced by fission, while $27.8 \cdot IY$ ^{86}As-atoms would be present at equilibrium (each of which would give birth to delayed neutrons according to the isotope's P_n!). This is even more astonishing considering that, according to JEFF-3.1.1, there is no difference between the cumulative and the independent yield of this isotope (see Tab. 3.4). Physically speaking this means that for JEFF-3.1.1 there are no delayed neutrons in the ^{86}As decay chain (only β^--decays), while ENDF/B-VII.0 assumes also β^-_n-decays (a lot of them!). Even if the order of magnitude is different, ^{86}As is not the only precursor whose decay properties are different in the two libraries. For example, for JEFF-3.1.1, ^{85}As's

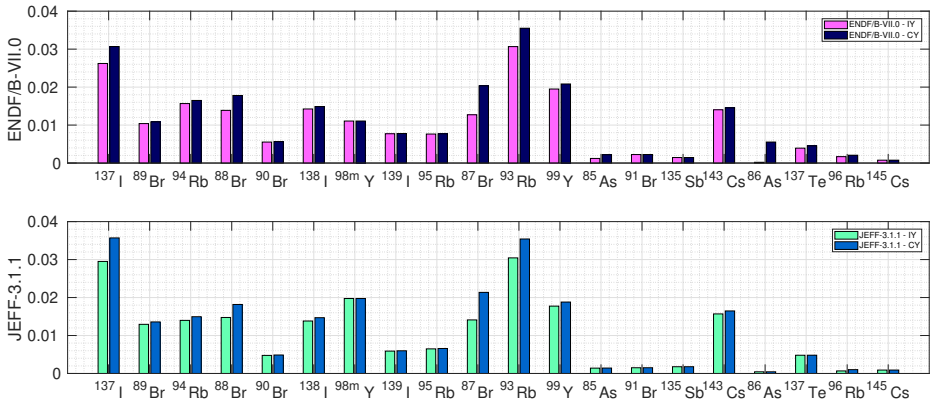

Figure 3.1: Cumulative vs independent yields taken from ENDF/B-VII.0 (upper plot) and JEFF-3.1.1 (lower plot).

CY and IY are the same, while for ENDF/B-VII.0 the first is almost twice the second.

Table 3.4: Cumulative vs independent yield ratio for some precursors.

$^{235}\mathbf{U_t}$	$\mathbf{CY}_i/\mathbf{IY}_i$	
Precursors	**ENDF/B-VII.0**	**JEFF-3.1.1**
^{86}As	27.8	1.0
^{85}As	1.8	1.0
^{96}Rb	1.2	1.5
^{137}Te	1.2	1.0

Note that at higher energies the difference between the results obtained with cumulative or independent yields is much smaller, being 4-5% for JEFF-3.1.1 and 6-7% for ENDF/B-VII.0, both physically reasonable.

2. **Calculated FYs**

Observation:
Calculated delayed-neutron precursors' fission yields (FIFRELIN and GEFY) are always overestimated.

FIFRELIN is a Monte Carlo code which simulates the fission and the decay-cascade of fission fragments by using decay data libraries, according to the branching ratios of each fission product. For that reason, it only provides independent yields. GEFY is a FY-library derived from the GEF code, which is based on a model and therefore provides both independent and cumulative yields. From Tab. 3.2 it is evident that, among the IY-libraries, the *calculated* ones give highly overestimated ν_d-values. Both GEFY-5.2 and FIFRELIN clearly provide exaggerated IYs. The same is true for GEFY's CYs. One could imagine FIFRELIN's eventual CYs to produce results comparable to GEFY-5.2's. It is worth specifying that FIFRELIN calculations depend on the pre-neutron input data ($IY(A)$, $IY(E)$, $IY(Z)$). In any case, due to the clear overestimation of the FY in these two libraries, only JEFF-3.1.1 and ENDF/B-VII.0 will be considered in the following.

3. **JEFF-3.1.1 vs ENDF/B-VII.0 Cumulative Yields**

Observation:
ENDF/B-VII.0's cumulative yields give a ν_d which is 15 to 20% larger than JEFF-3.1.1's cumulative yields in case of thermal fission. On the contrary, in the case of fast fission, the difference in the results ranges from 0 to 2% (JEFF-3.1.1 giving the largest values)

$$thermal = \left\{ \nu_d(CY)_{ENDF/B} > \nu_d(CY)_{JEFF} \qquad [\sim 15\text{-}20\%] \right.$$

$$fast = \left\{ \nu_d(CY)_{ENDF/B} > \nu_d(CY)_{JEFF} \qquad [\sim 0\text{-}2\%] \right.$$

Fixing the delayed-neutron emission probability library, the ν_d only depends on the chosen FY-library. It is evident that ENDF/B-VII.0's cumulative yields for the thermal fission of ^{235}U are somehow overestimated, leading to a result up to 20% larger than the recommended value. The comparison between JEFF-3.1.1 and ENDF/B-VII.0's cumulative fission yields is shown in Fig.3.2. As mentioned

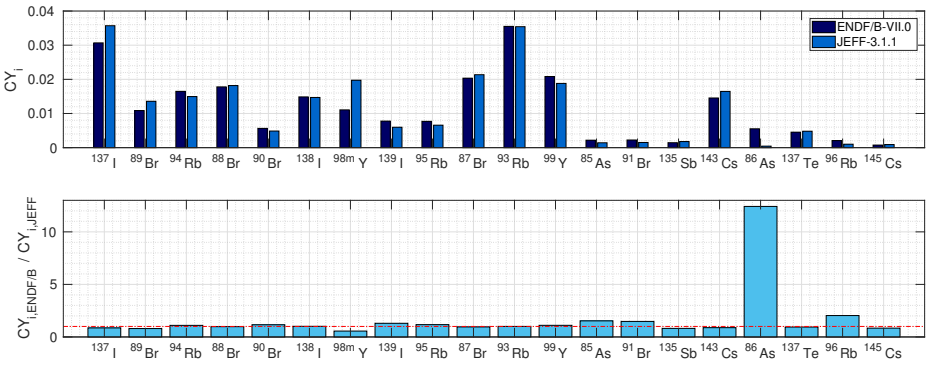

Figure 3.2: Cumulative yields for $^{235}U_t$ taken from JEFF-3.1.1 and from ENDF/B-VII.0. The first plot shows the cumulative fission yields while the second one shows the ratio of the CY of the two libraries, taking JEFF-3.1.1 as a reference.

before, the CY of ^{86}As is exaggerated, especially considering its P_n is not negligible. Less important, but still remarkable is the CY of ^{96}Rb, which is twice the one reported in JEFF-3.1.1. This is true in the case of thermal fission. However, in the case of fast fission, JEFF-3.1.1 and ENDF/B-VII.0 give almost the same ν_d, meaning that the two libraries have very similar fast cumulative yields.

4. **Energy dependence of the Cumulative Yields**

Observation:
While ENDF/B-VII.0's and GEFY-5.3's CY*s* seem to be energy insensitive (-2 to -6% ν_d-reduction when passing from 0.025 eV to 400 keV), JEFF-3.1.1's ones grow with energy, giving a ν_d 11 to 15% higher at 400 keV

$$\nu_d(CY)_t \rightarrow \nu_d(CY)_f = \begin{cases} GEFY & [\sim 2\text{-}6\%] \\ ENDF/B & [\sim 2\text{-}6\%] \\ JEFF & [\sim 11\text{-}15\%] \end{cases}$$

As shown in Tab. 3.1, the delayed-neutron yield for the fission of ^{235}U should not depend on neutron energy in the range 0.025 eV - 400 keV. This is true until the MeV region, after which the ν_d is supposed to decrease. Since the fast energy refers to 400 keV, the delayed-neutron yield should be very similar to the thermal one. Nevertheless, the comparison between Tab. 3.2 and Tab. 3.3 shows a different behavior depending on the FY-library. When using ENDF/B-VII.0's CY, the ν_d decreases by 2 to 6%, while when using JEFF-3.1.1 it increases by 11 to 15%. The reason for this discrepancy can again be found in the cumulative yields. Figure 3.3 shows how the fission yields change with energy in the two libraries. Obviously, only the 20 precursors of interest for the present study are considered. It is immediately evident that JEFF-3.1.1's CYs increase with energy more

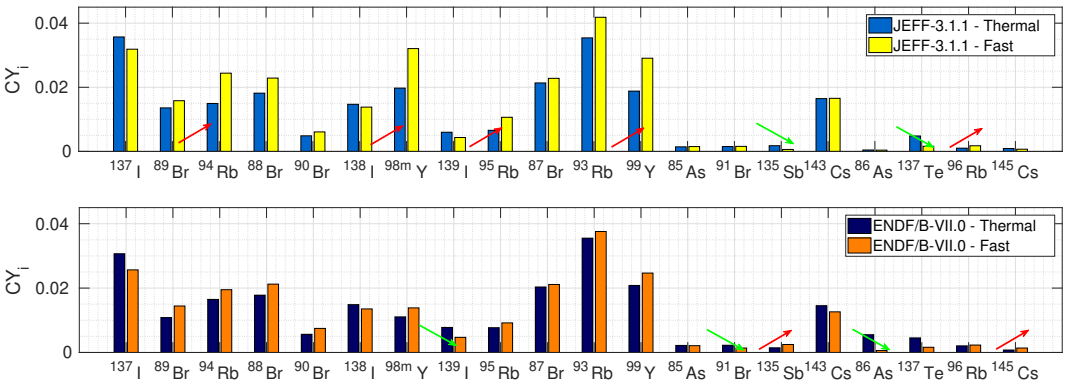

Figure 3.3: Energy dependence of the cumulative yields. The figures show the evolution of the CY from thermal to fast incident energy according to JEFF-3.1.1 (upper plot) and ENDF/B-VII.0 (lower plot). The arrows refer to the isotopes for which the increase/decrease by at least a factor of 1.5.

than ENDF/B-VII.0's when compared to their respective thermal-CYs and this could be at the origin of the previously mentioned difference. Furthermore, in the ENDF/B-VII.0 library not only some CY*s increase less* than in JEFF-3.1.1, but others *decrease more*. This is the case of ^{86}As, which at fast energy becomes 11% smaller than the thermal value in JEFF-3.1.1 and 89% smaller than the thermal in ENDF/B-VII.0. However, one should not be misled by the *right* energy-trend of the ν_d computed by ENDF/B-VII.0 (both CY and P_n), since it is only due to the *wrong* initial (thermal) CY of ^{86}As! Figure 3.4 shows the contribution of each precursor to the delayed-neutron yield (per 100 fissions). In the upper graph, the

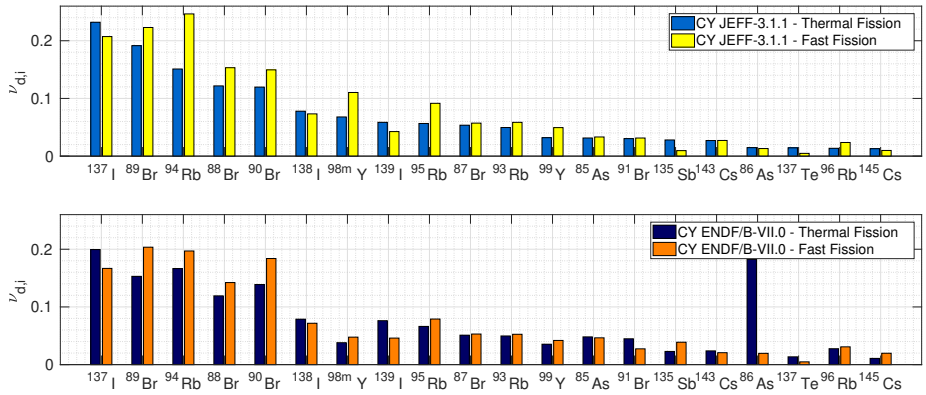

Figure 3.4: Energy dependence of the precursors' contribution to the ν_d of ^{235}U. In both figures the *CY* from JEFF-3.1.1 and ENDF/B-VII.0 are compared. The *FY* library is coupled with JEFF-3.1.1 (upper plot) or with ENDF/B-VII.1 (lower plot).

JEFF-3.1.1 library has been used for both P_n and *CY* data, while in the lower one both have been taken from ENDF/B-VII.0. It is immediately evident that in JEFF-3.1.1 there is no compensation among the precursors' *CY* when passing from thermal to fast energies. On the contrary, in ENDF/B-VII.0 this compensation occurs, due to an apparent huge decrease in the cumulative yield of ^{86}As by at least a factor of 9. This means that correcting the mistake in the thermal range of ENDF/B-VII.0 library would make the library lose its *right* energy-trend (due to the loss of the main compensating factor).

Radioactive Decay Data Libraries

1. **Deficiencies in RIPL-3 library**

Observation:
Between RIPL-3 and RIPL-3-2015 P_n-libraries there is a systematic difference of 8-16%, RIPL3 always giving the smallest ν_d value

$$\nu_d(P_n)_{RIPL\text{-}3} < \nu_d(P_n)_{RIPL\text{-}3\text{-}2015} \qquad [\sim 8\text{-}16\%]$$

From a quick glance at Tab. 3.2, it is evident an increase of the delayed-neutron yield when using RIPL-3-2015 rather than RIPL-3. The quality improvement of the latest version of RIPL-library is due to the addition of many isotopes previously missing (^{88}Br, ^{86}As, ^{96}Rb, ^{141}Te, ^{143}I, ^{153}Ba, ^{154}La, ^{155}La, ^{156}Ce, ^{157}Ce, ^{156}Pr, ^{157}Pr, ^{158}Pr, ^{159}Pr, ^{159}Nd, ^{160}Nd, ^{161}Nd, ^{160}Pm, ^{161}Pm, ^{162}Pm, ^{163}Pm, ^{163}Sm, ^{164}Sm, ^{165}Sm, ^{166}Eu, ^{167}Gd, ^{168}Gd, ^{169}Tb) and to the better estimation of the P_n for important delayed-neutron precursors Figure 3.5 shows these discrepancies.

2. **Other P_n-libraries**

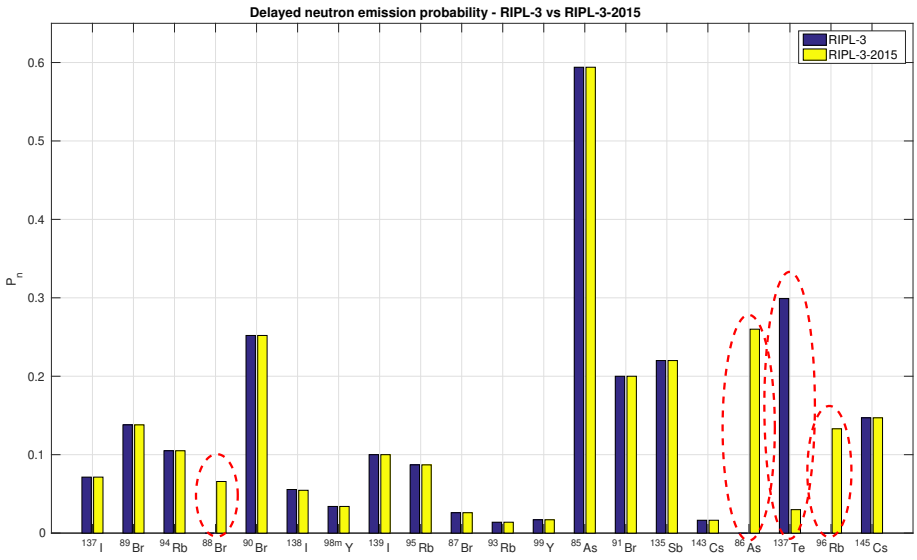

Figure 3.5: Delayed-neutron emission probability for the main precursors in two versions of RIPL-3 library.

Observation:
JEFF-3.1.1 P_n-library always gives a ν_d which is 5 to 10% smaller than the other P_n-libraries (RIPL-3 excluded)

$$\nu_d(P_n)_{JEFF\text{-}3.1.1} < \nu_d(P_n)_{others} \qquad [\sim 5\text{-}10\%]$$

Fixing the FY-library, it is possible to compare the effect of the P_n-database on the ν_d. As observed before, JEFF-3.1.1 seems to always underestimate the delayed-neutron emission probabilities compared to the other libraries (independently on the energy or the FY-library). Figure 3.6 shows the P_n of the 20 major delayed-neutron precursors. It becomes immediately evident that the neutron emission probability of ^{85}As is largely underestimated (0.22 vs an average of 0.57). Furthermore, some precursors have the P_n set to zero, as already pointed out in the work of L. Mathieu [31]. It is also interesting to note that while ENDF/B-VII.0 and Pfeiffer's P_n-libraries often give similar ν_d values, their individual precursor's neutron emission probabilities are not always the same (see ^{85}As, ^{91}Br and ^{86}As in Fig. 3.6), meaning that the similarity of the results is due to a sort of compensation effect.

Combination *FY-RDD*

1. **Precursor's importance depending on the libraries**

   In Section 1.3, the importance has been defined as the ratio between the individual contribution of a precursor to the ν_d and the global ν_d itself, where the latter is the result of the summation calculation by considering about 300 precursors. However, in this way, each case has its specific normalization. Another possibility to look at the problem could be «*Assuming the correct ν_d-value to be 1.62E-02, and assuming I only want to consider these 20 precursors, how much would each*

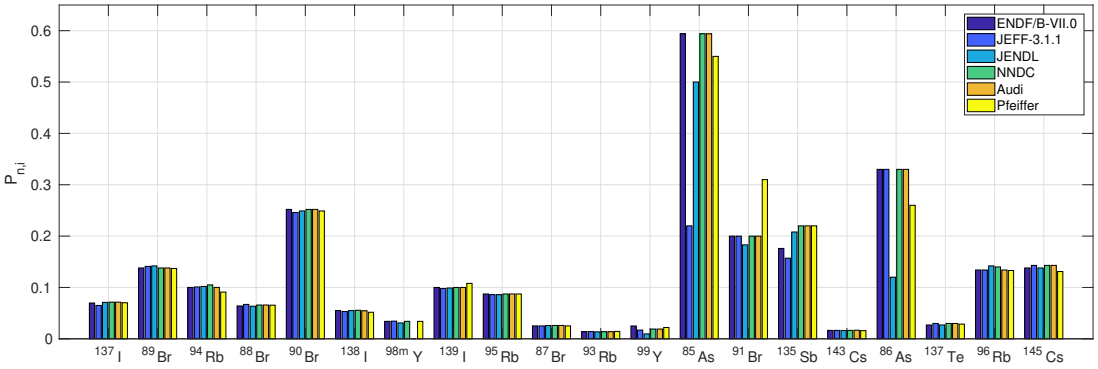

Figure 3.6: Delayed-neutron emission probability comparison.

of them contribute to it?» The answer is shown in Fig.3.7, where all the cases have the same normalization factor. The first plot has been obtained with JEFF-3.1.1's $CY s$, while the second one with ENDF/B-VII.0. Note the importance of ^{86}As, which jumps from the 17th to the 2nd position after ^{137}I. Another remarkable

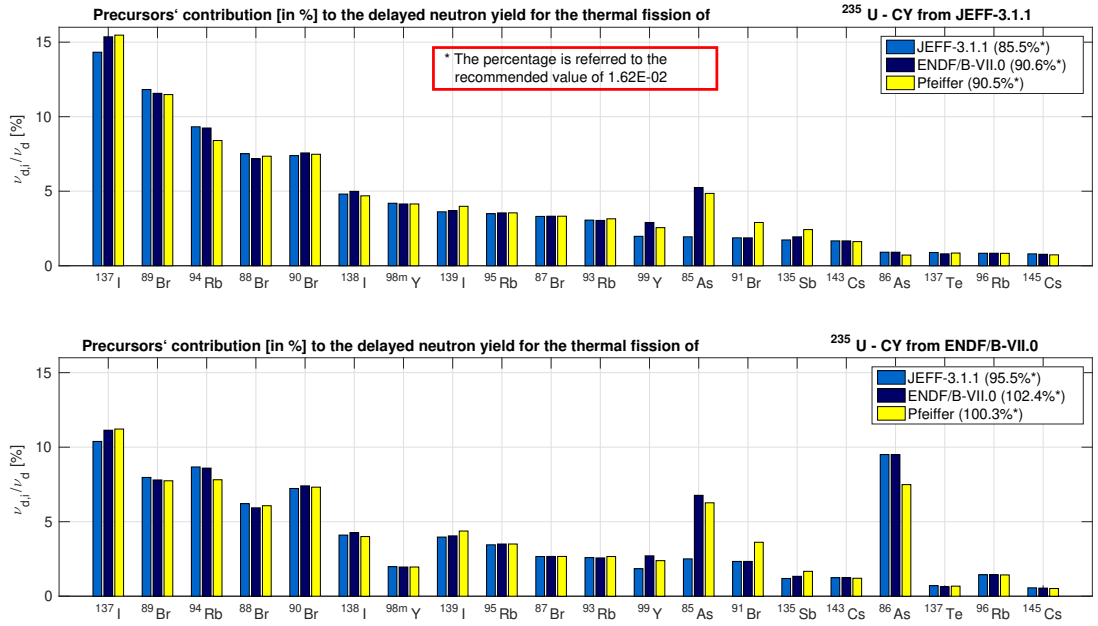

Figure 3.7: Precursors' contribution to the recommended $\overline{\nu_d}$ [in %] of ^{235}U$_t$. In both plots the *RDD* libraries JEFF-3.1.1, ENDF/B-VII.0 and Pfeiffer are compared. The upper plot uses the CY from JEFF-3.1.1 while the lower plot takes them from ENDF/B-VII.0.

difference is the ^{98m}Y-case, with an importance almost half the one of JEFF-3.1.1. The percentages reported in the legend are the sum of the 20 contributions. JEFF-3.1.1's P_n-library always gives an underestimated result, while ENDF/B-VII.0 and Pfeiffer's underestimate the ν_d when coupled with JEFF-3.1.1's CY-library and

slightly overestimate it when coupled with ENDF/B-VII.0's CY-library[8]. It is interesting to note that using the pair ENDF/B-VII.0(CY)-Pfeiffer(P_n) the right result could be obtained by only considering the 20 shown precursors! However, this choice is not advised, since it implies the use of a wrong cumulative yield. The best choices are therefore either the couple JEFF-3.1.1(CY)-ENDF/B-VII.0(P_n) or JEFF-3.1.1(CY)-Pfeiffer(P_n). At the time the comparison had been performed, ENDF/B-VII.1 was the latest version of the American library. In 2018, ENDF/B-VIII.0 was published. The main difference between the two is the correction of the P_n belonging to the ^{98m}Y. The considerations made for the ENDF/B-VII.0 are therefore still valid for ENDF/B-VIII.0.

3.2.5 Neutron-induced fission of ^{238}U and ^{239}Pu

The systematic analysis presented for the ^{235}U has been performed also for ^{238}U and ^{239}Pu. However, to facilitate the reading, only the main points will be discussed. Table 3.5 shows the average delayed-neutron yields computed by summation method using several libraries.

Table 3.5: ν_d calculation by summation method - other fissioning systems.

P_n		FY	
		JEFF-3.1.1	**ENDF/B-VII.0**
		CY	**CY**
^{238}U$_f$	**ENDF/B-VII.1**	4.51E-02 (3.5%)	4.22E-02 (6.6%)
	JEFF-3.1.1	4.04E-02 (3.2%)	3.79E-02 (6.0%)
	NNDC	4.46E-02 (4.3%)	4.19E-02 (7.1%)
	Pfeiffer	4.53E-02 (4.4%)	4.29E-02 (7.1%)
^{239}Pu$_t$	**ENDF/B-VII.1**	6.03E-03 (6.5%)	7.18E-03 (3.2%)
	JEFF-3.1.1	6.05E-03 (7.1%)	7.02E-03 (4.0%)
	NNDC	6.61E-03 (7.2%)	7.52E-03 (4.4%)
	Pfeiffer	6.52E-03 (7.1%)	7.45E-03 (4.4%)
^{239}Pu$_f$	**ENDF/B-VII.1**	6.54E-03 (6.4%)	6.32E-03 (9.7%)
	JEFF-3.1.1	6.75E-03 (6.8%)	6.04E-03 (10.0%)
	NNDC	7.33E-03 (7.1%)	6.63E-03 (9.8%)
	Pfeiffer	7.21E-03 (7.0%)	6.56E-03 (9.6%)

The following observations can be made for ^{238}U:

1. While the use of JEFF-3.1.1 or ENDF/B-VII.0's cumulative yields lead to a difference in the result of 15-20% for ^{235}U$_t$ and 0-2% for ^{235}U$_f$, in the case of ^{238}U$_f$ it gives a difference of 5-6%, this time JEFF-3.1.1 giving the largest ν_d. The reason is that JEFF-3.1.1 proposes larger yields than ENDF/B-VII.0 (except for ^{90}Br, ^{86}As and ^{96}Rb).
2. Contrary to ^{235}U, for which JEFF-3.1.1 P_n-library always gives a result 5-10% smaller than the other libraries, for ^{238}U the corresponding difference rises to 8-12%. One of the reasons could be found in the importance of the 20 considered

[8]The same is not true for the fast fission of ^{238}U,for which the 20 mentioned precursors only account for the 70% of the ν_d. This means that the top-20 list of precursors and their importance change with both the fissioning system and the energy, and that further studies are needed to identify the largest contributor to the ν_d for cases other than the thermal fission of ^{235}U.

precursors. It has been shown that the low P_n-value for ^{85}As in JEFF-3.1.1 could have been the main cause of the difference this library gives with respect to the others. This was reasonable since the 20 showed precursors were representative of more than 90% of the ν_d. Looking at Fig. 3.8, one could note that the precursors' importance has changed compared to ^{235}U and that now, the precursors for which JEFF-3.1.1's P_n were smaller, have slightly grown in importance (see ^{91}Br, ^{135}Sb, and ^{99}Y). Furthermore, since the mentioned precursors only account for about 70%

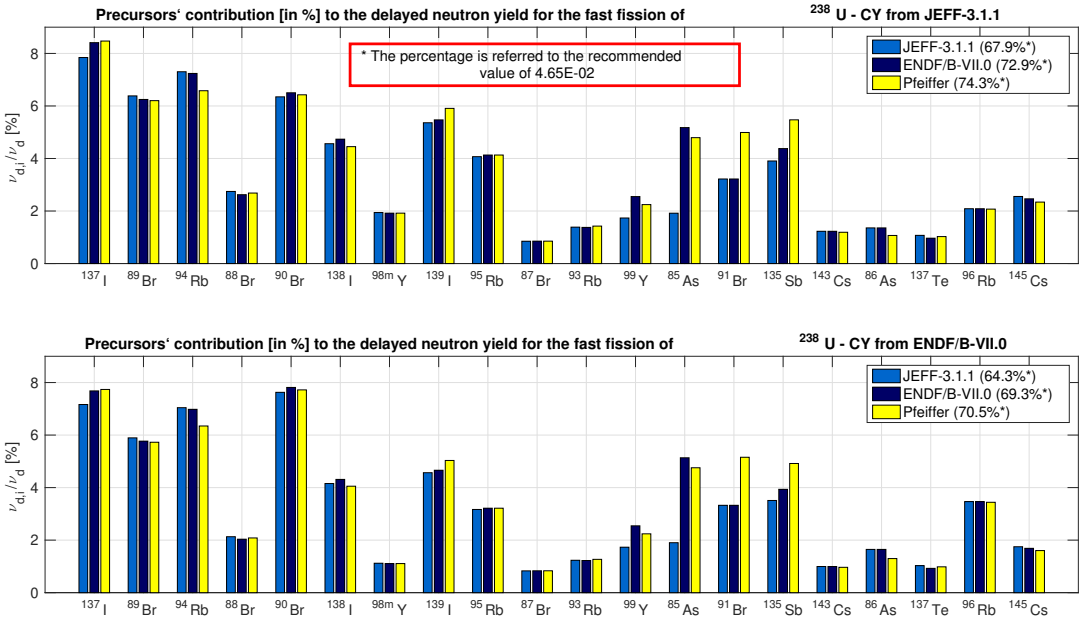

Figure 3.8: Precursors' contribution to the recommended ν_d[in %] of ^{238}U$_f$. In both plots the *RDD* libraries JEFF-3.1.1, ENDF/B-VII.0 and Pfeiffer are compared. The upper plot uses the *CY* from JEFF-3.1.1 while the lower plot takes them from ENDF/B-VII.0.

of the ν_d, there might be other important precursors for which the delayed-neutron emission probability is underestimated or missing.

3. As mentioned before, Fig. 3.8 shows the relative contribution of the 20 major precursors (chosen by considering the thermal fission of ^{235}U) to the ν_d. It is immediately evident that the order of importance is not the same as ^{238}U. Moreover, these 20 precursors are not sufficient to well reproduce the delayed-neutron production and therefore to compare the libraries. Further studies are needed to identify the other important isotopes in the delayed-neutron production following the fast fission of ^{238}U. The difference with respect to the ^{235}U is that the precursors' importance never overcomes 9% and therefore at least 35 isotopes have to be considered to obtain more than 90% of the ν_d. However, the relevant precursors continue to be those already mentioned, with the addition of ^{136}Sb, ^{141}I, ^{97}Rb, ^{137}Sb, ^{136}Te, ^{144}Cs and so on.

Last, but not least, the observations concerning ^{239}Pu are the following:

1. When increasing the energy range, JEFF-3.1.1, and ENDF/B-VII.0 have a different behavior, the first one leading to an increase of ν_d of 9-12% and the latest to a

decrease of 12-14%, while the recommended value is energy-independent. These differences find an explanation in Fig. 3.9. It is clear that at thermal energies

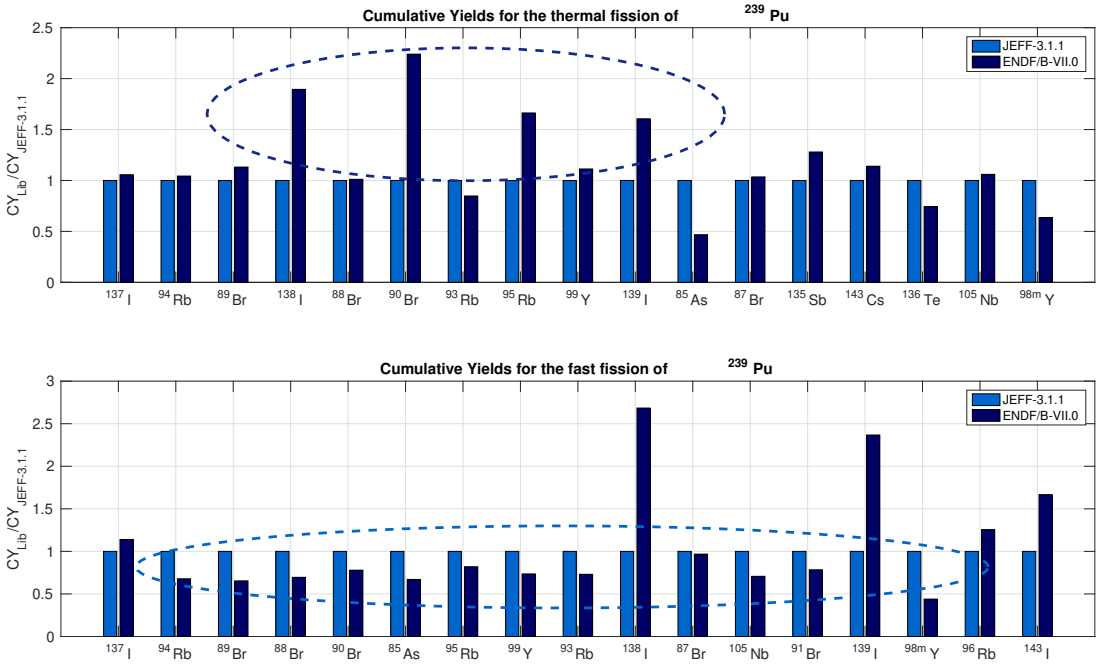

Figure 3.9: Cumulative yields for the thermal (upper plot) and fast (lower plot) fission of ^{239}Pu according to JEFF-3.1.1 and ENDF/B-VII.0.

ENDF/B-VII.0 has larger CY-values than JEFF-3.1.1, while at fast energies the situation is reversed. This is due to the fact that JEFF-3.1.1's CY increase with energy, while ENDF-B-VII.0's decrease

2. While for the other fissioning systems ENDF/B-VII.1 and Pfeiffer have always given similar results, for ^{239}Pu (at both energies) the difference overcomes 8%. The reason for the large difference between the two P_n-libraries (when fixing the FY-library) can be found in the precursors' importance list (see Appendix C.5). The case of ^{98m}Y is astonishing since, according to Pfeiffer, it is the second major contributor to the average delayed-neutron yield ($\sim$ 10% of importance), while according to ENDF/B-VII.1 it does not contribute more than 1% . Since the CY were the same in the two cases, the difference could not be anywhere else but in the P_n. By analyzing the DN emission probabilities it was possible to identify an error in the ENDF/B-VII.1 library. ^{98m}Y is known to be an important DN precursor due to its non-negligible P_n ($\sim$ 3E-02). The same is not true for its ground state (^{98}Y), characterized by a much smaller probability of emitting delayed neutrons ($\sim$ 3E-03). What happened in the ENDF/B-library is that when updating from version VII.0 to version VII.1, the metastable state of ^{98}Y was given the same P_n as its ground state and it therefore lost its importance as a precursor. It is normal then, that ENDF/B-VII.1 always underestimates the average DN yield since it neglects 8-9% of the precursors' contribution (the one of ^{98m}Y). The author discovered the error in March 2017 and alerted the responsible of the libraries at the time (Alejandro Sonzogni). He then checked and corrected the P_n value for the

Table 3.6: Delayed-neutron emission probability of ^{98}Y in the last three versions of ENDF/B. The author highlighted the mistake in 2017 and the P_n-value has been corrected before the release of ENDF/B-VIII.0.

Precursors	**ENDF/B-VII.0**	**ENDF/B-VII.1**	**ENDF/B-VIII.0**
^{98}Y	3.31E-03	3.31E-03	3.31E-03
^{98m}Y	3.20E-02	3.31E-03	3.40E-02

following release of the American library (ENDF/B-VIII.0), as shown in Tab. 3.6. Since the mistake in the *RDD* library has been corrected, for the rest of the work, ENDF/B-VII.1 has been replaced by ENDF/B-VIII.0, which appears to give better results.

3.3 Sensitivity of the ν_d to the CY and to the P_n

A result does not mean anything without its uncertainty. In this work every calculated or measured value is shown with its error. In order to gauge the effect of fission yield uncertainties and neutron emission probabilities, one possibility is to compute the error through Eq. 3.7 first, and then to repeat the calculation while setting σ_{CY} and σ_{P_n} alternatively to zero. This procedure has been done twice, each time with a different assumption regarding the missing data:

- $\sigma_X = 0$ when the absolute error in X was unknown (meaning 0% of relative error).
- $\sigma_X = X$ when the absolute error in X was unknown (meaning 100% of relative error).

Both the assumptions are strong, but they allow us to define the boundaries within which the real error lies. Table 3.7 shows the sensitivity of the ν_d to the CY and to the P_n for the thermal fission of ^{235}U.

Table 3.7: Uncertainty components for the ν_d associated with the thermal fission of ^{235}U.

$^{235}U_{thermal}$			FY	
			JEFF-3.1.1	
			$\sigma_X = 0$	$\sigma_X = X$
P_n	**JEFF-3.1.1**	ν_d	1.48E-02	1.48E-02
		σ_{ν_d}	5.34%	5.94%
		σ_{ν_d} $(\sigma_{CY} = 0)$	1.85%	3.19%
		σ_{ν_d} $(\sigma_{P_n} = 0)$	5.01%	5.01%
	ENDF/B-VIII.0	ν_d	1.61E-02	1.61E-02
		σ_{ν_d}	5.18%	5.30%
		σ_{ν_d} $(\sigma_{CY} = 0)$	1.63%	1.97%
		σ_{ν_d} $(\sigma_{P_n} = 0)$	4.92%	4.92%
	Pfeiffer	ν_d	1.62E-02	1.62E-02
		σ_{ν_d}	5.53%	5.55%
		σ_{ν_d} $(\sigma_{CY} = 0)$	2.70%	2.73%
		σ_{ν_d} $(\sigma_{P_n} = 0)$	4.83%	4.83%

In the table,

- ν_d is the average delayed-neutron yield computed by summation calculation when the system is at equilibrium (CY are directly used).
- σ_{ν_d} is the ν_d uncertainty (absolute error), computed through Eq. 3.7. The value found in the second row is the relative error in percentage.
- $\sigma_{\nu_d}(\sigma_{CY} = 0)$ is the ν_d uncertainty (absolute error), setting the error in the CY to zero. In that case, the uncertainty is only due to σ_{P_n}.
- $\sigma_{\nu_d}(\sigma_{P_n} = 0)$ is the ν_d uncertainty (absolute error), setting the error in the P_n to zero. In that case, the uncertainty is only due to σ_{CY}.

From Eq. 3.7 it is possible to see how the uncertainty formulation changes when σ_{CY} and σ_{P_n} are alternatively set to zero. Taking as an example the couple JEFF-3.1.1-JEFF-3.1.1 one could note that the uncertainty in the ν_d ranges from 5.37% (when a missing uncertainty means the variable is *fully known*) to 5.97% (when a missing uncertainty means the variable is *fully unknown*). The difference between the two is not enormous, meaning that the JEFF-library is pretty complete-in-uncertainty[9] on both fission yields and neutron emission probabilities (almost all the data have an associated value of uncertainty). The same is true when considering the other P_n-libraries. Other data shown in the table are the sensitivities of ν_d to the uncertainties of CY and P_n. Taking the first example (JEFF-3.1.1-JEFF-3.1.1, $\sigma_X = 0$) one could see that the variance computed when setting σ_{CY} to zero (known CY-values) is 12% of the total one. This 12% can be attributed to the P_n-library. On the other hand, when the neutron emission probabilities are considered to be well known ($\sigma_{P_n} = 0$), the variance is still 88% of the global one! In conclusion, it is reasonable to say that most of the uncertainty in the JEFF-3.1.1-JEFF-3.1.1 combination is due to the CY! Another thing to note is that the percentages change with the chosen assumption. For $\sigma_X = X$ (all the precursors have an associated uncertainty) the contribution of the P_n rises to 30% of the variance, evidence that there were missing data in the library.

As far as the other library-combinations are concerned, ENDF/B-VIII.0 and Pfeiffer *RDD* give very similar results and sensitivities and can be considered to be almost equivalent. It is worth mentioning that this statement would not be true if the American library had not been corrected. It has been shown indeed, that the ν_d computed using JEFF-3.1.1 *FY* and ENDF/B-VII.I *RDD* for the $^{235}\mathrm{U_t}$ is 1.57E-02, 3% lower than the one computed using Pfeiffer.

$$\sigma_{\nu_d} = \sqrt{\sum_i^N \left[\left(P_{n,i} \cdot \sigma_{CY_i} \right)^2 + \left(CY_i \cdot \sigma_{P_{n,i}} \right)^2 \right]} \tag{3.7}$$

$$\sigma_{\nu_d}(\sigma_{CY} = 0) = \sqrt{\sum_i^N \left(CY_i \cdot \sigma_{P_{n,i}} \right)^2} \tag{3.8}$$

$$\sigma_{\nu_d}(\sigma_{P_n} = 0) = \sqrt{\sum_i^N \left(P_{n,i} \cdot \sigma_{CY_i} \right)^2} \tag{3.9}$$

Table 3.7 shows the results for the thermal fission of ^{235}U. It is interesting to note that, in the JEFF-3.1.1-JEFF-3.1.1 case, setting a 100% relative error for precursors

[9] *complete-in-uncertainty* means that most of the data reported in the library have an associated value of uncertainty. This concept of completeness should not be confused with the concept of a library with a consistent set of data. Indeed, it has been shown before that JEFF-3.1.1's P_n-library is poor with respect to the others.

with unknown uncertainty is not sufficient to cover the discrepancy between the result (1.47E-02) and the recommended value (1.62E-02), due to missing data. To conclude, the larger the fission yields, the more important is the accuracy on the neutron-emission probabilities and vice-versa.

3.4 Alternative method to compute the ν_d

As mentioned at the beginning of Section 3.2, there are several ways to compute the average delayed-neutron yield. So far only the first method - the direct sum using the cumulative yields - has been presented. It is worth spending a few words on the second method, which uses the independent yields instead. The principle of such a technique is to reconstruct the build-up of the precursors during the irradiation phase until the complete saturation of their concentrations. At equilibrium, if the fission rate is set to 1, their contribution to the ν_d should be equivalent to the product $CY_i \cdot P_{n,i} \cdot x_i$, used in the first method. In this section, the two techniques are compared in order to draw some information on microscopic data. In order to compute the global delayed-neutron activity $n_d(t)$ from microscopic data, a solver has been developed: the *Bateman solver*, described in details in Section 4.1 of Chapter 4. The role of this solver is to reconstruct the family tree of each precursor and to compute its concentration at each point in time, taking into account that it is not only directly created by the fission event, but also by its fathers' decay. It is important to stress that a cumulative yield hides the information about the decay chain of the precursor it is referred to. So, combining JEFF-3.1.1's *IY* with ENDF/B-VIII.0's *RDD*, will not necessarily give JEFF-3.1.1's *CY*. Table 3.8 shows $^{235}\mathrm{U_t}$'s ν_d computed using the two methods. The fission yields are taken from JEFF-3.1.1 while the radioactive decay data from ENDF/B-VIII.0. It is evident that after 300 s of irradiation the delayed-neutron activity tends to the average delayed-neutron yield. Using the second method, the uncertainty in the computed ν_d is larger, due to the fact that *IY* are characterized by larger errors than *CY* (as it could be seen in Tab. 3.2). Furthermore, in the 6.7% are also included the uncertainties on the *IY* and P_n of all the fission products appearing in the decay chain of the precursors. In principle, a covariance matrix among the *IY* should include these effects and, if used in the calculation, would reduce the uncertainty on the ν_d to 5.2%. If such correlation matrix is not available, it is recommended to use the cumulative yields.

Table 3.8: Methods comparison for the estimation of the ν_d by summation calculation. The results refer to the thermal fission of ^{235}U, computed using JEFF-3.1.1's *FY* and ENDF/B-VIII.0's *RDD*.

t_{irr} [s]	ν_d [DN/fiss]	$\lim_{t_{irr}\to t_\infty} n_d(t_{irr})$ [DN/fiss]
0.5	1.61E-02 (5.2%)	2.15E-03 (8.1%)
1		3.66E-03 (7.9%)
5		9.15E-03 (7.8%)
10		1.15E-02 (7.7%)
20		1.32E-02 (7.4%)
50		1.49E-02 (6.9%)
100		1.57E-02 (6.8%)
300		1.60E-02 (6.7%)
600		1.60E-02 (6.7%)
1000		1.60E-02 (6.7%)

3.5 Results with the optimal *FY*-*RDD* combination

In the previous sections, several *FY* and *RDD* libraries have been merged and used to compute the ν_d as well as its uncertainty. Fission yields and P_n-values have also been compared. Errors in some of the libraries have been identified. Thanks to this work, two errors in the libraries have been identified (CY of ^{86}As in ENDF/B-VII.0 and P_n of ^{98m}Y in ENDF/B-VII.1) and corrected. Finally, comparing all the possible combinations, the couple JEFF-Pfeiffer is the best in terms of both results and associated uncertainties, even though further work would be needed to fix the wrong energy-dependence of the ν_d. Nevertheless, Pfeiffer is not an evaluated library and does not contain all the variables needed for reconstructing the family tree of each precursor (e.g. *RFS*, *type*). In order to reconstruct the delayed-neutron activity curve by summation method, the second-best *RDD* library has been chosen: ENDF/B-VIII.0. The ν_d calculation has been performed for many fissioning systems. The results are reported in Tab. 3.9 together with the evaluation made by Tuttle in 1979 [56] and with the values recommended by JEFF-3.1.1. Note that JEFF does not provide any uncertainty and that in Tuttle's evaluation some isotopes are missing. Globally, the summation calculation works fine for most of the fissioning systems. However, like any other calculation, the quality of the results depends on the input data. The discrepancies, shown in Tab. 3.9 for certain isotopes (^{233}U$_f$, ^{235}U$_f$, ^{241}Pu$_{t/f}$) point toward possible errors in the fission yield of those isotopes. Further work should be done to investigate the fission yields of those fissioning systems more thoroughly.

Table 3.9: ν_d computed by summation method using JEFF-3.1.1 cumulative fission yields (CY) and ENDF/B-VIII.0 radiactive decay data (*RDD*) as microscopic input data, and compared with Tuttle's evaluation and with JEFF-3.1.1 library.

Fissioning System	**This work**	**Tuttle**	**JEFF-3.1.1**
^{232}Th$_f$	6.11E-02 (4.5%)	-	5.27E-02
^{233}U$_t$	7.82E-03 (7.5%)	6.67E-03 (4.3%)	6.73E-03
^{233}U$_f$	1.12E-02 (7.6%)	7.3E-03 (4.9%)	7.4E-03
^{235}U$_t$	1.61E-02 (5.2%)	1.62E-02 (3.1%)	1.62E-02
^{235}U$_f$	1.80E-02 (5.1%)	1.67E-02 (2.1%)	1.63E-02
^{236}U$_f$	2.60E-02 (6.2%)	2.21E-02 (10.7%)	2.24E-02
^{237}Np$_f$	1.26E-02 (5.4%)	-	1.20E-02
^{238}U$_f$	4.49E-02 (3.4%)	4.39E-02 (2.3%)	4.78E-02
^{239}Pu$_t$	6.56E-03 (6.9%)	6.30E-03 (6.0%)	6.50E-03
^{239}Pu$_f$	7.22E-03 (6.8%)	6.30E-03 (2.5%)	6.50E-03
^{241}Pu$_t$	1.37E-02 (4.5%)	1.52E-02 (7.3%)	1.60E-02
^{241}Pu$_f$	1.41E-02 (5.1%)	1.52E-02 (7.3%)	1.60E-02
^{241}Am$_f$	4.44E-03 (12.9%)	-	4.30E-03

The correlations among the average delayed-neutron yields of different fissioning systems come from the fact that the fissioning isotopes share the radioactive decay data library. The correlation matrix is shown in Fig. 3.10 and in Table 3.10.

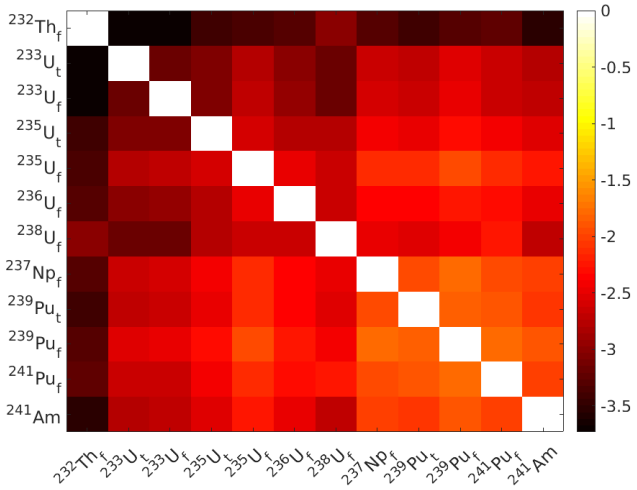

Figure 3.10: Correlations among the ν_d of several fissioning systems computed using JEFF-3.1.1 fission yields and ENDF/B-VIII.0 radiactive decay data. The values are represented in logarithmic scale.

Note that the correlation between the ν_d of the same fissioning system at two different energies is underestimated because it has been computed under the assumption that the fission yields were independent on each other. In reality, the correlation among the ν_d from thermal and fast fission of the same nuclide should be close to 1. At the moment, there is no international consensus on the correlation matrix to be adopted among the IY of the same isotope at different energies, so the author is obliged to consider them as independent.

Table 3.10: Correlation matrix among ν_d of different fissioning systems at different energies, computed by CONRAD® using JEFF-3.1.1 fission yields and ENDF/B-VIII.0 radiactive decay data as microscopic input data. Correlations are reported in logarithmic scale.

$^{232}\mathbf{Th}_f$	$^{233}\mathbf{U}_f$	$^{233}\mathbf{U}_t$	$^{235}\mathbf{U}_t$	$^{235}\mathbf{U}_f$	$^{236}\mathbf{U}_f$	$^{238}\mathbf{U}_f$	$^{237}\mathbf{Np}_f$	$^{239}\mathbf{Pu}_t$	$^{239}\mathbf{Pu}_f$	$^{241}\mathbf{Pu}_f$	$^{241}\mathbf{Am}_f$
1	0.024	0.025	0.033	0.035	0.038	0.051	0.038	0.033	0.037	0.04	0.029
0.024	1	0.041	0.047	0.062	0.05	0.042	0.072	0.068	0.081	0.069	0.064
0.025	0.041	1	0.048	0.066	0.053	0.041	0.076	0.072	0.086	0.071	0.068
0.033	0.047	0.048	1	0.076	0.064	0.062	0.088	0.085	0.098	0.088	0.077
0.035	0.062	0.066	0.076	1	0.083	0.07	0.121	0.116	0.138	0.119	0.109
0.038	0.05	0.053	0.064	0.083	1	0.071	0.096	0.092	0.107	0.099	0.084
0.051	0.042	0.041	0.062	0.07	0.071	1	0.082	0.079	0.087	0.104	0.067
0.038	0.072	0.076	0.088	0.121	0.096	0.082	1	0.14	0.166	0.145	0.131
0.033	0.068	0.072	0.085	0.116	0.092	0.079	0.14	1	0.164	0.147	0.129
0.037	0.081	0.086	0.098	0.138	0.107	0.087	0.166	0.164	1	0.169	0.154
0.04	0.069	0.071	0.088	0.119	0.099	0.104	0.145	0.147	0.169	1	0.132
0.029	0.064	0.068	0.077	0.109	0.084	0.067	0.131	0.129	0.154	0.132	1

3.6 Energy dependence

In reactor physics, it is important to master the energy dependence of the delayed-neutron yield of different fissioning systems, especially in fast reactors where the incident neutron energy ranges from some keV to some MeV.

3.6.1 State of the art

In 2002 D'Angelo wrote an overview of the measurements and evaluations of delayed-neutron data carried out for the WPEC-6 [21]. The β_{eff} experiments performed in reactors do not provide information on the energy dependence of the ν_d. The only consideration that can be made is the difference between the average thermal and fast values. As mentioned in Section 1.4, Tuttle, in his review of 1979, treated the energy dependence of delayed-neutron yields, especially for ^{233}U, ^{235}U and ^{239}Pu. He stated that the trend is linear in the energy intervals 0-3, 3-7, 7-11 and 11-14.5 MeV. In particular, he explained that in the first region one has to expect an increase of 5% for ^{235}U and ^{239}Pu and of 10% for ^{233}U. Then, a sharp decrease of 30% would follow in the second interval. However, as stressed in the paper of D'Angelo [21], these variations are not supported by strong evidences. Krick and Evans performed, in 1972, monoenergetic experiments in the range 0.05-1.75 MeV. Finally, in 2002, Piksaikin performed several measurements from 0 to 5 MeV for the main fissioning systems [35]. The difference between thermal and fast spectrum, is, according to them, the one shown in Tab. 3.11.

Table 3.11: Experimental energy dependence of the delayed-neutron yield. The values in the table represent the relative variation of the ν_d with the incident neutron energy, in the specified energy range.

	Krick and Evans (1972) [51] from 0 to 1 MeV	**Tuttle (1979) [56]** thermal to fast	**Piksaikin (2000) [35]** thermal to fast
^{233}U	2.2% (0.6%)	9.6% (6.5%)	2.5% (0.9%)
^{235}U	0.6% (1.0%)	3.2% (3.7%)	1.5% (1.0%)
^{239}Pu	2.0% (0.5%)	0.2% (6.5%)	4.9% (1.4%)

The average delayed-neutron yield as a function of the incident neutron energy can be found in the evaluated libraries (MF=1, MT=455). The origin of the recommended data is not always well defined. According to the references reported in the header of the file, the yields contained in the version 2.2 of the European Library JEFF (1989), come from a semi-empirical calculation performed by Eric Fort using Lendel's theoretical model [21]. According to them, the difference between thermal and fast spectrum ν_d is in the order of 0.3%, much smaller than the values reported in Tab. 3.11. In the following version, JEFF-3.0, the yields have the reference *England89* [23], the same as the American library ENDF/B-VI. Overlapping the two sets of data confirmed the coherence of the references. From JEFF-3.1 to JEFF-3.1.2, the reference stayed unchanged, even though a comparison of the curves shows a different energy dependence (see Fig. 3.11a).

The last two versions, JEFF-3.2 and JEFF-3.3 recursively refer to the previous versions, thus not revealing the origin of the yields reported from JEFF-3.1 on. Following researches led to the conclusion that the mysterious set of data comes from TENDL2009 and that the reference in the header of the file is wrong and misleading!
As far as the American library is concerned, the last version (ENDF/B-VIII.0) takes

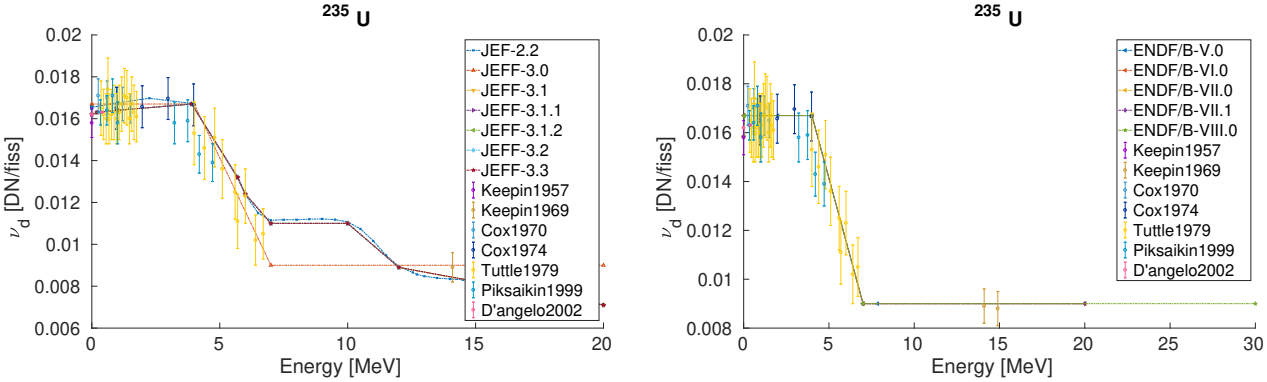

(a) JEFF library.

(b) ENDF/B library.

Figure 3.11: Library comparison of the average delayed-neutron yield as a function of energy for ^{235}U. Fig. 3.11a contains all the versions of JEFF library from the 2.2 to the 3.3. Fig. 3.11b contains all the versions of ENDF/B library from the V.0 to the VIII.0. Both figures show experimental data for comparison.

the ν_d from the previous ENDF/B-VII.1, which in turn took it from ENDF/B-VI (see Fig. 3.11b). Finally, ENDF/B-VI seems to have taken the yields from the already mentioned *England89* [23].

3.6.2 Summation calculation

Another way to asses the energy dependence of delayed-neutron yields is to compute them by summation method using fission yields and radioactive decay data libraries. This approach has already been used in the past. Mills (1999), Wilson and England (2002) and the author herself in this work (2019) performed this calculation and obtained the differences shown in Tab. 3.12.

Table 3.12: Calculated energy dependence of the delayed-neutron yield. The values in the table represent the relative variation of the ν_d with the incident neutron energy, from thermal to fast.

	Mills (1999) [21] *FY*: JEF-2.2 *RDD*: JEF-2.2	**Wilson and al. (2002) [21]** *FY*: not specified *RDD*: not specified	**Foligno (2019)** *FY*: JEFF-3.1.1 *RDD*: ENDF/B-VIII.0
^{235}U	+6.3%	-12.0%	+11.8%
^{239}Pu	+12.0%	+12.0%	+10.1%

Looking at the Tables 3.11 and 3.12, it seems that the energy dependence of calculated ν_d strongly differs from the experimental one. On the other hand, from Figure 3.12, which compares evaluated, experimental and calculated values, one realizes that the computed points lie within the statistical uncertainty of the experiments. Unfortunately, *FY* are only given at three energies (thermal, fast and high) in all the evaluated libraries, which is insufficient to infer anything on the energy trend. This works proposes to use GEF-FY energy dependence to extrapolate JEFF-FY at other energies.
GEF [45] is a Monte Carlo code able to provide *FY* at almost any neutron energy.

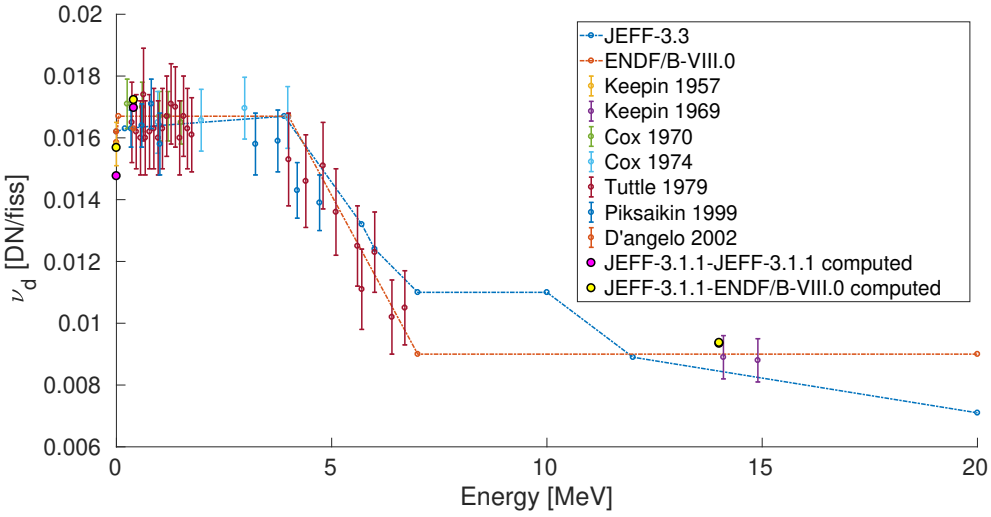

Figure 3.12: Summation calculation performed with JEFF-3.1.1 fission yields and with JEFF-3.1.1 and ENDF/B-VII.1 radioactive decay data for ^{235}U. Experimental data and evaluated libraries are shown for comparison.

When used in a calculation, the resulting ν_d are pretty far from the recommended values. This work aims at testing the energy dependence of GEF fission yields, which will be used to normalize the data of the JEFF library. The first step consists in choosing a reference energy (E_{ref}) per fissioning system, at which JEFF fission yields will be taken ($FY_{JEFF}(E_{ref})$). In this work the reference energy is 0.025 meV for ^{235}U and ^{239}Pu and 400 keV for ^{238}U. For each point in energy, the ratio of GEF fission yields at E and at E_{ref} is computed. The last step consists in applying the GEF energy dependence - the ratio $\frac{FY_{GEF}(E)}{FY_{GEF}(E_{ref})}$ - to the reference $FY_{JEFF}(E_{ref})$ (see Eq. 3.10).

$$FY_{JEFF}(E) = \frac{FY_{GEF}(E)}{FY_{GEF}(E_{ref})} FY_{JEFF}(E_{ref}) \tag{3.10}$$

The new sets of JEFF fission yields at different energies are then coupled with ENDF/B-VIII.0 radioactive decay data to perform a summation calculaton through which the quantities of interest can be estimated. The results of the calculation and the comparison with experimental data are shown in Fig. 3.13, where 3.13a, 3.13b and 3.13c, refer to ^{235}U, ^{238}U and ^{239}Pu, respectively. In the three plots the blue line corresponds to the summation calculation performed by using GEF-6.1 FY, while the orange one corresponds to JEFF-3.1.1 FY, corrected with GEF-6.1 energy dependence. As far as the ^{238}U is concerned, the shape of the orange curve, with a well-defined step-wise behavior, is promising. Furthermore the agreement with the experimental data, especially below 10 MeV, is reassuring. Applying GEF energy dependence to JEFF fission yields for ^{235}U and ^{239}Pu, an unexpected bump appears around 16-17 MeV, not far from the 3rd-chance fission energy. One hypothesis could be that the bump appears from a bad treatment of this physical phenomenon. Moreover, the expected flat behavior below 4 MeV as well as the experimental slope for ^{235}U are not reproduced by the calculation. Unfortunately, in the intermediate range (7 to 13 MeV) a lack of measurements prevents the author to draw any conclusion. The results highlighted that GEF energy dependence is not always suitable to reproduce experimental values and that more measurements are needed to further investigate the energy dependence of the delayed-neutron yields.

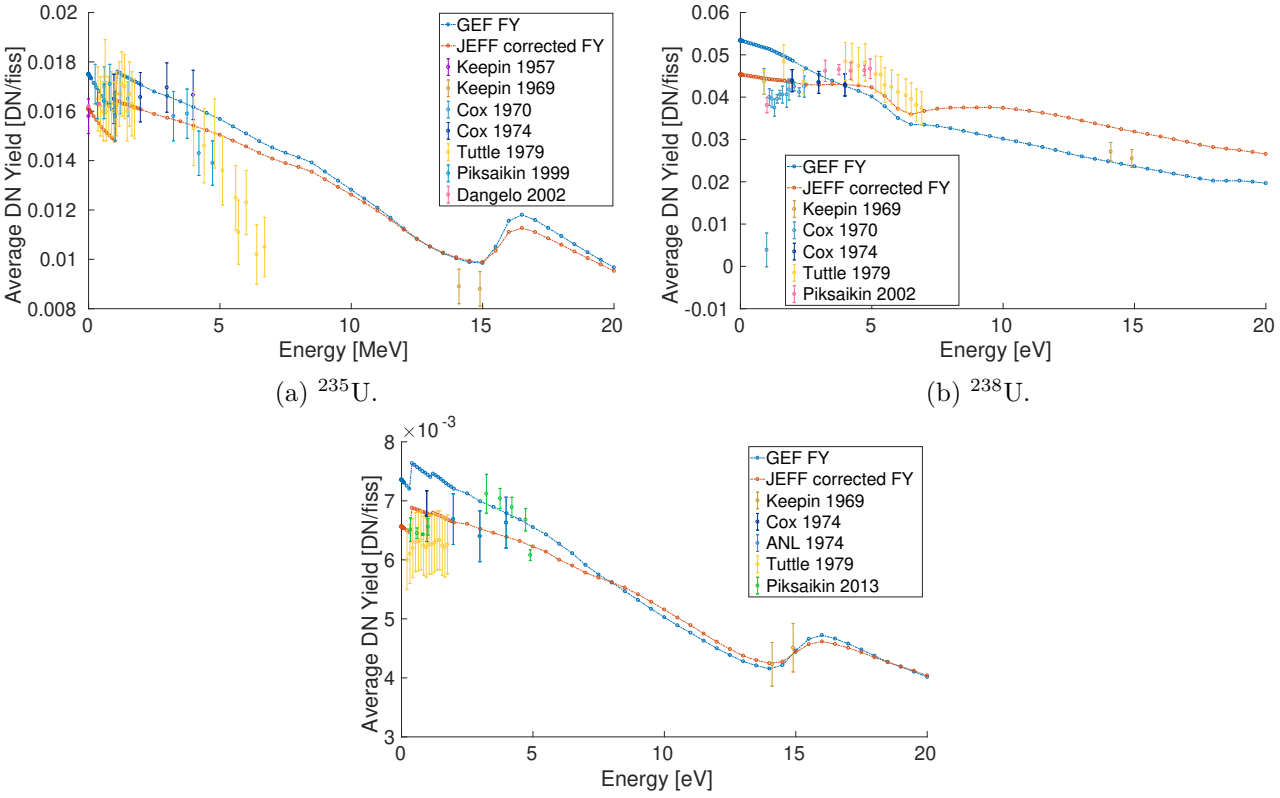

(a) ^{235}U.

(b) ^{238}U.

(c) ^{239}Pu.

Figure 3.13: Energy dependence of average delayed-neutron yield computed with GEF-6.1 *FY* and with JEFF-3.1.1 *FY* modified with GEF-6.1 energy dependence. Experimental values are reported for comparison.

Chapter 4

Kinetic Parameters

> We cannot change the cards we are dealt, just how we play the hand.
>
> Randy Pausch

Contents

4.1 Development and validation of the *Bateman solver* 63
4.1.1 Development 63
4.1.2 Validation with DARWIN 66
4.2 Estimation of the abundances by direct summation 68
4.2.1 Simple equivalence 69
4.2.2 Exponential equivalence 70
4.3 Estimation of the abundances by fit of the decay curve . . . 72
4.3.1 Analytical marginalization 72
4.3.2 Monte Carlo marginalization 74
4.4 Methods comparison 77
4.5 Other fissioning systems 81
4.6 Energy dependence 84
4.7 Delayed-neutron spectra 90

It is well known from the literature that the ν_d is not enough to define the kinetic behavior of a reactor. Therefore, the second chapter consists in computing the kinetic parameters able to describe the time-dependent behavior of the system. It is worth recalling that the summation method is generally employed for the estimation of the average delayed-neutron yield, and that only Brady and England used it for the kinetic parameters prediction in 1989. Section 4.1 focuses on the development and on the validation of a tool to solve the Bateman equations for the simulation of the DN activity. Section 4.2 deals with the calculation of the kinetic parameters through direct summation, thus by sorting the precursors into the 8 groups and estimating the abundances from the microscopic data. Two methods are tested and compared. Section 4.3 exploits another technique, which consists in simulating the DN activity by summation method and in fitting it with a sum of 8 exponentials. Three fitting models have been tested and compared. The comparison among the 5 sets of parameters derived so far is done in Section 4.4.

Once the most appropriate technique is chosen, the same procedure is applied to other fissioning systems in Section 4.5. Finally, Sections 4.6 and 4.7 briefly treat the energy dependence of the kinetic parameters and the eight-group delayed-neutron spectra.

4.1 Development and validation of the *Bateman solver*

4.1.1 Development

The Bateman Solver, developed by the author, is a home-made solver coded in C++ to follow the evolution of the precursors' concentration in a physical system during or after an irradiation phase. Existing codes like DARWIN [59] or CINDER [36] can perform this task. However, as input, they need a single database for all data. This means that it would have been impossible to mix data coming from different libraries, as done for the ν_d calculation. This is the reason why a new solver has been developed. The advantage of the solver is the flexibility in terms of nuclear data libraries. The user can decide to take the fission yields from a database and the radioactive decay data from another one. The program, starting from the IY of a library A and the branching ratios of a library B, builds the decay chains and computes the CY of the mix AB, which might be different from the CY of library A.

The ***delayed-neutron activity (n)*** is the number of delayed neutrons emitted per unit time. It can be measured or computed through the *summation method*, which consists in computing and summing up the contribution of each precursor to the delayed-neutron activity Eq. 4.1

$$n(t) = \sum_{i}^{N} x_i \, \lambda \, N_i(t) \, P_{xn,i}. \tag{4.1}$$

Equation 4.1 is nothing but the sum over all the precursors of the isotope's activity multiplied by the probability of emitting a delayed neutron after the decay. In order to use the formula, the real concentration of each precursor is needed at any time (cumulative yields are only valid in the case of an infinite irradiation). At equilibrium, the precursors' abundance corresponds to their cumulative yield. However, if a virgin sample is irradiated, the situation is very different. Since in the summation calculation all the precursors are considered, one could think about solving the balance equation to have the exact amount of each isotope according to the irradiation conditions (neutron flux, time of irradiation and fissioning system). In order to do that, it is necessary to treat irradiation-phase and decay-phase separately. In the following, a virgin sample (no fission products are present in the system at t = 0) is irradiated by a constant neutron flux Φ_c for a duration Δt_{irr}. Then, the flux stops to let the system decay. The two phases are shown in Fig. 4.1. Precursors are both directly created from fission and indirectly created from their fathers' decay, so in order to obtain the exact result, one should take into account the whole decay-chain. In this work, it is assumed that each precursor N_i can derive from the β^-, β_n^-, β_{2n}^-, β_{3n}^-, β_{4n}^-, IT decay of its fathers, as well as from direct fission. Figure 4.2 shows a general decay scheme.

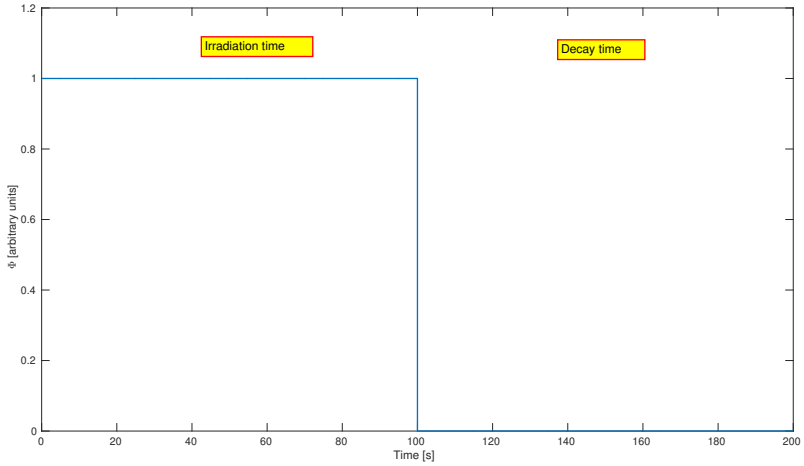

Figure 4.1: Neutron flux as a function of time used to simulate the irradiation and the decay phase of a sample. The duration of the phases as well as the intensity of the flux are arbitrary and have been chosen for illustrative purposes.

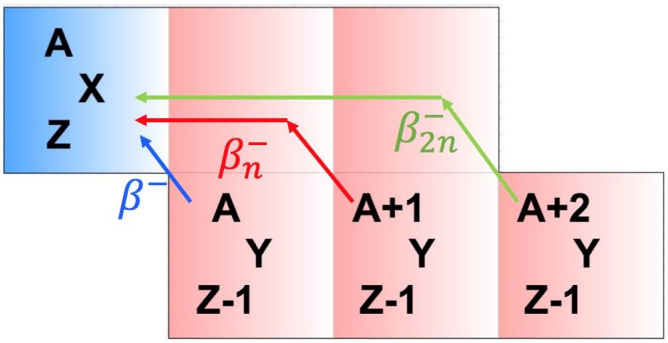

Figure 4.2: General decay scheme.

To be one of the precursor's fathers, the isotope has to fulfill three requirements:

1. $Z_f = Z_p - 1$: the father has to have one proton less than its daughter
2. $RFS_f = I_p$: the RFS (the excitation state of the daughter after the decay) of the father should be equal to the excitation state of the precursor
3. $A_f = A_p + x$: the mass number of the father should be consistent with the β^-_{xn}-decay

To give an illustration, Fig. 4.3 shows the complete family tree for ^{87}Br.

The system of differential equations (Eq. 4.2) describes the amount of a delayed-neutron

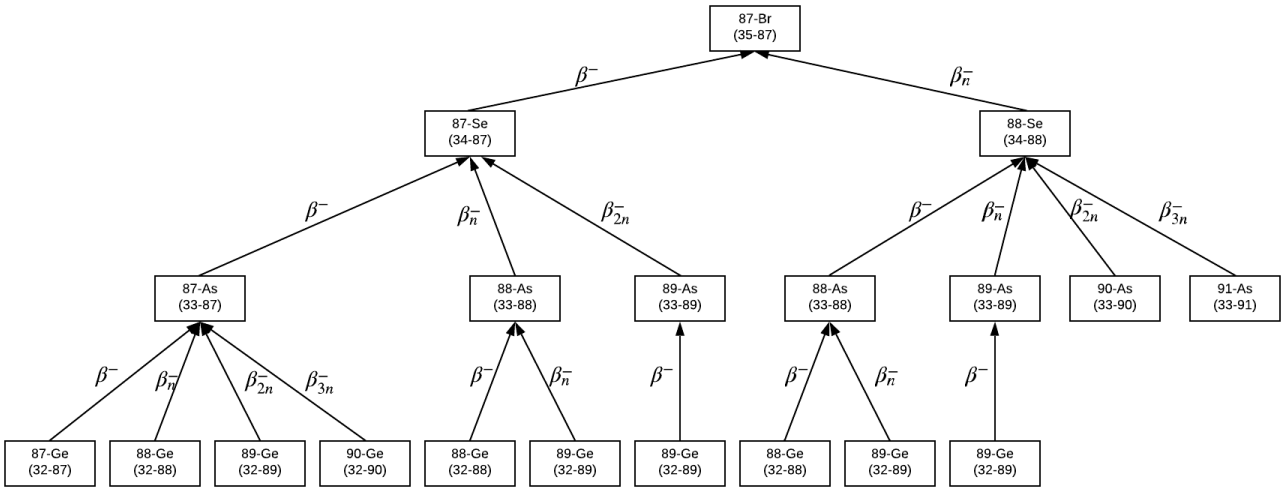

Figure 4.3: Complete decay scheme for ^{87}Br. It shows all the ways ^{87}Br can be created apart from direct fission.

precursor created and destroyed by a linear first-order phenomenon [30],

$$\begin{cases} \frac{\mathrm{d}N_1(t)}{\mathrm{d}t} &= -\lambda_1 \cdot N_1(t) + S_1 \\ \frac{\mathrm{d}N_2(t)}{\mathrm{d}t} &= -\lambda_2 \cdot N_2(t) + S_2 + \lambda_1 \cdot BR_{1\to 2} \cdot N_1(t) \\ &\vdots \\ \frac{\mathrm{d}N_i(t)}{\mathrm{d}t} &= -\lambda_i \cdot N_i(t) + S_i + \lambda_{i-1} \cdot BR_{(i-1)\to i} \cdot N_{i-1}(t) \\ &\vdots \\ \frac{\mathrm{d}N_n(t)}{\mathrm{d}t} &= -\lambda_n \cdot N_n(t) + S_n + \lambda_{n-1} \cdot BR_{(n-1)\to n} \cdot N_{n-1}(t) \end{cases} \tag{4.2}$$

where $N_i(t)$ is the i^{th}-precursor's concentration in at or $at \cdot cm^{-3}$, λ_i is the i^{th}-precursor's decay constant in s^{-1}, $BR_{(i-1)\to i}$ is the branching ratio of the $(i-1)^{th}$ isotope for the decay leading to i and S_i is the constant external source, which is given by

$$S_i = IY_i \cdot \Sigma_f \cdot \phi \tag{4.3}$$

in s^{-1}, with IY_i being the independent yield of the precursor i in $at \cdot fiss^{-1}$, Σ_f the macroscopic fission cross section in cm^{-1} and ϕ the neutron flux in $n \cdot cm^{-2} \cdot s^{-2}$.
The general solution is given by [30]

$$N_n(t) = \sum_{i=1}^{i=n} \left[\left(\prod_{j=i}^{j=n-1} \lambda_j \cdot P_{j\to(j+1)} \right) \cdot \sum_{j=i}^{j=n} \left(\frac{N_i^0 \cdot e^{-\lambda_j \cdot t}}{\prod_{\substack{p=i \\ p\neq j}}^{p=n} (\lambda_p - \lambda_j)} + \frac{P_i \cdot (1 - e^{-\lambda_j \cdot t})}{\lambda_j \cdot \prod_{\substack{p=i \\ p\neq j}}^{p=n} (\lambda_p - \lambda_j)} \right) \right] \tag{4.4}$$

where $N_i^0 = N_i(t=0)$ is the amount of i^{th} isotope at some arbitrary reference time zero. The assumptions behind the mentioned procedure are the following:

1. The neutron flux is constant during the irradiation phase ($\Phi(t) = \Phi_c$)
2. The energy and the space-dependence of the variables are neglected ($IY(E) = IY$, $\Sigma_f(E, \overrightarrow{r}) = \Sigma_f$)

The boundary condition is that during the irradiation phase N_i^0 is zero, while during the decay phase N_i^0 represents the isotope-i's concentration at the end of the irradiation phase. Note also that to compute the n^{th} species from different chains, the last term should not be added more than once since it represents the contribution of the n^{th} species to itself. The solver can also perform fits calling CONRAD® and plot figures writing MATLAB® files. However, the Bateman-solver does not take into account the creation and destruction of the precursors by transmutation, neutron capture or α-decay. Therefore, the close decay-chain never occurs.

4.1.2 Validation with DARWIN

The Bateman Solver has been validated by comparison with the reference CEA code for depletion calculations: the DARWIN code [59]. The comparison has been performed in the following conditions:

- **Nuclear data** Since both solvers use a microscopic approach, it was essential for the two codes to choose the same nuclear-data libraries. For this purpose, JEFF-3.1.1 has been chosen for radioactive decay data and JEFF-3.1 for fission yields
- **Fissioning system** The fissioning system used for the validation is 1 g (2.563E+21 at) of ^{235}U under a constant thermal ($E_n < 0.1$ eV) flux of 1 $n \cdot cm^{-2} \cdot s^{-1}$. The fission rate, given a fission cross-section of 536.525 b, resulted to be 1.375 fiss/s
- **Irradiation- and decay-phase** Three irradiation lengths were tested: 0.001 s, 10 s, and 600 s. From the end of the irradiation, the system decayed for 600 s. The fission products' concentration (in atoms) has been provided and compared for 21 points on the decay-curve: 0, 0.001, 0.01, 0.1, 0.5, 1, 2, 3, 5, 8, 10, 20, 30, 50, 70, 100, 150, 200, 300, 400, 500, 600 seconds after the end of the irradiation.

Figures 4.4, 4.5 and 4.6 show the time evolution of the most relevant precursors' concentration as computed by DARWIN and by the Bateman-solver for an irradiation of 600 s, 10 s, and 0.001 s, respectively.
The comparison aims at assessing the ability of the Bateman-solver to describe the time-dependent behavior of the system. The three main contributors to the average delayed-neutron yield are considered: ^{137}I, ^{88}Br and ^{87}Br. At the same time, Tab. 4.1 reports the discrepancies in the concentrations at the end of the irradiation. The results are given in percentage. The agreement between the two codes is remarkable.
The code has been written to study the delayed-neutron-precursors' behavior. The major contributors to the delayed-neutron emission are well characterized by the Bateman solver. Discrepancies larger than 1% are present for irrelevant precursors (the first occurrence is the 79th precursor in the sorted-by-importance ranking). The time-dependent behavior of the precursors is also well described by the Bateman solver [37]. In conclusion, the code has been validated for delayed-neutron studies. The author does not guarantee the quality of the current version of the code for other purposes, due to a reduced number of considered reactions. The main assumption of the Bateman solver

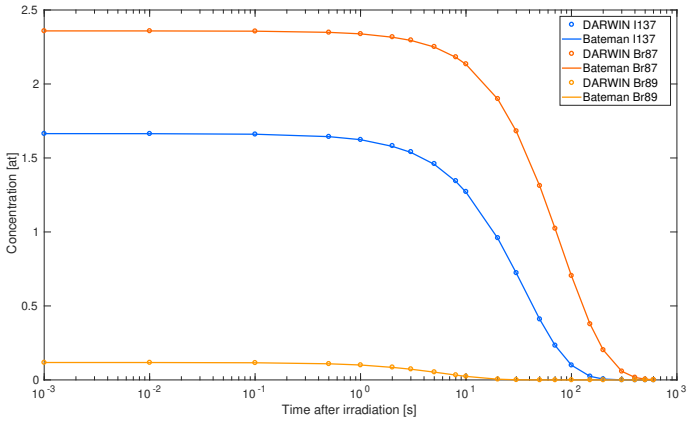

Figure 4.4: Time evolution of the most relevant precursors' concentration after an irradiation of 600 s.

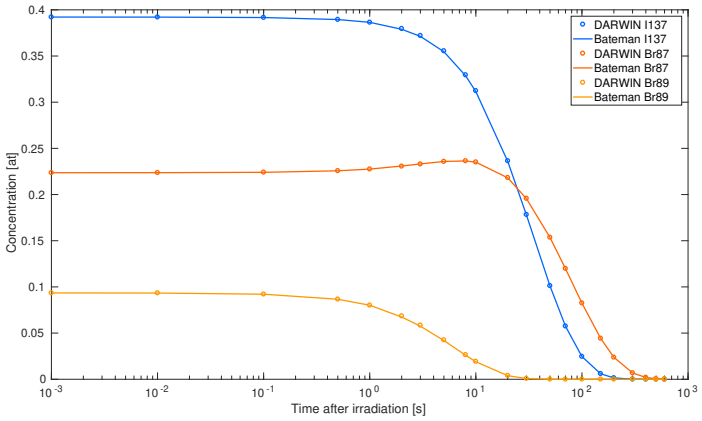

Figure 4.5: Time evolution of the most relevant precursors' concentration after an irradiation of 10 s.

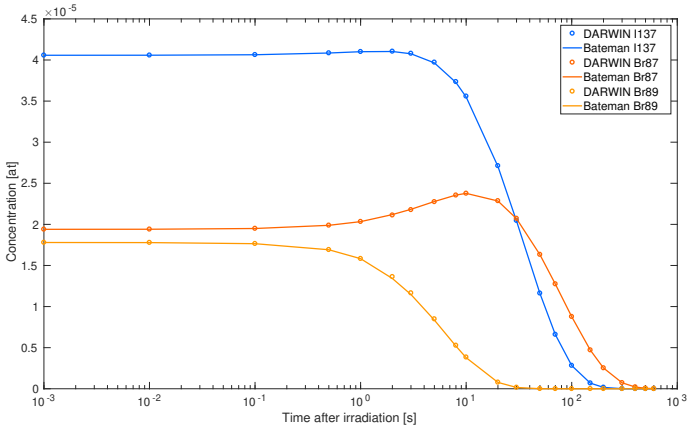

Figure 4.6: Time evolution of the most relevant precursors' concentration after an irradiation of 0.001 s.

Table 4.1: Discrepancies in the concentration at the end of the irradiation. [1], [2] and [3] refer to an irradiation length of 0.001 s, 10 s and 600 s, respectively. The precursors are shown in order of importance with respect to the delayed-neutron emission.

Z	A	I	Symbol	$(C - C_{ref})/C_{ref}$ [1]	$(C - C_{ref})/C_{ref}$ [2]	$(C - C_{ref})/C_{ref}$ [3]
53	137	0	I	0.002 %	0.008 %	-0.004 %
35	89	0	Br	-0.005 %	-0.009 %	-0.015 %
37	94	0	Rb	-0.003 %	-0.021 %	-0.023 %
35	88	0	Br	0.007 %	0.007 %	-0.003 %
35	90	0	Br	-0.031 %	-0.032 %	-0.036 %
53	138	0	I	-0.009 %	-0.005 %	-0.012 %
39	98	1	Y	-0.033 %	-0.032 %	-0.033 %
53	139	0	I	-0.028 %	-0.025 %	-0.029 %
37	95	0	Rb	-0.172 %	-0.178 %	-0.178 %
35	87	0	Br	0.007 %	0.013 %	-0.001 %
37	93	0	Rb	-0.001 %	-0.004 %	-0.009 %
39	99	0	Y	-0.031 %	-0.043 %	-0.043 %
33	85	0	As	-0.032 %	-0.031 %	-0.033 %
35	91	0	Br	-0.128 %	-0.125 %	-0.124 %
51	135	0	Sb	-0.040 %	-0.038 %	-0.039 %
55	143	0	Cs	-0.029 %	-0.035 %	-0.036 %
33	86	0	As	-0.071 %	-0.071 %	-0.072 %
37	96	0	Rb	-0.169 %	-0.230 %	-0.230 %
55	145	0	Cs	-0.118 %	-0.115 %	-0.114 %
53	140	0	I	-0.076 %	-0.077 %	-0.080 %
55	144	0	Cs	-0.028 %	-0.044 %	-0.044 %

is that an isotope can either be created by direct fission or by another isotope's decay, while it can only disappear by radioactive decay (no transmutation or absorption). As far as the decay types are concerned, only the following have so far been considered: IT, β^-,β_n^-, β_{2n}^-, β_{3n}^- and β_{4n}^-. Since other reactions and decay-types exist, it is recommended to use the solver only to estimate delayed-neutron precursors rather than for all the fission products.

4.2 Estimation of the abundances by direct summation

The delayed-neutron groups are an approximation of real physics. In principle, there should be as many groups as the precursors. The reason that led to the introduction of the group model is that delayed-neutron data have been estimated, for the first time, by an integral experiment. Due to the impossibility of fitting almost a thousand of parameters, an approximation had to be made. The assumption behind the 8-group model is that the global delayed-neutron emission - the sum of hundreds of exponentials - can be described as a sum of just eight exponentials. Equation 4.5 shows this approach

$$n_d(t) = F \sum_{j=1}^{N} CY_j \; x_j \; P_{n,j} \; e^{-\lambda_j \, t} \simeq F \; \nu_d \sum_{i=1}^{8} a_i \; e^{-\lambda_i \, t} \tag{4.5}$$

where j is one of the N delayed-neutron precursors and i is one of the 8 delayed-neutron groups. F is the fission rate, while the term $CY_j\ x_j\ P_{n,j}$ is nothing but the partial delayed-neutron yield of the precursor j, $(\nu_{d,j})$, in the case of N groups. Therefore,

$$\nu_d \sum_{i=1}^{8} a_i\ e^{-\lambda_i\ t} = \sum_{j=1}^{N} \nu_{d,j}\ e^{-\lambda_j\ t} \tag{4.6}$$

where

$$\alpha_j = \frac{CY_j\ x_j\ P_{n,j}}{\nu_d} = \frac{\nu_{d,j}}{\nu_d} \tag{4.7}$$

The direct summation method, developed by the author, consists in sorting the hundreds of delayed-neutron precursors in eight groups and in summing up their individual contributions to reconstruct the abundance of the group. Since the precursor rarely has a half-life corresponding to one of the fixed group half-lives, one has to define the α_j needed to preserve the equivalence of the exponentials (Eq. 4.6). The difference between the *simple equivalence* and the *exponential equivalence* is only related to the way of sorting the precursors in the eight groups. As far as the uncertainties are concerned, the classical propagation of uncertainties has been applied. For the analytical development please go to the Appendix B, Sections B.2 and B.3.

4.2.1 Simple equivalence

A scheme of the simple equivalence can be found in Fig. 4.7. The half-life axis is divided into eight boxes, corresponding to the eight groups. In each of them, the mean half-life of the group, taken from the WPEC-6 recommendations, is reported. The most delicate

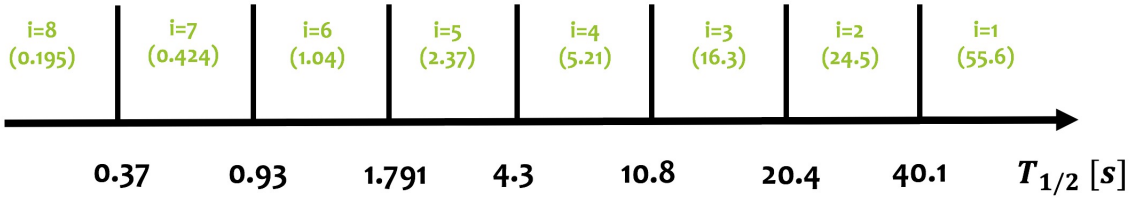

Figure 4.7: *Simple equivalence* scheme.

part of this method is to find the half-lives delimiting the groups. In this work, the values at the borders have been found in an iterative way. Initially, the limiting values have been set to the average of the two surrounding groups. Then, they have been iteratively adjusted to fit the recommended abundances of the $^{235}U_t$. Once the limiters were set, the abundances could be easily found as

$$a_i = \sum_{j \in i}^{N} \frac{CY_j\ x_j\ P_{n,j}}{\nu_d} = \sum_{j \in i}^{N} \alpha_j, \tag{4.8}$$

where a_i is the sum of all the α_j of the precursors j belonging to the group i. This method can be applied to any fissioning system to obtain a first estimation of the kinetic parameters. Table 4.2 report the results associated with the thermal fission of ^{235}U.
In the same fashion, it is possible to compute the importance of the delayed-neutron group as a function of time (Eq. 4.9, where $C_j(t)$ is the concentration of the precursor j). Figure 4.8 shows how the importance of the eight groups change with time. It

Table 4.2: Results of the *simple equivalence* method for the thermal fission of ^{235}U using JEFF-3.1.1 fission yields and ENDF/B-VIII.0 radioactive decay data. σ_{a_i} are given in percentage of a_i.

Group	1	2	3	4	5	6	7	8
a_i [%]	3.45	15.95	9.07	19.95	31.75	9.65	8.15	2.03
σ_{a_i} [%]	2.68	6.54	7.32	9.60	8.62	11.37	13.52	13.25

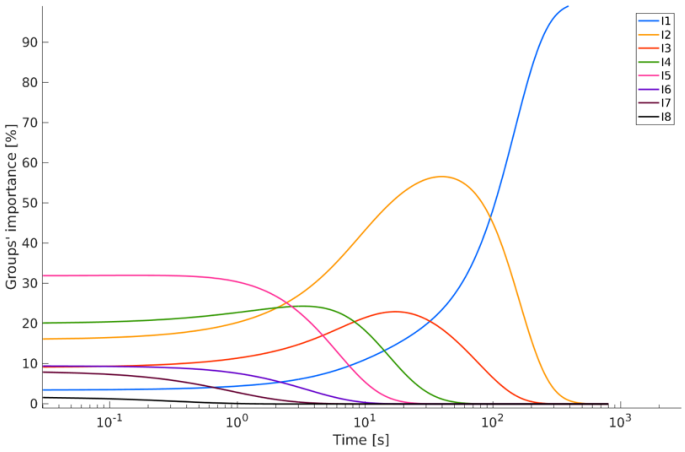

Figure 4.8: Importance of the eight delayed-neutron groups during the decay phase following a long irradiation. Long means that all the precursors reached their equilibrium concentration.

is evident that need to reduce the uncertainties related to the long-lived precursors' abundances (a_1 and a_2), especially if we are interested in what happens 100 s and more after the end of the irradiation.

$$I_i(t) = \sum_{j \in i}^{N} \frac{\lambda_j \, C_j(t) \, P_{n,j} \, x_j}{n_d(t)}, \tag{4.9}$$

4.2.2 Exponential equivalence

A scheme of the exponential equivalence can be found in Fig. 4.9. Rather than choosing

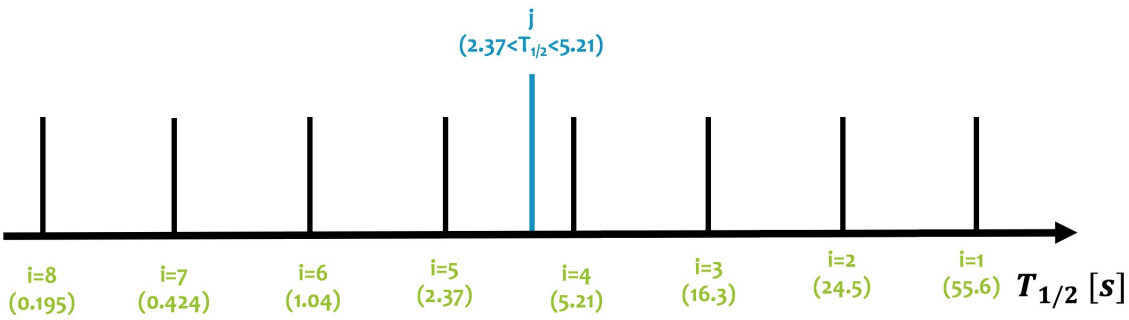

Figure 4.9: *Exponential equivalence* scheme.

defined half-life limits, each precursor is considered being spread over the two closest

groups, contributing to each of them by a certain percentage, which depends on the *distance* - in terms of half-life - from the two groups.
Table 4.3 reports the half-lives recommended by the WPEC-SG6. In this work, the first-group half-life has been replaced with the one of ^{87}Br according to ENDF/B-VIII.0 (55.65 s $\pm$ 0.2%), in order for the calculations to be consistent with the summation method which uses this version of the American *RDD* database.

Table 4.3: Half-lives associated with the 8 delayed-neutron groups according to the WPEC-6.

Group	1	2	3	4	5	6	7	8
$T_{1/2}[s]$	55.6	24.5	16.3	5.21	2.37	1.04	0.424	0.195

Let's assume that the isotope j has a half-life of 6.23 s, like ^{138}I, the 7$^{\text{th}}$ most important precursor. In that case, it will fall partly in the 4$^{\text{th}}$ group (5.21 s) and partly in the 3$^{\text{th}}$ group (16.3 s). To generalize, the 3$^{\text{rd}}$ group will have the index k and the 4$^{\text{th}}$ the index w. The relationship to be preserved is reported in Eq. 4.10

$$f_{k,j}\, e^{-\lambda_k\, t} + f_{w,j}\, e^{-\lambda_w\, t} = \alpha_j\, e^{-\lambda_j\, t}. \tag{4.10}$$

Since there are two variables, two boundary conditions are needed. The first one will be the equivalence at $t = 0$

$$B.C.\ 1: \qquad f_{k,j} + f_{w,j} = \alpha_j. \tag{4.11}$$

The second will be the conservation of the total number of delayed neutrons emitted during the decay-phase by the precursor under investigation

$$B.C.\ 2: \qquad \int_0^\infty f_{k,j}\, e^{-\lambda_k\, t}\, \mathrm{d}t + \int_0^\infty f_{w,j}\, e^{-\lambda_w\, t}\mathrm{d}t = \int_0^\infty \alpha_j\, e^{-\lambda_j\, t}\mathrm{d}t. \tag{4.12}$$

The two boundary conditions give the system of equations 4.13

$$\begin{cases} f_{k,j} + f_{w,j} = \alpha_j \\ \frac{f_{k,j}}{\lambda_k} + \frac{f_{w,j}}{\lambda_w} = \frac{\alpha_j}{\lambda_j} \end{cases} \tag{4.13}$$

which can be easily solved, giving the two fractions of the precursor j contributing to group k and group w

$$\begin{cases} f_{w,j} = \frac{\alpha_j\, \lambda_w}{\lambda_k - \lambda_w}\, (\frac{\lambda_k}{\lambda_j} - 1) \\ f_{k,j} = \alpha_j\, [1 - \frac{\lambda_w}{\lambda_k - \lambda_w} (\frac{\lambda_w}{\lambda_j} - 1)]. \end{cases} \tag{4.14}$$

Isotope j will finally contribute to group k by $x_{j,k} = f_{k,j}/\alpha_j$ and group w by $x_{j,w} = f_{w,j}/\alpha_j$. So, for example, ^{138}I, with a half-life of 6.23 s, will contribute to group 3 by 9.2% and group 4 by 90.8%. For the precursors belonging either to the first or to the last group, only one boundary condition is needed. The conservation of the total number of emitted neutrons seemed to be more consistent than the equivalence at the beginning of the decay phase. As a consequence,

$$B.C.: \qquad \int_0^\infty f_{k,j}\, e^{-\lambda_k\, t}\, \mathrm{d}t = \int_0^\infty \alpha_j\, e^{-\lambda_j\, t}\mathrm{d}t, \tag{4.15}$$

and therefore

$$\frac{f_{k,j}}{\lambda_k} = \frac{\alpha_j}{\lambda_j} \qquad \Rightarrow \qquad f_{k,j} = \alpha_j\, \frac{\lambda_k}{\lambda_j}. \tag{4.16}$$

Note that the kinetic relation a_i/λ_i is preserved, and so the reactivity. Table 4.4 reports the results associated with the thermal fission of ^{235}U.

Table 4.4: Results of the *exponential equivalence* method for the thermal fission of ^{235}U using JEFF-3.1.1 fission yields and ENDF/B-VIII.0 radioactive decay data. The group decay constants have been taken from WPEC-6 [40] except for λ_1, replaced by the λ of ^{87}Br according to ENDF/B-VIII.0. σ_{a_i} are given in percentage of a_i.

Group	1	2	3	4	5	6	7	8
a_i [%]	3.50	16.09	9.48	17.24	31.59	13.50	6.09	2.35
σ_{a_i} [%]	2.66	9.78	22.79	23.17	17.43	26.26	27.10	46.39

4.3 Estimation of the abundances by fit of the decay curve

The kinetic parameters can be obtained by fitting the measured decay curve with Eq. 4.17

$$n_d(t) = n_d(t_{irr}) \sum_{i=1}^{8} a_i (1 - e^{-\lambda_i t_{irr}}) e^{-\lambda_i (t - t_{irr})} \tag{4.17}$$

where $n_d(t_{irr})$ is nothing but the activity after an irradiation t_{irr}, which in case of an infinite irradiation corresponds to the product of the fission rate F in fiss/s and the average DN yield in DN/fiss. For this example, the fission rate has been set to 1 so that the normalization factor is directly the ν_d. Note that if this curve had to be experimentally measured, one should also include the detector efficiency in the normalization factor before proceeding to the fitting. For this calculation, an irradiation duration of 600 s has been used, in order to saturate the eight groups of precursors and not to apply any corrective factor. For simplicity, the curve is normalized before the fitting ($\frac{n_d(t)}{n_d(t_\infty)}$ is fitted rather than $n_d(t)$).

4.3.1 Analytical marginalization

One way to take into account the uncertainty in the library is to analytically marginalize the parameters that can affect the variable of interest ($\overrightarrow{\theta} = IY_{i=1:N},\ BR_{i=1:N},\ \lambda_{i=1:N}$) according to their uncertainty. The procedure consists of implementing the analytical model in CONRAD® and fitting the decay curve. Note that the analytical term $\frac{n_d(t)}{n_d(t_\infty)}$ represents more than 3000 lines of equation and that CONRAD® imposes Eq. 4.17 to be true for each time t and computes the uncertainty through analytical marginalization. There are several ways to guarantee that the sum of the abundances is equal to one during the fit. Two methods have been tested and compared:

1. *Two experiences*
2. *Self-normalization*

In the *two experiences*, CONRAD® is given the two equations and it is told that there is experimental evidence that the two are true. In that way, CONRAD® makes sure that the second equation is as true as the first one.

$$\begin{cases} \dfrac{n_d(t)}{n_d(t_\infty)} - \displaystyle\sum_{i=1}^{8} a_i (1 - e^{-\lambda_i t_{irr}}) e^{-\lambda_i (t - t_{irr})} \\ \displaystyle\sum_{i=1}^{8} a_i = 1 \end{cases} \tag{4.18}$$

Table 4.5 reports the abundances obtained through the *analytical marginalization* method with *two-experiences normalization* for the thermal fission of ^{235}U, while Fig. 4.10 shows the associated correlation matrix.

Table 4.5: Results of the *analytical marginalization* method with *two-experiences normalization* for the thermal fission of ^{235}U using JEFF-3.1.1 fission yields and ENDF/B-VIII.0 radioactive decay data. The group decay constants have been taken from WPEC-6 [40] except for λ_1, replaced by the λ of ^{87}Br according to ENDF/B-VIII.0. σ_{a_i} are given in percentage of a_i.

Group	1	2	3	4	5	6	7	8
a_i [%]	3.59	16.33	9.50	17.93	34.37	12.53	3.53	2.22
σ_{a_i} [%]	26.6	33.2	88.6	47.8	57	164	757	979

$$\begin{bmatrix}
1 & -0.784 & 0.853 & -0.833 & 0.850 & -0.862 & 0.864 & -0.866 \\
-0.784 & 1 & -0.894 & 0.829 & -0.915 & 0.884 & -0.893 & 0.893 \\
0.853 & -0.894 & 1 & -0.946 & 0.965 & -0.977 & 0.980 & -0.982 \\
-0.833 & 0.829 & -0.946 & 1 & -0.959 & 0.934 & -0.945 & 0.946 \\
0.850 & -0.915 & 0.965 & -0.959 & 1 & -0.985 & 0.986 & -0.989 \\
-0.862 & 0.884 & -0.9767 & 0.934 & -0.985 & 1 & -0.998 & 0.998 \\
0.864 & -0.893 & 0.980 & -0.945 & 0.986 & -0.998 & 1 & -0.999 \\
-0.866 & 0.893 & -0.982 & 0.946 & -0.989 & 0.998 & -0.999 & 1
\end{bmatrix}$$

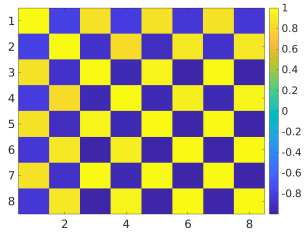

Figure 4.10: Correlation matrix associated with the abundances computed by *analytical marginalization* with the *two-experiences normalization* technique.

In the *self-normalization*, each abundance is described as a function of the others

$$a_i = 1 - \sum_{\substack{j=1 \\ j \neq i}}^{8} a_j \tag{4.19}$$

so that the sum of the a_i is forced to be 1 without any external constraint.

$$\frac{n_d(t)}{n_d(t_\infty)} - \sum_{i=1}^{8} \left(1 - \sum_{\substack{j=1 \\ j \neq i}}^{8} a_j\right)(1 - e^{-\lambda_i t_{irr}})e^{-\lambda_i (t - t_{irr})} = 0 \tag{4.20}$$

Table 4.6 reports the abundances obtained through the *analytical marginalization* method with *two-experiences normalization* for the thermal fission of ^{235}U, while Fig. 4.11 shows the associated correlation matrix.

From the abundances, as well as from the associated correlation matrices, it is quite clear that the fact of adding an external constraint ($\sum a_i = 1$) leads to strong uncertainties and strong correlations among the abundances. The correlation matrix of the *two models* method is like a chess board filled with 1 and -1. Applying the correlation matrix in the uncertainty propagation partially compensates for the large variances associated with the groups' yields. Among the two normalization methods, the self-normalization seemed more appropriate to the scope of the study.

Table 4.6: Results of the *analytical marginalization* method with *self-normalization* for the thermal fission of ^{235}U using JEFF-3.1.1 fission yields and ENDF/B-VIII.0 radioactive decay data. The group decay constants have been taken from WPEC-6 [40] except for λ_1, replaced by the λ of ^{87}Br according to ENDF/B-VIII.0. σ_{a_i} are given in percentage of a_i.

Group	1	2	3	4	5	6	7	8
a_i [%]	3.58	16.31	9.48	17.93	34.28	12.66	3.21	2.54
σ_{a_i} [%]	14.58	14.91	17.17	15.38	9.11	11.86	41.21	12.70

$$\begin{bmatrix} 1 & -0.031 & 0.116 & -0.101 & -0.206 & 0.15 & 0.014 & 0.129 \\ -0.031 & 1 & -0.178 & -0.12 & -0.451 & -0.228 & -0.002 & -0.136 \\ 0.116 & -0.178 & 1 & -0.265 & -0.283 & 0.276 & -0.089 & 0.188 \\ -0.101 & -0.12 & -0.265 & 1 & -0.414 & -0.453 & 0.063 & -0.282 \\ -0.206 & -0.451 & -0.283 & -0.414 & 1 & 0.049 & -0.273 & -0.088 \\ 0.15 & -0.228 & 0.276 & -0.453 & 0.049 & 1 & -0.366 & 0.331 \\ 0.014 & -0.002 & -0.089 & 0.063 & -0.273 & -0.366 & 1 & 0.144 \\ 0.129 & -0.136 & 0.188 & -0.282 & -0.088 & 0.331 & 0.144 & 1 \end{bmatrix}$$

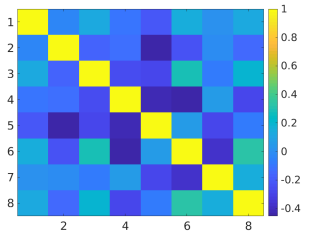

Figure 4.11: Correlation matrix associated with the abundances computed by *analytical marginalization* with the *self-normalization* technique.

4.3.2 Monte Carlo marginalization

In the Monte Carlo marginalization, all the variables with a reported uncertainty have been *perturbed* by a fraction of their error, this fraction being a normally distributed random number centered at zero and with a standard deviation of 1. Attention has been put to verify the validity of the individual perturbed parameters ($0 \leq BR \leq 1$, $IY > 0$ etc.) but more needs to be done to globally satisfy the physics (e.g. $\sum_i^N IY_i = 2$). Each variable has been modified by a different vector of random numbers, in order not to create unwanted correlations. As an example, IY_C is the vector containing the independent yields of the W precursors and σ_{IY_C} the vector containing their uncertainties.

$$IY_C = \begin{bmatrix} IY_{C_1} \\ IY_{C_2} \\ \vdots \\ IY_{C_W} \end{bmatrix} \qquad \sigma_{IY_C} = \begin{bmatrix} \sigma_{IY_{C_1}} \\ \sigma_{IY_{C_2}} \\ \vdots \\ \sigma_{IY_{C_W}} \end{bmatrix} \tag{4.21}$$

The first step consists in creating a $W \times K$ matrix of random numbers called v, W being the number of variables and K being the number of samples. The more the samples the better the statistics of the results.

$$v = \begin{bmatrix} v_{1,1} & v_{1,2} & \cdots & v_{1,K} \\ v_{2,1} & v_{2,2} & \cdots & v_{2,K} \\ \vdots & \vdots & \ddots & \vdots \\ v_{W,1} & v_{w,2} & \cdots & v_{W,K} \end{bmatrix} \tag{4.22}$$

Then, from the original vector IY_C, one could build a matrix of perturbed vectors IY'_c, where the single element would be

$$IY'_C(j,i) = IY_C(j) + \sigma_{IY_C}(j) \cdot v(j,i)$$

IY'_C is, therefore, a $W \times K$ matrix, where each column represents a perturbed sample of the original vector.

$$IY'_C = \begin{bmatrix} IY_{C_1} + \sigma_{IY_{C_1}} \cdot v_{1,1} & IY_{C_1} + \sigma_{IY_{C_1}} \cdot v_{1,2} & \cdots & IY_{C_1} + \sigma_{IY_{C_1}} \cdot v_{1,K} \\ IY_{C_2} + \sigma_{IY_{C_2}} \cdot v_{2,1} & IY_{C_2} + \sigma_{IY_{C_2}} \cdot v_{2,2} & \cdots & IY_{C_2} + \sigma_{IY_{C_2}} \cdot v_{2,K} \\ \vdots & \vdots & \ddots & \vdots \\ IY_{C_W} + \sigma_{IY_{C_W}} \cdot v_{n,1} & IY_{C_W} + \sigma_{IY_{C_W}} \cdot v_{W,2} & \cdots & IY_{C_W} + \sigma_{IY_{C_W}} \cdot v_{W,K} \end{bmatrix} \tag{4.23}$$

In the same fashion, all the other variables can be perturbed (Tab. 4.7), bearing in mind

Table 4.7: Original and perturbed parameters.

$[W \times 1]$	$[W \times K]$
IY_C	IY'_C
IY_{B_1}	IY'_{B_1}
IY_{B_2}	IY'_{B_2}
$P_{n,c}$	$P'_{n,c}$
$P_{B_1 \to C}$	$P'_{B_1 \to C}$
$P_{B_2 \to C}$	$P'_{B_2 \to C}$
λ_C	λ'_C
λ_{B_1}	λ'_{B_1}
λ_{B_2}	λ'_{B_2}

that each time a different matrix of random numbers has to be used (v, u, r, ...).
Finally, the delayed-neutron emission rate can be calculated with Eq. 4.4, replacing all the original variables by the perturbed ones.
From the computed delayed-neutron-emission rate it has been possible to derive a new set of abundances by a nonlinear least-square-fit of the decay curve, performed with CONRAD®. The eight-group decay constants have been fixed in the fitting procedure to the ones recommended by JEFF-3.1.1[1], except for λ_1 taken from the decay constant of ^{87}Br according to ENDF/B-VIII.0 (0.012455 rather than 0.012467). This choice is justified by the fact that the summation calculation has been performed taking the radioactive decay data from ENDF/B-VIII.0, and it is well-known that the asymptotic behavior of delayed neutrons only depends on the longest-lived precursors.
For each simulation k, the delayed-neutron activity has been computed and a nonlinear least-square fit performed. The procedure has been repeated K times ($K = 10000$ in this work). As a consequence, 10000 sets of fitted 8-group abundances have been produced. The abundances set is supposed to contain not only the uncertainties but also the covariances. For that reason, a number K of DN activity curves have been fitted through the previously mentioned nonlinear LSF (fixing the λ_i-set to the one suggested by the WPEC-SG6 [38] giving K sets of DN abundances, the matrix a

$$a = \begin{bmatrix} a_{1,1} & \cdots & a_{1,8} \\ \vdots & \ddots & \vdots \\ a_{K,1} & \cdots & a_{K,8} \end{bmatrix} \tag{4.24}$$

The K sets of abundances have been used to derive the standard deviations (see Eq. 4.26) and the covariance matrix (see Eq. 4.27) due to the random sampling.

[1] JEFF-3.1.1 contains the abundances and the decay-constants recommended by the WPEC-SG6 [40].

$$\overline{a_i} = \frac{1}{K}\sum_{k=1}^{k=K} a_{k,i} \tag{4.25}$$

$$\sigma_{a_{i,stat}} = \sqrt{\frac{\sum_{k=1}^{k=K}(a_{k,i} - \overline{a_i})^2}{K-1}} \tag{4.26}$$

$$cov_{stat}(a_i^{(k)}, a_j^{(k)}) = \frac{\sum_{k=1}^{k=K}(a_{k,i} - \overline{a_i})(a_{k,j} - \overline{a_j})}{K-1} \tag{4.27}$$

The CONRAD® code also provides the associated conditional covariance matrix, called $A^{(k)}$, which is the covariance matrix obtained when the set of input parameters $\overrightarrow{\theta}$ corresponds to the perturbed one $\overrightarrow{\theta}^{(k)}$. This covariance matrix is associated with the fit, and not with the random sampling.

$$A^{(k)} = cov_{fit}(a_i, a_j \mid \overrightarrow{\theta} = \overrightarrow{\theta}^{(k)}) \tag{4.28}$$

The next step has been to compute the expected value of the covariance matrix due to the fit ($\mathbb{E}(A^{(k)})$) in order to apply the *Total Covariance Theorem* (see Eq. 4.29), where the first term is computed from the K sets of fitted parameters and the second is the average of the K covariance matrices provided by CONRAD® and associated with the fitting procedure [14].

$$cov_{tot}(a_i, a_j) = cov_{stat}(a_i^{(k)}, a_j^{(k)}) + \mathbb{E}(A^{(k)}) \tag{4.29}$$

Finally, the total standard deviations have been computed by taking into account both the statistics and the quality of the fit (see Eq. 4.30) and used to derive the correlation matrix (see Eq. 4.31). On this account, an article has been published [19].

$$\sigma_{tot}^2 = \sigma_{stat}^2 + \sigma_{fit}^2 \tag{4.30}$$

$$corr(a_i, a_j) = \frac{cov_{tot}(a_i, a_j)}{\sigma_{a_{i,tot}}\ \sigma_{a_{j,tot}}} \tag{4.31}$$

Table 4.8 reports the abundances obtained through the *Monte Carlo marginalization* method for the thermal fission of ^{235}U, while Fig. 4.12 shows the associated correlation matrix.

Table 4.8: Results of the *Monte Carlo marginalization* method for the thermal fission of ^{235}U using JEFF-3.1.1 fission yields and ENDF/B-VIII.0 radioactive decay data. The group decay constants have been taken from WPEC-6 [40] except for λ_1, replaced by the λ of ^{87}Br according to ENDF/B-VIII.0. The computation has been done considering $K = 10000$. σ_{a_i} are given in percentage of a_i.

Group	1	2	3	4	5	6	7	8
a_i [%]	3.60	16.35	9.51	17.77	34.70	11.89	4.16	2.02
σ_{a_i} [%]	11.69	14.41	16.00	14.86	9.23	16.37	34.37	18.16

$$\begin{bmatrix} 1 & 0.013 & 0.125 & -0.063 & -0.239 & 0.086 & 0.056 & 0.118 \\ 0.013 & 1 & -0.145 & -0.175 & -0.467 & -0.050 & -0.052 & -0.033 \\ 0.125 & -0.145 & 1 & -0.182 & -0.241 & -0.003 & 0.019 & 0.002 \\ -0.063 & -0.175 & -0.182 & 1 & -0.400 & -0.316 & 0.036 & -0.214 \\ -0.239 & -0.467 & -0.241 & -0.400 & 1 & -0.154 & -0.138 & -0.220 \\ 0.086 & -0.050 & -0.003 & -0.316 & -0.154 & 1 & -0.507 & 0.532 \\ 0.056 & -0.052 & 0.019 & 0.036 & -0.138 & -0.507 & 1 & -0.074 \\ 0.118 & -0.033 & 0.002 & -0.214 & -0.220 & 0.532 & -0.074 & 1 \end{bmatrix}$$

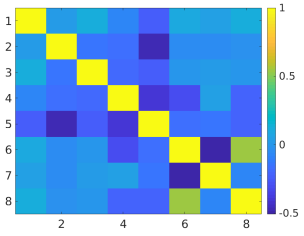

Figure 4.12: Correlation matrix associated with the abundances computed by *Monte Carlo marginalization*.

4.4 Methods comparison

Table 4.9 shows the abundances computed by the summation method with JEFF-3.1.1's fission yields and ENDF/B-VIII.0's radioactive decay data through the different methods mentioned so far, and compared with the WPEC-6 recommendations. The disparate techniques give all reasonable outcomes. The fissioning system under investigation is the $^{235}\mathrm{U_t}$. The first thing to note is the accuracy of the first group's abundance computed by

Table 4.9: Eight-group abundances for the thermal fission of ^{235}U calculated by summation method using different techniques and compared with the recommended values from the WPEC-SG6. The uncertainties are given in percentage of a_i.

	WPEC-6	Simple Eq.	Exponential Eq.	MC Margi.	AN Margi.
Group	a_i [%]	a_i [%]	a_i [%]	a_i [%]	a_i [%]
1	3.28 (12.8%)	3.45 (2.7%)	3.50 (2.7%)	3.60 (11.7%)	3.58 (14.6%)
2	15.4 (4.4%)	15.95 (6.5%)	16.09 (9.8%)	16.35 (14.4%)	16.31 (14.9%)
3	9.14 (9.8%)	9.07 (7.3%)	9.48 (22.8%)	9.51 (16.0%)	9.48 (17.2%)
4	19.7 (11.7%)	19.95 (9.6%)	17.24 (23.2%)	17.78 (14.9%)	17.93 (15.4%)
5	33.1 (2.0%)	31.75 (8.6%)	31.59 (17.4%)	34.70 (9.2%)	34.28 (9.1%)
6	9.03 (5.0%)	9.65 (11.4%)	1.35 (26.3%)	1.19 (16.4%)	1.27 (11.9%)
7	8.12 (2.0%)	8.15 (13.5%)	6.09 (27.1%)	4.16 (34.4%)	3.21 (41.2%)
8	2.29 (41.5%)	2.03 (13.2%)	2.35 (46.4%)	2.02 (18.2%)	2.54 (12.7%)
Sum	1.0006	1.0000	0.9983	1.0000	0.9999
$\overline{T_{1/2}}$	9.02 (3.0%)	9.24 (3.2%)	9.27 (6.6%)	9.45 (6.1%)	9.43 (6.4%)

direct summation. Independently on the type of equivalence, the first abundance results to be well estimated. This is due to the fact that the first group only contains ^{87}Br and therefore the uncertainty on a_1 only depends on the uncertainty in ^{87}Br's FY and P_n. Such error is inevitably smaller than the one coming from a fit, for which the abundances are interrelated. On the other hand, the other groups' abundances, except for the 8^{th} one, are characterized by larger uncertainties because they reflect the uncertainty in the FY and P_n of hundreds of isotopes. The last row of the table contains the mean precursors' half-life, which is another way to look at the abundances. This parameter is typical of the fissioning system and it is an indication of the time dependence of the decay curves. A calculated $\overline{T_{1/2}}$ smaller than the experimental value would highlight an underestimation of the long-lived precursors' contribution or an overestimation of the

short-lived precursors' contribution, and vice-versa. It is worth recalling that there is a direct relationship between the reactor period and the reactivity in the simplified Inhour equation. It is possible to compute the mean half-life by using the group abundances or by *direct summation*, dealing with the complete set of precursors

$$\overline{T_{1/2}} = \frac{\sum_i^k a_i \cdot T_{1/2,i}}{\sum_i^k a_i} = \frac{\sum_i^n P_{n,i} \cdot CY_i \cdot T_{1/2,i}}{\sum_i^n P_{n,i} \cdot CY_i} = \sum_i^n I_i \cdot T_{1/2,i}, \tag{4.32}$$

where i is a single precursor, CY_i is the cumulative fission yield of the precursor i, $P_{n,i}$ is the probability of the precursor i to emit a delayed-neutron, $T_{1/2,i}$ is the half-life of the precursor i (contained in the P_n-library) and n is the number of delayed-neutron precursors. Note that Eq. 4.32 refers to a system at equilibrium and it is not representative of the system during a transient. The $\overline{T_{1/2}}$ computed by direct summation is 9.25 s $\pm$ 3.9% for the thermal fission of ^{235}U. Figure 4.13 and Figure 4.14 show, from a graphical point of view, a comparison between computed and recommended $\overline{T_{1/2}}$ and a_i, respectively. Note that correlations have been taken into account in the

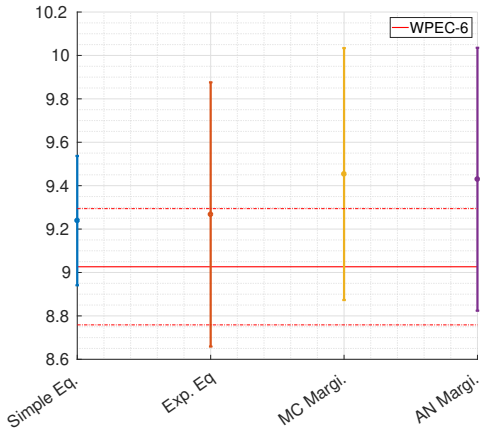

Figure 4.13: Mean precursors' half-life for the thermal fission of ^{235}U calculated using the abundances derived by summation method using different techniques and compared with the recommended values from the WPEC-SG6.

uncertainty propagation, when available. The first thing that comes to mind is that the $\overline{T_{1/2}}$ are coherent and that all the results are covered by the uncertainties bars. The method giving the closest outcome to the WPEC-6 recommendations is obviously the *simple equivalence*. The reason is that the half-life boundaries have been chosen with the purpose of reproducing the WPEC-6 abundances for the $^{235}U_t$. Nevertheless, it has been verified that the boundaries chosen for the $^{235}U_t$ are not appropriate for other fissioning systems. Furthermore, the choice of the group limits makes this method subjective. For that reason, the simple equivalence will be, from now on, discarded. As far as the mean half-life is concerned, *simple* and *exponential equivalence* give very close results. As far as the fit is concerned, *Monte Carlo* and *analytical marginalization* methods give the same global result and the same uncertainty, which is quite reassuring. A thorough look into the abundances reveals small discrepancies in the 7th and 8th groups, largely covered by the associated uncertainties. In conclusion, it has been shown that *exponential equivalence* and the two *marginalization* techniques are equivalent. Among them, the *MC. marginalization* is the slowest, taking about a day to compute the abundances of a

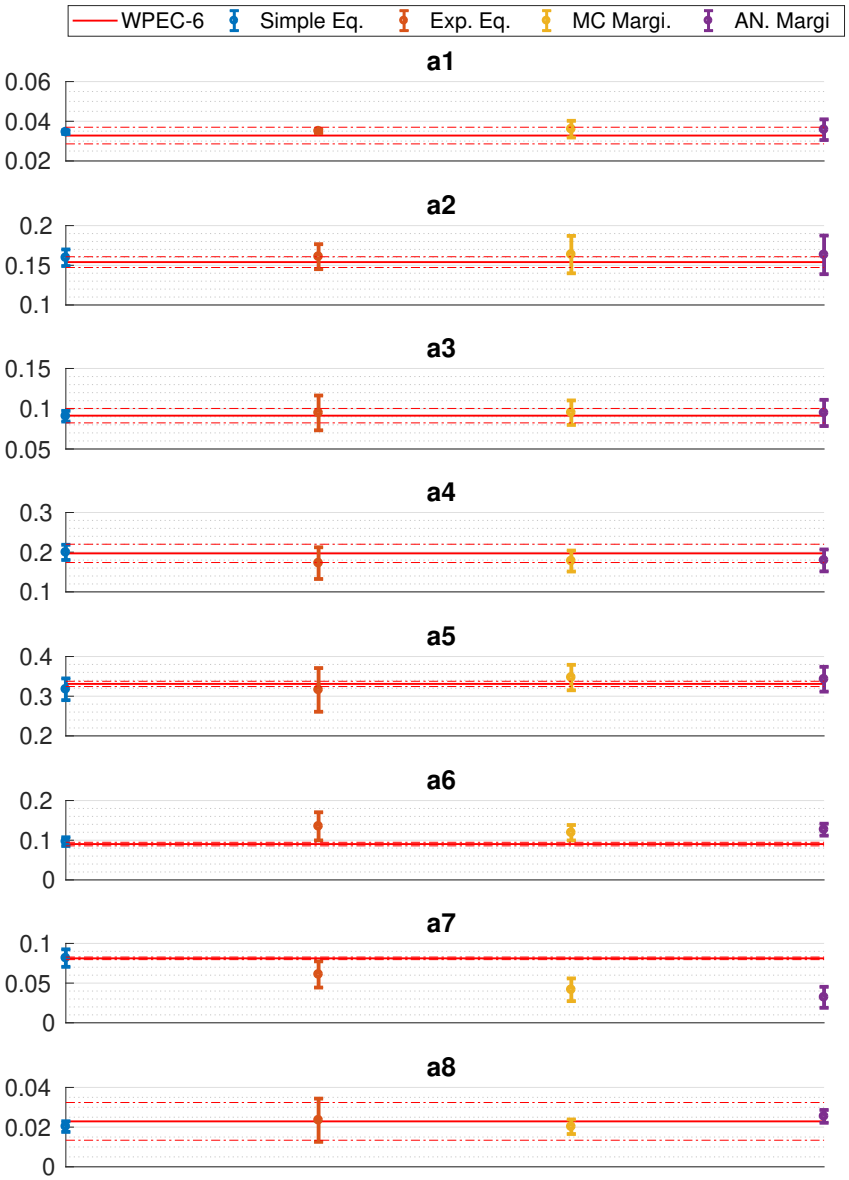

Figure 4.14: Eight-group abundances for the thermal fission of ^{235}U calculated by summation method using different techniques and compared with the recommended values from the WPEC-SG6.

single fissioning system. The remaining two are both very quick.
In the late 50's, the group approximation appeared as a necessary compromise to fit the decay curve. In the first years of the 21th century, the 6-group parameters have been expanded under the assumption that they were able to accurately reproduce the decay curve. However, the quality of the group model in reproducing the original decay curve has never been assessed. In the previous section, the delayed-neutron emission

rate simulated by summation method has been used to produce the 8-group kinetic parameters through different techniques. In this section, the decay curve has been reconstructed, using abundances and decay constants, and compared to the curve that originated them. Figure 4.15a shows the ratio between the activity computed using the 8-group model and the one calculated by summation method. Figure 4.15b is the analogous ratio, but for the reactivity.

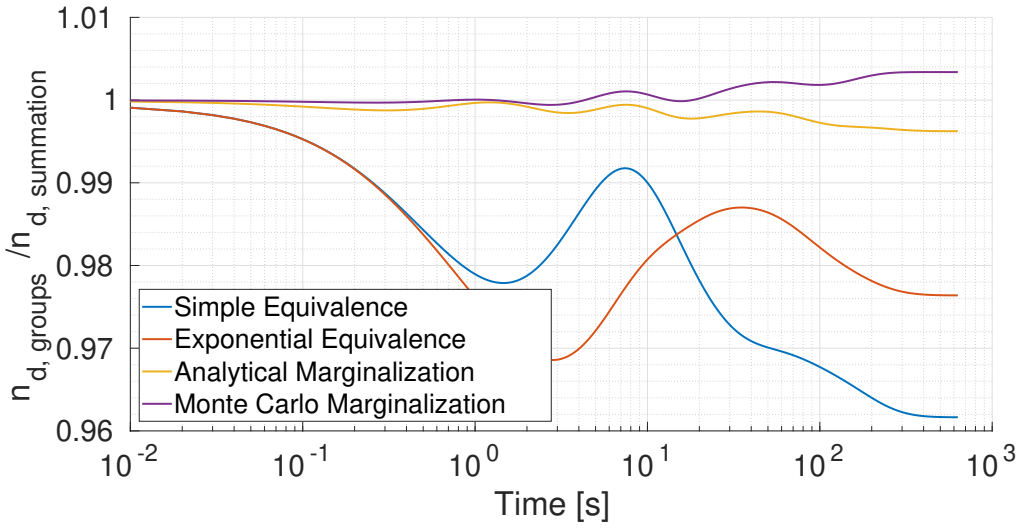

(a) Activity.

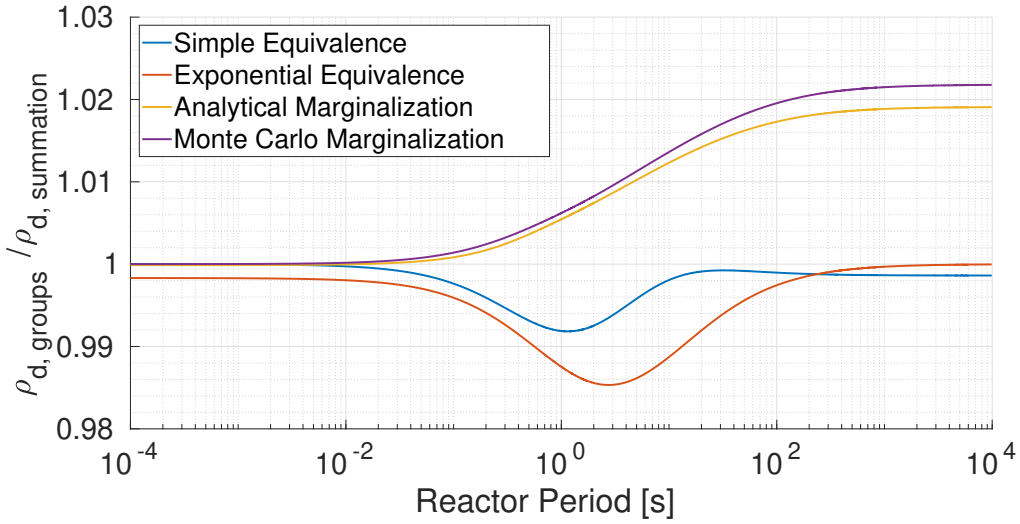

(b) Reactivity.

Figure 4.15: Figure (a) shows the ratio between the activity computed using the 8-group model and the one calculated by summation method. Figure (b) is the analogous ratio, but for the reactivity.

The first thing to note is that the different techniques are not equivalent in reproducing the activity and the reactivity. Two main categories can be identified: the fitting methods and the direct-summation methods. The first one includes analytical and Monte Carlo marginalization and is particularly suited to reconstruct the delayed-neutron activity curve (maximum 0.3% of discrepancy). Besides, the reactivity is overestimated by

about 2.2%. The second category includes simple and exponential equivalence and, even though the activity might be underestimated by 2.5 to 4%, the reactivity is perfectly reproduced. The reason is that, for long periods, the reactivity strongly depends on the mean precursors' half-life, which is better estimated by direct summation than by a fit. Since all studies in the field of delayed neutrons aim at improving the prediction of the reactivity, the *exponential equivalence* has been chosen as the reference summation technique.

4.5 Other fissioning systems

In this section, the exponential equivalence has been used to estimate the abundances of other fissioning systems. Please remember that the quality of the summation method highly depends on the quality of the microscopic input data. This means that, even if the model is correct, fissile isotopes for which the fission yields and the radioactive decay data are not well known, will never be accurately predicted by microscopic calculations. Table 4.10 reports the mean precursors' half-life and the associated uncertainty for the main fissioning systems, computed by summation method and recommended by the WPEC-6. The fissioning isotopes taken into account are: $^{232}\mathrm{Th_f}$, $^{233}\mathrm{U_t}$, $^{233}\mathrm{U_f}$, $^{235}\mathrm{U_t}$, $^{235}\mathrm{U_f}$, $^{236}\mathrm{U_f}$, $^{237}\mathrm{Np_f}$, $^{238}\mathrm{U_f}$, $^{239}\mathrm{Pu_t}$,$^{239}\mathrm{Pu_f}$, $^{241}\mathrm{Pu_t}$, $^{241}\mathrm{Pu_f}$, $^{241}\mathrm{Am_f}$.

Table 4.10: Average mean precursors' half-life for the main fissioning systems. The *direct summation* is an average of the individual precursors' half-lives weighted on the isotope's contribution to the ν_d. The $\overline{T_{1/2}}$ under the other two columns are computed using the respective abundances sets.

Fiss. Syst.	$\overline{\mathbf{T_{1/2}}}$ **[s]**		
	Direct Summ.	**Exp. Eq.**	**WPEC-6**
$^{232}\mathrm{Th_f}$	6.07 (3.5%)	6.11 (6.0%)	6.99 (2.7%)
$^{233}\mathrm{U_t}$	11.87 (7.8%)	11.88 (8.9%)	12.78 (4.0%)
$^{233}\mathrm{U_f}$	10.63 (7.4%)	10.63 (9.4%)	12.39 (3.4%)
$^{235}\mathrm{U_t}$	9.25 (3.9%)	9.27 (6.6%)	9.02 (3.0%)
$^{235}\mathrm{U_f}$	8.42 (4.1%)	8.44 (6.6%)	9.11 (1.0%)
$^{236}\mathrm{U_f}$	6.99 (5.5%)	7.01 (8.3%)	7.34 (8.5%)
$^{237}\mathrm{Np_f}$	8.75 (5.9%)	8.77 (7.7%)	8.87 (0.8%)
$^{238}\mathrm{U_f}$	5.08 (5.3%)	5.11 (4.8%)	5.32 (2.0%)
$^{239}\mathrm{Pu_t}$	10.47 (9.2%)	10.49 (9.0%)	10.69 (8.1%)
$^{239}\mathrm{Pu_f}$	9.13 (9.1%)	9.14 (9.8%)	10.35 (10.0%)
$^{241}\mathrm{Pu_t}$	9.13 (4.0%)	9.14 (6.2%)	7.78 (4.9%)
$^{241}\mathrm{Pu_f}$	8.57 (4.5%)	8.59 (6.7%)	7.85 (6.8%)
$^{241}\mathrm{Am_f}$	10.41 (18.3%)	10.42 (16.6%)	9.99 (11.5%)

Note that the WPEC-6 column is computed from kinetic parameters coming from the evaluation of integral experiments. The other two columns contain $\overline{T_{1/2}}$ calculated by using JEFF-3.1.1's fission yields and ENDF/B-VII.0's radioactive decay data. Their values reflect the databases' content and can be used to draw conclusions on the quality of the libraries and on the observables to be further investigated. Let's take the $^{235}\mathrm{U_f}$ as an example. The sum of hundreds of precursors gives an average half-life which is shorter than the measured one. This means that either the long-lived precursors' yields are underestimated, or the short-lived overestimated. In Section 3.2 it has been

shown that, as far as the ^{235}U is concerned, JEFF-3.1.1's CY undergo a sudden increase when moving from thermal to fast energy. This rise in the yields leads to a highly overestimated ν_d. The main precursors for which this statement is true, have been identified and listed in Sec. 3.2 and among them, there are ^{94}Rb, ^{98m}Y, ^{95}Rb and ^{99}Y, all important rather-short-lived precursors. The overestimation of the contribution of those short-lived precursors is reflected in a $\overline{T_{1/2}}$ which is on average smaller than it should be. The same kind of reasoning can be applied to the other fissioning systems to infer something about the microscopic nuclear data. It is important though, to look at the mean half-life and at the average yield simultaneously, to extract the maximum of information. Another example could be the ^{239}Pu. At thermal energy, the calculated ν_d and $\overline{T_{1/2}}$ both agree with the recommendations. However, at fast energy, the DN yield seems overestimated (7.22E-03 rather than 6.50E-03), as if some of the precursors were given exaggerated yields. At the same time, the mean half-life is underestimated by at least one second. From the information on the ν_d, one could deduce that some of the FYs are too large. As well as that, the information on the $\overline{T_{1/2}}$ narrows the spectrum of isotopes to investigate. It is known that the ν_d is almost constant up to 4 MeV. The average DN yield should, therefore, be almost the same at thermal and fast energies. Looking at the importance of the precursors (Appendices C.5 and C.6), it appears that the most important isotope is the ^{137}I for both thermal and fast fission of ^{239}Pu, but that its importance decreases from 27% to 19%. At the same time, ^{94}Rb's importance rises from 12% to 16%. Knowing that the global yield has increased with energy, this rise points towards an even larger increment of ^{94}Rb's CY. All these hypotheses can be verified by looking at the fission yields of ^{239}Pu in Tab. 4.11.

Table 4.11: Energy evolution of the ^{239}Pu cumulative yields according to JEFF-3.1.1.

Precursor	$\mathbf{T_{1/2}}$ [s]	$\mathbf{CY_{thermal}}$	$\mathbf{CY_{fast}}$	**Difference [%]**
^{137}I	17 s	2.30E-02	1.76E-02	-23.48
^{94}Rb	3 s	6.97E-03	9.90E-03	42.04
^{89}Br	4 s	3.08E-03	5.0730E-03	64.70
^{138}I	7 s	6.77E-03	3.90E-03	-42.39
^{88}Br	16 s	5.02E-03	7.83E-03	56.09
^{90}Br	1 s	9.58E-04	1.50E-03	56.36

It is evident that the CY of relevant short-lived precursors sharply increases with energy and might be overestimated. The isotopes listed in the table could be a good starting point for the precursors to be investigated. Of course, this kind of reasoning requires the combination of ν_d, $\overline{T_{1/2}}$ and importance. Looking into details on all fissioning systems goes beyond the scope of this Ph.D. but the method is promising for the identification of the FY to be further investigated. Table 4.12 reports the abundances computed by *exponential equivalence* for all the mentioned fissioning system.

Table 4.12: Results of the *Exponential Equivalence* method using JEFF-3.1.1 fission yields and ENDF/B-VIII.0 radioactive decay data. The group decay constants have been taken from WPEC-6 [40] except for λ_1, replaced by the λ of ^{87}Br according to ENDF/B-VIII.0. Note that the uncertainties are given in percentage of the a_i value.

Fiss. Syst.	**Group**	**1**	**2**	**3**	**4**	**5**	**6**	**7**	**8**
^{232}Th$_f$	a_i [%]	2.72	6.87	7.25	12.51	32.07	21.44	11.62	4.88
	σ_{a_i} [%]	9.41	8.09	11.27	13.94	14.14	20.46	21.31	17.94
^{233}U$_t$	a_i [%]	7.85	13.88	14.33	17.76	29.94	10.67	3.93	1.51
	σ_{a_i} [%]	6.31	27.40	30.05	36.84	22.32	34.57	34.66	61.40
^{233}U$_f$	a_i [%]	7.66	8.92	13.78	19.18	33.89	10.85	3.95	1.67
	σ_{a_i} [%]	9.83	31.77	22.59	33.66	21.75	39.28	39.91	64.15
^{235}U$_t$	a_i [%]	3.50	16.09	9.48	17.24	31.59	13.50	6.09	2.35
	σ_{a_i} [%]	2.66	9.78	22.79	23.17	17.43	26.26	27.10	46.39
^{235}U$_f$	a_i [%]	3.34	12.74	9.47	17.53	34.97	12.08	6.53	3.16
	σ_{a_i} [%]	4.72314	11.16	21.26	20.61	15.55	29.48	28.82	41.37
^{236}U$_f$	a_i [%]	2.35	11.10	7.15	14.48	35.10	16.06	8.86	4.57
	σ_{a_i} [%]	16.59	10.22	37.06	32.06	17.86	25.93	30.87	39.85
^{237}Np$_f$	a_i [%]	3.22	15.54	8.24	15.51	35.13	13.21	6.12	2.85
	σ_{a_i} [%]	5.58	15.27	28.20	23.93	16.24	28.49	30.22	45.08
^{238}U$_f$	a_i [%]	0.93	9.10	4.37	11.73	30.18	20.66	14.33	7.88
	σ_{a_i} [%]	4.45	6.27	15.81	10.51	11.78	16.41	14.41	13.21
^{239}Pu$_t$	a_i [%]	2.72	25.17	6.93	14.99	30.70	12.24	5.06	2.01
	σ_{a_i} [%]	5.96	16.44	56.00	30.09	20.40	33.39	31.33	54.14
^{239}Pu$_f$	a_i [%]	3.06	17.46	8.16	15.81	35.49	12.36	5.23	2.27
	σ_{a_i} [%]	4.64	22.19	40.13	28.78	18.62	35.00	34.77	55.73
^{241}Pu$_t$	a_i [%]	1.30	23.53	5.96	15.07	29.24	15.23	6.94	2.55
	σ_{a_i} [%]	9.97	6.94	37.19	20.57	16.58	22.45	22.10	35.07
^{241}Pu$_f$	a_i [%]	1.33	21.54	5.16	14.94	31.48	13.81	7.70	3.78
	σ_{a_i} [%]	3.36	7.98	41.21	27.71	17.19	25.16	21.82	29.41
^{241}Am$_f$	a_i [%]	5.38	16.87	8.94	16.57	34.47	12.06	4.01	1.57
	σ_{a_i} [%]	25.27	40.75	102.84	63.85	30.10	49.38	55.26	97.90

4.6 Energy dependence

While the energy dependence of the ν_d has been largely studied and measured, the same is not true for the abundances and for the mean half-lives. It must be recalled that the eight abundances reflect the behavior of hundreds of precursors. It is well known that fission yields change with incident neutron energy and that the precursors the DN groups try to reproduce, should change accordingly. In this section the same procedure used for the energy dependence of the ν_d is employed. This time, the GEF energy trend of fission yields is used to infer the trend of the groups' abundances, and therefore, of the system's behavior. Figures 4.16 to 4.23 show the abundances calculated by summation method using JEFF-3.1.1 *FY* in their original version (full blue line) and corrected by the energy dependence of GEF-6.2 *FY* (orange dotted line). Some experimental values are reported for comparison. The yellow points have been measured by V. Piksaikin [35] and are the most recent. Unfortunately his experiments never went beyond 5 MeV. To have an order of magnitude of the behavior of the ν_d at higher energies, some older measurements have been added to the graphs. The first abundance (Fig. 4.16) is the contribution of ^{87}Br only to the total yield. For the three fissioning systems, this group seems to be quite well estimated. Obviously, the old experimental points are so sparse and uncertain that it is difficult to assess if the trend is right or not. Besides, JEFF-3.1.1's *FY s* allow the computation of 2-3 points in energy, so that it becomes impossible to conclude any energy dependence from it. The second abundance, shown in Fig.4.17, as well seems to be properly estimated. The use of GEF-6.2 energy trend allows the almost perfect reproduction of Piksaikin's experimental abundances. For this group JEFF-3.1.1's point are particularly incompatible with experiments, especially for ^{238}U. As far as the third abundance is concerned (Fig. 4.18), taking GEF-6.2 energy dependence is not sufficient to follow the experimental values. Neither of the 2 summation calculations is good. Since the third group is only made of ^{88}Br, maybe some experiments should be dedicated to the study of the change of its fission yield as a function of energy. From the fourth abundance on, the group is no longer made of a single precursor. This means that the agreement with respect to experiments can only be assessed from a integral point of view and that compensation of effects could hide potential errors in the fission yields. For the 4^{th} group the conclusion depends on the fissioning system. For ^{235}U and ^{239}Pu, original and modified JEFF agree, with the only difference that for the first one they are both close to the experiments, while for the second one they are both shifted downwards. On the other hand, for ^{238}U calculations agree with Piksaikin's values (below 5 MeV) while at high energies the dispersion of the experiments is so large that no conclusion can be drawn. For the short-lived groups the discrepancies between calculation and measurement become larger. Nevertheless, some systematic behavior can still be pointed out and might be of use for suggesting a class of precursors to be measured in priority. The fifth and the sixth abundances seem to be systematically overestimated by calculations, for all fissioning systems under consideration. On the contrary, the seventh and the eight groups are systematically underestimated.

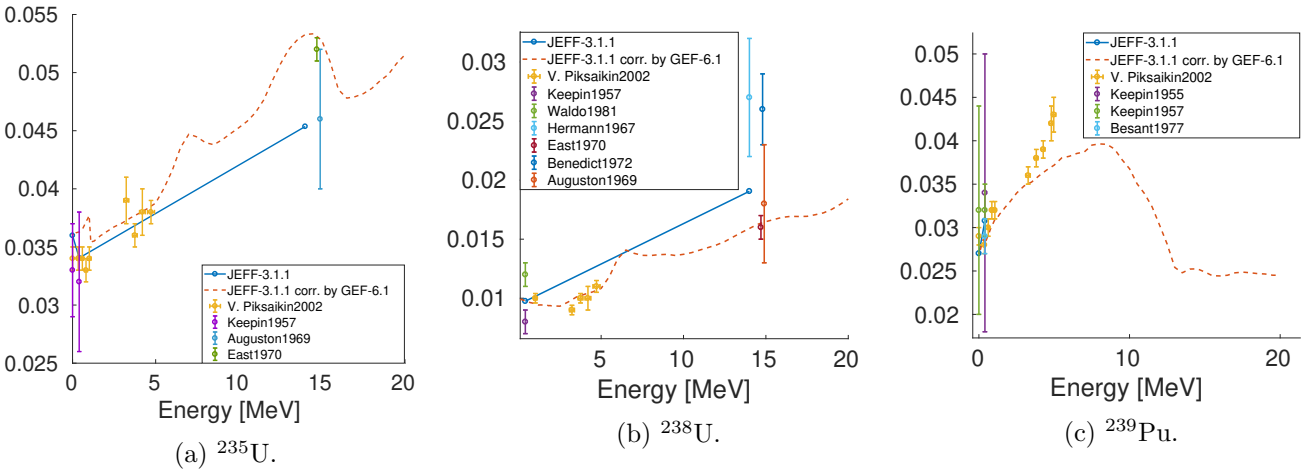

(a) ^{235}U. (b) ^{238}U. (c) ^{239}Pu.

Figure 4.16: Energy dependence of the first abundance computed with the original JEFF-3.1.1 *FY* and with the with JEFF-3.1.1 *FY* modified with GEF-6.1 energy dependence. Experimental values are reported for comparison.

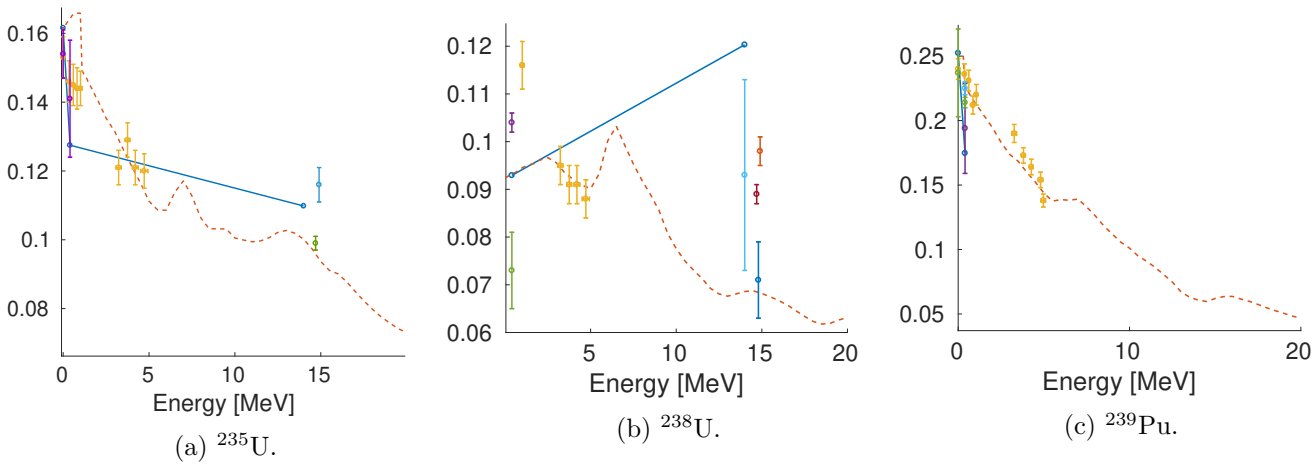

(a) ^{235}U. (b) ^{238}U. (c) ^{239}Pu.

Figure 4.17: Energy dependence of the second abundance computed with the original JEFF-3.1.1 *FY* and with the with JEFF-3.1.1 *FY* modified with GEF-6.1 energy dependence. Experimental values are reported for comparison. For the legend please refer to Fig. 4.16.

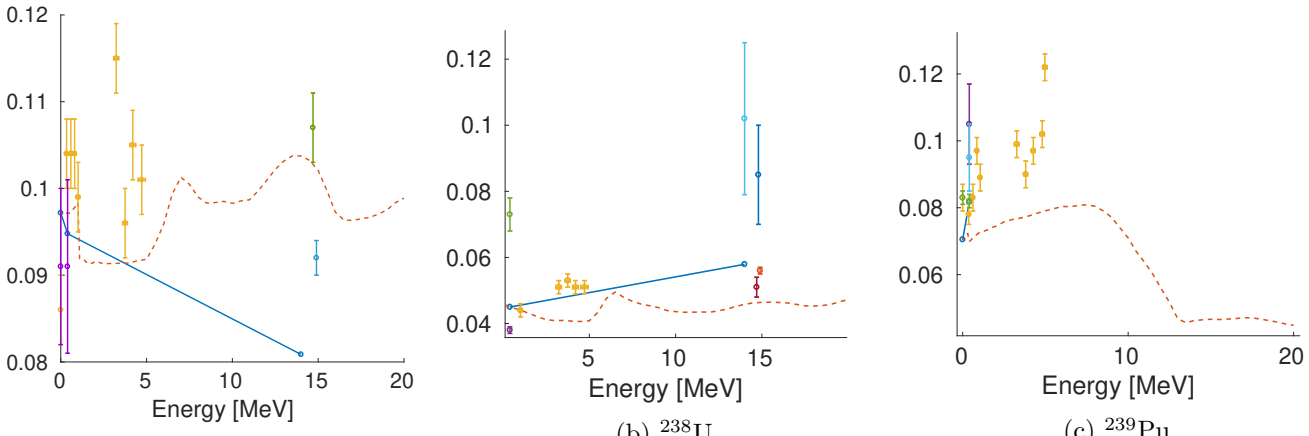

(a) ^{235}U. (b) ^{238}U. (c) ^{239}Pu.

Figure 4.18: Energy dependence of the third abundance computed with the original JEFF-3.1.1 *FY* and with the with JEFF-3.1.1 *FY* modified with GEF-6.1 energy dependence. Experimental values are reported for comparison. For the legend please refer to Fig. 4.16.

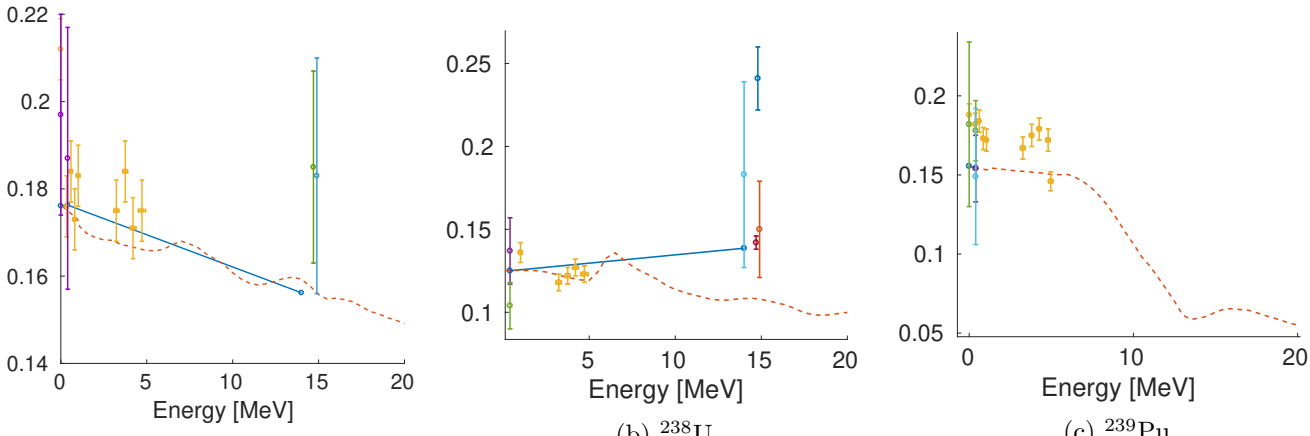

(a) ^{235}U. (b) ^{238}U. (c) ^{239}Pu.

Figure 4.19: Energy dependence of the fourth abundance computed with the original JEFF-3.1.1 *FY* and with the with JEFF-3.1.1 *FY* modified with GEF-6.1 energy dependence. Experimental values are reported for comparison. For the legend please refer to Fig. 4.16.

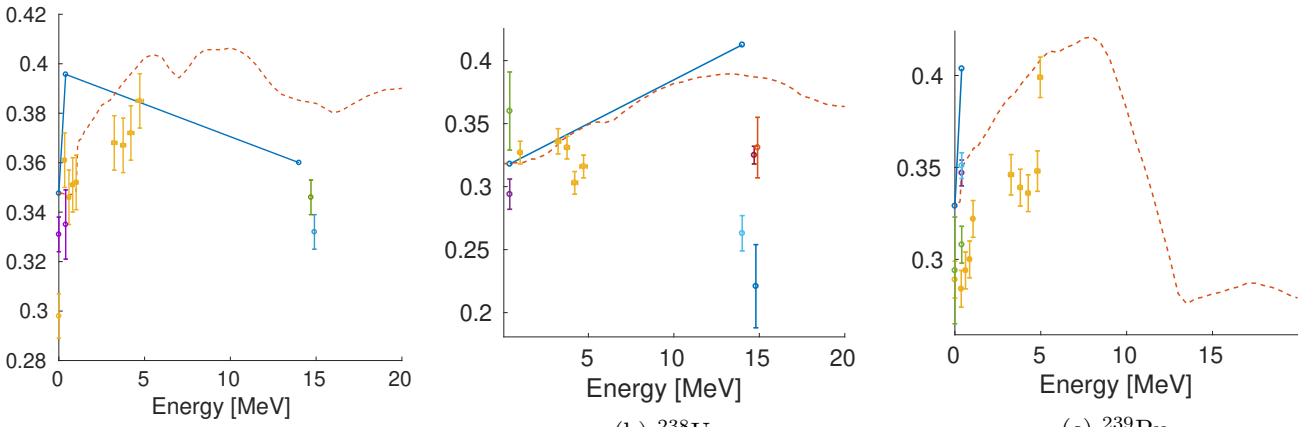

(a) ^{235}U. (b) ^{238}U. (c) ^{239}Pu.

Figure 4.20: Energy dependence of the fifth abundance computed with the original JEFF-3.1.1 *FY* and with the with JEFF-3.1.1 *FY* modified with GEF-6.1 energy dependence. Experimental values are reported for comparison. For the legend please refer to Fig. 4.16.

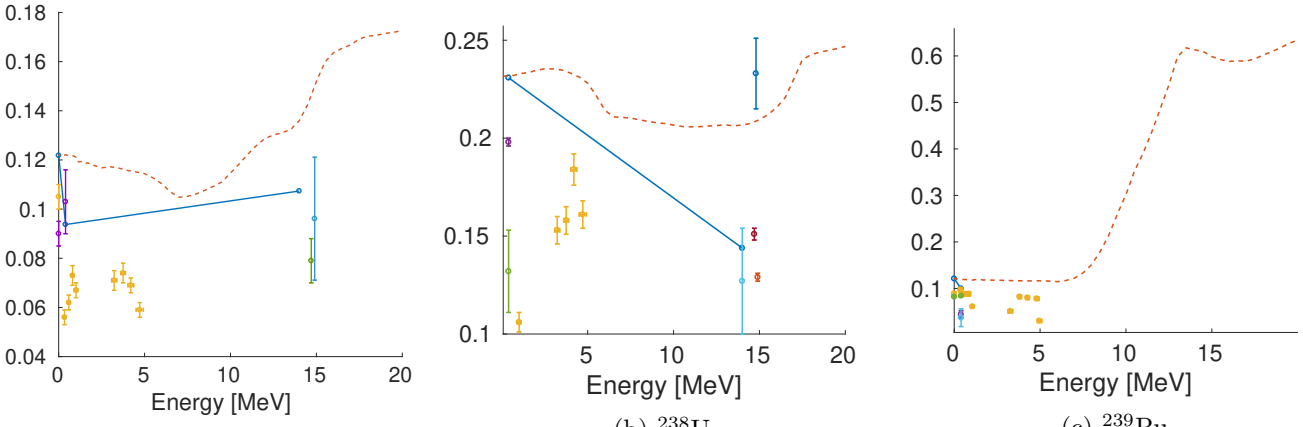

(a) ^{235}U. (b) ^{238}U. (c) ^{239}Pu.

Figure 4.21: Energy dependence of the sixth abundance computed with the original JEFF-3.1.1 *FY* and with the with JEFF-3.1.1 *FY* modified with GEF-6.1 energy dependence. Experimental values are reported for comparison. For the legend please refer to Fig. 4.16.

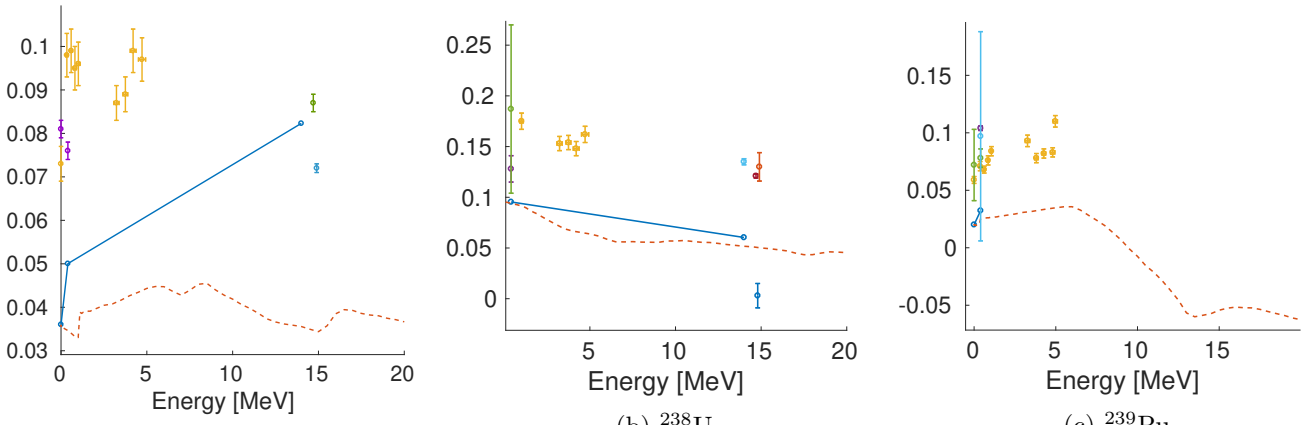

(a) ^{235}U. (b) ^{238}U. (c) ^{239}Pu.

Figure 4.22: Energy dependence of the seventh abundance computed with the original JEFF-3.1.1 *FY* and with the with JEFF-3.1.1 *FY* modified with GEF-6.1 energy dependence. Experimental values are reported for comparison. For the legend please refer to Fig. 4.16.

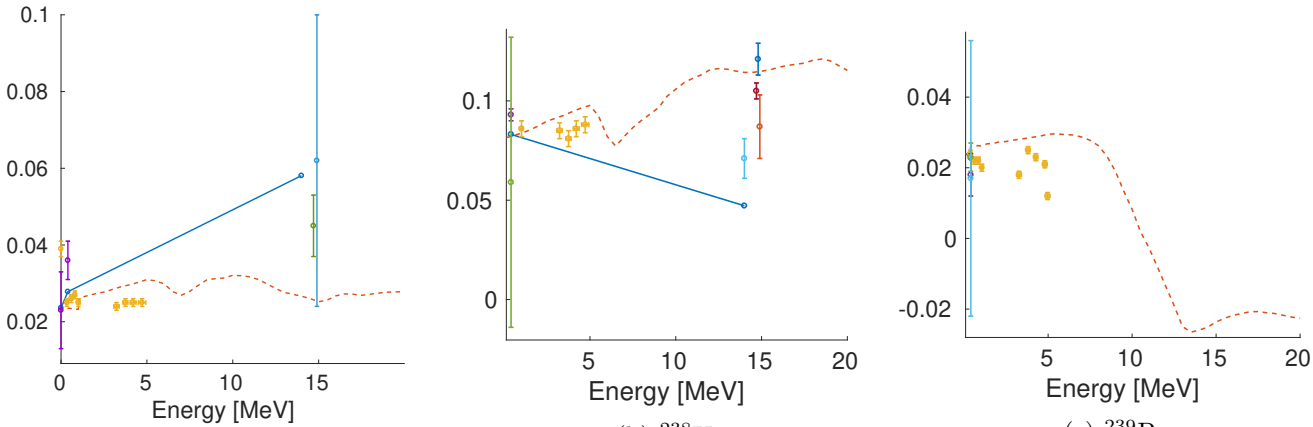

(a) ^{235}U. (b) ^{238}U. (c) ^{239}Pu.

Figure 4.23: Energy dependence of the eigth abundance computed with the original JEFF-3.1.1 *FY* and with the with JEFF-3.1.1 *FY* modified with GEF-6.1 energy dependence. Experimental values are reported for comparison. For the legend please refer to Fig. 4.16.

Keep in mind that abundances are all correlated and that if the contribution of a group is largely overestimated due to a wrong fission yield, it is normal for another group to be underestimated, even though its absolute $\nu_{d,i}$ might be correct. This could be the case for the fast fission of ^{235}U. It has been shown, in Section 3.2, that, for certain isotopes, the FY recommanded by JEFF-3.1.1 incresed too much from thermal to fast energy. It is the case for ^{94}Rb (2.7 s), ^{98m}Y (2.0 s), and ^{99}Y (1.5 s). All these precursors, due to their half-life, fall into the group number 5. It is not surprising then to see that JEFF-3.1.1 largely overestimates a_5 at 400 keV. This work helps to identify the source of error hidden in the global behavior of hundreds of isotopes. A set of DN abundances is always associated with a set of decay constants and they cannot be considered separately. One way to evaluate a set of kinetic parameters (a_i, λ_i) is to compute the derived quantity $\overline{T_{1/2}}$. Looking at Figure 4.24 it seems that for ^{235}U, JEFF-3.1.1 FY modified with GEF-6.1 better reproduce the experimental data than the original ones. The same is true for ^{238}U, except at 14 MeV, where the experiments are spread and too far from each other to draw any conclusion. Finally, for ^{239}Pu, the trend is pretty good but a lack of measurements beyond 5 MeV prevents us to comment on the quality of the results. Unfortunately, measurements in those energy ranges are very thorny to perform, due to the difficulty of finding good monoenergetic neutron sources in this energy domain.

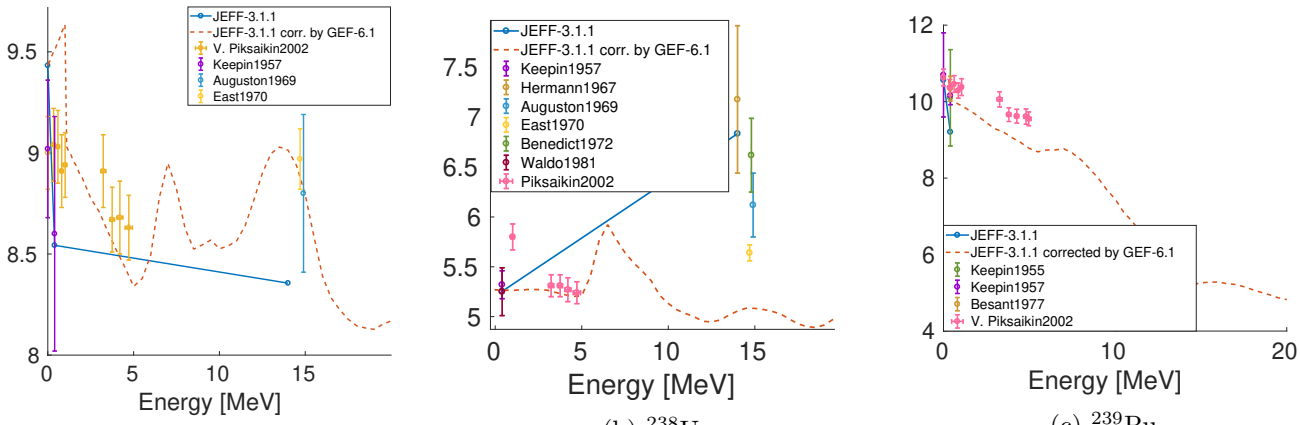

(a) ^{235}U. (b) ^{238}U. (c) ^{239}Pu.

Figure 4.24: Energy dependence of the mean precursors' half-life computed with the original JEFF-3.1.1 FY and with the with JEFF-3.1.1 FY modified with GEF-6.1 energy dependence. Experimental values are reported for comparison. For the legend please refer to Fig. 4.16.

GEF-6.1 energy dependence has been tested, and for the moment it is not always able to reproduce experimental data. However, the method of applying the energy dependence of a specific set of FY to another set looks promising, especially for estimating quantities of interest at energies where measurements are missing. For example, since JEFF-3.1.1 gives evaluated FY at maximum 3 energies while GEF-6.1 gives calculated FY up to 20 MeV, the mentioned method could provide JEFF FY at almost all energies. Of course, for the method to be exploitable, GEF-6.1 should be able to reproduce JEFF-3.1.1 fission yields at energies different from the one taken as reference. For the moment this is not the case, but an improvement of GEF-6.1 energy dependence of FY could, in the future, find an application for this method. Even though the single abundances aren't always well estimated by the modified JEFF, the global effect on the mean half-life is pretty

good for the 3 fissioning systems, which is not the case for the original JEFF.

4.7 Delayed-neutron spectra

Neutron spectra are the most poorly known delayed-neutron quantity. As mentioned in Section 1.4, Brady and England performed an extensive work on spectra. One of the major objectives in Brady's Ph.D. [12] was to improve the spectral data for the individual precursors. At that time, only 34 precursors had a measured spectra. Thirty years later, the number is always the same. Brady and England affirm that in the case of the equilibrium spectra, the fraction of delayed neutrons being produced from precursors with a measured spectrum is 84.04% for $^{235}U_t$, 80.24% for $^{238}U_f$ and 85.84% for $^{239}Pu_t$ [13]. Then, they predicted the delayed-neutron spectrum of other 237 precursors using a modified evaporation model [49]. Comparison with the measured spectra led to the conclusion that such model did not allow the estimation of the measured spectra variations. Another possible use of the Bateman solver is the computation of the equilibrium spectrum and of the average energy. In order to do that, the combination *FY-RDD* must be coupled with a library containing the precursors spectra. JEFF-3.1.1 only contains the 34 measured spectra while ENDF/B-VIII.0 also includes the 237 computed by Brady and England. The average energy can be easily computed as

$$\overline{E} = \frac{\sum_{k=1}^{N} CY_k \overline{P_{n,k}} E_{avg,k}}{\sum_{k=1}^{N} CY_k \overline{P_{n,k}}}. \tag{4.33}$$

Performing the summation calculation using JEFF-3.1.1 or ENDF/B-VIII.0, the average energy of delayed neutrons results to be 61 or 481 keV, respectively. The results are shown in Tab. 4.13 and the equilibrium spectrum from ENDF/B-VIII.0 is presented in Fig. 4.25.

Table 4.13: Average energy computed by summation method using JEFF-3.1.1's *FY* and ENDF/B-VIII.0's *RDD*.

	Spectra ENDF/B-VIII.0	Spectra JEFF-3.1.1
Nb. precursors	270/276 (97.8%)	48/276 (17.4%)
$\overline{E}$ [keV]	481.4 ± 7.9/142.1	61.3 ± 8.0

Note that while JEFF-3.1.1 is missing many precursor's energy values, ENDF/B-VIII.0 uses computed energies but is missing the uncertainty associated with them. This is visible in Tab. 4.13, where JEFF-3.1.1 has a strongly underestimated average energy but a single value of uncertainty. On the other hand, ENDF/B-VIII.0 gives a reasonable average energy but it is presented with two values of uncertainty: one using the existing uncertainties[2] and one replacing the missing uncertainties with 100% of the energy value. Figure 4.25 show the group and the global delayed-neutron spectra for the thermal fission of ^{235}U, computed by summation calculation using JEFF-3.1.1's *FY* and ENDF/B-VIII.O's *RDD* and spectra. JEFF-3.1.1's individual precursors' spectra have not been used because most of them are presented in discrete rather than in continuous form. In 2018 a collaboration between the CEA and the IPPE (*Institute of Physics*

[2]Uncertainty associated with the average energy of the delayed neutrons emitted by a precursor.

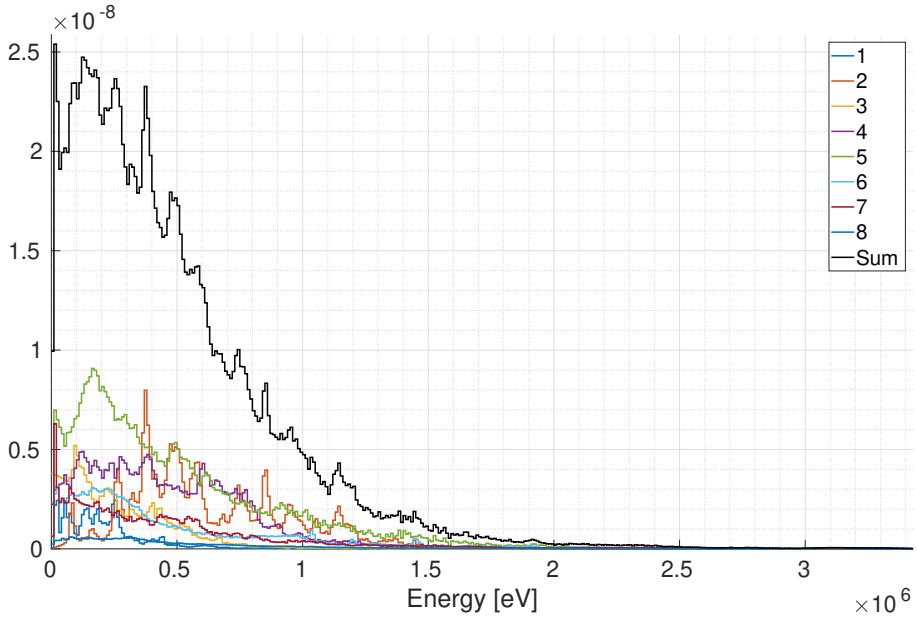

Figure 4.25: Group and equilibrium spectra for the thermal fission of ^{235}U computed by summation method using ENDF/B-VIII.0's individual precursors' spectra.

and Power Engineering, Obninsk, Russia) started. It focused on the 8-group model and on the delayed-neutron spectra. The IPPE measured the equilibrium spectrum of several fissioning systems but also the spectrum emitted by individual delayed-neutron precursors. The collaboration aimed at combining the work done so far on microscopic data and Russian's measured spectra to produce 8-group delayed-neutron spectra with uncertainties and correlations. Finally, due to a lack of time and data, priority has been given to the other delayed-neutron quantities.

Part III

Macroscopic Approach

Chapter 5

Basics of neutron detection

> The moment one gives close attention to any thing, even a blade of grass it becomes a mysterious, awesome, indescribably magnificent world in itself.
>
> Henry Miller

Contents

5.1 Interaction of radiation with matter 93
5.1.1 Heavy Particles 94
5.1.2 Gamma Rays 94
5.1.3 Neutrons 95
5.2 Neutron detectors 99
5.2.1 ^{3}He proportional counters 100
5.2.2 Fission chambers 102

The objective of this chapter is to give an insight, to an inexperienced reader, on neutron detection. The main interactions of radiation with matter are described in Section 5.1. A focus on neutron detectors, and in particulars on the types used in the ALDEN experiment (^{3}He proportional counters and fission chambers), is made in Section 5.2.

5.1 Interaction of radiation with matter

To understand the working principle and the differences among detectors, as well as the choices made for the ALDEN experimental campaign, one should first get an insight into how the radiation interacts with matter. Subatomic particles (electrons, protons, neutrons, alpha particles, gamma rays...) do not behave in the same way when traveling through matter. This section will deal with the interaction of radiation with matter, in order to understand how a detector works and the main characteristics of gamma sensitivity. For further details, the author suggests the Ph.D. work of Rossi [57]. All particles traveling through a medium lose energy, even though the process through which they do it depends on the particles themselves and on their energy. The quantity of

interest for detector studies is the *energy loss per unit path length* or *linear stopping power*, whose total value is the sum of different contributions; such as collision and radiation for neutrons, pair production, photoelectric effect, and Compton scattering for γ-rays.

$$-\left(\frac{\mathrm{d}E}{\mathrm{d}x}\right)_{tot} = -\left(\frac{\mathrm{d}E}{\mathrm{d}x}\right)_{coll.} - \left(\frac{\mathrm{d}E}{\mathrm{d}x}\right)_{rad.} - \left(\frac{\mathrm{d}E}{\mathrm{d}x}\right)_{pair} - \left(\frac{\mathrm{d}E}{\mathrm{d}x}\right)_{p.e.} - \left(\frac{\mathrm{d}E}{\mathrm{d}x}\right)_{com.} \cdots \quad (5.1)$$

5.1.1 Heavy Particles

Heavy charged particles are energetic ions with a mass greater than 1 atomic mass unit. They include protons, alpha particles, and fission fragments and they usually interact with matter through Coulomb forces between their positive charge and the negative charge of the electrons within the absorber atoms [57]. When a heavy particle encounters another medium, it finds itself surrounded by an electronic cloud. Those electrons, belonging to the matter the heavy particles are passing through, *feel* the electromagnetic interaction and either get excited (passing to the next electronic shell) or get torn off from the atom (ionization). The final products of the slowing down of such particles are therefore either excited atoms or ion pairs. The energy transferred due to the collision electron-heavy particle is very small, meaning that many interactions are needed to slow down the primary particles [57]. By definition, the *range* of a particle is the distance the particle needs to travel before losing all its energy. It depends on the particle itself, on its energy and on the material it is crossing[1].

5.1.2 Gamma Rays

Gamma rays, or photons, are electromagnetic radiations produced in the disintegration of radioactive nuclei and in the decay of subatomic particles. The emission of gamma rays does not alter the number of protons or neutrons in the nucleus but instead has the effect of moving the nucleus from a higher to a lower energy state. Gamma-ray emission frequently follows radioactive decay processes and can interact with matter in different ways. The three major mechanisms are photoelectric absorption, Compton scattering, and pair production [57]. The predominant mode of interaction depends on the photon energy and on the atomic number of the material it is crossing. Similarly to heavy particles, gamma rays lose energy, and at the end of the process, they either disappear or are scattered off the medium.

Photoelectric absorption

The photoelectric effect is the phenomenon by which a photon gives all of its energy to an electron. If the energy of the gamma ray is sufficiently large - larger than the binding energy of an electron belonging to the most tightly bound shell - an inner electron is ejected (called *photoelectron*), leaving a vacancy. Afterward, an electron from another shell of the atom quickly fills the vacancy, usually emitting a characteristic X-ray photon, and leaves another vacancy, which will be filled in turn by another electron, thus creating a cascade of X-rays. Occasionally, instead of a photon, an Auger electron is emitted [57]. This process is generally the main mechanism of interaction for gamma rays of low energy (keV region).

[1] In reality, the energy loss is a statistical process and the range follows a Gaussian distribution. This phenomenon is called *range straggling* [57]. The theoretical mean of the distribution is, therefore, an approximation of the real range.

Compton scattering

Compton scattering is the phenomenon through which a gamma ray scatters on a free electron[2], transferring a fraction of its energy. The electron leaves the atom (recoil electron) and the gamma ray is deflected by an angle θ. The loss of energy of the electromagnetic radiation explains the shift in the wavelength of the scattered ray (larger wavelength, lower energy) and can range from zero to a significant fraction of the initial energy. The Compton effect proves that electromagnetic radiations can behave like a stream of particles. The probability a gamma ray interacts with matter through this mechanism depends on the number of available electrons and therefore it linearly increases with the atomic mass of the material and with the energy of the γ-ray.

Pair production

Pair production is the mechanism of interaction for energetic gamma rays. It becomes possible when the energy of the photons is larger than twice the rest-mass energy of the electron (1.02 MeV) [57]. The gamma ray is transformed into an electron-positron pair, which carries the excess energy of the photon as kinetic energy. The positron quickly loses energy crossing the medium and annihilates when it encounters an electron. As a consequence, two well-known photons are emitted in opposite directions. It is the principle of the PET[3].

5.1.3 Neutrons

Neutrons are uncharged particles and do not interact with the electronic cloud of the atoms. Being insensitive to the Coulomb forces, they can penetrate the nucleus and interact with it through the strong force. A neutron beam traveling through matter indeed loses intensity because of the nuclear reactions. A nuclear reaction is usually reported in one of the two following forms

$$a + X \rightarrow Y + b, \qquad X(a,b)Y, \tag{5.2}$$

where a is the incident particle, X the target and Y and b the heavy and the light reaction products [47]. In general, Y quickly loses energy and stops into the target, while b leaves the target and can, therefore, be detected. In the following part, the most important types of neutron interaction with matter are described. They can be sorted in two main categories: *scattering* and *absorption* [20]. According to the notation introduced before, if the incident and the outgoing particles are the same, then the process is called *scattering*. According to the energy of the reaction products we distinguish the *elastic* and the *inelastic* scattering. If, instead of being scattered, the neutron is *absorbed*, then many different reactions can follow. In that case, the incoming particle and the target are within the range of nuclear forces for a certain time. For very short times, the projectile interacts with a single nucleon and the reaction is called *direct*. For longer times, projectile and target merge and share their energy, creating what is called *compound nucleus*, which quickly decays emitting a nucleon [47]. This type of reaction is called *compound nuclear reaction*. The most important feature of the intermediate state is that its decay only depends on the total energy and on the spin of the system and not on the way it has been formed [47]. Among the absorption reactions we recall: *radiative capture*, *fission*, *other*.

[2] If the gamma ray's energy is larger than the binding energy of a valence electron (loosely bound), then the electron can be considered to be free.

[3] Positron Emission Tomography.

Elastic scattering The scattering process is called *elastic* if the total kinetic energy of the incident particle and of the target is conserved [20]. In that case, the reaction products are in their ground state [47]. The reaction is usually written as

$$A(n,n)A. \tag{5.3}$$

This is the principal mechanism of energy loss for fast neutrons [48]. Thanks to the conservation laws one can conclude that for elastic scattering of a neutron on a nucleus of atomic weight A, the energy of the scattered neutron lies within the range [57]

$$\left(\frac{A-1}{A+1}\right)^2 E_0 \leq E \leq E_0. \tag{5.4}$$

This expression shows that the lighter the target nucleus, the more efficient is the *moderation*[4]. For that reason, hydrogenous materials are usually used as *moderators* (water, polyethylene...).

Inelastic scattering Unlike the elastic scattering, the *inelastic* scattering is a process in which the nucleus is left in an excited state [57]. It is usually represented as

$$A(n,n')A^*. \tag{5.5}$$

The total kinetic energy of the reaction products is lower than the one of the incoming particle plus the target. This is due to the fact that some of the energy is used to internally rearrange the residual nucleus into an excited state [20]. The excited product generally goes back to the ground state releasing radiation. Inelastic scattering is another process that leads to neutron moderation, but it can only take place if the neutron has sufficient energy to excite the nucleus ($\approx$ 1 MeV) [48].

Neutron capture

The term *capture* includes all the absorption reactions leading to the emission of radiation (gamma or charged particle): (n,γ), (n,p), (n,t) and (n,α). A common feature to all these reactions is that, at low energies, the cross section is inversely proportional to the incident neutron speed. The explanation is that the neutron is slow and therefore it spends more time near the nucleus [57]. The products of the reaction are emitted back-to-back but their direction is random since the compound nucleus loses all information about the incident neutron. Neutron capture is at the basis of neutron detection because the secondary particles can be easily detected.

Nuclear fission

Nuclear fission is the process exploited in nuclear reactors to produce energy. The reaction can be spontaneous or particle-induced (n, p, T, $\alpha \cdots$). Isotopes susceptible to undergo fission are called fissile and are all unstable heavy nuclei. The instability comes from the conflict between the strong Coulomb force which tries to push the protons away, and the strong nuclear force which tries to keep the nucleons together. When they absorb an extra neutron, the excited compound nucleus splits into two smaller

[4]Moderation is the process through which the neutrons lose energy until they reach the thermal equilibrium with the medium [57]. Such neutrons are called *thermal*. The concept of efficiency is linked to the number of collisions needed to thermalize the neutrons.

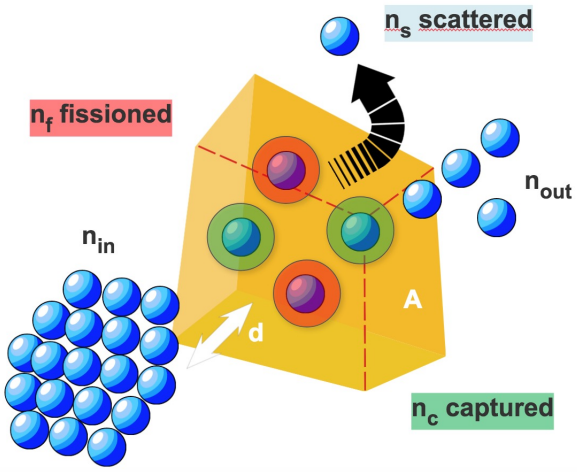

Figure 5.1: Simplified scheme of the neutron interaction with matter. n represents the number of neutrons and the indices *in*, *out*, *c*, *s*, and *f* represent the neutrons entering, exiting, being captured, being scattered and causing fission, respectively. S is the surface of the bulk material while d represents its thickness.

nuclei, some neutrons and some secondary radiation [57]. The mass difference between the fission fragments and the starting compound nucleus ($\approx$ 200 MeV) is evacuated as thermal energy. The fission cross section follows the 1/v trend, meaning that that slower the neutron, the higher the probability for it to cause fission.

The neutron cross section

The probability of a nuclear reaction to occur is expressed through a quantity called *cross section*. As mentioned before, an incident neutron beam crossing a material loses intensity. What happens is that some of the neutrons are captured, some are scattered, some others might cause fission, and the rest emerges from the sample. Each event has its own probability of occurring. The microscopic cross section (σ) is defined as the ratio between the probability of the event to occur and the number of target atoms per unit surface (areal atom density) [20]. Figure 5.1 shows a simplified scheme of the neutron interaction with matter. Let's assume that there is a very thin layer of a certain material[5], having thickness d and surface S. And let's assume that a fraction of each nucleus of the material behaves like an obstacle for the incoming neutrons; obstacle that will cause the neutrons to undergo a certain reaction (fission, scattering, capture...). Those obstacles have a transverse area σ. If the neutron-nucleus interactions were purely mechanical, then σ would have been the real transverse surface of the obstructive part of the nucleus. However, nuclear reactions cannot be treated as simple collisions and σ is an artificial surface representing what the neutron *sees* as an obstacle according to its own energy. Of course, each type of reaction has its own σ. If the bulk material has a density ρ (g/cm^3) and a molar mass M (g/mol), then the number of atoms per volume is given by

$$N = \frac{\rho N_A}{M} \qquad [\text{at/cm}^3], \tag{5.6}$$

[5] *thin* with respect to the nuclear dimensions so that the probability of the atoms to overlap is very small.

where N_A is the Avogadro number in at/mol. Therefore in the total volume $V = S\ d$ there are $N\ S\ d$ particles and $\sigma_c\ N\ S\ d$ is the global surface of the obstacles causing the neutron capture. The probability that a neutron beam sent through the layer would hit the obstacles causing capture is the ratio between the obstructive surface $\sigma\ N\ S\ d$ and the total surface S

$$P_c = \frac{\sigma_c\ N\ S\ d}{S}. \tag{5.7}$$

Dividing the probability by the thickness d of the layer, we obtain the neutron's capture probability per unit length Σ_c, usually called *macroscopic cross section*

$$\Sigma_c = \frac{\sigma_c\ N\ d}{d} = \sigma_c\ N. \tag{5.8}$$

because it depends on the density of the material. Dividing by the atomic density of the bulk material, one obtain σ_c, the *microscopic cross section*, which is the probability of interaction per unit area[6], which is in the order of 10^{-28} m^2. In this regard, a special unit has been introduced: the *barn*

$$1\ \text{b} = 10^{-28}\ \text{m}^2 = 10^{-24}\ \text{cm}^2. \tag{5.10}$$

Note that even if it has the dimension of an area, it must be considered as a quantity which is proportional to the probability of interaction [47].
Figure 5.2 shows the total, the elastic scattering, and the fission cross section of the fissile isotope ^{235}U. The probability of interaction is plotted as a function of the incident neutron energy.

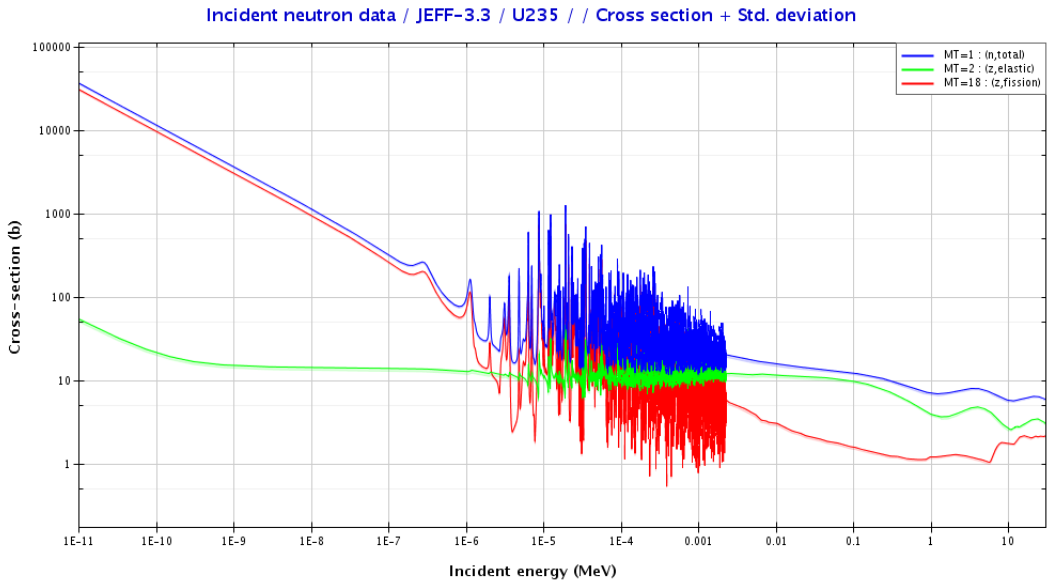

Figure 5.2: Total, elastic scattering and fission cross section for the fissile isotope ^{235}U according to JEFF-3.1.1.

[6]According to Fig. 5.1, the microscopic cross section could also be computed as

$$\sigma_c = \frac{n_c}{n_{in}\ S}. \tag{5.9}$$

The concept does not change since it remains the probability for the neutron to undergo a certain reaction (n_c/n_{in}) per unit area.

It is important to know that there is a strong relationship between neutron energy and velocity [20]. Such connection comes from the classical kinetic equation

$$E = \frac{1}{2}mv^2 \tag{5.11}$$

which is valid since the rest mass energy of a neutron ($\approx$ 940 MeV) is much larger than typical neutron kinetic energies for reactor applications [20]. Neutrons are customarily classified according to their energy. A neutron is called *thermal* if it has an energy of 0.0253 eV, which corresponds to a speed of 2200 m/s. At this speed, neutrons are in equilibrium with the movement of the medium atoms. A neutron is called *cold* if its energy is below 0.0253 eV, *epithermal* if it is between thermal and a few hundreds eV, *fast* if it is in the range 500 keV - 14 MeV, and *high* if it is beyond 14 MeV. Cross section is a quantity that strongly depends on the incident neutron energy. Figure 5.2 shows that the cross section might have large peaks at specific energies. Those peaks are called *resonances* and occur at energies where the reaction with the nucleus is enhanced because together, neutron and target form an excited state of the compound nucleus. Thermal neutrons have a high probability of causing fission in fissile materials. Such probability then decreases for fast and high-energy neutrons. On the other hand, fertile isotopes' cross section presents a threshold, which means that fission become possible if the neutron brings enough energy to pass the fission barrier.

5.2 Neutron detectors

Neutrons are neutral particles and the only way to detect them is to push them to undergo some reaction leading to the production of charged particles, which can be detected due to the ionization and excitation of the atoms inside the detector [48]. There are several types of neutron detectors. The most commonly used are ionization detectors and scintillators. In the ionization detectors, the charged particles created by the neutron reaction with the gas atoms inside the detector create ion-electron pairs. Electrons are then collected, producing an electric current signal. On the other hand, scintillators exploit the ionization and the excitation of the gas to enhance the transition of the atoms to a higher level. When coming back to the ground state, those atoms release the excess energy under the form of light. The signal coming from scintillators can be amplified through electron tube devices called photomultipliers. This section will focus on gas-filled ionization detectors. There are three main operating conditions: the ionization chamber, the proportional counter, and the Geiger-Muller counter [48]. Figure 5.3 shows a schematic of an ionizing detector.
A cylindrical container made of conductive material and having a thin end window is filled with a gas. Inside the cylinder (cathode), a conductive wire (anode) is connected to a positive voltage ($+V_0$). In this configuration, when a voltage is applied to the detector, a radial electric field appears. The purpose of the electric field is to accelerate the electrons and the ions created by the ionization of the gas during the passing of the radiation. Electrons are attracted by the anode while ions are pushed towards the cathode. Figure 5.4 shows the operating condition of the three main ionizing modes. In the absence of an electric field, the pairs recombine by Coulomb attraction. A low voltage is sufficient to create a current out of the accelerated electrons. When all the pairs are collected, an increase of the voltage has no effect on the detector. This is the typical working region for an ionization chamber, which produces a very small signal and is mainly used to detect gamma radiation[48]. Increasing the voltage, the current start to

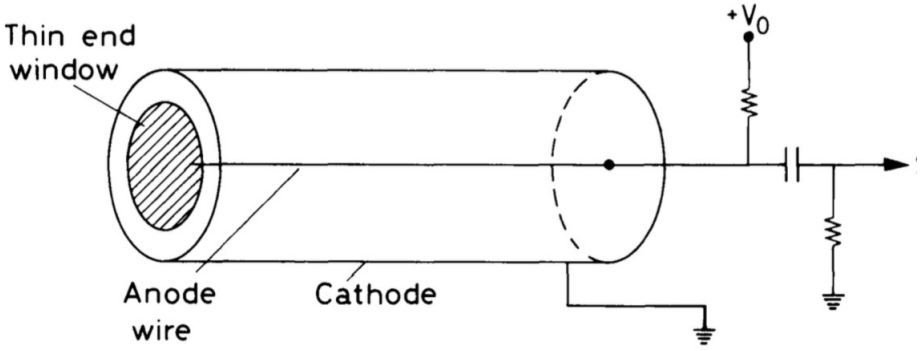

Figure 5.3: Scheme of a gas-filled ionization detector [48].

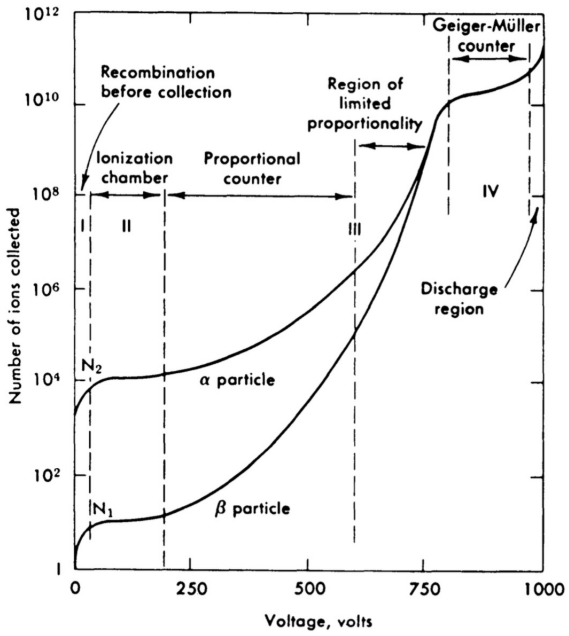

Figure 5.4: Operating conditions of gas-filled ionization detectors [48].

rise again. The reason is that the electric field is sufficiently strong to accelerate electrons enough to ionize the gas themselves. The secondary electrons are also accelerated enough to ionize the gas. This is called *ionization cascade*. In the typical working region of a proportional counter, the number of electron-ion pairs in the cascade is proportional to the number of primary electrons. This means that the electric field amplified the current. Finally, if the voltage is further increased, the electric field is distorted and the current is no longer proportional to the input. This is the region of the Geiger-Muller counters, in which the output always has the same amplitude.

5.2.1 ^{3}He proportional counters

Proportional counters for neutron detection are filled with a gas having a high neutron capture cross section (BF_3 or ^{3}He). The pressure can be adjusted to increase the density of the gas and therefore the efficiency of the detector. The electric field in a cylindrical counter has a 1/r dependence, meaning that the field is stronger next to the anode wire and weaker elsewhere. Thanks to this phenomenon, the electrons and the ions are

drifted towards their electrodes and when the electrons reach the wire, the field is strong enough to cause a cascade. The multiplication occurs in a very small region so that the amplitude of the signal does not vary with the position at which the ionization occurred. Free electrons must drift towards the anode. For this reason, the gas filling the detector must be insensitive to the electrons. That is why noble gases are usually employed (Ar or He). The most common choice of gas for neutron detection is ^{3}He, which converts neutrons into ions through the following reaction

$$^1n +^3 He \rightarrow^1 H +^3 H. \tag{5.12}$$

The Q-value of the reaction is 764 keV, which is shared between the proton (573 keV) and the tritium (191 keV)[57]. Those fragments collide with the atoms of the surrounding gas, ionizing it. The ^{3}He capture cross section for thermal neutron is very large (5333 b), which is an advantage since it implies a good detection efficiency. ^{3}He and BF_3 are the only gases which can act as neutron converter and proportional counter at the same time, but BF_3 is toxic. Besides, the price of ^{3}He is very high and its availability is very limited[57]. If the detector is only filled with ^{3}He, the PHA (*Pulse Height Amplitude*) - which represents the energy deposited in the detector - would be the one shown in Fig. 5.5.

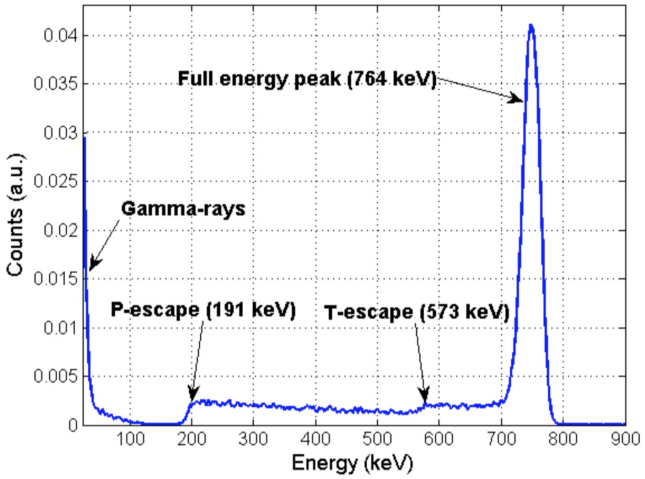

Figure 5.5: Pulse Height Amplitude of a typical ^{3}He detector [57]. Note that gamma rays indirectly ionize the gas and appear as a low energy peak in the PHA.

When the reaction products release the whole Q-value in the detector, the PHA presents the full energy peak. However, it might happen that one of the fragment escapes from the detector's walls before losing all its energy (*wall effect*). Only one of the two particles can escape at the time because they are emitted back-to-back[57]. The escaping fragment deposits only part of its energy, which explains the continuum in Fig. 5.5 (tritium and proton shoulders). Note that some heavier gases can be added to increase the density and reduce the range of reaction products, thus reducing the wall effect. The signals in the low energy region are caused by gamma radiation and electronic noise. One important step to be done before any experiment is the choice of the amplitude threshold. This is necessary to discriminate between noise and neutrons. One way to do it is to set the threshold in the neutron valley. However, alpha-particle decays are a pernicious background for ^{3}He detectors used in low counting-rate applications. The rate of alpha

particle decays originating from the walls of the counter can be comparable to, or even exceed, the rate of neutron captures. Alpha particles arise primarily from daughters in the uranium and thorium decay chains. The amount of energy deposited in the detector can be from essentially zero to several MeV, spanning the region of the neutron capture products. Thus, energy discrimination alone is not sufficient to reject background events from alpha particles. The method of risetime discrimination provides a straightforward method to reject a large fraction of these events. Because the neutron capture on ^{3}He has a two-body final state, the charged particles will be emitted in opposite directions. If the ionization tracks are parallel to the central anode wire, all of the charges will be collected at approximately the same time, leading to a short risetime of the detected signal. However, if the particles are emitted perpendicular to the anode wire, one particle will be moving towards the wire while the other is moving away. The collected charge will be spread out in time due to the radial variation caused by the track geometry. Beta emitters, electrons from gamma-interactions, and cosmic rays leave long tracks and deposit little energy resulting in small signals with a wider range of risetimes. Alpha particles with much higher specific energy loss leave shorter tracks and deposit more of their energy, which yields large signals with a relatively fast risetime.

5.2.2 Fission chambers

A fission chamber is an ionization chamber composed of two conductive plates on which a thin layer of fissile material is deposited. The detector is filled with a gas. An electric field perpendicular to the plates is generated by applying a high voltage on one of the plates and by connecting the other to the ground. The difference with respect to proportional counters is the reaction used to detect neutrons: fission rather than capture. Neutrons hit the fissile material (actinides or minor actinides), and two fragments are emitted into the gas, causing its ionization. Finally, thanks to the electric field, the ion-electron pairs are drifted towards the plates and collected. The sensitive layer is usually very thin because fission fragments have a small range in the dense actinide and would not be able to exit from the layer if it was thicker.

Chapter 6

ALDEN set-up

When you're experimenting you have to try so many things before you choose what you want, and you may go days getting nothing but exhaustion.

Fred Astaire

Contents

6.1 Principles of the ALDEN experiment 104
6.2 LOENIE long counter 106
6.2.1 LOENIE-V1 106
6.2.2 Purpose and Design of LOENIE-V2 106
6.2.3 Detectors' arrangement 109
6.2.4 Efficiency as a function of the position 110
6.3 The fissile target 111
6.4 The fast-shutter 112
6.5 Acquisition System and Pulse Processing 114
6.5.1 Traditional analog chain 114
6.5.2 Caen DPP firmware 115
6.5.3 Acquisition system in the ALDEN experiment 117
6.6 Description of the first experimental campaign 119

The objective of this chapter is to describe the ALDEN experimental campaign. Section 6.1 details the aim as well as the set-up of the experiment. Section 6.2 introduced LOENIE-V1 long counter together with its purpose and design. At the same time, it highlights the need for revisiting the detector and describes the process that led to the production of LOENIE-V2. The target, a miniaturized fission chamber, is treated in Section 6.3, while the fast shutter, needed to stop the neutron beam, in Section 6.4. Finally, Section 6.5 introduces the acquisition system used in the ALDEN experiment and Section 6.6 describes the first experimental campaign.

6.1 Principles of the ALDEN experiment

The objective of the ALDEN experiment was to measure the delayed-neutron emission rate after the irradiation of a fissile sample with the aim of:

1. improving the accuracy of the delayed-neutron data with respect to Keepin [41]
2. providing an experimental delayed-neutron activity curve to the international community for testing any modification of the group model. It is worth recalling that the expansion technique (equivalence between the 8-groups and the expanded 8-groups) has never been tested on a measured curve. If the model had to change again, an experimental curve could be used to verify its features
3. providing correlations among the kinetic parameters, missing in most of the delayed-neutron data measurements.

In this work, the decay curve has been used to determine the average delayed-neutron yield (ν_d), the kinetic parameters (a_i), and the mean half-life ($T_{1/2}$). To measure the delayed-neutron activity, the first step consisted in irradiating a fissile target for a certain time t_{irr}. Neutrons hitting the target caused fissions. For each fission, fission products were emitted together with 2 or 3 prompt neutrons. The second step consisted in interrupting the neutron beam with a beam shutter. The fission process stopped, together with the prompt neutron emission. At that moment, only delayed neutrons were present in the system and their activity, which followed the precursors' decay, could be measured. The equation related to the decay phase is

$$n_{dec}(t) = F\nu_d \sum_{i=1}^{8} \epsilon_{d,i} a_i (1 - e^{-\lambda_i \Delta t_{irr}}) e^{-\lambda_i \Delta t_0} e^{-\lambda_i (t - \Delta t_{irr} - \Delta t_0)} + b_{dec}(t) \tag{6.1}$$

where a_i are the DN group abundances, ν_d the average delayed-neutron yield, b_{dec} the background rate (n/s) during the decay phase, F the fission rate in fiss/s and $\epsilon_{d,i}$ the detector efficiency per DN group. Figures 6.1a and 6.1b show a simplified scheme of the two steps.

(a) Irradiation phase.

(b) Decay phase.

Figure 6.1: Simplified scheme of the experimental set-up during the two phases of the ALDEN experiment.

Note that a veto time t_0 has been set due to the fact that slow neutrons arriving after the beam had already been shut down, cause fission and create a fission tail. The veto time was in the order of 30 ms. Figure 6.2 shows a typical run with 50 s of irradiation. Once the raw data has been processed and corrected for the dead time, the last step of the analysis could be performed. For $t = t_0$ (end of the irradiation), Eq. 6.1 becomes

$$n_{dec}(t = t_0) = F\nu_d \sum_{i=1}^{8} \epsilon_{d,i} a_i (1 - e^{-\lambda_i \Delta t_{irr}}) e^{-\lambda_i \Delta t_0} + b_{dec}(t_0) \tag{6.2}$$

which could be used to derive the ν_d if the other parameters are known. For that purpose, it was necessary to extrapolate the counting rate at $t = t_0$, which was hidden

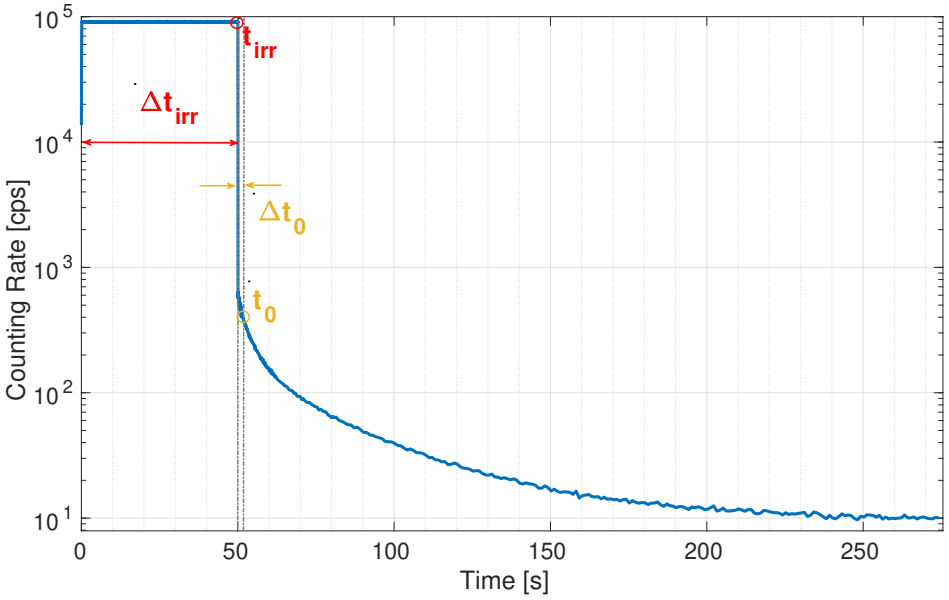

Figure 6.2: Typical irradiation run of the ALDEN experiment.

by the fission tail. Once the ν_d was found, the abundances could be estimated by fitting the activity during the whole decay phase. Several cycles of irradiation-decay have been performed, with different irradiation duration, to excite either the long-lived or the short-lived DN groups.

Figure 6.3 shows the experimental set-up of ALDEN experiment. The experiment took place in the PF1B experimental zone of ILL, where a neutron guide provided an adjustable collimated cold neutron flux coming from the ILL reactor. The capture neutron flux at the exit of the neutron guide was estimated to $1.3{\cdot}10^{10}$ n cm^{-2}s^{-1}. The neutron

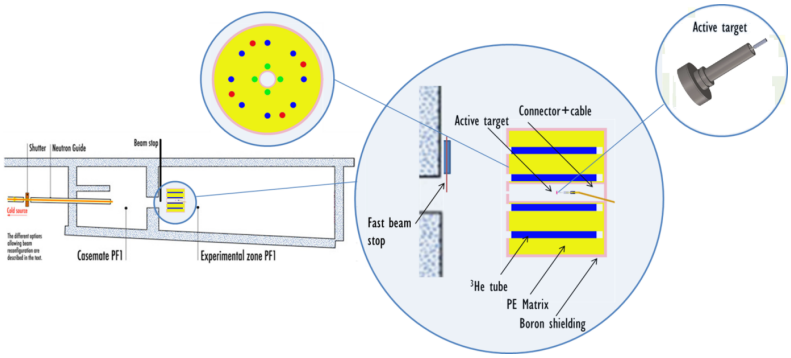

Figure 6.3: ALDEN experimental set-up.

beam entered the experimental area through a vacuum tube and could be reduced from 6×10 cm^2 up to 2×2 cm^2 through a series of collimators made of B4C. At the entrance of the experimental zone, a beam shutter (BS) made of 5 mm of B4C and 50 mm of Pb, was placed to interrupt the neutron beam. It was activated through a button equipped with a key. When the beam was on, no one could enter the experimental zone. Unfortunately, the ILL beam shutter response was too slow for the ALDEN experiment's purposes, which required a shut down in less than 10 ms. Furthermore, the original

shutter could not be programmed to be automatic, nor could it be remotely piloted. In addition to that, the experiment required a beam shutter which could be synchronized with the acquisition system. For that reason, a *Fast Shutter* (FS) has been designed and produced specially for the experiment and will be described in details in Section 6.4. The FS has been placed in the Casmate PF1, just in front of the BS, and used to control the neutron flux while the BS has been kept open during the whole experiment. LOENIE long counter, made of ^{3}He proportional counters, has been placed just in front of the neutron guide so that when the FS was open, the neutron beam passed through the central hole of the detector and hit the fissile target placed at its center.

6.2 LOENIE long counter

6.2.1 LOENIE-V1

In the framework of his postdoc, L. Mathieu designed a neutron long counter in order to measure the delayed-neutron emission probability of some specific precursors. His experiment was to take place at the Institute Laue-Langevin (ILL), in particular in the PF1B LOHENGRIN experimental area. LOENIE-V1 (*LOng counter with Energy Independent Efficiency*) was an octagonal polyethylene matrix with 18 holes dug in two concentric rings to host the neutron counters, as shown in Fig. 6.4a. The geometry was such to optimize the detector response in order to be independent of the neutron energy.

Even though LOENIE-V1 and its tubes were available at the beginning of the Ph.D., the differences in the experimental set-up made the detector not suitable for the ALDEN experiment. In the first place, an internal and an external shielding against thermal neutrons was needed. At the same time, the insertion of an internal shielding would have significantly altered the efficiency trend of LOENIE-V1, making it lose the flat behavior in the energy range of interest. Equally important, an optimization in the design could have led to an improvement of the efficiency with just 16 counters. Finally, it would have been preferable to have a symmetric long counter, for verification purposes. LOENIE-V2 has been designed in response to ALDEN requirements. However, 17 of the 18 original ^{3}He tubes have been recovered and tested and 16 have been used in LOENIE-V2. The test consisted in the comparison of the detectors' response when placed in the same hole (H1) of LOENIE-V1[1] under the neutron flux of a certified AmBe source belonging to IRSN (23000 n/s). As shown in Fig. 6.4b, the average efficiency resulted to be 1.56% with a dispersion of 2.3E-4 (less than 1.5%).

6.2.2 Purpose and Design of LOENIE-V2

LOENIE-V2 has been specifically designed for the ALDEN program, based on TRIPOLI4® Monte Carlo simulations using JEFF-3.2 nuclear data library. The external dimension of LOENIE-V2 is the same as LOENIE-V1, but a cylindrical shape has been preferred to the octagonal one, for simplicity of manufacturing. The central hole has been reduced from 8.5×11 to a circle of 7.2 cm radius. The polyethylene (PEHD500) matrix has been manufactured in two blocks (Fig. 6.5a). The radial symmetry allows controlling the detector response in equivalent positions. LOENIE-V2 contains 16 holes

[1] LOENIE-V1 was not symmetric and the position of the hole affected the response of the tube it contained. For that reason, all the tubes have been tested in the same hole, in order for them to be in the same conditions.

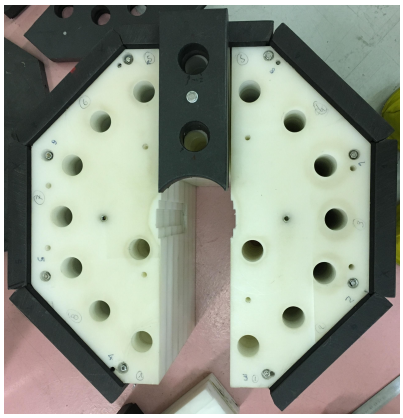

(a) LOENIE-V1.

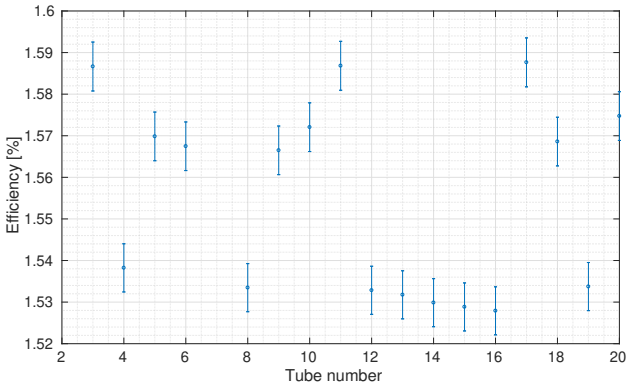

(b) Detectors' efficiency.

Figure 6.4: LOENIE-V1 long counter and efficiency of its 17 ^{3}He tubes.

for the ^{3}He-tubes (Fig 6.5b) since at the time of the design, only 17 out of the 18 tubes from LOENIE-V1 were available. The borated polyethylene of LOENIE-V1 has been

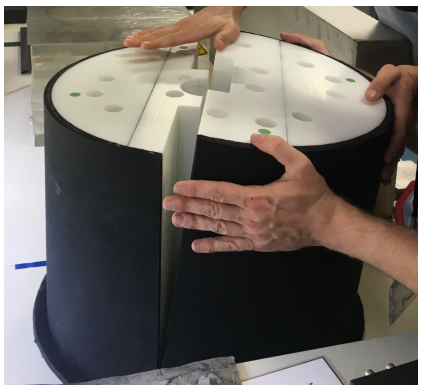

(a) Assembling the polyethylene matrix.

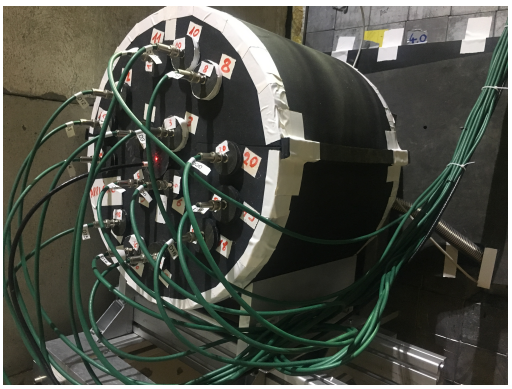

(b) Final system including detectors and cables.

Figure 6.5: LOENIE-V2 detector.

replaced by flexibore so that LOENIE-V2 is now equipped with an internal (7 mm) and an external (10 mm) shielding to minimize the detection of cold neutrons directly coming from the PF1B neutron beam. The main feature of LOENIE-V2 is the flat efficiency as a function of incident neutron energy in the energy range 100 keV - 1 MeV. This is obtained by an optimization of the ring radius, as well as of the number of tubes per ring. It is important to note that LOENIE-V1 had already been designed to have a flat efficiency. The problem is that it had no internal shielding since it was not needed for L. Mathieu's measurement of the P_n. Adding an internal layer of flexibore to reduce the background, would have led to a strong deformation of the efficiency curve. That is why a new design was needed.

Figure 6.6 shows the detection efficiency associated with the ^{3}He(n,p)^{3}H reaction of a ^{3}He tube as a function of its radial position and of the incident neutron energy. Having the detector response as a function of the radius and of the energy, the optimum configuration has been found by minimizing the variation of the efficiency curve in the energy range of interest. The best solution resulted to be a cylindrical matrix made of 3 rings of ^{3}He tubes in a $\pi/2$ symmetry, as shown in the TRIPOLI4® model presented in Fig. 6.7a:

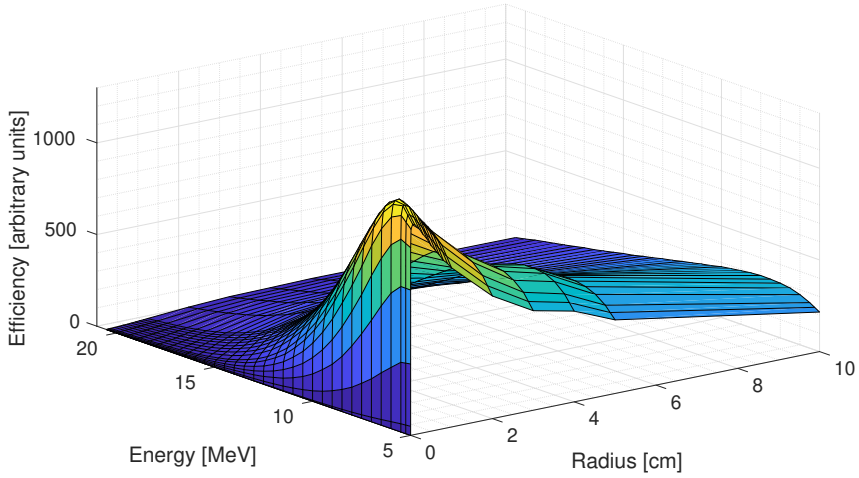

Figure 6.6: Detection efficiency associated with the ^{3}He(n,p)^{3}H reaction of a ^{3}He tube as a function of the incident neutron energy and of the distance from the center.

- *inner ring* (4 tubes) placed at r = 5.3 cm
- *intermediate ring* (8 tubes) placed at r = 15.0 cm
- *outer ring* (4 tubes) placed at r = 16.0 cm.

This configuration gives an efficiency curve which varies at most by 1.5% in the energy range 100 keV - 1 MeV, as shown in Fig. 6.7b, where the simulated global efficiency is plotted as a function of the neutron energy. It also shows that the flexibore plays its role in absorbing all neutrons below 100 meV (cold neutrons coming from the beam), which would have introduced a significant background.

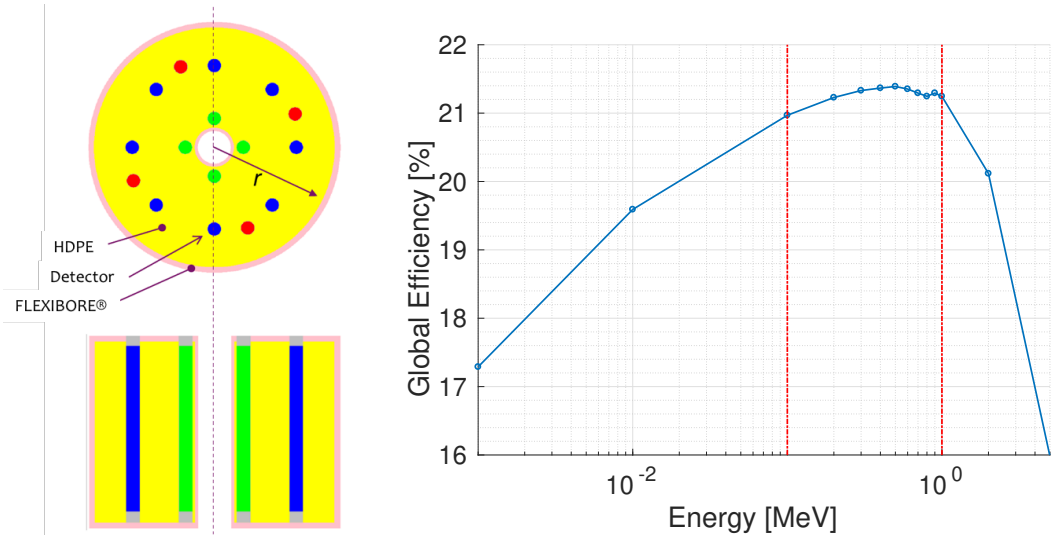

(a) LOENIE-V2 scheme.

(b) Global efficiency as a function of energy.

Figure 6.7: TRIPOLI4® simulation of LOENIE-V2 long counter.

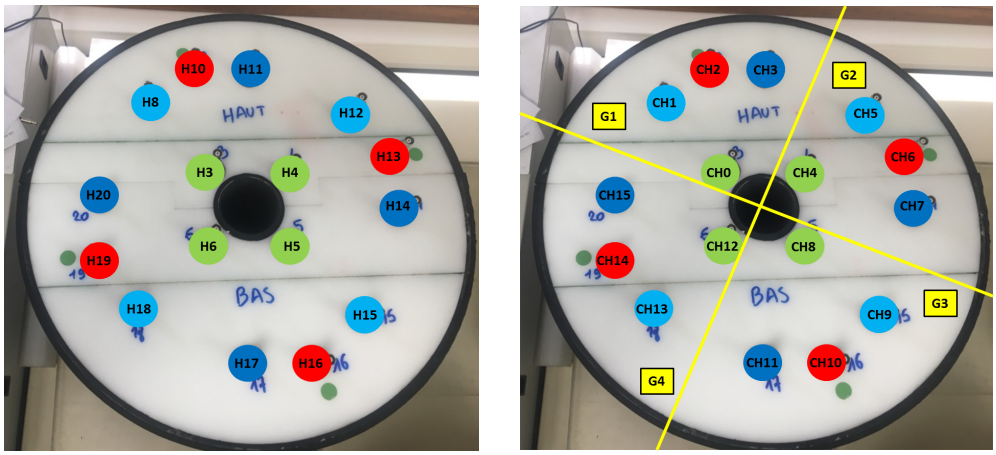

(a) Holes distribution.

(b) Channel distribution.

Figure 6.8: Nomenclature of holes (H), detectors (H), quadrants (G) and channels (CH).

6.2.3 Detectors' arrangement

Figure 6.8 as well as Tab. 6.1 report the configuration used for all tests and experiments. The groups of detectors connected to the same cable RJ45 for the data transfer are indicated as G1, G2, G3, and G4. The notation H_i represents the hole number. Note that the hole takes the name of the tube it carries (tube i is placed in hole i). Finally, CH_i is the channel number according to the acquisition system .

Table 6.1: Detectors configuration.

Quadrant	^{3}He tube	Preamplifier	Caen Card	Channel
G1	H3	0	0	CH0
	H8	1	0	CH1
	H10	2	0	CH2
	H11	3	0	CH3
G2	H4	4	0	CH4
	H12	5	0	CH5
	H13	6	0	CH6
	H14	7	0	CH7
G3	H5	8	1	CH8
	H15	9	1	CH9
	H16	10	1	CH10
	H17	11	1	CH11
G4	H6	12	1	CH12
	H18	13	1	CH13
	H19	14	1	CH14
	H20	15	1	CH15

6.2.4 Efficiency as a function of the position

This test aimed at checking the response of the detectors in the different holes of the new matrix. A ^{241}AmBe source of 50 mCi has been used. The half-life of ^{241}Am is 458 y. A typical ^{241}AmBe source emits neutrons with an average energy of 4.5 MeV at a rate of about 2200 neutrons per second per mCi of ^{241}Am. This means that for this test the emission rate was about 1.1E+05 n/s. At first, the response of the 17 tubes placed in the same hole has been tested. Once the identical response of the detectors had been guaranteed, a test on the whole detector could be performed. Figure 6.9 shows the counting rate as a function of the channel. Each channel corresponds to a

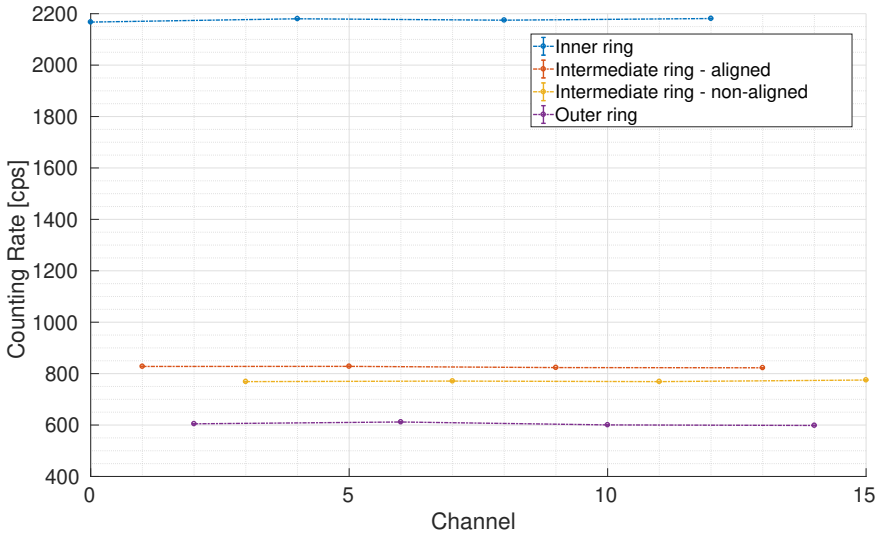

Figure 6.9: Counting rate of the 16 ^{3}He tubes sorted by their ring.

^{3}He tube. In the plot, the tubes are sorted in rings. Note that the intermediate ring, which was supposed to contain 8 detectors, shows two behaviors. Half of the tubes (CH11, CH14, CH17, CH20) counts a bit less than the other half (CH1, CH5, CH9, CH13). The detectors counting less are the ones non-aligned with the first ring. One reason could be that, before reaching the non-aligned detectors, neutrons have to pass through a larger thickness of polyethylene than the ones going to the aligned detectors. Since the intermediate ring is more sensitive to fast neutrons, the polyethylene, further thermalizing the neutrons,could have the effect of reducing the efficiency. Anyway, it has been demonstrated that all the detectors worked fine and that the long counter was perfectly symmetric, with a maximum deviation of 1% among the four groups of tubes. Figure 6.10 shows the PHA of the 16 detectors as well as their sum. The curves belonging to the same ring have the same amplitude. However, the neutron peak is slightly shifted, probably due to a slight difference in the polarization voltage or in the internal geometry of the counters.

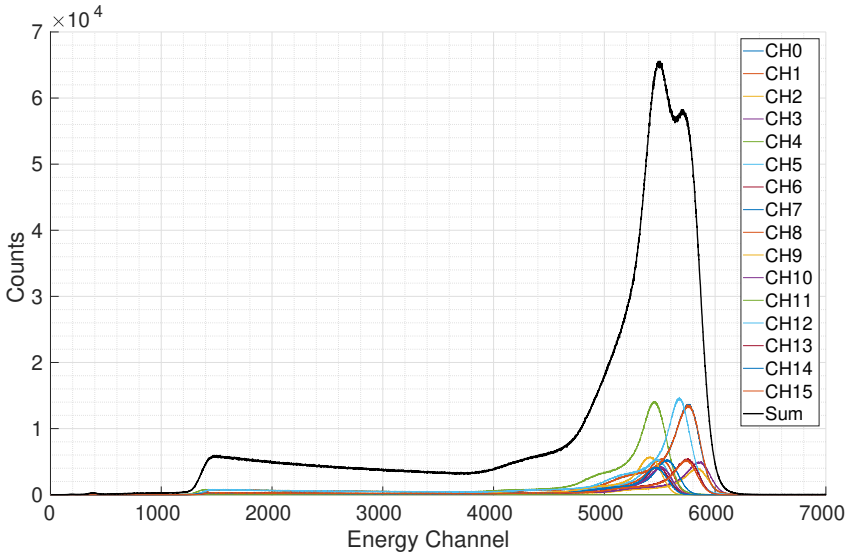

Figure 6.10: Pulse Height Amplitude of the 16 ^{3}He, together with their sum.

6.3 The fissile target

The target used in the ALDEN experiment was a miniaturized flat fission chamber detector filled with 12 bar of pure Argon (CFP12 n. 2328). It has been designed and produced at the *Laboratory of Dosimetry, Sensors, and Instrumentation* of CEA Cadarache. A detailed scheme and a picture of the real fission chamber can be found in Fig. 6.11. It was, at the same time, a detector and a target since it contained the fissile

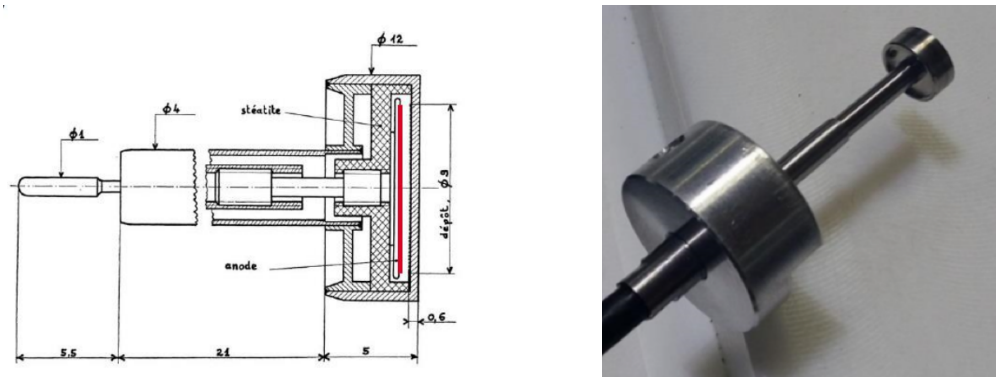

(a) Detailed fission chamber scheme.

(b) Picture of the fission chamber.

Figure 6.11: CFP12 n. 2328, produced at the Laboratory of Dosimetry, Sensors, and Instrumentation at CEA.

material under investigation. The fissile deposit has been put in place on a titanium support by electrodeposition, over a surface of 8 mm in diameter. The rest of the fission chamber was also made of titanium. A coaxial cable with a special connector made the link to the CFP12 through a pin situated at the back of the chamber and which was inserted in the connector itself. The cable fed the chamber with the voltage and got back the signals caused by the fission events. The amount of fissile material has been determined in such a way not to exceed 10 kHz on each of the ^{3}He tubes during the irradiation phase, under the assumption of an equivalent 25 meV neutron flux of $4 \cdot 10^8$

$cm^{-2}s^{-1}$. The limit aimed at preserving the integrity of the detectors and avoiding dead time effects. All the simulations have been performed taking into account the irradiation phase. The amount of fissile material needed to limit the counting rate in the inner tubes to 10 kHz was 210 μg of ^{235}U and 140 μg of ^{239}Pu, as shown in Tab. 6.2 Three targets have been produced in 2018: ^{235}U, ^{239}Pu and a dummy chamber without deposit for the background estimation. Before the experiment, the CFP12 has been tested under an X-ray flux, giving a correct signal.

Table 6.2: Features of the two fission chambers produced in 2019 for the ALDEN experiment, and expected counting rates.

Characteristic	^{235}U	^{239}Pu
Mass [μg]	210	140
Maximum fission rate [kHz]	124	104
Maximum neutron emission rate [kHz]	301	299
Counting rate in one of the inner tubes during the irradiation phase [kHz]	10	9.9
Counting rate in the whole detector during the irradiation phase [kHz]	63.6	63.2

6.4 The fast-shutter

ILL provided a system to shut the neutron beam down. Unfortunately, the original mechanism was too slow for ALDEN's purposes. A new beam shutter, compact and light in order to limit the moment of inertia of the neutronic screens, has therefore been designed by the CEA. It consisted of a turning brushless motor supporting an aluminum plate on which 2 neutronic screens were placed (see Fig. 6.12a). The size, the thickness, and the absorbing materials have been chosen in such a way to reduce the fission rate in the target by a factor of 10^8 when closed. The screens were made of a 2 mm-layer of B4C followed by 1 mm-layer of Cd (see Fig. 6.12b). The B4C was a square of 5 cm of side. The two absorbing layers have been designed to minimize the energetic gamma resulting from an eventual screen entirely made of Cd. At the same time, they guaranteed a better absorption than a screen entirely made of B4C.

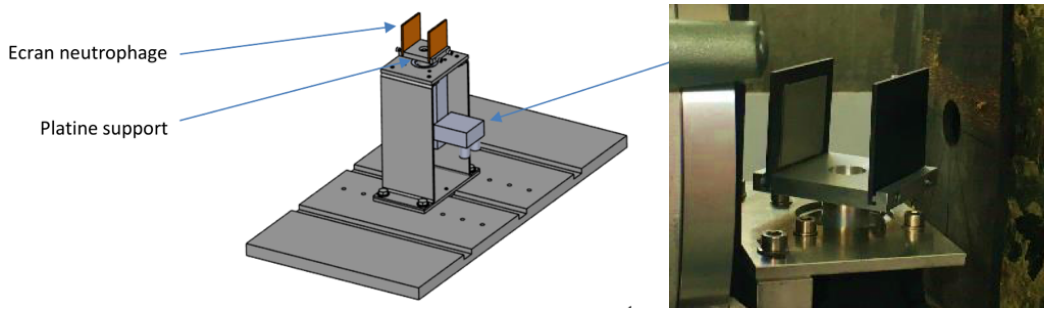

(a) Fast shutter scheme. (b) Fast shutter picture.

Figure 6.12: Fast shutter designed at CEA Cadarache.

Figure 6.13 shows the working principle of the system. In the first row the beam is closed, while in the second one the beam is open. The complete opening (steps 4 to 5) and shut down (steps 8 to 1) occurred in 10 degrees. The system could also be used to adjust the intensity of the neutron flux.

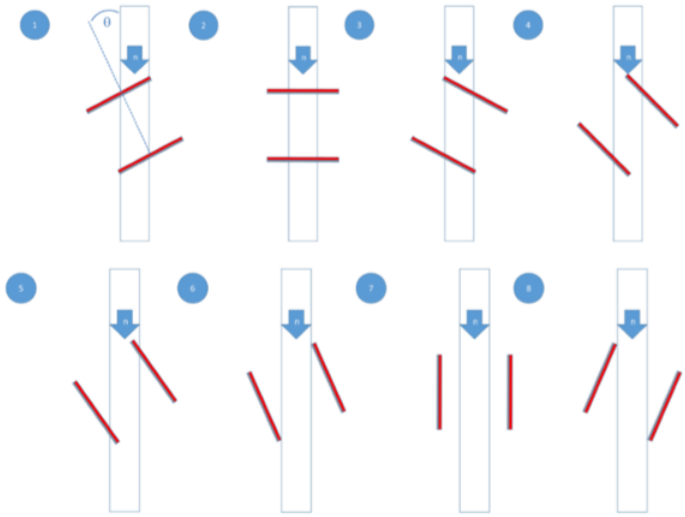

Figure 6.13: Opening and closing steps of the fast shutter.

The speed of the fast-shutter has been estimated through a video with a quality of 239 frames per second, one of which is shown in Fig. 6.14. The screens were replaced by an aluminum foil. From the analysis, it has been estimated that the closing time of the beam would not overcome 4.2 ms. The reference angle was 28° with respect to the incident neutron beam. To reach the highest speed, the optimal rotation appeared to be from -140° to +140° around the reference angle.

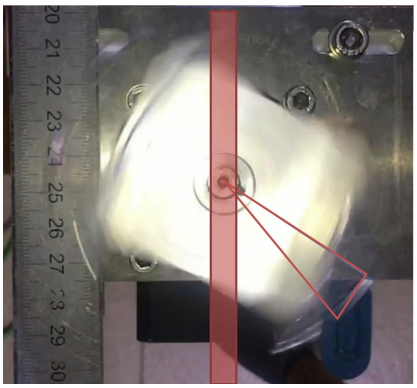

Figure 6.14: One of the frames used for the estimation of the fast-shutter speed.

6.5 Acquisition System and Pulse Processing

6.5.1 Traditional analog chain

The NIM[2] is a standard system used particularly in nuclear physics experiments. It is built in such a way that each function is performed by a module having the same dimensions and specifics. Each module is inserted in a single *rack* (see Fig. 6.15a) for power supply. Detectors give information in the form of electrical signals. Those signals are generally very weak and need to be amplified without losing the original information. For that reason, the detector is usually followed by the *charge-sensitive preamplifier*, which must be placed close to the detector in order to reduce losses (see Fig. 6.15b). The latter is an electronic device able to integrate a current signal and to provide a

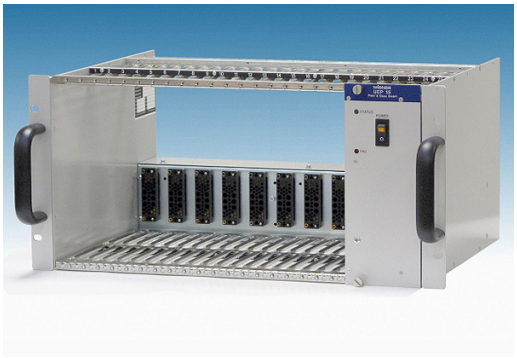

(a) Rack NIM, taken from [5].

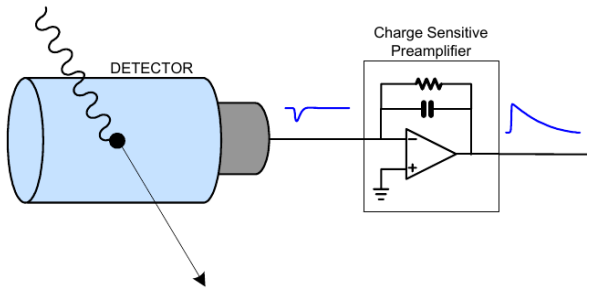

(b) Signal transformation from the detector to the preamplifier, taken from [9].

Figure 6.15: Elements of the acquisition system.

potential difference signal with the amplitude proportional to the input charge. The pulse rise time of the output signal is defined as the interval between the time at which the signal reaches 10% of its final amplitude and the time it reaches 90% of it [46]. It is also called leading edge and it represents the time over which the charge deposited in the detector is integrated across the capacitance of the collection circuit [46]. The decay time depends instead on the time constant of the collection circuit. In good preamplifiers the decay constant of the outgoing impulsion (20 μs - 10 ms) is much larger than the rising constant, so to ensure the complete charge collection. For that reason, such pulses are sometimes called *tail pulses*. For high counting rates, impulsions might pile-up if the preamplifier saturation level is reached. Another function of the preamplifier is to supply the detectors with the voltage. After the preamplifier, there is, in general, a *shaping amplifier*, whose functions consist in amplifying and filtering the signal from the noise. It can be analog or digital. The filter shapes to the tail pulse coming from the preamplifier, reducing its width and increasing its amplitude [46]. The shaped analog pulses need then to be converted into logic pulses. This is the role of the *discriminator*, which can be *integral* or *differential*. The integral discriminator is a module which checks if the pulse amplitude overcomes a certain threshold (*discrimination level* or *pulse height bias level* of the counting system) or not and converts the signal from analogic to digital. Unfortunately, this technique is not suitable for most physics applications because of the baseline fluctuation, pulse pile-up, noise, etc... The differential discriminator (also called Single-Channel Analyzer) is a module which processes the pulse only if its amplitude lies

[2] *Nuclear Instrument Module.*

between two levels. The digital filters are able to reject the noise, cancel the baseline and to do shape and timing analysis for this purpose. After the shaping amplifier, there can also be a *Multichannel Analyzer* (Peak Sensing ADC) for the PHA acquisition mode. Figure 6.16 shows the main transformations a signal undergoes in an typical analog chain.

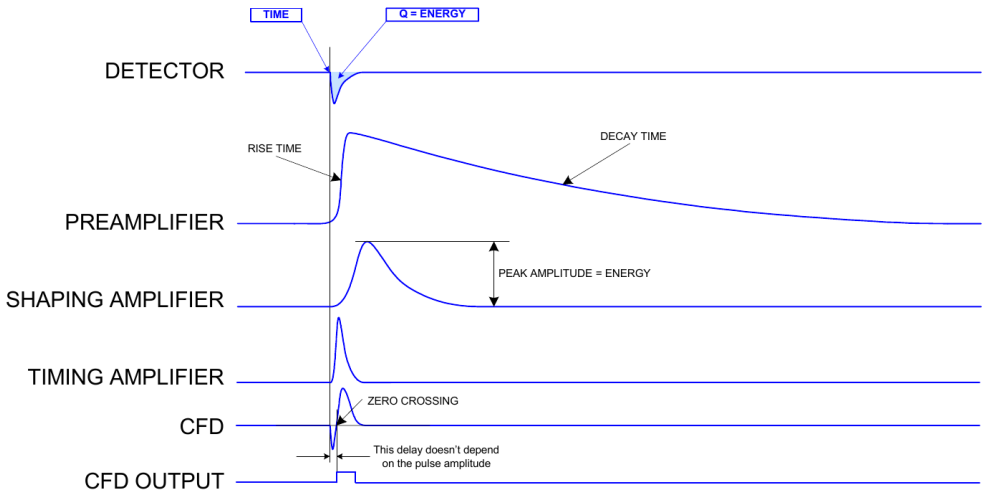

Figure 6.16: Signal transformation in the analog chain, taken from [9].

6.5.2 Caen DPP firmware

Caen developed a new approach: the DPP (*Digital Pulse Processing*) [9]. The aim of the DPP is to implement a digital version of the analog chain made of shaping amplifier and peak sensing ADC. The DPP is implemented in the Model V1724 (14 bit, 100MS/s), used as a digitizer in the ALDEN experiment (see Fig. 6.17).

Figure 6.17: CAEN V1724 digitizer, taken from [1].

The block diagram of the DPP is shown in Fig. 6.18. The output of the charge sensitive preamplifier is directly connected to the input of the digitizer. The DPP method allows the determination of the arrival time (if the events are separated by at least 10 ns) as well as the energy of the pulses. It proceeds to the subtraction of the baseline, it stores the events into a memory buffer which is freed, when full, through USB, VME or optical

link. Finally, it also allows detecting pile-up conditions and correcting the loss of counts.

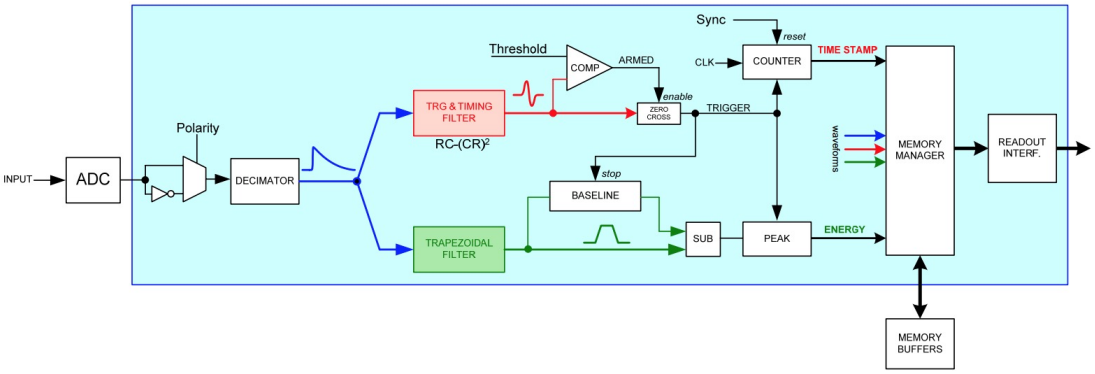

Figure 6.18: Block diagram of the DPP-PHA, taken from [9].

Whenever a pulse is found, the relevant energy (or other quantities) is calculated and written in the memory buffers, thus making a list of energies. As soon as the list reaches a certain size, the data buffer is made available for the readout while the acquisition continues in another buffer without any dead-time. Thanks to the extremely reduced number of data to save and transfer, this mode is normally able to sustain a continuous acquisition, even in the case where the pulse rate is very high (up to 1 Mcps!) [9]. Figure 6.19 shows how the DPP determines time and energy of a pulse.

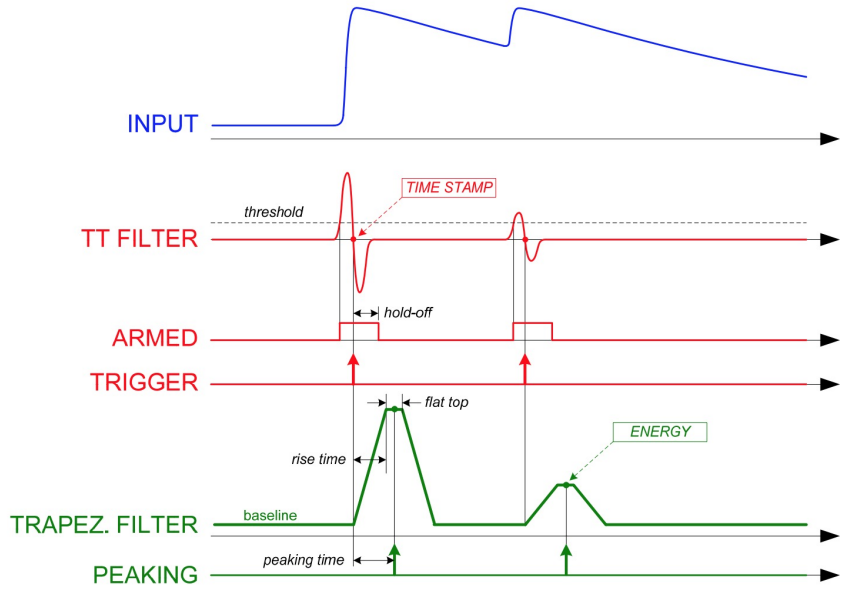

Figure 6.19: DPP filters, taken from [67] The TT filter transforms the tail pulse into a bipolar pulse. When the latter crosses the zero, the time stamp is registered and the trigger is sent to the TF, which starts the trapezoidal shaping of the pulse.

The signal passes through two filters:

- *Trigger and Timing Filter (TTF)*, which identifies pulses and determines the time stamps (arrival time of the event) and triggers for the trapezoid filter. There are

many types of TTFs. CAEN has developed RC-$(CR)^N$ filters able to reject the high frequency noise (RC filter = mean filter), restore the baseline and cancel the low frequency fluctuations (CR^N filter = derivative) and transform the unipolar pulses into bipolar signals whose zero crossing can be used for the determination of the time stamp (see Fig. 6.20) [9]. This makes the timing information independent of the pulse amplitude. This method allows the identification of the pulses even in pile-up conditions.

- *Trapezoid Filter (TF)*, which shapes the tail pulse into a trapezoid, restores the baseline and computes the pulse height spectrum. The TF transforms the typical exponential decay signal generated by a charge sensitive preamplifier into a trapezoid that presents a flat top whose height is proportional to the amplitude of the input pulse and therefore to the energy released by the particle in the detector. This trapezoid plays more or less the same role as the shaping amplifier in a traditional analog acquisition system. The rise/fall time of the trapezoid corresponds to the shaping time (see Fig. 6.20): higher rise times result in better resolution but also in a higher probability of pile-up (dead time). The baseline is calculated by averaging a programmable number of samples before the start of the trapezoid. Flat top duration, peaking time (position of the peak in the flat top) and peaking averaging are also programmable for an optimum ballistic deficit correction [9].

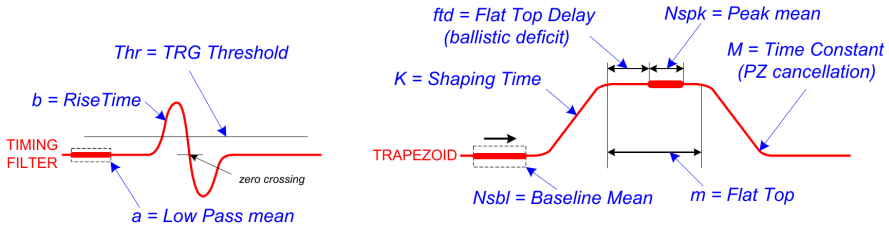

Figure 6.20: Details of the DPP filters, taken from [67].

The Memory Manager combines time stamp, energy, and channel and builds the events in list mode. The pile-up is treated in the following way (see Fig. 6.21 for a scheme):

- *case 1: the second trapezoid starts on the falling edge of the first one.* Both the energy and the time of the two events are well coded
- *case 2: the second trapezoid starts on the rising edge or on the flat top of the first one.* The energy of the two pulses cannot be determined, but the second derivative of the input signal allows the accurate determination of the two time stamps
- *case 3: the two pulses pile up on their rising edge.* The TT-Filter is not able to distinguish the two signals. Only one trigger is created and one event recorded. The energy of the final pulse is the sum of energies of the two pulses. It will produce peaks at twice, three times, four times ... the energy of the main energy peak.

6.5.3 Acquisition system in the ALDEN experiment

The scheme of the acquisition system used in the ALDEN experiment is shown in Fig. 6.22. The 16 ^{3}He-tubes were connected to a preamplifier box (32 channels fed at the same voltage of 2100 V, shown in Fig. 6.23a). Four cables RJ45 went from the preamplifier into a converter RJ45-Lemo before going, through 16 Lemo-cables, into the

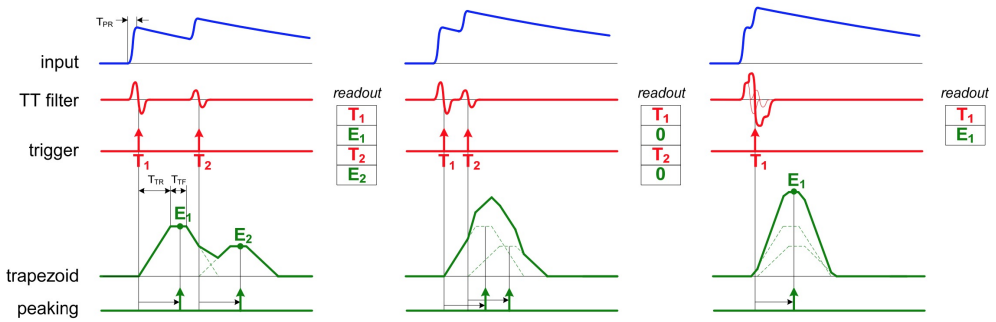

Figure 6.21: Pile-up treatment in the DPP, taken from [67].

2 digitizers Caen 1724 in the rack 6U-VME64 (Fig. 6.23b). The signal was transformed from analog to digital form in the digitizer and transferred to the PC through a USB cable.

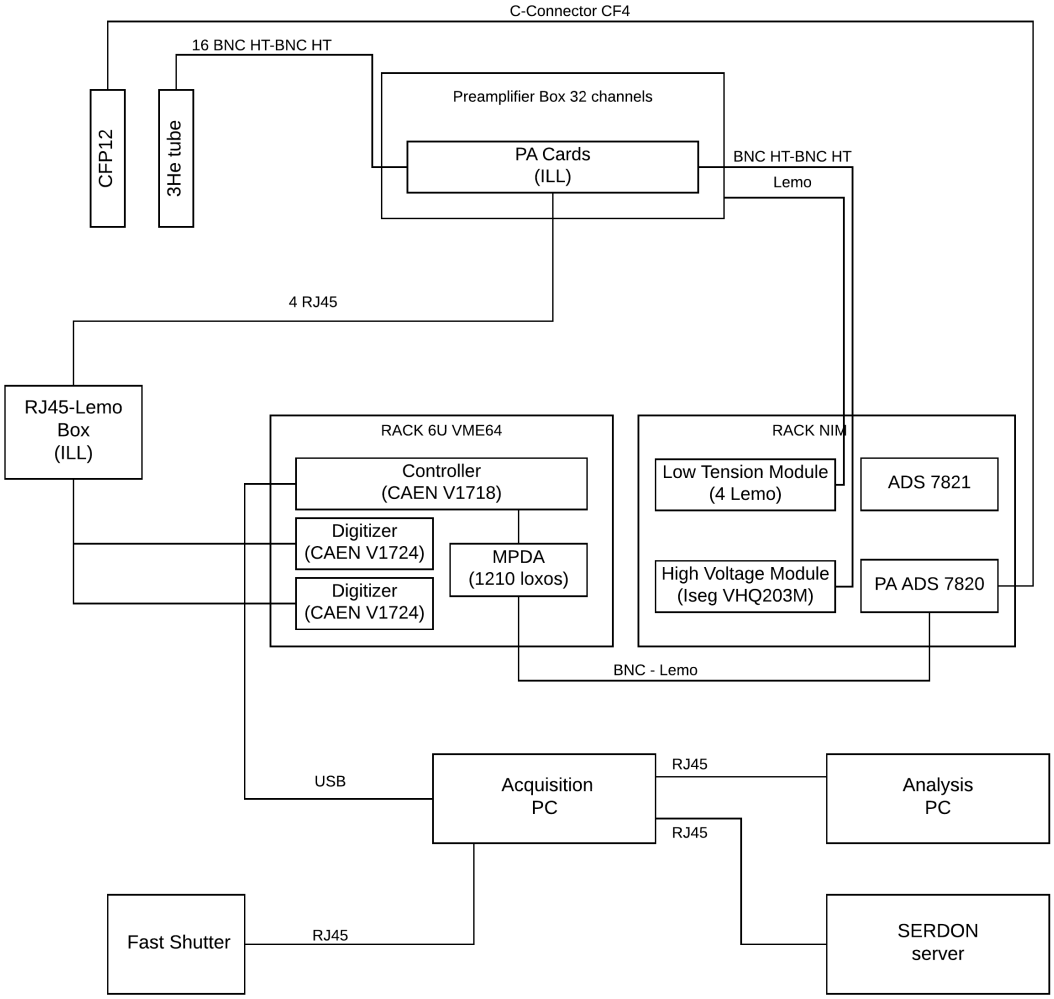

Figure 6.22: Acquisition system scheme.

The fission chamber CFP12 was directly connected to a preamplifier on the RACK

NIM (PA ADS 7820), which brought the signal to the digitizer MPDA on the Rack 6U-VME64. Then, a USB cable transferred the signal to the acquisition laptop (PC ALDEN) through the controller. The program used to access the memory of the digitizer and to

(a) LOENIE-V1 and the preamplifier box with 32 channels.

(b) Acquisition system and converter RJ45-Lemo.

Figure 6.23: Pictures of the acquisition system.

transfer the data on the disk has been provided by ILL and it is called *Nomad*. Through Nomad interface it was possible to set a certain number of parameters which defined the way the signals would be processed by the digitizer. Particular attention had to be put on the choice of the trigger threshold, which set the minimum amplitude a pulse should have to be treated as a neutron signal. Table 6.3 reports the parameters used for the ALDEN experimental campaign in 2018.

Table 6.3: Nomad parameters common to all experiments.

Common Parameter	Detectors	CFP12
DC offset [LSB]	40	?
Pre Trigger	0.3	300
Trigger Smoothing	32	32
Trigger Hold Off	1	1
Trigger Window Size [μ]	0.3	?
Trigger Threshold [LSB]	350	350
Decay Time [μs]	1.65	160
Trapezoidal Rise Time [μs]	2	2
Trapezoidal Flat Top [μs]	1.5	1.5
Flat Top [μs]	1.2	1.5
Peak Mean	1	4
Baseline Mean	3	1024
Base Hold Off [μs]	1	1
Peak Hold Off [μs]	1	1
Gain	4	1

6.6 Description of the first experimental campaign

For the ALDEN experiment, several campaigns have been carried out, as listed in Tab. 6.4. The most important one took place at ILL in September 2018.

Table 6.4: List of the experimental campaigns.

Place	Date	Type	Objective
ILL	09/18	Reactor	DN activity
ILL	09/18	Reactor	Background
ILL	09/18	Reactor	Dead-Time
NPL	01/19	Sources	Absolute Efficiency
AMANDE	03/19	Accelerator	Relative Efficiency
Cadarache	03/19	Pulser	Dead-time and pile-up

It consisted in the cyclic irradiation of a fissile sample, followed by the decay of the fission products. Some information about the performed cycles is listed in Tab. 6.5.

Table 6.5: Long cycles.

Name	Type	Wait	Nb. runs
Cycle 1	50-350	No	168
Cycle 3	50-450	Yes	86
Bdf-Cycle 1	50-350	Yes	9

In the table, *Cycles* are the experiments performed using the ^{235}U fission chamber, while *Bdf-Cycles* are the identical experiments performed with the dummy chamber, for the background estimation. The *type* is the duration of the irradiation and the decay phase. So, for example, type 50-350 means that 50 s of irradiation have been followed by 350 s of decay. The *wait* was an option that had been added after realizing that Nomad needed a certain initialization time before being ready to count. Before adding this waiting time of 1 s, at the beginning of the run, the fast shutter opened the neutron beam but Nomad needed about 200 ms to initialize before starting the counting. This means that in the cycles without the wait, the first hundreds of ms of the neutron activity are lost. Another set of measurements has been done for the dead-time and pile-up estimation, as explained in Section 7.2. It consisted of a series of irradiations at different neutron flux levels with the aim of exploiting the ring ratio for the dead-time estimation and correction. As far as the efficiency is concerned, two campaigns have been performed: at NPL[3] in England with well-characterized neutron sources for the absolute efficiency estimation; and at IRSN[4] AMANDE accelerator for the relative efficiency estimation. Finally, a test with a pulser was needed to better understand the behavior of the acquisition system with respect to dead-time and pile-up.

[3] *Nuclear Physics Laboratory.*
[4] *Institut de Radioprotection et de Sûreté Nucléaire.*

Chapter 7

Data regression analysis

> Science is bound, by the everlasting vow of honour, to face fearlessly every problem which can be fairly presented to it.
>
> Lord Kelvin

Contents

7.1 From a binary file to a proper decay curve 122
7.1.1 Nomad output files 122
7.1.2 Analysis types 122
7.1.3 Energy Range Of Interest 123
7.1.4 Reference Bin 124
7.1.5 C++ Procedure 125
7.1.6 Average background estimation 125
7.1.7 Optimizing the mesh 126
7.2 Loss of counts correction 126
7.2.1 Detector dead time in proportional counters 127
7.2.2 Estimation of the electronic dead time with the distribution of arrival times 128
7.2.3 Loss of counts estimation with a pulser 129
7.2.4 Check on the quality of the correction: ring ratio test 131
7.3 Absolute efficiency calibration at NPL 133
7.4 Irradiation duration 135
7.5 Analysis of the decay curve 136
7.5.1 F from the spectroscopy of the fission chamber and of a dosimeter 137
7.5.2 F from the fission chamber signal 138
7.5.3 F from the irradiation phase 139
7.5.4 From F to ν_d 140
7.5.5 Adopted procedure 141
7.6 Results from the ALDEN experiment 142

The objective of this chapter is to describe the procedure that has been used for the regression analysis. Section 7.1 includes all the steps from the binary output files generated by the acquisition system, to the final curve to be fitted. Section 7.2 follows with the estimation and the correction of the dead time of the detection system. Section 7.3 describes the absolute efficiency calibration, that took place at NPL, in England. The estimation of the irradiation duration is detailed in Section 7.4 while the method used to exploit the decay curve is described in Section 7.5. To conclude, Section 7.6 reports all the results of this first experimental campaign.

7.1 From a binary file to a proper decay curve

7.1.1 Nomad output files

At the end of the experimental campaign, we left Grenoble with 150 GB of binary files containing, for each event, the following information: arrival time, energy channel and detector in which the event has been detected. The time was coded with a precision of 10 ns. During the acquisition, apart from the list mode, an ASCII file was generated, with a time-histogram associated to the fission chamber. A C++ code (*Alproc*) has been written to translate the binary file into a 3 columns ASCII file (time, energy, channel) and to correct a bug in Nomad which periodically coded one event at a wrong arrival time.

7.1.2 Analysis types

For the data regression analysis, a solver has been written in C++ (*Alden*) by the author to sort the data in well-defined classes and to produce a clean decay curve. The user is free to decide what cycle to treat, which runs to use, the ROI (*Range Of Interest*) and the analysis he wants to perform. Four options are possible:

- **MCS**: the user chooses the ROI (see Subsection 7.1.3) and the time-bin of the MCS (*Multi-Channel Scaling*), which is a histogram in time. The MCS is produced for all the channels (channel = one ^{3}He counter) of all the selected runs. The user can decide to print only the average of all the considered runs or to have the results of each run and each channel separately. Before averaging the runs, the user can decide to shift them according to their *reference bin* (see Subsection 7.1.4), which corresponds to the end of the irradiation phase. The MCS can also be corrected for a user-defined non-paralyzable dead-time if the option is selected. The user can also print the counting rate, rather than the MCS.

- **PHA**: the events are analyzed one by one and sorted, according to their energy, into a *Pulse Height Amplitude* (from energy channel 0 to 32768). The user can also choose three sections of time he wants the PHA of. So, for example, in the case of an irradiation followed by a decay phase, one could cut the time in three parts and have the PHA during the irradiation phase, during the first seconds of decay and during the rest of the decay. Obviously, it is the user who decides the time limits of these three regions. An example is shown in Fig. 7.1.

- **POISSON**: it produces the arrival-time distribution of the events, which is supposed to be an exponential for Poissonian-distributed events. This distribution is

a histogram of the difference of the arrival times of two consecutive events. Under a certain time difference, no more counts are present due to the intrinsic dead-time of the acquisition system

- **CFP12**: it computes the MCS of the fission chamber.

The last three options are needed to evaluate the quality of the experiment and to make decisions about the setting parameters for the MCS. In particular, the ROI is deduced from the PHA while the dead-time could be deduced with the POISSON option. The MCS is the main tool to produce a clean decay curve.

7.1.3 Energy Range Of Interest

The choice of the energy range of interest (ROI) took several months and hundreds of tests. Figure 7.1 shows the integral PHA corresponding to the irradiation (0-50 s), to the first seconds of decay (50-60 s) and the rest of the decay phase (50-250 s) of 168 runs of Cycle 1. The PHA of the different runs has been averaged.

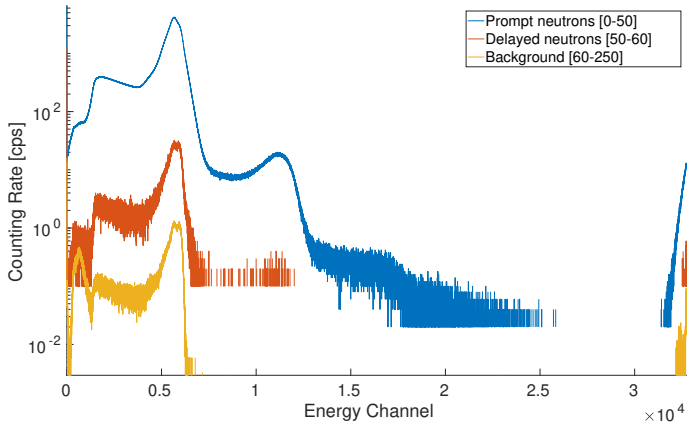

Figure 7.1: Pulse Height Amplitude of one of the four inner counters. The three spectra are shown, corresponding to irradiation, decay, and background phases.

In Section 5.2 the PHA of a typical ^{3}He detector is shown. It is easy to distinguish the neutron signal from the low-energy noise. After several tests, the most appropriate ROI seemed to be 1100-28000. The lower limit is in the neutron valley and therefore the global counting should be insensitive to any small variation of this limit. The upper limit has been set to 28000 to avoid taking the rising edge at high energies, which in reality are low-energy counts badly coded. What happens during the pulse processing is that the energy is coded in unsigned integer in 15 bit (the 16^{th} bit is a flag) and if the *DC offset* is too low, then the energy results to be negative and will be coded as a very large integer. This is why it will appear in the upper part of the spectrum, even though it should be in the lower region. As far as the low-energy peak below the neutron signal is concerned, it is not clear yet if it is due to gamma, noise or other. Further tests will be needed to identify the origin of the peak.

7.1.4 Reference Bin

The reference bin of an MCS is the index of the last point of the irradiation phase. The runs are not synchronized, due to the variable initialization time of Nomad before any acquisition, and need to be shifted in time for them to have the same end of irradiation before being summed. The reference bin is automatically found by the Alden program through an iterative process in 3 steps, graphically shown in Fig. 7.2.

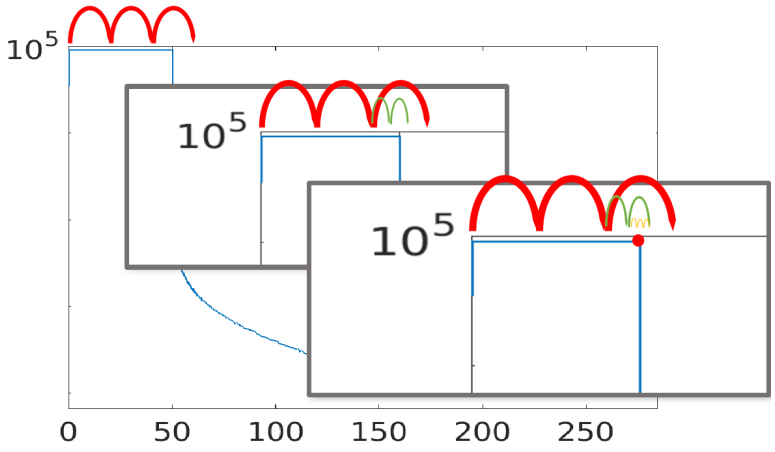

Figure 7.2: Iterative procedure to find the index corresponding to the end of the irradiation.

The procedure starts fitting the first hundreds of points of the irradiation plateau through a linear LSF (*Least Square Fit*). Then, 10 s (meaning 1000 points) are added to the vector and a new fit is performed. The χ^2 of the two fits are compared and if their difference is below a certain threshold, then the procedure continues and another step of 10 s is done. Of course, when the 10 s increment falls into the decay phase, the quality of the fit (described by the χ^2) is strongly reduced and the program exits from the loop and goes one step behind. The first step is made of coarse increments of the vector to be fitted. The second step is characterized by a medium increment (1 s) and the third step by a fine one (10 ms). The LSF procedure has been taken from *Leo* [48] and performed as follows. If $y = f(x; a1, a2, ...a_m)$ is the function to be fitted, a_j are m unknown parameters to be determined while x_i are the n points at which y_i has been measured with an error σ_i. If $n > m$ the least square method states that the best values of a_j are those for which the sum of the squared deviation of the points from the curve $f(x_i)$ weighted by the respective errors on y_i

$$S = \sum_{i=1}^{n} \left[\frac{y_i - f(x_i; a_j)}{\sigma_i} \right]^2 \tag{7.1}$$

is a minimum. If the prior distribution $f(x_i)$ is normally distributed with variance σ_i, the method is also called chi-squared minimization. The problem's solution is found by solving the system of equations

$$\frac{\partial S}{\partial a_j} = 0. \tag{7.2}$$

In the case of a linear fit ($y = f(x) = ax + b$), Eq. 7.1 becomes

$$S = \sum_{i=1}^{n} \left(\frac{y_i - ax_i - b}{\sigma_i} \right)^2 \tag{7.3}$$

and the partial derivatives with respect to the parameters a and b are

$$\begin{cases} \dfrac{\partial S}{\partial a} = -2 \displaystyle\sum_{i=1}^{n} \dfrac{(y_i - ax_i - b)x_i}{\sigma_i^2} = 0 \\ \dfrac{\partial S}{\partial b} = -2 \displaystyle\sum_{i=1}^{n} \dfrac{(y_i - ax_i - b)}{\sigma_i^2} = 0 \end{cases} \tag{7.4}$$

The system 7.4 can be written as

$$\begin{cases} 2\left(-E + aD + bA\right) = 0 \\ 2\left(-C + aA + bB\right) = 0 \end{cases} \tag{7.5}$$

where

$$\begin{aligned} A &= \sum_{i=1}^{n} \frac{x_i}{\sigma_i^2} \qquad B = \sum_{i=1}^{n} \frac{1}{\sigma_i^2} \qquad C = \sum_{i=1}^{n} \frac{y_i}{\sigma_i^2} \\ D &= \sum_{i=1}^{n} \frac{x_i^2}{\sigma_i^2} \qquad E = \sum_{i=1}^{n} \frac{x_i y_i}{\sigma_i^2} \qquad F = \sum_{i=1}^{n} \frac{y_i^2}{\sigma_i^2} \end{aligned} \tag{7.6}$$

whose solutions are

$$a = \frac{EB - CA}{DB - A^2} \qquad b = \frac{DC - EA}{DB - A^2} \tag{7.7}$$

7.1.5 C++ Procedure

As mentioned before, for each acquisition Nomad produced a binary file in list mode. The procedure used to derive a clean decay curve consisted in employing the PHA option of the Alden solver to determine the ROI. Then, the MCS option could be used to select the energies of interest and to produce one MCS per run and per channel. The dead time correction takes place at this moment. After that, the 16 channels are summed up together, giving birth to a single MCS per run. Adding the option *shift and sum*, the Alden solver firstly finds the reference point of each run and then uses it to shift the curves with respect to the end of the irradiation. Finally, it sums all the runs up and computes an average MCS with associated uncertainty, as shown in Eq. 7.8 and 7.9

$$\overline{MCS} = \frac{1}{runs} \sum_{i=1}^{runs} MCS_i \tag{7.8}$$

$$\sigma_{\overline{MCS}} = \frac{\sigma_{MCS_i}}{\sqrt{runs}} = \sqrt{\frac{\overline{MCS}}{runs}}. \tag{7.9}$$

7.1.6 Average background estimation

For the background estimation, a specific experiment has been performed using the dummy fission chamber. The procedure to obtain the average MCS for the background measurement was the same as for the other cycles. On the other hand, since the background had no dependence in time, it seemed logical to describe it through two average values: one for the irradiation phase and one for the decay phase

$$\overline{b_x} = \frac{1}{n}\sum_{i=1}^{n} b_x(t) \tag{7.10}$$

$$\sigma_{\overline{b_x}} = \frac{\sigma_{b_x}}{\sqrt{n}} = \sqrt{\frac{\overline{b_x}}{n}}, \tag{7.11}$$

where x corresponds either to the irradiation or to the decay phase, σ_{b_x} is the dispersion of the points and $\sigma_{\overline{b_x}}$ is the uncertainty in the average background rate.

7.1.7 Optimizing the mesh

To avoid large fluctuations and improve the quality of the fit, the mesh of the curve has been optimized. The first instants of decay, important for the estimation of the short-lived group's abundance, were characterized by a mesh of 10 ms. With time, the mesh became coarser, until reaching 1 s for the last hundreds of seconds. Figure 7.3 shows one decay curve before and after the optimization of the mesh. Obviously, the uncertainty has been recomputed for each bin, in order to take into account the averaged points.

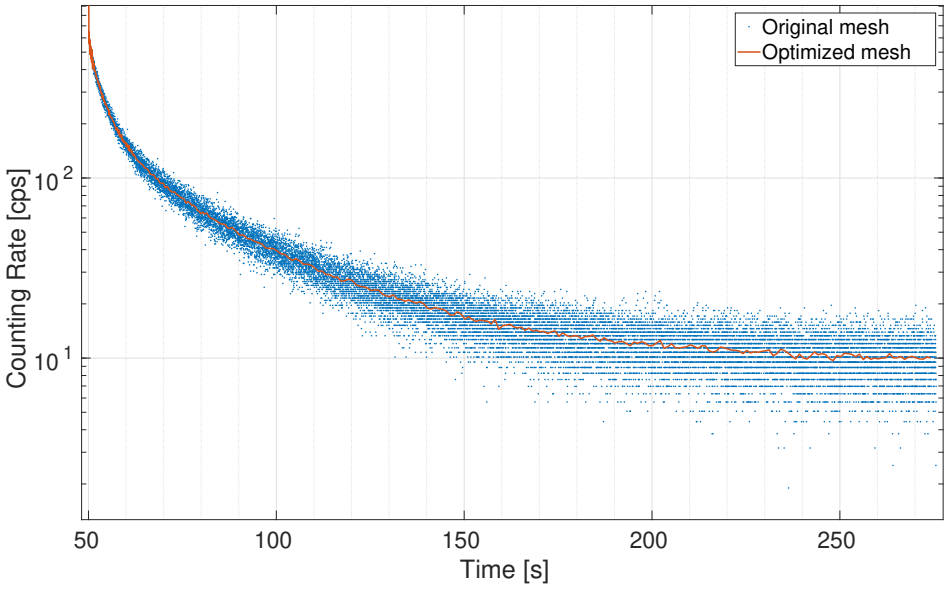

Figure 7.3: Decay curve in the original and in the optimized mesh.

7.2 Loss of counts correction

A very important characteristic of a detector is the minimum amount of time that must separate two events for the detector to record them as separate [58]. There is, indeed, a defined period of time after the triggering of an event during which a second event cannot be accepted [48]. The limiting time could be due to the recovery time of the detector itself or to the associated electronics. By definition, the *dead time* is the finite time required by a detector to process an event [48]. The loss of counts can be corrected if both the nature and the effects of the dead time are known. As mentioned in Section 6.5, counts can be lost also due to the *pile-up* phenomenon. The main difference between dead time and pile-up is the reason behind the loss of counts. The dead time causes the

loss of the events following the one that triggered the system, due to the fact that the system is insensitive during this time. On the other hand, in the pile-up case, the system sees these events but cannot properly process them. As a consequence, either the energy is not recognized (the events are assigned to the energy channel zero) or the multiple events are recognized as a single one of multiple energy. It is worth stressing that while deadtime only provokes a loss of counts, pile-up also causes the energy degradation of the detector response.

7.2.1 Detector dead time in proportional counters

Dead time can be affected by geometry, material, and design of the detector as well as applied voltage, temperature, and pressure [58]. As explained in Section 5.2, the passage of radiation ionizes the gas. The electron-ion pairs are then accelerated by the radial electric field created by the applied voltage. The accelerated electrons ionize the gas themselves, creating the avalanches (or cascades). In proportional counters, the ion pair production is proportional to the energy deposited in the gas. If other events arrive within the charge collection time of a first event, they will pile-up to the first one, giving birth to a pulse with higher energy. On the other hand, if the first event has been properly detected and the second one takes place before the electric field is completely established, then the second event will be considered to have a reduced amplitude. When dealing with dead time, the whole detection system must be considered. Indeed, the time needed by the electronics to treat the signal is much larger than the intrinsic dead time of a proportional counter. Researchers have tried in many ways to model this phenomenon. The main assumption behind the most famous models is that the particles hitting the detector follow a Poisson distribution. Feller and Evans developed two types of idealized models [58]: nonparalyzable and paralyzable, respectively. The behavior of the two models as a function of the real counting rate is shown in Fig. 7.4.

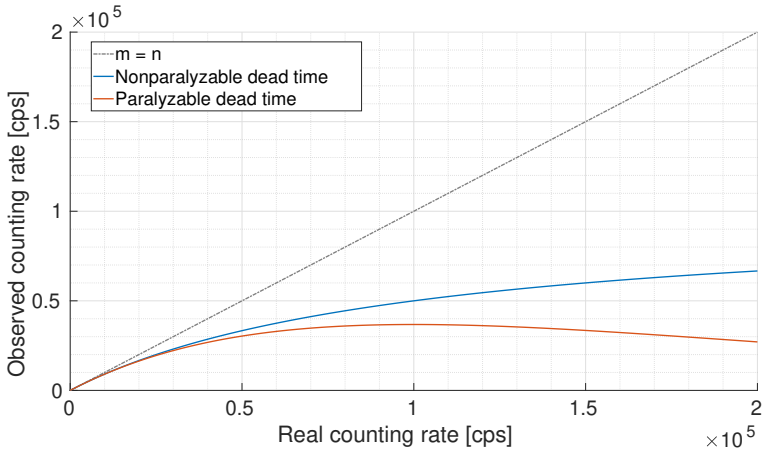

Figure 7.4: Idealized dead time models for a τ of 10 μs.

When a detector is affected by nonparalyzable dead time, it is insensitive to the particles arriving during the recovering time due to a previous event. So to say, when a particle arrives, the detection system needs a defined time τ to process the signal and during this time interval, it cannot consider other events. The system is *dead* for a fixed time τ after each recorded particle [58]. If m is the observed counting rate, the nonparalyzable

dead time model says that the real counting rate n is given by

$$n = \frac{m}{1 - m\tau} \tag{7.12}$$

When a detector is affected by paralyzable dead time, the detector remains sensitive to the pulses following the one that triggered the system. In this case, before a second event can be counted, a time τ needs to elapse. If the second event arrives during the resolving time of the first event, such time is extended by a τ. So to say, the system is dead until a time τ has passed without any detection. In that case, the observed counting rate is given by

$$m = ne^{-n\tau} \tag{7.13}$$

The two models are equivalent for low counting rates. In real life, detection systems are affected by a mix of the two behaviors, which led researchers to develop hybrid deadtime models. For more information, see the extensive review of Usman and Patil [58].

7.2.2 Estimation of the electronic dead time with the distribution of arrival times

Radioactive decay is a Poissonian process. For a process following the Poisson distribution, the probability of adjacent pulses having a separation between t and $t + \mathrm{d}t$ is given by Eq. 7.14 and is shown in Fig. 7.5.

$$q_1(t)\mathrm{d}t = \lambda e^{-\lambda t}\mathrm{d}t \tag{7.14}$$

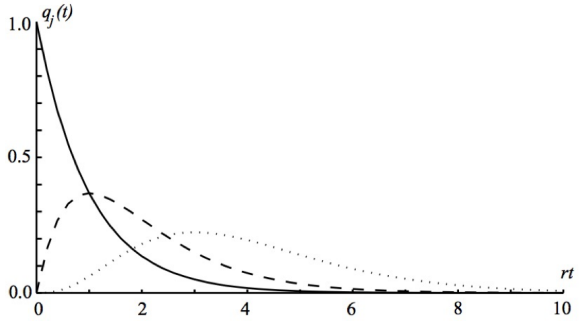

Figure 7.5: Distribution of arrival times for a Poissonian process, taken from [48].

In the presence of dead time or pile-up, the events separated by less than τ seconds cannot be recorded. That is to say that the distribution of arrival time of the events will be truncated at a time corresponding to the limits of the acquisition system. Figure 7.6 shows the real distribution in one of the inner tubes during the irradiation phase of the ALDEN experiment. From the plot, it is evident that there are no events separated by less than 1 μs. From the study of the DPP processing we know that these events are the ones for which the time filter could not identify the two events as separate and fall into the pile-up case. At the same time, it is clear that events separated by less than about 6 μs do not follow the Poissonian distribution. All the events constituting the weird peak are stored in the channel zero. For that reason, it has been decided not to take into account such channel and to correct for it with a pulser. The second ALDEN campaign showed that such effect was due to the choice of an unsuitable low threshold.

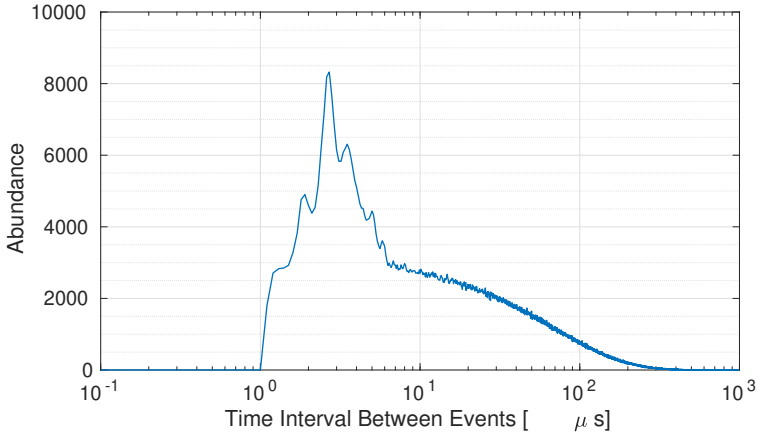

Figure 7.6: Distribution of arrival time in one of the inner tubes.

7.2.3 Loss of counts estimation with a pulser

The pulser is a digital detector emulator. The model used for the test, the CAEN DT5800D allowed choosing the signal shape (rise time and decay time), the amplitude (which is linked to the energy) and the pulse distribution (constant or Poissonian). The typical rise time and decay time of a neutron signal are about 0.2 and 1.6 μs, respectively. The pulser test consisted in increasing the frequency of the Poissonian-distributed signals sent to the acquisition system. The amplitude has been kept constant, at 1 V. The objective was to check the response of the acquisition system, in time and energy, knowing the source signals' characteristics. Table 7.1 shows, for each run, frequency sent by the pulser as well as the response of the acquisition system.

Table 7.1: Pulser test. For each run, the frequency of the pulser is reported, as well as the response of the acquisition system.

Run	Pulser [kHz]	Run	Pulser [kHz]
2794	0.5	2806	3.5
2795	0.6	2807	4.0
2796	0.8	2808	4.5
2798	1.0	2809	5.0
2799	1.2	2810	10.0
2800	1.4	2811	15.0
2801	1.6	2812	20.0
2802	1.8	2813	25.0
2803	2.0	2814	30.0
2804	2.5	2790	80.0
2805	3.0	2815	100.0

The response has been divided into *ROI* (1100-28000) and *CH-0*. *Sum* is the sum of ROI and CH-0. Figure 7.7 shows the PHA of the tests performed with the pulser, meaning a histogram as a function of the energy channel coded by the acquisition system. Since the pulser was set to send monoenergetic pulses, the expected PHA was a single peak centered at the energy channel corresponding to the chosen amplitude. Nevertheless, the distribution of the events coded by the digitizer presented peaks at energies corre-

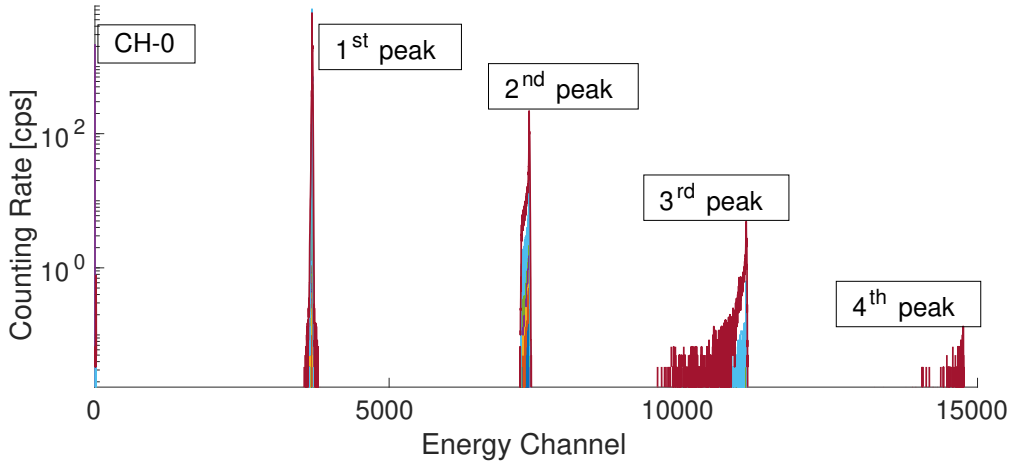

Figure 7.7: Pulser PHA in response to a 1 V signal.

sponding to a multiple of the energy of the main peak. Furthermore, a non-negligible amount of counts fell in channel 0. In Section 6.5, the pulse processing of the digitizer used in the ALDEN experiment is described. From the PHA it is clear that the 1st peak corresponded to the events sufficiently far away from each other in time for the system to properly code time and energy of the two events. When two events arrive almost at the same time and the time filter is not able to distinguish them, it triggers the trapezoidal filter only once and only one trapezoid is created, with an amplitude which depends on how many events have been accumulated. This is the explanation of the several peaks at multiple energies. Channel zero contained the events which were far enough for the time filter to recognize them as being separate but too close for the trapezoidal filter to estimate their energy. Between the two types of pileup, the most difficult to correct was channel zero. In fact, the multiple peaks had no serious effect on the final counting rate, due to the fact that, when choosing an ROI corresponding to the neutron signal, they surely contained neutrons. If two low-energy noise events piled-up in time, the resulting pulse would still have low energy and would probably be cut off by the ROI. If there were one neutron and one gamma, the counting rate would stay the same and the neutron would appear with slightly higher energy. The upper limit of the ROI (28000) was sufficiently high for the neutron-gamma pile-up not to represent a problem since it would be counted as one neutron. If the pile-up contained two neutrons, the resulting small reduction of the counting rate could easily be corrected. On the other hand, channel zero was a problem because the acquisition system completely lost the information about the energy of the events and it became impossible to recognize the neutrons from the noise through the energy discrimination[1]. Furthermore, the proportion of events going into channel zero was not constant and changed from experiment to experiment. Figure 7.8 shows the MCS corresponding to a background measurement with and without considering the channel zero. It is clear that for experiments with a few neutrons, channel zero mostly contained noise, and could not be fully taken into account. For that reason, after many tests, it has been decided not to include the channel zero into the ROI but to correct for it. Figure 7.9 shows, for each frequency of the pulser, the counting rate falling into the channel zero (in blue) or in the rest of the spectrum (in orange).

[1]Remember that pile-up leads to the energy degradation of the detector response, while deadtime does not.

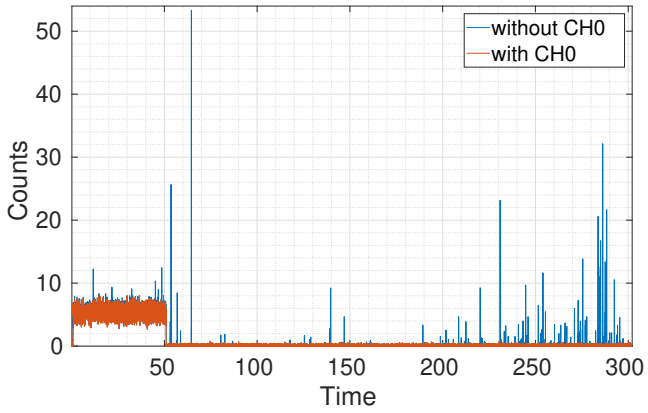

Figure 7.8: Effect of the channel 0 on the background of Cycle 1.

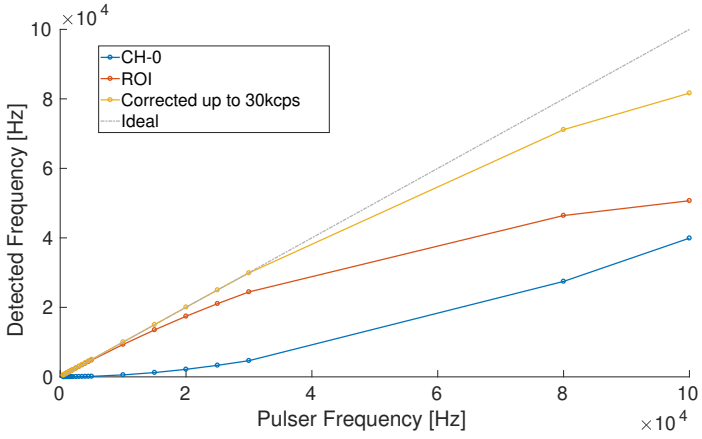

Figure 7.9: Dead-time correction.

The gray dotted line represents what the acquisition system should have recorded. The neutron events in channel zero have not been included in the analysis because they are mixed up with noise. In addition to that, the pile-up events appearing as peaks at multiple energies have only been counted once. Although this might be true, a polynomial empirical correction accounting for both the effects has been estimated and applied up to 30 kHz.

7.2.4 Check on the quality of the correction: ring ratio test

During the experimental campaign at ILL, one specific experiment has been performed for the loss-of-counts estimation. Figure 7.10a shows one quadrant of LOENIE-V2 long counter. In the absence of any loss, the counting rate detected by each tube is proportional to the incident neutron flux ($C = k \cdot \Phi$). The ratio of two detectors' counts should, therefore, stay constant independently on the flux level

$$\frac{C_{inner}}{C_{outer}} = \frac{k_{inner} \cdot \cancel{\Phi}}{k_{outer} \cdot \cancel{\Phi}} = R. \tag{7.15}$$

In the presence of dead time or pile-up, the detectors of the inner ring are the most affected by this effect and they undergo a stronger loss of counts. The ratio between the counts in the inner and the outer detector of the same quadrant should, therefore,

decrease with the increasing flux. The experiment consisted in the gradual opening of the neutron beam, thanks to the special fast-shutter designed for the ALDEN experiment, which allowed going from 10% to 100% of the maximum flux in 8 steps (see Figure 7.10b).

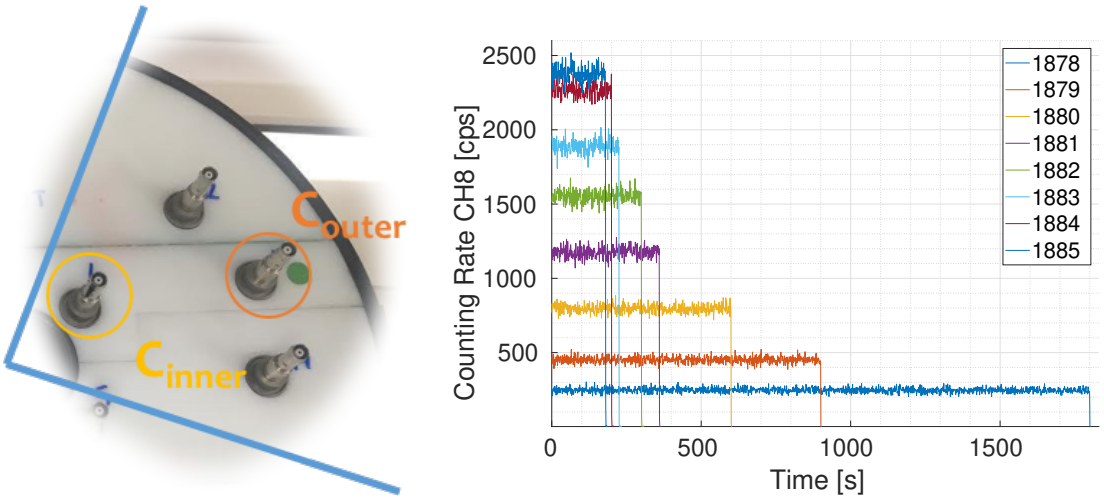

(a) LOENIE-V2 quadrant.

(b) Counting rate of an inner channel at different flux levels.

Figure 7.10: Ring ratio test.

Figures 7.11a and 7.11b show the ratio between each detector and its respective outer detector, before and after the correction.

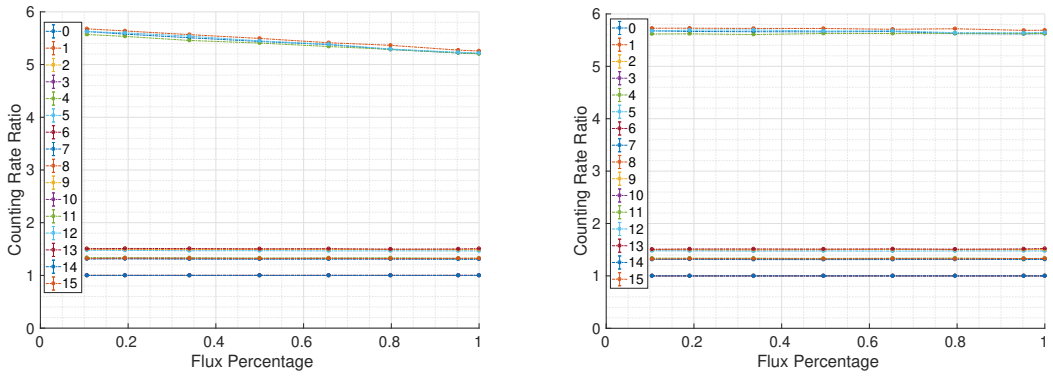

(a) Before correction.

(b) After correction.

Figure 7.11: Ring ratio.

The slope and the difference at 100% of the flux with respect to a straight line are reported in Tab. 7.2 for each tube. To give an illustration, the ratio between the detectors 4 and 6 reached 7% when the neutron beam was completely open, and was reduced to -0.06% after correction. Globally, with the open beam, the ring ratio was 4.6% smaller than when only 10% of the flux was present. Such percentage went down to 0.22% after correction. The uncertainty in the correction is conservatively assumed to be 1.5% at 30 kHz, thus 0.05% at 1 kHz, which means that it is definitely negligible in the decay phase.

Table 7.2: Slope and loss estimation before and after correction channel by channel.

CH	Outer CH	R	Before correction		After correction	
			Slope [10^{-6}]	Loss [%]	Slope [10^{-6}]	Loss [%]
0	2	5.68	-203	8.11	-25	0.94
1	2	1.50	-2	0.50	+3	0.94
2	2	1.00	-0	0.00	-0	-0.27
3	2	1.32	-2	0.43	+2	0.00
4	6	5.61	-173	7.04	+6	-0.06
5	6	1.48	-6	0.96	-1	-0.15
6	6	1.00	-0	0.00	0	0.21
7	6	1.31	-3	0.44	0	0.00
8	10	5.73	201	7.98	18	0.66
9	10	1.50	5	0.67	0	-0.12
10	10	1.00	-0	0.00	0	0.00
11	10	1.34	-5	0.83	2	0.31
12	14	5.69	-201	7.75	22	0.48
13	14	1.51	3	-0.09	3	-0.91
14	14	1.00	-0	0.00	0	0.00
15	14	1.32	-1	-0.20	3	-0.72
Sum				4.60		0.22

7.3 Absolute efficiency calibration at NPL

After a detector has been designed and produced, it must be calibrated, to be sure that it behaves as expected and that the efficiency is close to the one simulated during the design phase. The calibration is an essential phase in the field of experimental physics because it consists in measuring the response of the detector. It is a way to get to know the detector. The procedure is standard: a well-known input is sent to the detector and its response is recorded. The ratio between what is detected and what was supposed to be detected defines the efficiency of the system. This estimation is of extreme importance to reconstruct, from the detected signal during the experimental campaign, what was the real input signal. In the framework of the ALDEN experience, two calibrations took place. In January 2019, LOENIE-V2 has been carried to the UK for the measurement of its absolute efficiency at different energies. NPL (*National Physical Laboratory*) is a national measurement standard laboratory of the United Kingdom. The institute owns well-characterized neutron sources which can be used to calibrate neutron detectors. The sources used for calibration are listed in Tab. 7.3, together with their main features. Figure 7.12 shows the anisotropy of the sources, which have been taken into account in the TRIPOLI4® simulations of the detector efficiency. Another energy-dependent quantity that can help to test the quality of the fit is the ring ratio. The ratio between the sum of the detectors in the inner ring, and the sum of all the other detectors, is indeed an indicator of LOENIE-V2's response at different energies. The simulated ring ratio has been used to design the long counter, and in particular to define the arrangement of the ^{3}He tubes. The measurements at NPL allowed checking if the detector had been manufactured as designed.

Figure 7.13 compares the results of the experiment to the simulations performed with

Table 7.3: NPL sources' characteristics.

Source	Serial Number	Avg. Energy [MeV]	Emission Rate [s^{-1}]	90° Anisotropy
Am-Li	3250Li	0.471	2.07E+05 (0.74%)	1.0753 (0.73%)
Am-F	7582F	1.30	1.32E+05 (0.60%)	1.0224 (0.49%)
Cf	4774	2.13	7.83E+05 (0.39%)	1.0177 (0.22%)
Am-B	7584B	2.72	4.24E+05 (0.60%)	1.0345 (0.52%)
Am-Be	1679	4.15	7.57E+04 (0.84%)	1.0127 (0.40%)
Am-Be	1152	4.15	2.26E+05 (0.82%)	1.0144 (0.37%)

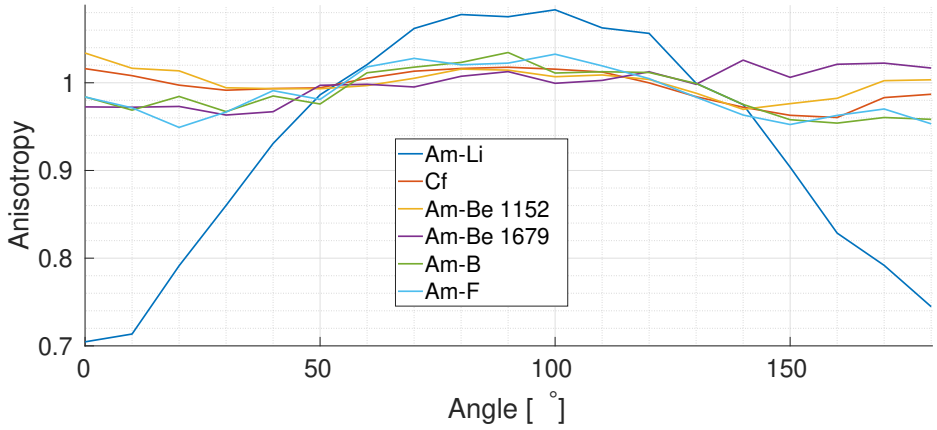

Figure 7.12: Anisotropy of NPL sources.

TRIPOLI4® using JEFF-3.2 library. The upper plot shows LOENIE-V2's efficiency at different energies. Each point is an independent measurement, performed with a different source. The last point is the Am-Be case, for which 2 sources were available. Note that the two samples had different emission rates. It is important to highlight that the dead time has been estimated in such a way to correct the experiments up to 30 kHz. The main purpose of the experimental campaign at NPL was to verify out the predictive power of the simulations to estimate the eventual scaling factor for the derivation of quantities that could not be directly measured. In the estimation of the delayed-neutron data, the absolute efficiency for prompt and delayed neutrons were both needed. Unfortunately, there were no calibrated sources with exactly such spectra. Delayed neutrons spectrum is close to the one of the Am-Li, while prompt neutron spectrum is close to the one of the Cf. The efficiency to prompt and delayed neutrons can be simulated but not measured. The purpose of the NPL measurements was to estimate these absolute efficiencies from the simulations and the scaling factor. As shown in Fig. 7.13, the ring ratio is perfectly simulated, while the efficiency is overestimated by a certain factor. Nevertheless, the trend of the efficiency curve is correct. For that reason, a scaling factor (γ) could be determined, as shown in Eq. 7.16. The uncertainty in the γ-parameter is obtained through the error propagation of the simulated and computed efficiencies.

$$\gamma = \frac{\sum_{i=1}^{N} \epsilon_{i,exp}}{\sum_{i=1}^{N} \epsilon_{i,sim}} = 0.9493 \quad (0.29\%). \tag{7.16}$$

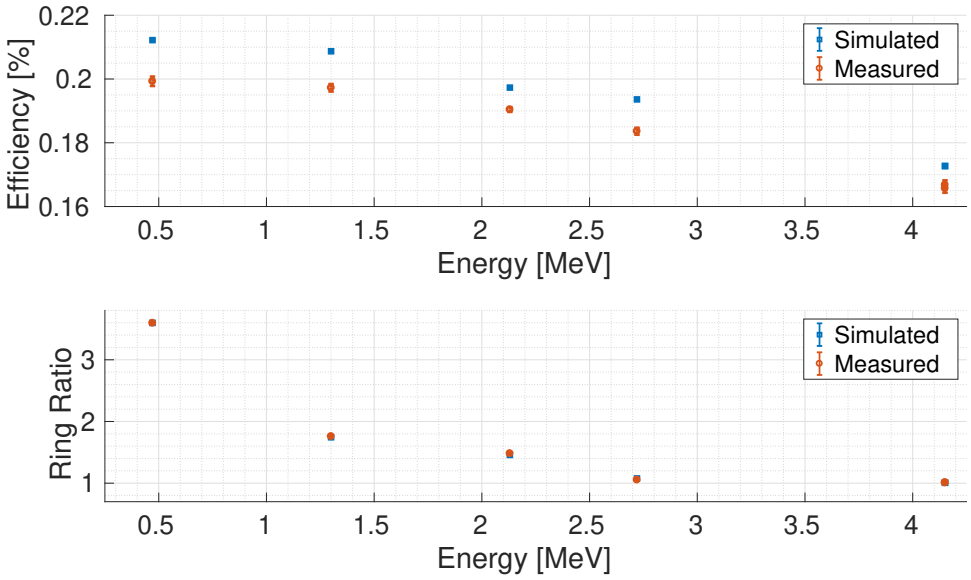

Figure 7.13: Comparison between simulation and measurement of the efficiency and of the ring ratio for NPL sources.

This factor could then be used to predict, from the simulation of the DN and the PFNS efficiencies, the respective *real* values, as $\epsilon_{exp} = \gamma \cdot \epsilon_{sim}$. The results are shown in the last two rows of Tab. 7.4, together with their uncertainties.

Table 7.4: Efficiency and ring ratio for the different NPL sources.

Source	ϵ_{sim} [%]	ϵ_{exp} [%]	(C-E)/E [%]	RR_{sim} [-]	RR_{exp} [-]	(C-E)/E [%]
Am-Li	21.22 (0.1%)	19.93 (0.7%)	6.47 (1.6%)	3.598 (0.2%)	3.596 (0.001%)	0.07 (3.2%)
Am-F	20.87 (0.1%)	19.73 (0.6%)	5.81 (1.7%)	1.744 (0.3%)	1.759 (0.001%)	-0.84 (0.3%)
Cf	19.73 (0.1%)	19.04 (0.4%)	3.61 (2.9%)	1.458 (0.3%)	1.482 (0.001%)	-1.62 (0.2%)
Am-B	19.36 (0.1%)	18.36 (0.6%)	5.43 (2.0%)	1.077 (0.3%)	1.054 (0.001%)	2.15 (0.2%)
Am-Be	17.27 (0.2%)	16.68 (0.8%)	3.53 (3.4%)	1.007 (0.3%)	1.014 (0.003%)	-0.64 (0.5%)
Am-Be	17.27 (0.2%)	16.57 (0.8%)	4.24 (2.9%)	1.007 (0.3%)	1.008 (0.0003%)	-0.07 (4.8%)
235U PFNS	20.13 (0.1%)	19.18 (0.3%)				
DN	21.340 (0.1%)	20.33 (0.3%)				

7.4 Irradiation duration

At the beginning of the campaign, no one was aware of the fact that Nomad needed a certain initialization time. For each acquisition, Nomad started to count about 200 ms after the fast shutter had opened the neutron beam. This means that the beginning of the irradiation phase was always missing and that it was not possible to verify that the irradiation duration was exactly the chosen one. Luckily, all the experiments have been performed with two sets of input parameters (1 and 2). For the set 2, a feature of Nomad has been used: the *wait*, which allowed the system to start counting after a given time

(here 1 s). What changed between the two sets was just the detectors' threshold, which in the set 2 was too low and made the detector signals very noisy and impossible to exploit. On the other hand, the fission chamber was properly set and its signal could be used to verify the duration of irradiation for the three cycles. Note that all the results in this work have been performed with the set number 1. For each run, the first and the last point of irradiation have been found. Their distribution is shown in Fig. 7.14 for Cycle 3.

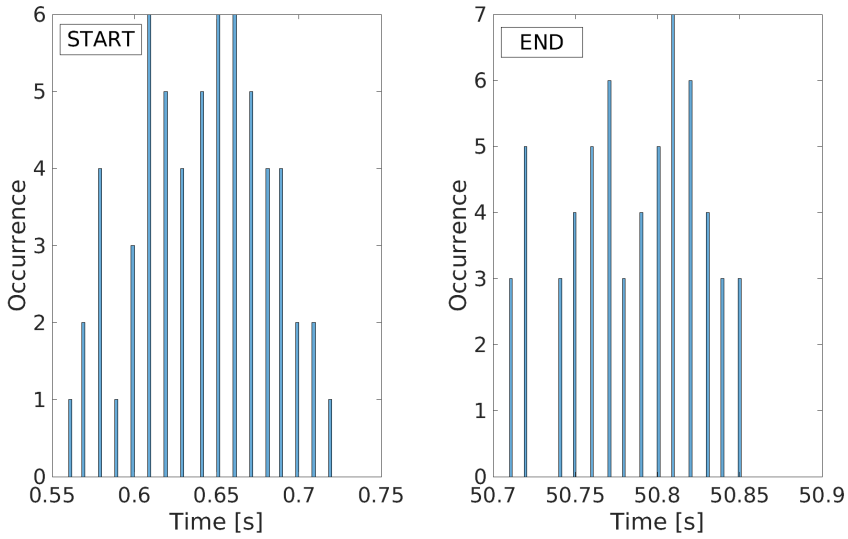

Figure 7.14: Distribution of the starting and ending point of the irradiation phase.

Then, the distribution of the duration has been derived, together with its mean and standard deviation. The results for the two main cycles are reported in Tab. 7.5.

Table 7.5: Estimated cycle duration.

Cycle	Average Duration [s]
1	50.13 ± 0.01
3	50.13 ± 0.01

7.5 Analysis of the decay curve

Once a proper curve had been obtained and the efficiencies estimated, it was possible to proceed with the analysis of the decay phase and the derivation of the parameters of interest. The neutron activity during the decay phase, already corrected for the dead time, can be described as

$$n_{dec}(t) = F\nu_d\epsilon_d \sum_{i=1}^{8} f_i a_i (1 - e^{-\lambda_i t_{irr}})(1 + e^{-\lambda_i t_m})e^{-\lambda_i t_0} e^{-\lambda_i t} + b_{dec} \tag{7.17}$$

where a_i are the DN group abundances, ν_d the average delayed-neutron data yield and b_{dec} the background rate (n/s) during the decay phase. Note that in principle there

should be one efficiency per DN group ($\epsilon_{d,i}$), since the different groups have distinct spectra and particular average energies. In Eq. 7.17, ϵ_d represents the average efficiency weighted over the 8 groups' abundances

$$\epsilon_d = \frac{\sum_{i=1}^{8} a_i \epsilon_{d,i}}{\sum_{i=1}^{8} a_i}. \tag{7.18}$$

The average efficiency has been factorized and carried out of the sum, while the factors f_i become

$$f_i = \frac{\epsilon_{d,i}}{\overline{\epsilon_d}}. \tag{7.19}$$

Their deviation from unity, reported in Tab. 7.6, are due to the non-perfectly flat energy dependence of the detector efficiency.

Table 7.6: Efficiency of the group with respect to the global efficiency.

i	1	2	3	4	5	6	7	8
f_i	0.9921	1.0056	0.9935	1.0014	0.9996	0.9996	0.9982	1.0019

Several factors are present in Eq. 7.17. The $1-e^{-\lambda_i t_{irr}}$ term takes into account the build-up of the different DN groups during the irradiation phase. To correct for the build-up due to the repeated cycles of irradiation and decay, the $1+e^{-\lambda_i t_m}$ term is added. The $e^{-\lambda_i t_0}$ factor takes into account the decay occurring during the veto time. Finally, $e^{-\lambda_i t}$ allows determining the activity at each time t after the end of the veto interval. Note that in order to use Eq. 7.17, the fission rate (F, in fiss/s) needs to be known. Several methods have been tested to obtain it. The first one consists in performing a spectroscopy of the fission chamber and of an Au-dosimeter. The second one exploits the signal from the fission chamber directly. The third one consists in deriving it from the detected counts during the irradiation phase, which includes prompt and delayed neutrons.

7.5.1 F from the spectroscopy of the fission chamber and of a dosimeter

This method consisted in determining F from the combination of the following terms

$$F = N_{FS} \cdot \sigma_{f,FS} \cdot \Phi, \tag{7.20}$$

where N_{FS} is the number of atoms of the fissioning system (FS), $\sigma_{f,FS}$ its microscopic fission cross section in b and Φ the neutron flux in n cm^{-2} s^{-1}. The atomic density can be derived from the ^{235}U activity, which has been measured by spectroscopy of the fission chamber and appeared to be 1.634E+1 (1.6%) Bq. The activity is given as

$$A_{235U} = \lambda_{235U} N_{235U}, \tag{7.21}$$

and knowing that the ^{235}U half-life is 704E+6 y, then the number of atoms N_{235U} has been estimated to 5.23E+17 at (1.6%), which corresponds to a mass of 204.27 μg (1.6%). As far as the neutron flux is concerned, it could be estimated from the analysis of a neutron activation foil, which has been irradiated for 3 hours during the experimental campaign. The dosimeter was an Al-0.1%Au activation detector. The gold undergoes the following nuclear reaction

$$^{197}Au(n,\gamma)^{198}Au \tag{7.22}$$

when irradiated. From the gamma emission, it was possible to recover the activity of the sample at the end of the irradiation, which can be described as

$$A_{197Au}(t_{irr}) = N_{197Au}\ \sigma_{(n,\gamma),197Au}\ \Phi\ (1 - e^{\lambda_{198Au}\ t_{irr}}). \tag{7.23}$$

The number of atoms N_{197Au} had to be determined from the activation detector composition, knowing that the dosimeter's mass was $m_{dosimeter} = 14.019$ mg and that $k = 1005$ was the mg of Au per kg of dosimeter. The mass of gold and its atoms could therefore be found, knowing the gold molar mass (M_{Au}), as

$$m_{Au} = k \cdot m_{dosimeter} \tag{7.24}$$

$$N_{197Au} = \frac{m_{Au} N_{av}}{M_{Au}}. \tag{7.25}$$

In the certificate, the activity was given per gram of dosimeter ($a = 5387$ (2.7%) Bq/g), so that the global activity of the foil was

$$A_{197Au} = a \cdot m_{dosimeter} \qquad [Bq] \tag{7.26}$$

Finally, the fission rate could be computed as

$$\begin{aligned} F &= N_{235U}\ \sigma_{f,235U}\ \Phi_{235U} \\ &= N_{235U}\ f\ \sigma_{(n,\gamma),197Au}\ \Phi_{197Au} \\ &= \frac{N_{235U}\ f\ A_{197Au}(t_{irr})}{N_{197Au}\ (1 - e^{\lambda_{198Au}\ t_{irr}})} = 171.0 \text{ kHz } (3.12\%) \end{aligned} \tag{7.27}$$

where f is the cross section ratio in the experiment configuration and is equal to 5.89 (0.13%).

$$f = \frac{\sigma_{f,235U}\ \Phi_{235U}}{\sigma_{(n,\gamma),197Au}\ \Phi_{197Au}} \tag{7.28}$$

Both the detector and the dosimeter have been simulated with TRIPOLI4®. Note that the ratio is 0.6% smaller than the cross section ratio at thermal energies.

7.5.2 F from the fission chamber signal

The fission rate can be estimated from the fission chamber signal through Eq. 7.29

$$F = \frac{1}{\epsilon_{CFP12}} \left(\frac{F_m}{1 - \tau F_m}, \right) \tag{7.29}$$

where F_m is the measured counting rate, ϵ_{CFP12} is the efficiency of the fission chamber and the term $(\frac{F_m}{1-\tau F_m})$ represents the dead time correction of the CFP12 counting rate. Figure 7.15 shows the distribution of the average counting rate during the irradiation phase of the 168 runs of cycle 1.
The average value (F_m) and the standard deviation were 171.3 kHz and 0.02%. Correcting for a dead time τ of 90 ns, the counting rate became 174.0 kHz (0.02%). The fission chamber had not been calibrated and in order to estimate the uncertainty some assumption had to be made. Figure 7.16 shows the PHA of the CFP12 recorded during the irradiation phase.
The right peak represents the energy-rich fission fragments' signal, whose voltage is easily distinguishable from the background. To determine the efficiency of the detector, one has to know the shape of the neutron signal below channel 100. Several theories could

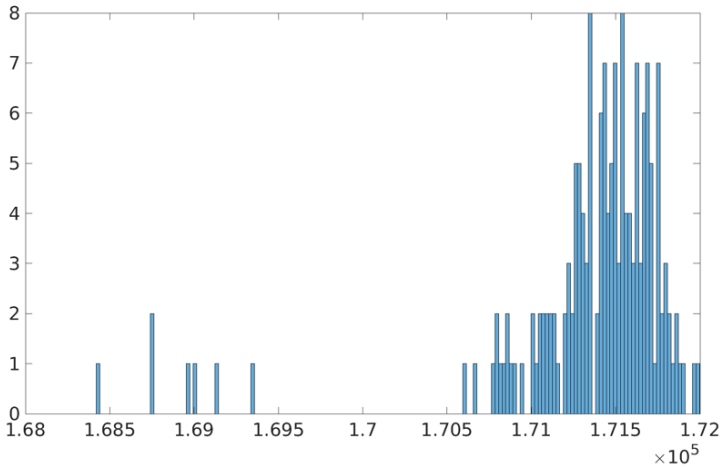

Figure 7.15: Distribution of the average counting rate during the irradiation phase of the 168 runs of cycle 1.

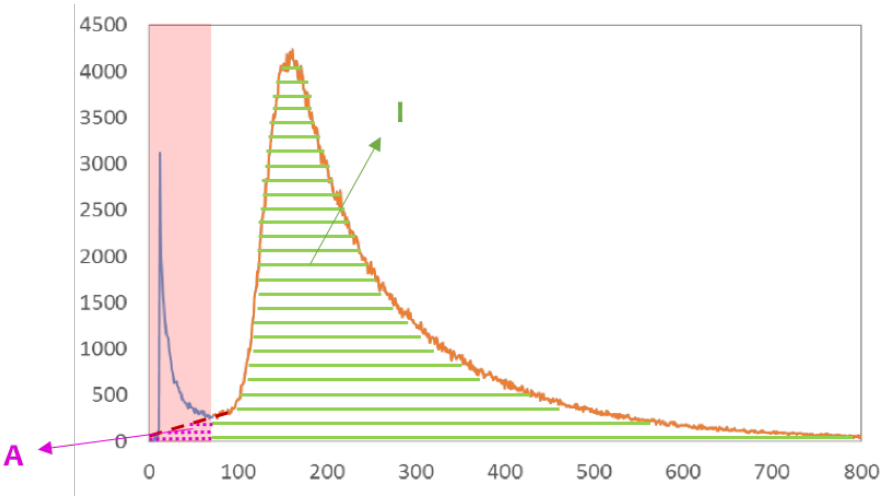

Figure 7.16: PHA of the CFP12 during the irradiation phase.

be applied. For this study, the neutron peak has been assumed to go to zero as shown by the dashed line. The efficiency could be determined as follows

$$\epsilon_{CFP12} = \frac{I}{I + A} \approx 97\% \ (3.0\%) \tag{7.30}$$

where I is the integral of the neutron signal falling in the ROI and A is the integral of the discarded counts. Correcting the counting rate by the estimated efficiency, the fission rate F became 179.4 kHz (3.0 %). The result is a bit higher than the one obtained through the previous method. However, the two values are consistent and overlap each other within the respective uncertainties.

7.5.3 F from the irradiation phase

The last technique consists in deriving the fission rate from the total neutron emission, therefore from the irradiation plateau. It is worth noting that it is possible to exploit this method only because a dummy chamber has been used to estimate the background

during both the irradiation and the decay phase. Furthermore, the elastic scattering cross section of ^{235}U is weak with respect to $\nu\sigma_f$, and scatters thermal neutrons which are absorbed by the flexibore. The neutron activity measured during the irradiation phase can be described as

$$\overline{n_{irr}} = F(\nu_p\epsilon_p + \nu_d\epsilon_d) + b_{irr}, \tag{7.31}$$

where $\overline{n_{irr}}$ (n/s) is an average over the irradiation plateau[2], b_{irr} (n/s) is the background rate during the irradiation phase, ν_p and ν_d (n/fiss) are the average prompt and delayed-neutron data yields and ϵ_p and ϵ_d are LOENIE-V2's efficiencies for a prompt and delayed-neutron data spectrum, respectively. Taking the ν_d from the summation calculation, ν_p from JEFF-3.1.1, ϵ_p and ϵ_d from simulations and the rest from the ALDEN experiment, one obtains a fission rate of 194.1 kHz (0.4%), which is inconsistent with the previous two methods.

7.5.4 From F to ν_d

Once the fission rate and its uncertainty are known, it is possible to derive the average delayed-neutron yield from the fit of the decay curve, shown in Eq. 7.17. Note that all the input parameters affected by uncertainty (F, n_{dec}, ϵ_d, a_i, t_{irr}, t_0, and b_{dec}) have been marginalized, while λ_i and f_i have been kept constant. For the estimation of the ν_d, only a small part of the curve has been exploited, the first 500 ms. The objective was to extrapolate the counting rate just at the end of the irradiation, once the prompt neutrons disappeared. This quantity had to be extrapolated due to the veto time imposed by the fission tail. The choice of the first 500 ms came from an optimization of the uncertainty. The more the points, the lower the statistical uncertainty. At the same time, the larger the distance from the end of the irradiation, the stronger the correction to be applied to perform the extrapolation. The corrective factor contains uncertain parameters, and this is reflected in an increasing systematic uncertainty with time. Figure 7.17 shows the behavior of the two components of the uncertainty, together with their combination. It is evident that it is not advantageous to take the whole decay curve. Using this method, the optimum has been estimated at around 400-500 ms.
Table 7.7 shows the impact of the fission rate estimation technique on the result of the fit. The first thing to note is that the first two techniques, which gave similar F, strongly

Table 7.7: Results of the fit of the decay curve using a fission rate estimated through different methods.

	F [kHz]	ν_d [DN/fiss]
Spectroscopy	171.0 (3.1%)	1.857E-02 (3.4%)
Fission chamber signal	179.4 (3.0%)	1.770E-02 (3.3%)
Irradiation phase	194.1 (0.4%)	1.636E-02 (1.4%)

overestimate the ν_d. From Eq. 7.17, it is clear that an overestimation of the ν_d points towards an underestimation of the product $F\ \epsilon_d$. This means that either the fission rate or the efficiency were underestimated. Since two independent techniques (spectroscopy and fission chamber signal) gave consistent F, we suspect a systematic bias shifting down

[2]Note that the first 30 s of the plateau are not included in the average in order to let the delayed neutrons reach their equilibrium concentration

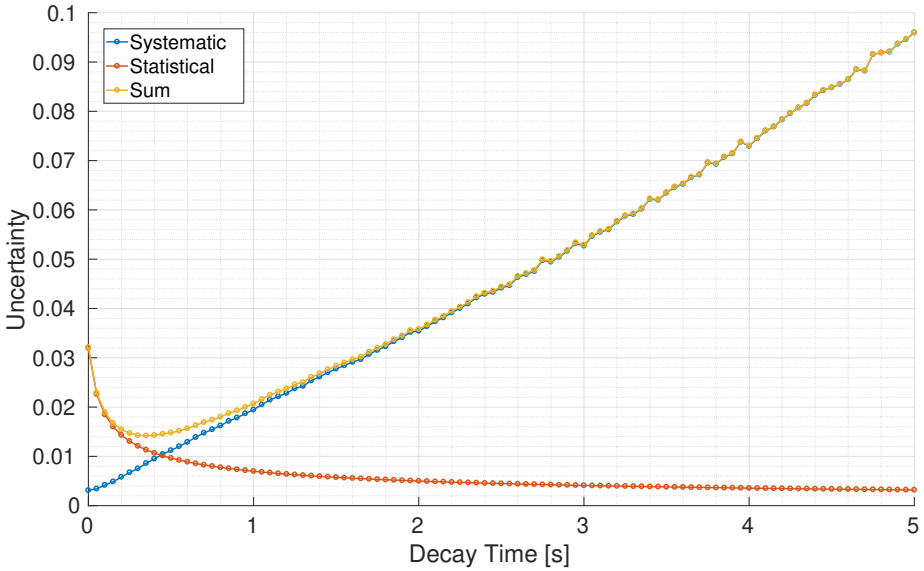

Figure 7.17: Uncertainty components as a function of the length of the fitted decay curve.

the efficiencies measured at NPL. As far as the third technique is concerned, it is worth highlighting that the efficiencies appear in the denominator of F

$$F = \frac{\overline{n_{irr}} - b_{irr}}{\nu_p \epsilon_p + \nu_d \epsilon_d}, \tag{7.32}$$

and that to estimate the ν_d only the ratio of the efficiencies counts

$$\nu_d \approx \frac{X}{F\epsilon_d} \approx Y \frac{\nu_p \epsilon_p + \nu_d \epsilon_d}{\epsilon_d} = Y\left(\nu_p \frac{\epsilon_p}{\epsilon_d} + \nu_d\right). \tag{7.33}$$

As a consequence, by employing this technique, any systematic bias in the efficiencies will be cancelled out as long as their ratio is correct. The extremely good agreement between simulated and measured ring ratio and the accurate efficiency trend made us confident regarding the application of this method.

7.5.5 Adopted procedure

Since it has been shown that a systematic bias affects the efficiencies, the last method has been retained and slightly modified to avoid imposing any prior knowledge on the ν_d and any direct estimation of the fission rate. Indeed, by replacing Eq. 7.32 in Eq. 7.17 one obtains a formulation of the problem which bypasses the explicit estimation of F

$$n_{dec}(t) = \frac{\nu_d \epsilon_d}{\nu_p \epsilon_p + \nu_d \epsilon_d} \frac{(\overline{n_{irr}} - b_{irr}) \sum_{i=1}^{8} f_i a_i (1 - e^{-\lambda_i t_{irr}})(1 + e^{-\lambda_i t_m}) e^{-\lambda_i t_0} e^{-\lambda_i t}}{\sum_{i=1}^{8} a_i} + b_{dec}. \tag{7.34}$$

The fitting procedure consisted of two steps:

1. **Step 1:** estimation of the ν_d through the fit of the first 500 ms of the decay curve

- fitted: ν_d
- marginalized: a_i, t_0, t_m, $\overline{n_{irr}}$, b_{irr}, b_{dec}, ν_p, ϵ_d, ϵ_p
- constant: λ_i, f_i

2. **Step 2:** estimation of the a_i through the fit of the whole decay curve
   - fitted: a_i
   - marginalized: ν_d
   - constant: t_0, t_m, $\overline{n_{irr}}$, b_{irr}, b_{dec}, ν_p, ϵ_d, ϵ_p, λ_i, f_i

In the first step, the first instants of the decay curve were fitted to obtain the average delayed-neutron data yield. The CONRAD® code was given a guessed value (*prior*) of the ν_d of 2E-02 ± 2E-02 in order to leave the fit completely free. All the parameters having an uncertainty were marginalized. In that way, the uncertainty in the fitted ν_d would integrate all the others. The a_i used in this step were the ones found by summation method through exponential equivalence. In the second step, the a_i were fitted. This time, the ν_d used as prior was the one found in Step 1. On the other hand, the abundances were left completely free to converge to any value, since the prior was 0.125 ± 1E+03 for each a_i. The only marginalized parameter was the ν_d, since the uncertainty in the other parameters had already been taken into account in Step 1 and was integrated into the ν_d. Step 2 used the whole decay curve since the first seconds were mostly sensitive to the short-lived groups while after 100 s only the precursors belonging to group 1 and 2 were left.

7.6 Results from the ALDEN experiment

Since Cycle 1 and Cycle 3 had the same irradiation duration, it was possible to combine them and treat them as two independent experiments. A single theory has been written for the two cycles and the two curves have been given to CONRAD® as experimental evidence. For the reasons mentioned in Section 7.5, the fission rate has been estimated from the irradiation plateau, and the fit has been performed following the model presented in Eq. 7.34. Table 7.8 shows the delayed-neutron data before and after the fit of the experimental curve, while Fig. 7.18 reports the correlation matrix associated with the obtained abundances. Please keep in mind that the given prior's uncertainty is surrealistically large in order not to bias the result.

$$\begin{bmatrix}
1 & -0.728 & 0.833 & -0.466 & 0.462 & -0.341 & 0.343 & -0.379 \\
-0.728 & 1 & -0.852 & 0.716 & -0.373 & 0.248 & -0.052 & -0.082 \\
0.833 & -0.852 & 1 & -0.783 & 0.656 & -0.48 & 0.378 & -0.34 \\
-0.466 & 0.716 & -0.783 & 1 & -0.814 & 0.652 & -0.375 & 0.184 \\
0.462 & -0.373 & 0.656 & -0.814 & 1 & -0.919 & 0.753 & -0.622 \\
-0.341 & 0.248 & -0.48 & 0.652 & -0.919 & 1 & -0.889 & 0.702 \\
0.343 & -0.052 & 0.378 & -0.375 & 0.753 & -0.889 & 1 & -0.932 \\
-0.379 & -0.082 & -0.34 & 0.184 & -0.622 & 0.702 & -0.932 & 1
\end{bmatrix}$$

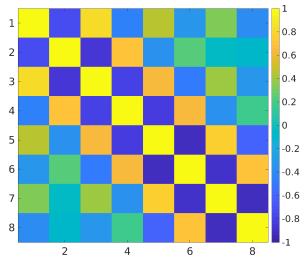

Figure 7.18: Correlation matrix associated with the abundances derived from the fit of the ALDEN experimental decay curve through *analytical marginalization*.

Table 7.8: Results of the ALDEN experiment. *Prior* are the guessed values given to CONRAD® in order not to constrain the fit, while *Posterior* are the results of the fit.

Quantity of interest	Prior	Posterior	WPEC-6
ν_d [DN/fiss]	2.000E-02 (100%)	1.631E-02 (1.4%)	1.62E-02 (-)
a_1	1.25E-01 (800000%)	3.64E-02 (2.7%)	3.28E-02 (12.8%)
a_2	1.25E-01 (800000%)	1.31E-01 (3.3%)	1.54E-01 (4.4%)
a_3	1.25E-01 (800000%)	1.15E-01 (4.9%)	9.14E-02 (9.8%)
a_4	1.25E-01 (800000%)	1.66E-01 (4.8%)	1.97E-01 (11.7%)
a_5	1.25E-01 (800000%)	3.55E-01 (5.2%)	3.31E-02 (2.0%)
a_6	1.25E-01 (800000%)	6.92E-02 (40.8%)	9.03E-02 (5.0%)
a_7	1.25E-01 (800000%)	8.15E-02 (49.3%)	8.12E-02 (2.0%)
a_8	1.25E-01 (800000%)	4.58E-02 (66.3%)	2.29E-02 (41.5%)
$\overline{T_{1/2}}$ [s]	13.20 (385880%)	8.93 (5.72%)	9.02 (3.0%)
$\overline{T_{1/2}}$ with corr [s]	13.20 (385880%)	8.93 (0.98%)	9.02 (3.0%)

The average delayed-neutron yield is compared with previous experiments in Fig. 7.19. The first thing to note is that the fit converges towards reasonable values. The ν_d is very close to the one recommended by the WPEC-6, with the only difference that it is equipped with an uncertainty. Figure 7.19 shows the measured DN yield for the $^{235}U_t$ as a function of the year in which the experiment took place. The red band is the

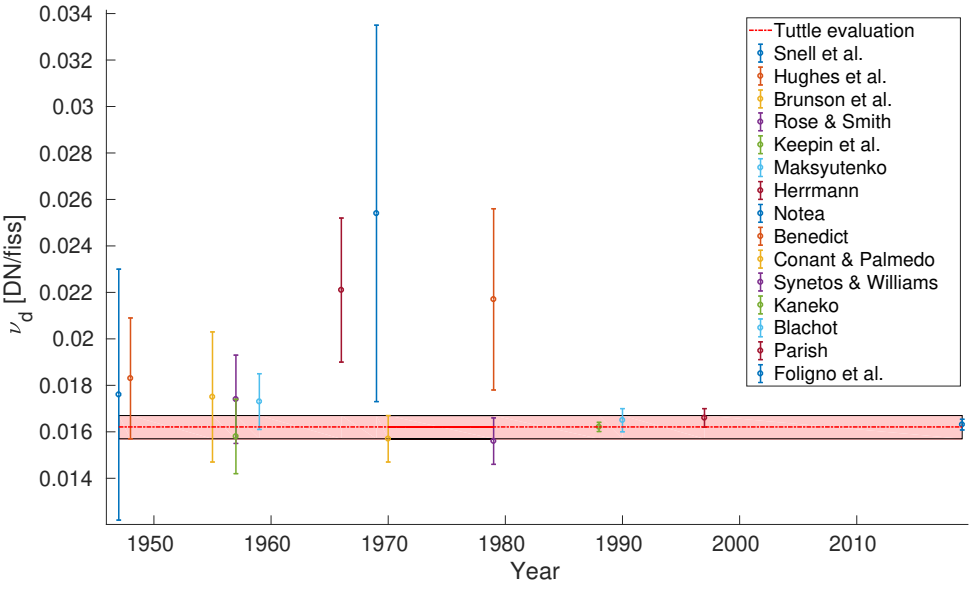

Figure 7.19: Experimentally measured ν_d for $^{235}U_t$ as a function of the year in which the experiment took place. The red band represents the values recommended by Tuttle in his evaluation of 1979.

uncertainty range of Tuttle's evaluation, which was performed in 1979 and included all the previous measurements. The WPEC-6 (2002) took into account also the most recent experimental campaigns, among which Parish's, which predicted a ν_d of 1.66E-02 with

an uncertainty of 3%. Even though the uncertainties were available, the WPEC-6 did not recommend any. The ALDEN experiment (see Foligno et al. in Fig. 7.19) is in agreement with both Tuttle and the WPEC-6. Furthermore, it provided a ν_d with an accuracy of 1.4%, about half of Parish's one.
The mean precursors' half-life computed with the obtained abundances is compared with previous experiments in Fig. 7.20. Even though Foligno's $\overline{T_{1/2}}$ agrees with experiments,

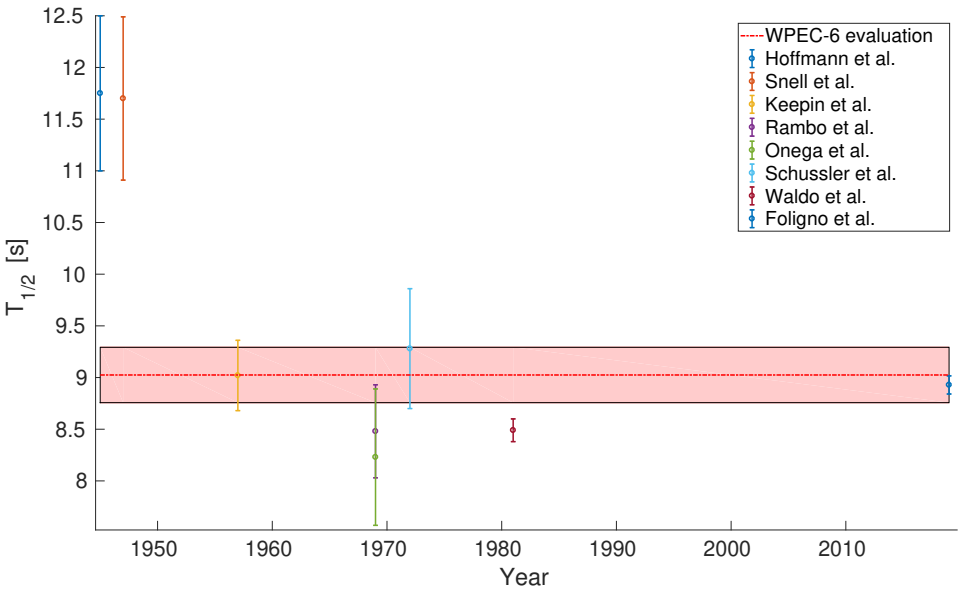

Figure 7.20: Experimentally measured $\overline{T_{1/2}}$ for $^{235}\mathrm{U_t}$ as a function of the year in which the experiment took place. The red band represents the values recommended by Tuttle in his evaluation of 1979.

there are discrepancies in the single abundances that are beyond the uncertainties. Furthermore, it seems that the experiment could not bring sufficient information on the short-lived precursors, which are consequently affected by large uncertainties. For that reason, a second experimental campaign has been planned. This time, priority will be given to short cycles in order to gather information on the short-lived groups. Please, keep in mind that the results shown in Tab. 7.8, have been obtained with no prior and that suggesting qualitatively good data would constrain the fit and would lead to a reduction of the uncertainties. Finally, the measured mean half-life is a global parameter and it agrees with the WPEC-6 recommendations.

Part IV

Evaluation and Benchmarking

Chapter 8

Evaluation and Benchmarking

> All true science must aim at objective truth, and that means that the human observer must never allow himself to get emotionally mixed up with his subject-matter. His concern is to understand the universe, not to improve it. Detachment is obligatory.
>
> *Sir Edmund Ronald Leach*

Contents

8.1 Bayesian assimilation of experimental data 147

8.2 Neutron reactor noise analysis 150

8.3 Validation of the average DN yield 151

8.3.1 MISTRAL1 151

8.3.2 IPEN/MB-01 154

8.3.3 SNEAK7B 156

8.4 Validation of the kinetic parameters 158

8.5 Uncertainty propagation on the reactivity for a PWR-type reactor 161

The objective of Section 8.1 is the Bayesian assimilation of the ALDEN experiment into the summation calculation. Then, the following benchmarks aim at testing the obtained ν_d and kinetic parameters to see if they are coherent with the C/E discrepancies from JEFF-3.1.1. Section 8.2 describes the theory of the neutron reactor noise analysis. Section 8.3 focuses on the effect of the ν_d on the β_{eff} estimation, while Section 8.4 is centered on the influence of the kinetic parameters on the prediction of the reactivity. Finally, Section 8.5 highlights how the uncertainty in the input data affects the precision of the calculated reactivity.

8.1 Bayesian assimilation of experimental data

As already mentioned, Bayesian inference is very useful because it allows improving the estimate of some measurements by making assumptions about the answer. It is time to apply the theorem to the delayed-neutron data estimation, using a *prior* (the quantities computed by summation method), a *model* (Eq. 7.17) and an evidence (the decay curve measured during the ALDEN experiment). Basically, what changes with respect to the method used to estimate the results presented in Sec. 7.6, is the guessed set of parameters given as prior. As mentioned before, this time the prior will be coming from summation calculations. Table 8.1 shows the ν_d as well as the abundances, before and after the fit, while Fig. 8.1 reports the correlation matrix associated with the *posterior* abundances.

Table 8.1: Results of the Bayesian assimilation of the ALDEN experiment. *Prior* are the guessed values given to the CONRAD® code and taken from the summation calculation, while *Posterior* are the results of the fit.

Quantity of interest	Prior	Posterior	WPEC-6
ν_d [DN/fiss]	1.609E-02 (5.2%)	1.645E-02 (1.6%)	1.620E-02 (-)
a_1	3.50E-02 (2.7%)	3.55E-02 (1.8%)	3.28E-02 (12.8%)
a_2	1.61E-01 (9.8%)	1.38E-01 (2.4%)	1.54E-01 (4.4%)
a_3	9.48E-02 (22.8%)	1.08E-01 (3.8%)	9.14E-02 (9.8%)
a_4	1.72E-01 (23.2%)	1.78E-01 (3.5%)	1.97E-01 (11.7%)
a_5	3.16E-01 (17.4%)	3.37E-01 (3.4%)	3.31E-02 (2.0%)
a_6	1.35E-01 (26.3%)	9.51E-02 (15.0%)	9.03E-02 (5.0%)
a_7	6.09E-02 (27.1%)	7.32E-02 (16.3%)	8.12E-02 (2.0%)
a_8	2.35E-02 (46.4%)	3.51E-02 (25.3%)	2.29E-02 (41.5%)
$\overline{T_{1/2}}$ [s]	9.27 (6.6%)	8.98 (2.2%)	9.02 (3.0%)
$\overline{T_{1/2}}$ with corr. [s]	9.27 (6.6%)	8.98 (0.6%)	9.02 (3.0%)

$$\begin{bmatrix} 1 & -0.696 & 0.693 & -0.303 & 0.226 & -0.07 & 0.003 & -0.102 \\ -0.696 & 1 & -0.876 & 0.686 & -0.387 & 0.322 & -0.131 & -0.246 \\ 0.693 & -0.876 & 1 & -0.751 & 0.554 & -0.306 & 0.093 & -0.004 \\ -0.303 & 0.686 & -0.751 & 1 & -0.848 & 0.651 & -0.26 & -0.191 \\ 0.226 & -0.387 & 0.554 & -0.848 & 1 & -0.823 & 0.384 & -0.021 \\ -0.07 & 0.322 & -0.306 & 0.651 & -0.823 & 1 & -0.705 & -0.025 \\ 0.003 & -0.131 & 0.093 & -0.26 & 0.384 & -0.705 & 1 & -0.519 \\ -0.102 & -0.246 & -0.004 & -0.191 & -0.021 & -0.025 & -0.519 & 1 \end{bmatrix}$$

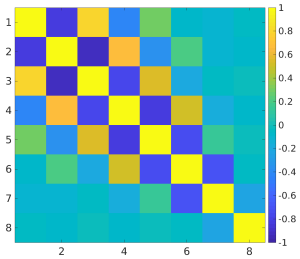

Figure 8.1: Correlation matrix associated with the abundances derived from the Bayesian assimilation of the ALDEN experiment through *analytical marginalization*.

The first thing to note is that nothing has changed for the ν_d, neither in the value or in the uncertainty. This means that the calculation did not bring any additional information to the experiment. The same is not true for the abundances. While the long-lived precursors' a_i are closer to the experiment than to the summation method, the short-lived ones, which were affected by large experimental uncertainties, are constrained by the calculation. It is interesting to see how, for the 7^{th} group, the combination of two large uncertainties (>40%) led to a much smaller one (14%). Probably, this effect is due to the

non-negligible correlations among the abundances, which cannot be treated individually. As far as the mean half-life is concerned, the Bayesian inference gives the closest to the recommended value. Furthermore, the resulting uncertainty has been strongly reduced. Note that the percentage shown in the table are the uncertainties computed using the correlation matrix associated to the set of abundances under consideration. It is worth mentioning that, neglecting the correlations, the error of the mean half-life would have been about 5% for the experiment and 1% for the Bayesian assimilation. This is due to the fact that the abundances are *anticorrelated* and that the use of the matrix in the error propagation process leads to a reduction of the global uncertainty. In conclusion, all the quantities of interest (ν_d, a_i, and $\overline{T_{1/2}}$) underwent a significant reduction of the uncertainty. Such amelioration will be reflected in a better prediction of the reactivity, as it will be shown later through the IPEN benchmark. To sum up, Tab. 8.2 reports the evolution of the quantities of interest in the different steps: calculation, experiment, and combination of the two.

Table 8.2: Summary of the abundances and average yields obtained in the different steps of this work: summation calculation, experiment, and Bayesian combination of the two.

Quantity	**WPEC-6**	**Foligno et al.**		
		Summation	**Experiment**	**Bayesian inference**
ν_d [DN/fiss]	1.620E-02 (-)	1.609E-02 (5.2%)	1.631E-02 (1.4%)	1.645E-02 (1.6%)
a_1	3.28E-02 (12.8%)	3.50E-02 (14.6%)	3.64E-02 (2.7%)	3.55E-02 (1.8%)
a_2	1.54E-01 (4.4%)	1.61E-01 (14.9%)	1.31E-01 (3.3%)	1.38E-01 (2.4%)
a_3	9.14E-02 (9.8%)	9.48E-02 (17.2%)	1.15E-01 (4.9%)	1.08E-01 (3.8%)
a_4	1.97E-01 (11.7%)	1.72E-01 (15.4%)	1.66E-01 (4.8%)	1.78E-01 (3.5%)
a_5	3.31E-02 (2.0%)	3.16E-01 (9.11%)	3.55E-01 (5.2%)	3.37E-01 (3.4%)
a_6	9.03E-02 (5.0%)	1.35E-01 (11.9%)	6.92E-02 (40.8%)	9.51E-02 (15.0%)
a_7	8.12E-02 (2.0%)	6.09E-02 (41.2%)	8.15E-02 (49.3%)	7.32E-02 (16.0%)
a_8	2.29E-02 (41.5%)	2.35E-02 (12.7%)	4.58E-02 (66.3%)	3.51E-02 (25.3%)
$\overline{T_{1/2}}$ [s]	9.02 (3.0%)	9.27 (6.6%)	8.93 (5.7%)	8.98 (2.2%)
$\overline{T_{1/2}}$ with corr [s]	9.02 (3.0%)	9.27 (6.6%)	8.93 (1.0%)	8.98 (0.6%)

Three benchmarks have been considered: MISTRAL1, IPEN/MB-01, and SNEAK7B. All of them have been simulated with TRIPOLI4® using two sets of parameters: *JEFF-3.1.1* and *Foligno et al.*, which differ in the abundances, in the first decay constant and in the average DN yield of $^{235}U_t$ and $^{238}U_f$. Table 8.3 summarises the differences between the two sets, which will be at the origin of the discrepancies in the results of the simulations. Note that, as far as Foligno's parameters are concerned,

- λ_1 corresponds to the decay constant of ^{87}Br according to ENDF/B-VIII.0
- the values for $^{235}U_t$ come from the Bayesian assimilation of the ALDEN experimental results into a calculation performed by summation method
- the values for $^{238}U_f$ are calculated by summation method using JEFF-3.1.1's fission yields and ENDF/B-VIII.0's radioactive decay data.

Foligno's work suggests a slight increase in the ν_d for $^{235}U_t$ and a stronger reduction in the ν_d for $^{238}U_f$. The first leads to a rise while the second to a decrease of the β_{eff}. A compensation of the two is expected, whose magnitude however, depends on the core composition. All the benchmarks took place in zero-power reactors. Two of them

Table 8.3: Input data comparison. As far as *Foligno*'s parameters are concerned, $^{238}U_f$'s are the results of the summation calculation while $^{235}U_t$'s come from the Bayesian assimilation of calculation and experiment.

Fissile isotope	Quantity of interest	JEFF-3.1.1	Foligno et al.
-	λ_1 [s^{-1}]	0.012467	0.012455
$^{235}U_t$	ν_d [DN/fiss]	1.6200E-02 (-)	1.645E-02 (1.6%)
	a_1	3.28E-02 (12.8%)	3.55E-02 (1.8%)
	a_2	1.54E-01 (4.4%)	1.38E-01 (2.4%)
	a_3	9.14E-02 (9.8%)	1.08E-01 (3.8%)
	a_4	1.97E-01 (11.7%)	1.78E-01 (3.5%)
	a_5	3.31E-01 (2.0%)	3.37E-01 (3.4%)
	a_6	9.03E-02 (5.0%)	9.51E-02 (15.0%)
	a_7	8.12E-02 (2.0%)	7.32E-02 (16.0%)
	a_8	2.29E-02 (41.5%)	3.51E-02 (25.3%)
	$T_{1/2}$ [s]	9.02 (3.0%)	8.98 (0.6%)
$^{238}U_t$	ν_d [DN/fiss]	4.780E-02 (-)	4.492E-02 (3.4%)
	a_1	8.40E-03 (5.5%)	9.31E-03 (4.5%)
	a_2	1.04E-01 (2.1%)	9.10E-02 (6.3%)
	a_3	3.75E-02 (2.0%)	4.37E-02 (15.8%)
	a_4	1.37E-01 (14.6%)	1.17E-01 (10.5%)
	a_5	2.94E-01 (4.1%)	3.02E-01 (11.8%)
	a_6	1.98E-01 (1.2%)	2.07E-01 (16.4%)
	a_7	1.28E-01 (10.2%)	1.43E-01 (14.4%)
	a_8	9.31E-02 (3.7%)	7.88E-02 (13.2%)
	$T_{1/2}$ [s]	5.32 (2.0%)	5.12 (4.8%)

are made in UOX fuelled systems (MISTRAL1 and IPEN/MB-01), with an optimal moderation ratio, while one of them is done in a MOX fuelled system (SNEAK7B). It is clear that the behavior of the first ones will be driven by ^{235}U data, while the last core will have a large dependence on ^{238}U data.

It is worth recalling that JEFF-3.1.1 adopted the ν_d recommended by the WPEC-6, and that the recommendations of WPEC-6 are based on adjusting the ν_d in order for calculations to fit the benchmarks. D'Angelo, who participated in the WPEC-6 evaluation, explains it as follows [21]:

> *Although the accuracy of the data for individual fission product isotopes has improved during the past decade, for β_{eff} calculations reliance must still be placed on the macroscopic measurements of the delayed-neutron emission data for the major isotopes and the validation of the data using reactor measurements of β_{eff} and time-dependent effects. Indeed, it is by adjusting the yield data to improve the agreement with measured values of β_{eff} that the data most suitable for β_{eff} calculations is obtained.*

In the WPEC-6 report [38] it is explicitly stated that the yields adjusted are the JEF-2.2 values. So for example, the ν_d for $^{235}U_t$ has been modified from 0.0165 (recommended by Kaneko in 1988 and adopted by JEF-2.2) to 0.0162. MISTRAL1 and SNEAK7B are among the benchmarks taken into account by D'Angelo. It is not surprising then that,

using JEFF-3.1.1 to reproduce such benchmarks, the discrepancy never exceeds 3%. The same is not true for IPEN/MB-01, performed years later.

8.2 Neutron reactor noise analysis

Reactor noise is nothing but neutron fluctuations. Neutronic reactions are a random process, which means that the neutron population is naturally characterized by statistical fluctuations. Reactor noise can be used to measure time constants and dynamic characteristics of the reactor, as well as to identify unexpected malfunctions or abnormalities [28]. In zero-power reactors, the external sources of reactivity (coolant temperature, control rod movement) can be neglected [25]. The whole system can be seen as an input-output loop in which to a given input reactivity corresponds an output neutron fluctuation. A scheme can be seen in Fig. 8.2, where $\rho(\omega)$ is the input reactivity as a function of the frequency, $N(\omega)$ is the output neutron fluctuation and $H_0(\omega)$ is the reactor transfer function.

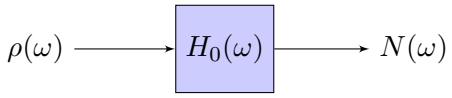

Figure 8.2: Reactor transfer function scheme [25].

The reactor transfer function is the frequency response of the reactor and can be experimentally measured by neutron noise analysis. Neutron noise analysis consists in exploiting the inherent reactivity fluctuations of the reactor. This is very convenient because it is an experiment that can be performed without perturbing the reactor with external sources. One drawback of this technique is that it does not provide any information on the phase of the $H_0(\omega)$ since the input is not fully characterized [25]. However, the kinetic parameters of interest for delayed neutrons can be directly obtained from the frequency of the transfer function. For a fluctuating signal $x(\omega)$, the *Auto Power Spectral Density* (APSD or PSD) is defined as the power per unit frequency of the fluctuating signal, as a function of the frequency [25]. The PSD is nothing but a measure of the strength of the variations as a function of the frequency. In other words, it shows at which frequencies variations are strong and at which frequencies variations are weak. From a mathematical point of view, it is defined as the product of the function itself with its complex conjugate

$$G_x(\omega) = \overline{x}(\omega)x(\omega). \tag{8.1}$$

To improve the accuracy of the reactor noise technique, two detectors can be used instead of one. In that case, the *Cross Power Spectral Density* (CPSD) is computed, which allows the suppression of the background noise present in APSD measurements [25]. The CPSD of two functions x_ω and y_ω is given as

$$G_{xy}(\omega) = \overline{x}(\omega)y(\omega). \tag{8.2}$$

If $G_\rho(\omega)$ and $G_N(\omega)$ are the power spectral density function of input reactivity fluctuations and of output neutronic fluctuation, it follows that

$$G_N(\omega) = |H(\omega)|^2 G_\rho(\omega), \tag{8.3}$$

where $H_0(\omega)$ is the so wanted reactor transfer function. Since the reactivity fluctuations in a nuclear reactor have a large frequency range, they appear as white noise and have a

constant magnitude independently of the frequency. This means that $G_\rho(\omega)$ is constant and Eq. 8.3 can be used to estimate $H_0(\omega)$ directly from $N(\omega)$ [25].

The evolution in time of the neutron population is described by the *point reactor kinetic equations*, shown in Eq. 8.4 [34]

$$\begin{cases} \frac{\partial \delta N}{\partial t} & = \frac{\rho-\beta_{eff}}{\Lambda}\delta N + \frac{N}{\Lambda}\delta\rho + \sum_{j=1}^{n}\lambda_j \delta C_j \\ \frac{\partial \delta C_j}{\partial t} & = \frac{\beta_j}{\Lambda}\delta N - \lambda_j \delta C_j \qquad\qquad j = 1, \cdots, n \end{cases} \tag{8.4}$$

Note that the system has been written in such a way to take into account the fluctuations of N, C_j (concentration of jth DN precursor) and ρ. Fourier transforms allow to rewrite the linear differential system as a linear algebraic system

$$\begin{cases} i\omega\delta N(\omega) & = \frac{\rho-\beta_{eff}}{\Lambda}\delta N(\omega) + \delta s(\omega) + \sum_{j=1}^{n}\lambda_j \delta C_j(\omega) \\ i\omega\delta C_j(\omega) & = \frac{\beta_j}{\Lambda}\delta N(\omega) - \lambda_j \delta C_j(\omega) \qquad\qquad j = 1, \cdots, n \end{cases} \tag{8.5}$$

where $\delta s(\omega)$ replaced $\frac{N}{\Lambda}\delta\rho(\omega)$. Extracting the $\delta C_j(\omega)$ from the second equation of system 8.5

$$\delta C_j(\omega) = \frac{\beta_j}{\Lambda}\frac{\delta N(\omega)}{(i\omega + \lambda_i)} \tag{8.6}$$

and replacing it in the first equation, one obtains the expression

$$i\omega\delta N(\omega) = \frac{\rho-\beta_{eff}}{\Lambda}\delta N(\omega) + \delta s(\omega) + \sum_{j=1}^{n}\frac{\lambda_j\beta_j}{\Lambda}\frac{\delta N(\omega)}{(i\omega+\lambda_j)} \tag{8.7}$$

from which, after some algebraic steps, it is possible to derive $\delta N(\omega)$

$$\delta N(\omega) = \frac{\Lambda\delta s(\omega)}{i\omega(\Lambda + \sum_{j=1}^{n}\frac{\beta_j}{i\omega+\lambda_j}) - \rho} \tag{8.8}$$

The reactor transfer function is then given by the ratio between the output neutron noise and the input reactivity fluctuations

$$H(\omega) = \frac{\delta N(\omega)}{\delta s(\omega)} = \frac{\Lambda}{i\omega(\Lambda + \sum_{j=1}^{n}\frac{\beta_j}{\lambda_j+i\omega}) - \rho} \tag{8.9}$$

Noise techniques allow the measurement of the β_{eff} with an uncertainty of at least 2.5%, since the Diven factor itself accounts for about 1.3% [21].

8.3 Validation of the average DN yield

8.3.1 MISTRAL1

MISTRAL1 is an experimental program that took place in EOLE critical facility from 1996 to 2000 [34]. EOLE was a zero-power research reactor situated at CEA Cadarache. Two critical cores have been used for the MISTRAL experiments: UOx (MISTRAL1) and MOx (MISTRAL2). The first one was a regular LWR core with UO_2 enriched at

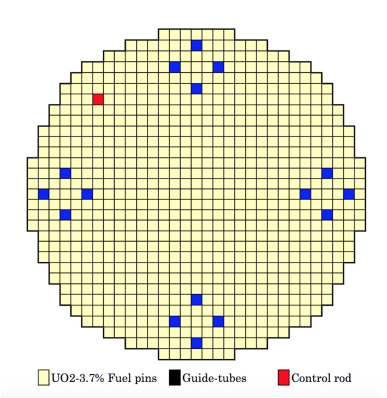

(a) Radial cross section of the MISTRAL1 core.

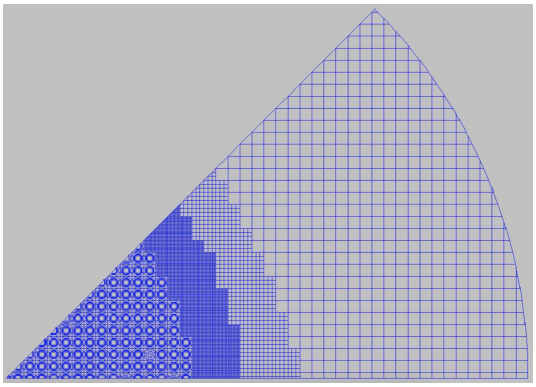

(b) MOC mesh for MISTRAL1 core calculation, taken from [34].

Figure 8.3: MISTRAL1 core scheme.

3.7% of ^{235}U. The core was made of 750 fuel pins, of the PWR type, arranged as shown in Fig. 8.4. The moderator-to-fuel ratio (V_{mod}/V_{fuel}) was 1.7 [34]. The core was made critical by changing the boron concentration. The objective of MISTRAL1 experiment was to measure the effective delayed-neutron fraction β_{eff} of the core through the CPSD method [34] (see Section 8.2 for a description of the technique). Computing the auto power spectral densities[1] of the neutron population and of the reactivity fluctuations, Eq. 8.3 becomes

$$|\delta N(\omega)|^2 = |H(\omega)|^2 |\delta s(\omega)|^2. \tag{8.10}$$

It has been mentioned in Section 8.2 that the reactivity fluctuations, having a large range of frequencies, appear as white noise. As a consequence, their APSD is constant and can be described as [34]

$$\overline{|\delta s(\omega)|^2} = 2\frac{N}{\Lambda}\frac{\overline{\nu(\nu-1)}}{\overline{\nu}} = 2\left(\frac{N}{\Lambda}\right)^2\frac{D}{F}. \tag{8.11}$$

Replacing Eq. 8.3 and 8.11 in Eq. 8.1 and rearranging the terms, one gets

$$\frac{|\delta N(\omega)|^2}{N^2} \approx 2\frac{D}{F}\frac{1}{(\beta_{eff}-\rho)^2} \tag{8.12}$$

which is valid for APSD analysis. Using two counters and applying the Fourier transformation to their signals, it is possible to correlate them [34]. In that case, the method is called CPSD and Eq. 8.12 becomes

$$\frac{CPSD}{V_1 V_2} \approx 2\frac{D}{F}\frac{1}{(\beta_{eff}-\rho)^2} \tag{8.13}$$

from which the effective delayed-neutron fraction can be determined as

$$\beta_{eff}^2 \approx 2\frac{D}{F}\frac{1}{(1+|\rho_\$|)^2}\frac{V_1 V_2}{CPSD}. \tag{8.14}$$

Note that V_1 and V_2 are the voltages of the two fission chambers placed in the core, D the Diven factor, and F the fission rate. The Diven factor is a computed parameter and

[1] It is worth to recall that the auto power spectral density is given by the product of the fluctuating function and its complex conjugate. Remember also the following property of complex conjugates: $\overline{z}z = |z|^2$.

is equal to $D = 0.800$ (<2%) [34]. The fission rate has been estimated through a fission chamber placed in the core, corrected by a simulated factor which took into account the ratio between the total fission rate in the core and the one in the detector. The other parameters have all been experimentally measured.

Table 8.4 shows the effect of the input data on the results of a TRIPOLI4® simulation[2]. The first thing to note is the expected increase and reduction in the contribution of $^{235}U_t$ and $^{238}U_f$ to the global β_{eff}, respectively. Such changes directly reflect the differences in

Table 8.4: Effect of the DN input data on the simulated β - MISTRAL1.

Isotope	T4-JEFF-3.1.1	T4-Foligno
^{234}U	0.03 (20.14%)	0.03 (20.14%)
^{235}U	693.2 (0.14%)	704.1 (0.14%)
^{238}U	100.7 (0.36%)	94.6 (0.37%)
Mix	793.9 (0.13%)	798.8 (0.13%)

the average delayed-neutron yields. In the MISTRAL1 core, the two effects are almost perfectly compensated, leading to a total effective delayed-neutron fraction which differs by only 4.9 pcm (+10.9 for the $^{235}U_t$ and -6.1 for the $^{238}U_f$). The $^{234}U_f$ can be neglected, as demonstrated in Tab. 8.5, where the contribution of the different nuclides to the β_{eff} is shown. It is worth mentioning that the uncertainties associated with the simulated

Table 8.5: Contribution of the different fissioning systems to the β_{eff} of the MISTRAL1 core. f_x is the contribution of x to the β_{eff} of the mix.

	T4-JEFF-3.1.1	T4-Foligno
β_{eff} [pcm]	793.9	798.8
f_4 [%]	0.003	0.003
f_5 [%]	87.3	88.1
f_8 [%]	12.7	11.9

quantities are an indication of the simulation's convergence and do not, in any case, reflect the errors in microscopic nuclear data. The fact that the ALDEN experiment allowed a reduction in the uncertainty of the ν_d for $^{235}U_t$ is therefore not taken into account in this section. The same is true for the larger uncertainty in the $^{238}U_f$'s ν_d, as it came from a calculation. The propagation of nuclear data uncertainties will be treated in Section 8.5. It is interesting to note that the measurement performed in MISTRAL1 core produced a β_{eff} with an uncertainty of 1.6%, where 1% was due to the Diven factor. At the same time D'Angelo, in his paper [21], stated that noise techniques are generally accurate to 2.5%, where about 1.3% is due to the Diven factor. The comparison between simulated (C) and measured (E) effective delayed-neutron fraction is shown in Tab. 8.6. Evidently, the compensation of the β_{eff} of the two main fissioning systems, leads to almost the same C/E. Note that the uncertainty reported in Tab. 8.6 is the one associated with the experimental value.
In the MISTRAL1 program, the difficulty in the standard experimental technique based on neutron noise analysis was due to the need to include data which were difficult

[2]It is recalled that the difference between *JEFF-3.1.1* and *Foligno et al.* is in the set of abundances, in the first decay constant, and in the average DN yield of $^{235}U_t$ and $^{238}U_f$, as shown in Tab. 8.3.

Table 8.6: β_{eff} simulation comparison for the MISTRAL1 core. Note that the uncertainties associated with the (C-E)/E are nothing but the uncertainties on the experiment (E).

Quantity	MISTRAL1 [pcm]	T4-JEFF-3.1.1 (C-E)/E [%]	T4-Foligno (C-E)/E [%]
β_{eff}	788.2 (1.5%)	$+0.73 \pm 1.5\%$	$+1.3 \pm 1.5\%$

to calculate or to measure. One of these data is especially the Diven factor which is related to the knowledge of the probability distribution neutron multiplicity and which is commonly reported with an uncertainty of 1-2% (1σ). Another difficult data to evaluate is the fission integral which requires both a measurement of the the critical system's absolute power and an accurate calculation of the fission rate distribution within the core.

8.3.2 IPEN/MB-01

The second benchmark is an experimental program which took place in the IPEN/MB-01 critical mock-up facility located in Sao Paulo, Brazil. The core, shown in Fig. 8.4, was a 28×26 lattice of stainless steel cladded fuel pins made of UO_2 (4.35% ^{235}U), with a moderation ratio of about 2.7 (slightly larger than a typical PWR). Criticality was reached through the adjustment of two groups of Ag-In-Cd control rods. The experiment

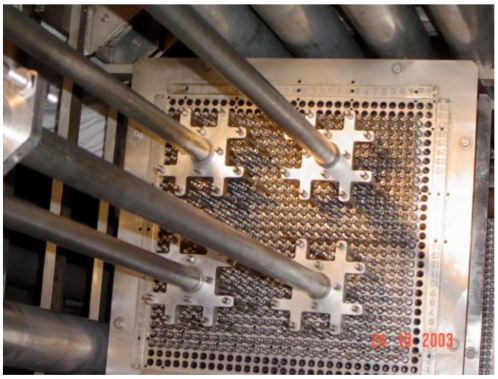

Figure 8.4: Picture of the IPEN/MB-01 core, taken from [32].

was made of a macroscopic and a microscopic part. The latter consisted in microscopic noise experiments to obtain β_{eff}, Λ and β_{eff}/Λ. It could be considered as a combination of Rossi-α and Feynman-α noise techniques [32]. Compared to MISTRAL1, this method allowed the estimation of the parameters without having to compute or measure D or F. Figures 8.5a and 8.5b show the contribution of the different isotopes to the reactivity as a function of the reactor period.
The first one reports the single reactivities and their sum in dollars. The second one details the contribution of each fissioning system in percentage of the total reactivity. It is clear from the two figures that ^{235}U dominates in this type of reactor, and that the uncertainty in the reactivity will be mostly driven by the uncertainties in the nuclear data associated with the ^{235}U.
Remember that the main difference between JEFF-3.1.1 and Foligno lies not in the values they recommend but in the associated uncertainties. Table 8.7 shows the effect

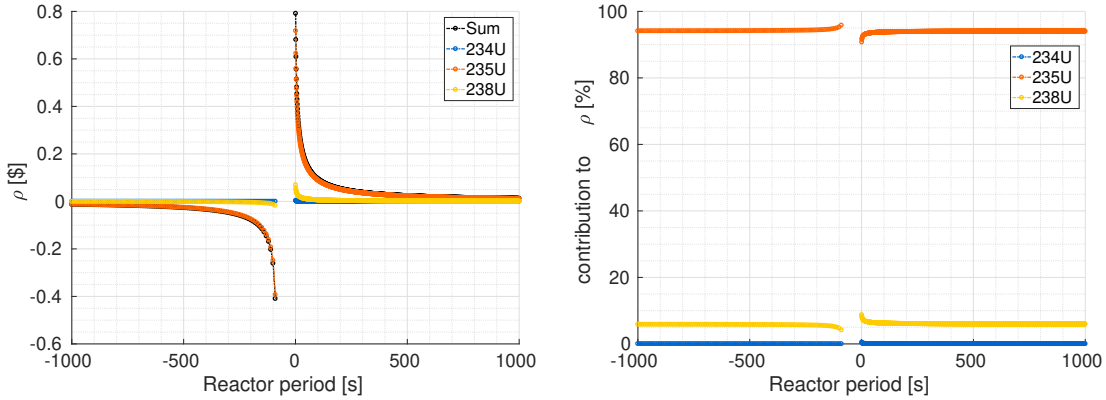

(a) Absolute contribution to the reactivity.

(b) Relative contribution to the reactivity.

Figure 8.5: Decomposition of the reactivity in the IPEN/MB-01 core.

of the input data on the results of the simulation.

Table 8.7: Effect of the DN input data on the simulated β - IPEN/MB-01.

Isotope	T4-JEFF-3.1.1	T4-Foligno
^{234}U	0.03 (20.53%)	0.03 (20.53%)
^{235}U	700.2 (0.13%)	711.2 (0.13%)
^{238}U	74.2 (0.42%)	69.7 (0.42%)
Mix	774.3 (0.13%)	780.9 (0.13%)

Again, an increase in the β $^{235}\mathrm{U_t}$ is followed by a reduction in the β $^{238}\mathrm{U_f}$. This time, the compensation of the two effects is weaker due to higher enrichment of the core in ^{235}U. This is reflected in a larger contribution of this fissioning system to the global effective delayed-neutron fraction (see Tab. 8.8).

Table 8.8: Contribution of the different fissioning systems to the β_{eff} of the IPEN/MB-01 core. f_x is the contribution of x to the β_{eff} of the mix.

	T4-JEFF-3.1.1	T4-Foligno
β_{eff} [pcm]	774.3	780.9
f_4 [%]	0.003	0.003
f_5 [%]	90.4	91.1
f_8 [%]	9.6	8.9

The comparison between simulated and measured quantities is done in Tab. 8.9. Both calculations overestimate the β_{eff} by more than 3%, JEFF-3.1.1 being closer to the experimental value.

Table 8.9: TRIPOLI4® β_{eff} simulation comparison for the IPEN/MB-01 core. Note that the uncertainties associated with the (C-E)/E are nothing but the uncertainties on the experiment (E).

Quantity	IPEN [pcm]	JEFF-3.1.1 (C-E)/E [%]	Foligno et al. (C-E)/E [%]
β_{eff}	750.0 (0.67%)	+3.25 ± 0.67%	+4.12 ± 0.67%

8.3.3 SNEAK7B

The last benchmark aims at studying more in detail the effect due to the reduction of the ν_d for ^{238}U. For that purpose, a MOX core for which ^{238}U contributes by more than 50% to the β_{eff} [21], has been chosen. The benchmark under consideration took place in the SNEAK facility. SNEAK (*Schnelle Null-Energie-Anordnung, Fast Zero-Power Facility Karlsruhe*) was a zero-power liquid metal fast reactor situated in Karlsruhe. Two cores have been used: SNEAK7A and SNEAK7B (Fig. 8.6), both fueled with PuO_2-UO_2 (26.6% PuO_2 containing 8% of ^{240}Pu) and reflected by metallic depleted uranium [22].

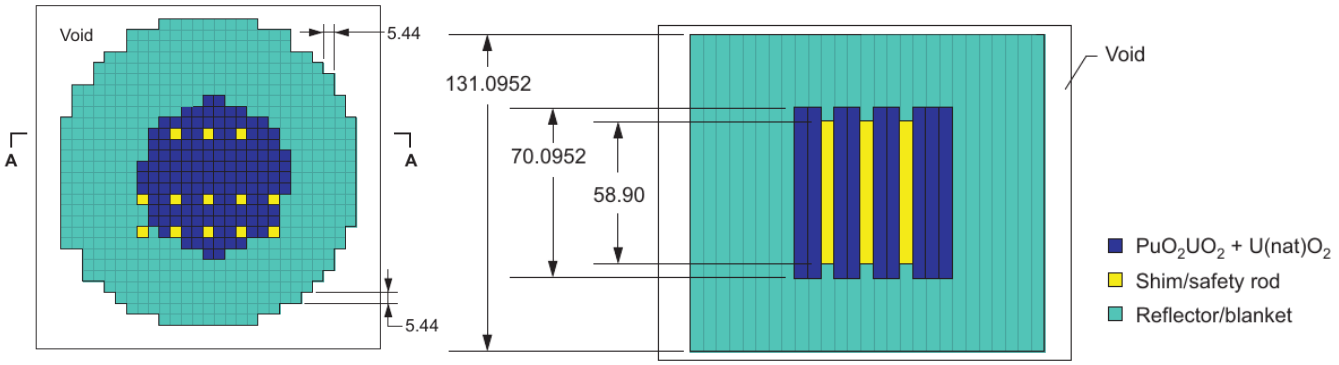

(a) Mid-plane section of the SNEAK7B core.

(b) Vertical section of the SNEAK7B core.

Figure 8.6: Scheme of the SNEAK7B core, taken from [22].

SNEAK7A was made of sandwiches of PuO_2-UO_2 and graphite platelets. On the other hand, SNEAK7B was made of sandwiches of PuO_2-UO_2 and natural UO_2 platelets, thus reducing the PuO_2 content of the core to 13%. Table 8.10 reports the contribution of the different fissioning systems to the β_{eff} of the SNEAK7B core.
Experiments for SNEAK7B were completed in the second half of 1971. The effective delayed-neutron fraction and the reactivity worth have been measured through pile-oscillator. In SNEAK7B the calibrated automatic control rod has been used to determine the reactivity effect of the oscillating sample. The frequency analysis was performed with two sets of coupled ^{3}He-detectors, positioned at the core mid-plane of the assembly. The fluctuations and the mean values of the ionization chamber currents were amplified separately [22]. Then, the integrated mean value was obtained using an analog-to-digital converter and an impulse counter. Note that the experimental system was calibrated with a reference signal before and after each measurement since to determine the β_{eff} an absolute measurement of the power spectral density was needed. The β_{eff} measurements were performed employing two different techniques:

Table 8.10: Contribution of the different fissioning systems to the β_{eff} of the SNEAK7B core. f_x is the contribution of x to the β_{eff} of the mix.

	T4-JEFF-3.1.1	T4-Foligno
β_{eff} [pcm]	433.3	419.2
f_5 [%]	11.4	12.0
f_8 [%]	57.1	55.5
f_9 [%]	29.8	30.8
f_0 [%]	0.9	0.9
f_1 [%]	0.8	0.9
f_2 [%]	0.005	0.005

1. measurement of β_{eff} by using ^{252}Cf source
2. measurement of β_{eff} using noise analysis

In the first one, the β_{eff} was measured using a known ^{252}Cf source. The procedure consisted in measuring ρ_{Cf} and the absolute fission rate R_f at the core center, which were then normalized to the reactor power. A corrective factor Φ^+_{Cf}/Φ^+_f was applied to take into account the difference between fission and ^{252}Cf neutrons. In the second technique, the classical reactor noise analysis has been used. In principle, these two measurements could be considered as independent, even though corrective factors have to be calculated in the two cases. At the end of the benchmark, the recommended value of β_{eff} is the one obtained using the ^{252}Cf source. The uncertainty in the β_{eff} is considered to be made of two components: uncertainty of the method and statistical uncertainty of the measurements. Note that for the simulation with Foligno's parameters only ^{235}U and ^{238}U have been modified. The reason is that, as shown in Sections 3.5 and 4.5, the results of the microscopic calculations for ^{239}Pu are very close to JEFF-3.1.1. Furthermore the objective of this benchmark was to isolate the effect of ^{238}U. Table 8.11 reports the results of the simulation performed with JEFF-3.1.1 and with Foligno's data. This time, the increase in the ^{235}U yield is much weaker, due to the composition of the

Table 8.11: Effect of the DN input data on the simulated β - SNEAK7B.

Isotope	T4-JEFF-3.1.1	T4-Foligno
^{235}U	49.4 (0.55%)	50.2 (0.55%)
^{238}U	247.4 (0.25%)	232.6 (0.25%)
^{239}Pu	128.9 (0.34%)	128.9 (0.34%)
^{240}Pu	4.0 (1.97%)	4.0 (1.97%)
^{241}Pu	3.6 (2.08%)	3.6 (2.08%)
^{242}Pu	0.02 (24.6%)	0.02 (24.6%)
Mix	433.3 (0.19%)	419.2 (0.19%)

core. Changing the input data, the main effect is a significant reduction in the β_{eff} associated with the ^{238}U. As a consequence, the effective delayed-neutron fraction of the mix loses about 14 pcm. Table 8.12 shows the (C-E)/E for the β_{eff} of the core. As far as the simulated values are concerned, JEFF-3.1.1's is closer to the measured one, but no conclusions can be drawn due to the large experimental uncertainty but also due to the fact that other factors play a role in fast spectrum reactors, like ^{239}Pu ν or ^{239}Pu(n,f) [29].

Table 8.12: β_{eff} simulation comparison for the SNEAK7B core. Note that the uncertainties associated with the (C-E)/E are nothing but the uncertainties on the experiment (E).

Quantity	SNEAK7B [pcm]	T4-JEFF-3.1.1 (C-E)/E [%]	T4-Foligno (C-E)/E [%]
$\beta_{eff,Cf}$	429.0 (5.0%)	+1.00 ± 5.0%	-2.30 ± 5.0%

8.4 Validation of the kinetic parameters

The macroscopic part of the IPEN/MB-01 experiment consisted of a macroscopic noise measurement. The innovation with respect to MISTRAL1 was to apply the technique to the group kinetic parameters (λ_i, β_i). They have been obtained through a LSF of the measured APSD and CPSD, which can be described as

$$\Phi_{kk}(f) = 2D\frac{\gamma}{P\Lambda^2}I_k^2|H_0(f)|^2|H_{ek}(f)H_{fk}(f)|^2 + 2|H_{ek}(f)H_{fk}(f)|^2 I_k\overline{q} \tag{8.15}$$

and

$$\Phi_{kl}(f) = 2D\frac{\gamma}{P\Lambda^2}I_k I_l|H_0(f)|^2[H_{ek}(f)\overline{H_{el}(f)}][H_{fk}(f)\overline{H_{fk}(f)}] \tag{8.16}$$

respectively, where γ is the energy per fission, P the reactor power, I the detector current of detector k and l, H_0 the reactor transfer function (Eq. 8.3), H_e the electrometers transfer function, H_f the filter amplifiers transfer function and $\overline{q}$ the mean electric charge released per detected neutron. The fit allowed the estimation of an experimental set of Λ, β_i and λ_i, which have then been used to validate the relation between the reactivity and the reactor period, based on the Inhour equation. Such quantities can as well be calculated through simulations, and used to estimate the reactivity. The comparison between simulated and measured abundances is shown in Tab. 8.13.

Table 8.13: TRIPOLI4® abundances simulation comparison for the IPEN/MB-01 core. Within brackets, the relative uncertainty of the abundances is reported. Note that the uncertainties associated with the (C-E)/E are nothing but the uncertainties on the experiment (E).

Quantity	IPEN [%]	JEFF-3.1.1 (C-E)/E [%]	Foligno et al. (C-E)/E [%]
a_1	3.57 (0.8%)	-12.7 ± 0.8%	-4.9 ± 0.8%
a_2	14.18 (3.5%)	+2.7 ± 3.5%	-7.9 ± 3.5%
a_3	7.60 (10.1%)	+17.1 ± 10.1%	39.2 ± 10.1%
a_4	18.13 (7.2%)	+6.7 ± 7.2%	-3.9 ± 7.2%
a_5	34.44 (2.8%)	-5.9 ± 2.8%	-4.1 ± 2.8%
a_6	10.17 (7.9%)	-0.7 ± 7.9%	+3.7 ± 7.9%
a_7	8.62 (3.7%)	-0.3 ± 3.7%	-7.6 ± 3.7%
a_8	3.29 (21.3%)	-9.6 ± 21.3%	+18.8 ± 21.3%

Clearly, the individual groups are characterized by larger discrepancies than the β_{eff} , due to both the abundances and the ν_d of the two main fissioning systems. At first sight, it seems that the use of Foligno's parameters leads to an improvement in the simulation of some group abundances (1, 4, and 5) and to a deterioration of others (2,

3, 6, 7, and 8) with respect to JEFF-3.1.1. Luckily, the groups contributing the most to the delayed-neutron emission (4 and 5), belong to the first category. Nevertheless, it has been shown in Section 4.4 that deriving the a_i from the fit of the decay curve is more conservative with respect to the activity, while using the direct summation better preserves the reactivity. In this work, the exponential equivalence has been used to estimate the prior for the Bayesian assimilation of the ALDEN experiment, in order to prioritize the prediction of the reactivity. The Inhour equation can be used to estimate the reactivity from the measurement of the reactor period. The fact that the reactivity has been measured during the IPEN/MB-01 experiment, allows the direct comparison C/E to see if the data associated with delayed neutrons are sufficiently well known to reconstruct the reactivity. Table 8.14 reports the measured reactivity values as well as the deviation (C-E)/E when performing a TRIPOLI4® simulation. This time, the results obtained using the American library are reported for comparison.

Table 8.14: Reactivity simulation comparison for the IPEN/MB-01 core. Note that the uncertainties associated with the (C-E)/E are nothing but the uncertainties on the experiment (E).

T	IPEN ρ [\$]	ENDF/B-VIII.0 (C-E)/E [%]	JEFF-3.1.1 (C-E)/E [%]	Foligno et al. (C-E)/E [%]
-200	-0.076 (6.5%)	-13.1 ± 6.5%	+3.0 ± 6.5%	+3.4 ± 6.5%
-100	-0.268 (5.2%)	-14.9 ± 5.2%	-2.0 ± 5.2%	+0.9 ± 5.2%
-90	-0.437 (4.3%)	-16.1 ± 4.3%	-5.3 ± 4.3%	-0.7 ± 4.3%
-85	-0.761 (3.3%)	-18.1 ± 3.3%	-8.7 ± 3.3%	-2.0 ± 3.3%
1	0.776 (0.6%)	-3.7 ± 0.6%	+0.9 ± 0.6%	0.3 ± 0.6%
10	0.379 (1.8%)	-8.6 ± 1.8%	+2.5 ± 1.8%	+1.7 ± 1.8%
100	0.092 (4.3%)	-12.8 ± 4.3%	+3.5 ± 4.3%	+3.0 ± 4.3%
200	0.052 (3.8%)	-12.8 ± 3.8%	+3.3 ± 3.8%	+2.8 ± 3.8%

Large periods correspond to small reactivity insertions, which can be approximated as

$$\rho \approx \frac{\beta_{eff}\overline{T_{1/2}}}{\tau}. \tag{8.17}$$

The estimation of the reactivity from the measurement of the reactor period therefore depends on both the effective delayed-neutron fraction and the mean lifetime. Foligno's parameters give a slightly larger β_{eff} than JEFF-3.1.1 (6.5 pcm, thus 0.8% of the one simulated with JEFF-3.1.1). At the same time, as far as $\overline{T_{1/2}}$ is concerned, Foligno's is 0.9% (-0.05 s) and 3.7% (-0.20 s) smaller than JEFF-3.1.1 for ^{235}U and ^{238}U, respectively. The global effect is that the reactivity simulated with Foligno's parameters is, for all periods, closer to the measured one. In particular, a strong improvement occurs for large negative reactivities. Figure 8.8 shows the C/E for both sets of parameters. It is evident that Foligno's data leads to a small worsening of the C/E for some of the individual abundances, compensated by a significant improvement of the predictive power for negative large reactivity insertions. This amelioration is highlighted in Fig. 8.8. Note that the American library, which recommends the same kinetic parameters since 1989, strongly underestimates the negative reactivities, reaching 20% of discrepancy for a period of -85 s.

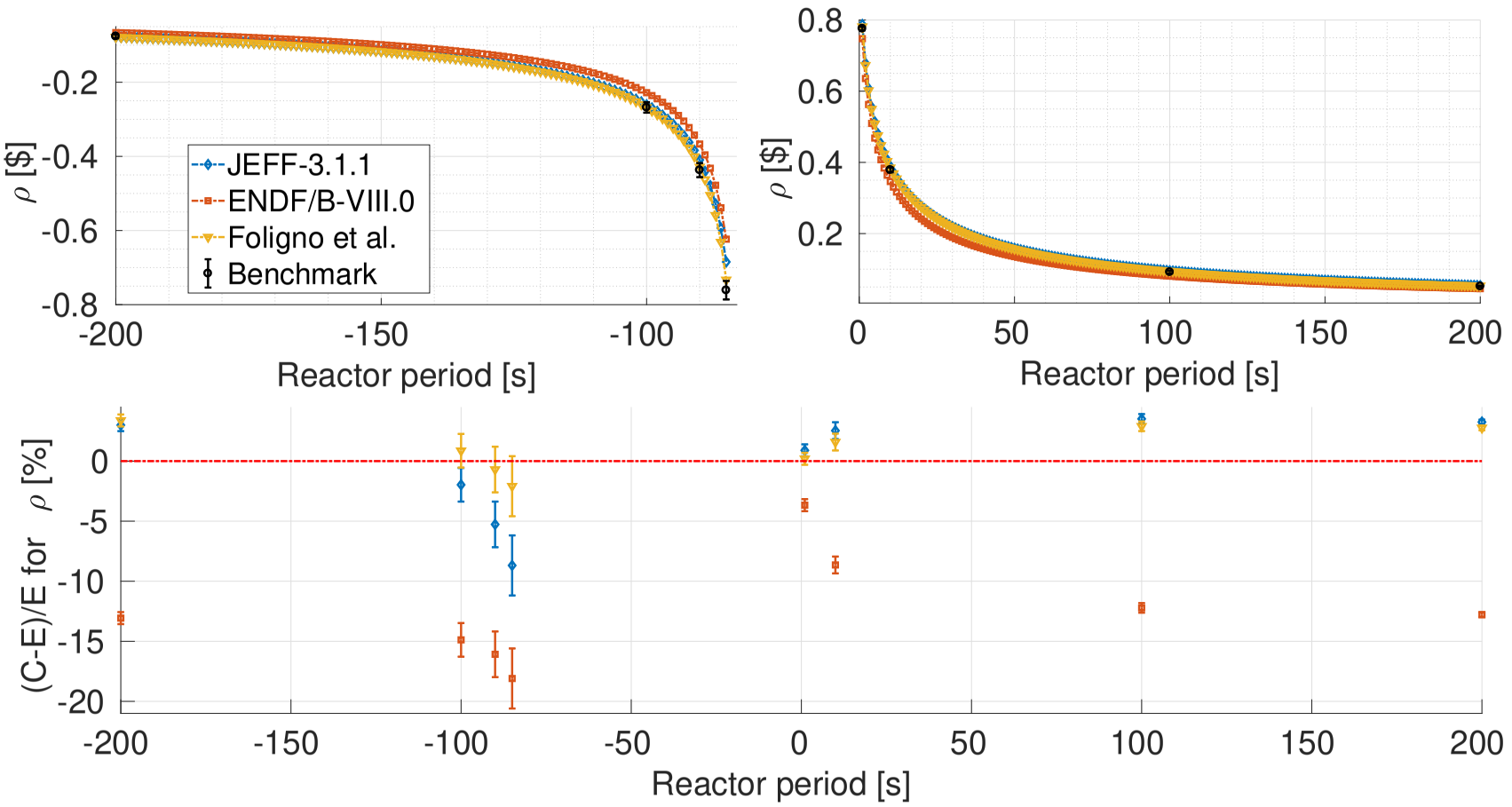

Figure 8.7: Reactivity comparison.

Figure 8.8: Reactivity simulation comparison for the IPEN/MB-01 core. Note that the uncertainties associated with the (C-E)/E are nothing but the uncertainties on the experiment (E).

8.5 Uncertainty propagation on the reactivity for a PWR-type reactor

The comparison done in the previous Section dealt with the *accuracy* of the prediction, meaning how far the simulated quantity was from the true value (the measured one). Clearly, another important factor to consider is the *precision* of such quantity, thus the dispersion of the calculated values.
Subsections 8.3 and 8.4 focused on the *accuracy* of the simulation, meaning that it showed the impact of the input data on the *value* of the predicted reactivity. This subsection focuses instead on the *precision* of the simulation, thus on the impact of the input data on the *uncertainty* associated with the predicted reactivity. It is worth to recall that the quantities computed by summation method, like for ^{238}U, are characterized by larger uncertainties than the recommended values. At the same time, the work performed on the $^{235}U_t$, which consisted of a combination of calculations and measurements, led to a strong reduction of the uncertainties associated with the DN data of this isotope, especially when using the correlation matrix in the uncertainty propagation. It is time to see the effect of this reduction on the reactivity error. The reactivity for a single fissioning system x, expressed in pcm, is given by

$$\rho_{pcm,x} = \frac{\Lambda}{\tau} + \beta_x \sum_{i=1}^{8} \frac{a_i}{\lambda_i \tau + 1}. \tag{8.18}$$

For a mix of isotopes, ρ becomes

$$\rho_{mix} = f_4\rho_4 + f_5\rho_5 + f_8\rho_8, \tag{8.19}$$

where f_x represents the contribution of x to the β_{eff} of the mix, reported in Tab. 8.8 for the IPEN/MB-01 experiment
The term $f_4\rho_4$ is so small that it can be neglected in the uncertainty propagation. The error associated with the total reactivity therefore becomes

$$\sigma_{\rho_{mix}} = \sqrt{(f_5\sigma_{\rho_5})^2 + (f_8\sigma_{\rho_8})^2} \tag{8.20}$$

which can be developed as

$$\begin{aligned}\sigma_{\rho_x} &= \sqrt{\left(\frac{\partial\rho}{\partial\Lambda}\sigma_\Lambda\right)^2 + \left(\frac{\partial\rho}{\partial\beta_{eff}}\sigma_{\beta_{eff}}\right)^2 + \sum_{i=1}^{8}\sum_{j=1}^{8}\frac{\partial\rho}{\partial a_i}\frac{\partial\rho}{\partial a_j}corr(a_i,a_j)\sigma_{a_i}\sigma_{a_j}} \\ &= \sqrt{\left(\frac{\sigma_\Lambda}{\tau}\right)^2 + \left(\sigma_{\beta_{eff}}\sum_{j=1}^{8}\frac{a_i}{\lambda_i\tau+1}\right)^2 + \sum_{i=1}^{8}\sum_{j=1}^{8}\left(\frac{\beta_{eff}\sigma_{a_i}}{\lambda_i\tau+1}\right)\left(\beta_{eff}\frac{\sigma_{a_j}}{\lambda_j\tau+1}\right)corr(a_i,a_j)}.\end{aligned} \tag{8.21}$$

Thanks to the ALDEN experiment, Foligno's parameters are characterized by much lower errors than JEFF-3.1.1, and this must be reflected in the uncertainty of the reactivity estimated through the measurement of the reactor period. Notably, for small reactivities, the reactor period is governed almost completely by the delayed-neutron properties. This means that the uncertainty in the reactivity will only depend on the accuracy of β_{eff} and $\overline{T_{1/2}}$ associated with the main fissioning systems. It is worth to underline that β_{eff} depends on several parameters (ν_d, prompt- and delayed-neutron spectra, fission cross sections etc.). However, Kodeli [29] showed that more than 90% of the uncertainty in the

β_{eff} comes from the uncertainty in the average delayed-neutron yield. In this section, it is assumed that $\sigma_{\beta_{eff}} = \sigma_{\nu_d}$. As far as JEFF-3.1.1 library is concerned, the mean precursors half-life is given with an uncertainty of 3.0%. Note that JEFF-3.1.1 does not provide uncertainties for the average delayed-neutron yields. For that reason, the values suggested by Tuttle [56] have been used in the uncertainty propagation (3.1% for ^{235}U and 2.3% for ^{238}U). As far as Foligno's parameters are concerned, the ν_d and the $\overline{T_{1/2}}$ for ^{235}U are recommended with an uncertainty of 1.6% and 0.6%, respectively. For ^{238}U, these quantities become 3.4% and 4.8%.
Figure 8.9 shows the calculated uncertainties as a function of the reactivity expressed in pcm, for the two sets of input data under consideration, with and without the use of the correlation matrix.

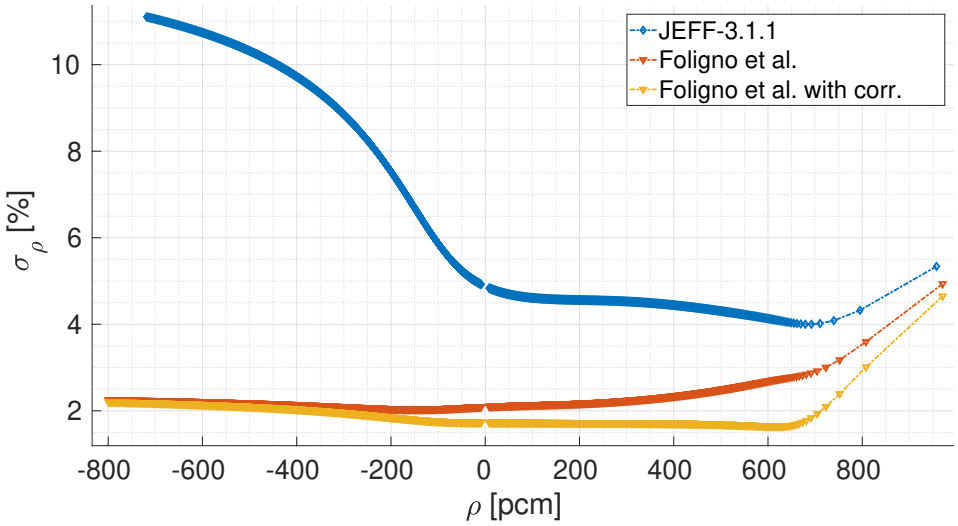

Figure 8.9: Effect of the input data on the uncertainty in the simulated reactivity.

For long periods ($\rho \to 0$), the uncertainty in the reactivity reaches an asymptotic value of 4.9% for JEFF-3.1.1 and 2.1% for Foligno. When taking into account the correlation matrix in the uncertainty propagation, such asymptote reaches 1.7%. It is evident that the error is driven by the product $\overline{T_{1/2}}\ \beta_{eff}$. For large positive reactivity insertions ($\rho_\$ > 0.95$), Λ becomes the dominating parameter (prompt criticality). To show this effect, a symbolic uncertainty of 15% has been assigned to Λ, which is responsible for the rise in the right part of the plot. For smaller reactivities, its uncertainty has no effect at all. Finally, for large negative reactivities, the decay of the precursors will supply neutrons at their natural decay rate, independently of the amount of inserted reactivity. Thus, the asymptotic period only depends on the longest-lived DN precursor's half-life.

Looking at the whole range of reactor periods, JEFF-3.1.1 is able to predict the reactivity with an uncertainty which goes from 4.0 to 11.1%. For the same periods, Foligno's parameters give a flatter uncertainty curve, ranging from 1.6 to 2.2%. The rise above 0.95\$ is due to the uncertainty in the prompt neutron generation time - assumed to be 15% - which does not depend on this work.

Conclusions and Perspectives

> The world is round and the place
> which may seem like the end
> may also be only the beginning.
>
> Ivy Baker Priest

Microscopic Approach

Before the beginning of this Ph.D., the usual way to treat delayed neutron data was to measure the parameters related to the major isotopes and to compute the ones for which experiments were poor or missing. The innovation of this work was to apply, for delayed neutron data, the same procedure generally used for cross section evaluation [54]. The technique consists in carrying out a calculation using microscopic data for the estimation of the quantities of interest together with their uncertainties and covariances. The second step consists in adding information through the Bayesian assimilation of integral experiments. This technique, more comprehensive than just a simple experiment or calculation, has been tested on the delayed neutron data associated with the thermal fission of ^{235}U.

For that purpose, a bibliographic study on the state of the art of delayed neutron data and uncertainty management methods has been followed by a thorough work on the microscopic databases comparison. The latest allowed the identification of two errors in the evaluated libraries (the FY of ^{86}As in ENDF/B-VII.0[3], and the Pn of ^{98m}Y in ENDF/B-VII.1[4]), which have been pointed out at the *6th Workshop on Nuclear Fission* in 2017 and led to a first publication [18]. At the end of the microscopic data comparison, a combination FY-RDD has been chosen to perform all the calculations presented in the manuscript. The fission yields are taken from JEFF-3.1.1 while the radioactive decay data from ENDF/B-VIII.0[5].

In order to easily and quickly perform summation calculations with the versatility required to perform sensitivity analysis, a solver has been coded in C++: the *Bateman solver*. Such program allows translating the databases from the ENDF-6 format into an easily readable text file and computing any quantity associated with delayed neutrons.

[3] This error has been independently found by A. Sonzogni as well. When the author told the responsible of this mistake, he was already aware of it

[4] Contrary to the previous error, this one passes unnoticed. When the author found it, no one knew about it and the responsible made sure that it would be corrected in the following version of the library

[5] The RDD recommended by the CRP in 2019 have not been used because not yet published at the time of the manuscript writing

The ν_d can be estimated both directly, using the cumulative yields of the precursors, or by reconstructing the decay chain of each precursor, and using the independent yields coupled with the branching ratios of the chosen RDD library. Note that CY depend on IY and RDD. As a consequence, the CY derived by using JEFF-3.1.1's IY and ENDF/B-VIII.0's RDD will not exactly correspond to JEFF-3.1.1's CY. However, the discrepancies are so low that they have no effect on the final value of ν_d. The average DN yield has been computed for the main fissioning systems ($^{232}\mathrm{Th_f}$, $^{233}\mathrm{U_f}$, $^{235}\mathrm{U_t}$, $^{235}\mathrm{U_f}$, $^{236}\mathrm{U_f}$, $^{238}\mathrm{U_f}$, $^{237}\mathrm{Np_f}$, $^{239}\mathrm{Pu_t}$, $^{239}\mathrm{Pu_f}$, $^{241}\mathrm{Pu_t}$, $^{241}\mathrm{Pu_f}$, $^{241}\mathrm{Am_f}$) and compared with the recommended values. Another innovation of this work is the production of the first correlation matrix among the yields of different fissioning systems. These correlations owe their origin to the fact that fissioning systems share the same branching ratios and decay constants. However, it has been demonstrated that correlations are very weak, which justify the use of the different ν_d as if the fissioning systems were independent of each other.

The Bateman solver allows also the estimation of the kinetic parameters using 4 different techniques. Two of them are direct estimation, which means that the abundances come from the direct calculation of the contribution of each precursor to its group. In the *Simple Equivalence*, each precursor belongs to a group, while in the *Exponential Equivalence* the contribution of a precursor is spread over the two adjacent groups according to its half-life. The other two techniques consist in the calculation of the delayed neutron activity curve, followed by a fit of the curve. What changes between the two methods of fitting is the uncertainty propagation technique. In the *Analytical Marginalization* the central value of the parameters is used in the fitting model. At the same time, the parameters are perturbed according to their error[6] for the estimation of the uncertainty in the fitted quantities. On the contrary, in the *Monte Carlo Marginalization*, the model is directly used with the perturbed parameters, and the procedure is repeated for a certain number of times. If this number is sufficiently large, the fitted values converge to the ones computed by analytical marginalization. The uncertainty in the two cases, is supposed to be the same, because it depends on the uncertainty of the marginalized parameters.

Perspective: In the Annex 3 of the WPEC-SG6 report [38], Spriggs states that the expansion technique is an acceptable *temporary* technique to transform unconstrained 6-group parameters into equivalent 8-group ones. The reason is that the equivalent model is different from an original constrained 8-group fit. Spriggs and his colleagues tested the validity of the expansion technique using the experimental data of $^{237}\mathrm{Np}$ and demonstrated that there are some noticeable discrepancies, particularly in the short-lived groups. Even though they are both able to adequately reproduce the decay curve, one must not forget that they are two different mathematical functions. V. Piksaikin recently measured the decay curve for different fissioning systems and obtained unconstrained 6-groups kinetic parameters, from which he derived the equivalent 8-group abundances. In light of Spriggs' work, it would be interesting to reprocess the Russian raw activity data to obtain constrained 8-groups kinetic parameters to be compared with the ones recommended by the IPPE. Obviously, such comparison should include uncertainties and correlations.

[6] We say that the parameters are *marginalized*

Energy Dependence

The energy dependence of both the average delayed neutron yield and the kinetic parameters has been investigated. The evaluated libraries provide fission yields at three energies only, which is insufficient to infer any energy trend. Furthermore, thanks to the databases comparison, it has been demonstrated that the behavior of the calculated ν_d was never satisfying, which points toward a problem in the fission yields. Some of the isotopes that need to be better investigated have already been identified. Contrary to the evaluated libraries, GEF computes the FY from nuclear models. This means that it can provide FY at any energy. Another innovation of the Ph.D. consisted in applying GEF energy dependence to JEFF-3.1.1's FY. The resulting ν_d and kinetic parameters have been compared with experimental values. The conclusion is that the method has a good potential, but to date, normalizing to the thermal value, GEF is not able to reproduce the measured ν_d at 0.4 and 14 MeV. When this will be the case, the GEF energy trend of FY could be use to infer ν_d and a_i at any energy. It is also true that most of the measurements at energies other than thermal are old, sparse and of poor quality.

Perspective: It would be interesting, as a perspective, to perform the ALDEN experiment at different energies using an accelerator, and to compare with calculations. The same is true for fission yields measurements. Recently, M.E. Gooden and his team [44] performed experiments on the energy dependence of fission product yields from ^{235}U, ^{238}U, and ^{239}Pu, for energies between 500 keV and 14.5 MeV. Unfortunately, they focused on products that are not precursors and do not emit delayed neutrons. It is conceivable to repeat the experiments for delayed neutron precursors.

Delayed neutron spectra

Neutron spectra are the most poorly known delayed neutron quantities. The Bateman code is able to perform a summation calculation in order to estimate the equilibrium spectrum as well as the 8-group spectra. Unfortunately, an extensive work is needed to improve the individual precursors' spectral data, using both measurements and models.
Perspectives: The ALDEN experiment could be exploited to draw information on the group delayed neutron spectra. LOENIE-V2 is made of three rings of ^{3}He detectors, each being more sensitive to neutrons of a certain energy. It is worth recalling that the inner tubes are more sensitive to thermal neutrons, while the other tubes are more sensitive to fast neutrons. This phenomenon is highlighted in Fig. 8.10a, where the simulated ring ratio at different energies is plotted. As far as the ALDEN experiment is concerned, the ring ratio evolution in time reflects the change in the delayed neutron spectra due to the precursors' decay. Figure 8.10b shows the measured ratio between the signals from the inner ring and the signals of the other rings . During the decay phase, the contribution of the different groups to the activity changes, and since they are characterized by different average energies, the ring ratio will evolve accordingly. Such information could be used for validation purposes of new evaluated delayed-neutron spectra.

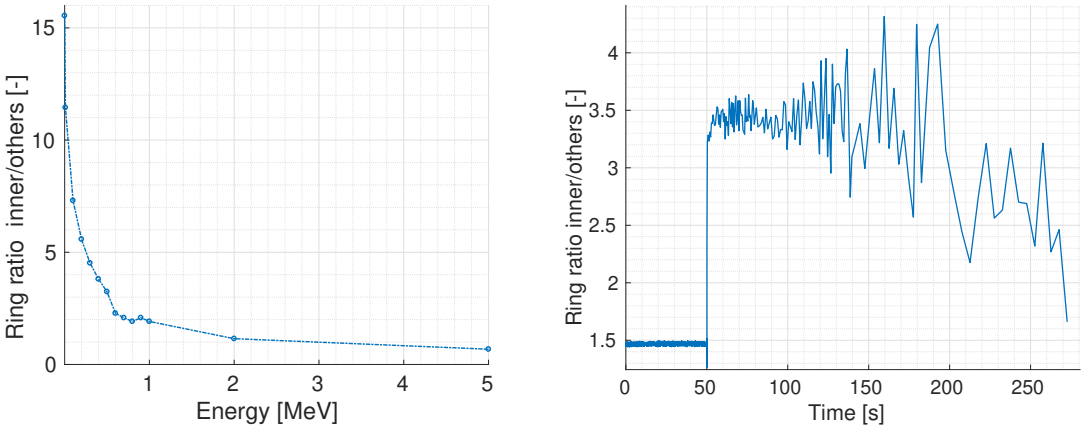

(a) As a function of energy (simulated).

(b) As a function of time (measured).

Figure 8.10: Ratio between the inner ring (4 counters) and the other rings (12 counters).

Macroscopic Approach

In the framework of this Ph.D., the ALDEN project has been launched with the aim of measuring the delayed neutron data associated with the thermal fission of ^{235}U. For that purpose, LOENIE-V2 long counter has been designed with the main feature of having a flat efficiency in the energy range of interest for delayed neutron (100 keV - 1 MeV). Sixteen ^{3}He detectors filled LOENIE's holes. After many tests on the tubes and on the global long counter, the experiment took place in the experimental area PF1B of ILL. About 200 μg of fissile material composed what would be at the same time target and fission chamber deposit. A remotely-controlled fast shutter has been designed on purpose for the ALDEN experiment. Thanks to its speed[7], it has been possible to adjust the irradiation and the decay duration of the cycles. The longest cycle consisted of 50 s of irradiation followed by 450 s of decay, while the shortest cycles were made of an irradiation and a decay of 0.25 s each. Unfortunately, the threshold for neutron detection employed for the short cycles had been badly chosen and the runs could not been exploited.

Perspectives: One perspective, apart from performing the experiment using other fissioning systems, could be to re-perform the short cycles for $^{235}U_t$ increasing the threshold. In that way, the irradiation would mostly solicit short-lived precursors and the estimation of the abundances belonging to the short-lived groups could be improved. Another possibility could be to better use the neutron beam. Since for the ν_d estimation only the first 500 ms of decay are needed, instead of cycles of the type 50-350, one could bring the precursors at saturation and perform short decays followed by a longer (but still short) irradiations. One example could be 500 ms of decay and 5 s of irradiation. In that way, the use of the beam would be optimized and with the same experiment duration the statistics would be greatly improved. LOENIE-V2's absolute efficiency has been measured at NPL, while its relative efficiency has been measured at AMANDE accelerator. As far as the first one is concerned, simulations reproduce the measured efficiency trend as a function of energy, even though a positive scaling factor must be

[7]The beam was shutdown in less than 4.5 ms

applied to the calculations to bring the curve to the level of the experimental one. Moreover, the agreement between computed and measured ring ratio is astonishing. Unfortunately, due to a lack of time, the the relative efficiency could not be processed. It would be interesting to analyze AMANDE's data to see if it is in accordance with TRIPOLI4 simulations. In addition to that, new experimental campaigns are foreseen to investigate the delayed neutron data associated with the thermal fission of ^{239}Pu, ^{241}Pu, ^{233}U and ^{245}Cm.

Benchmarks

The experimental decay curve has been fitted to obtain both the average delayed neutron yield and the kinetic parameters for the $^{235}U_t$, which have been compared with older experiments. Then, the information brought by the ALDEN experiment has been assimilated to the summation calculations through the Bayesian inference, in order to reduce the uncertainties associated with the quantities of interest. The results for ^{235}U, together with the calculated values for ^{238}U, have been tested in three benchmarks: MISTRAL1 (87% ^{235}U, 13% ^{238}U), IPEN (90% ^{235}U, 10% ^{238}U), and SNEAK 7B (11% ^{235}U, 59% ^{238}U, 28% ^{239}Pu) giving satisfying solutions with respect to the effective delayed neutron fraction. The main achievement of this work is, however, the great improvement in the predicted reactivity, especially for negative periods. In particular, the predicted reactivity is accompanied by an extremely good precision. To give an example, looking at the whole range of reactor periods, JEFF-3.1.1 is able to predict the reactivity with an uncertainty ranging from 4.0 to 11.1%. For the same periods, Foligno's parameters give a flatter uncertainty curve, from 1.6 to 2.2%. Such reduction is achieved thanks to the drop in the uncertainty of the ν_d, but above all of the $\overline{T_{1/2}}$, realized through the use of the correlation matrix associated with the abundances. Remember that the industry assumes the β_{eff} to be known with an uncertainty of 5%, which combined with the 3% of $\overline{T_{1/2}}$ leads to about 6% of uncertainty on the reactivity!

Perspectives: Foligno's parameters could be used to estimate certain neutronic quantities of the benchmark, like the reactivity coefficient or the integral effect of the absorbers, which had been measured using kinetic parameters [34]. It has to be stressed that benchmarks for light water reactors are scarce. Indeed, in the ICSBEP[8] and IRPhE[9] databases, most of the experiments are performed on fast spectra. In the next years, CEA aims at performing β_{eff} measurements in critical facilities having a thermal spectrum (CROCUS at EPFL or LR-0 in Czech Republic), as well as in power reactors (ILL). For this purpose, a Ph.D. has been recently launched with the objective of designing a system to measure the reactor transfer function at very low frequencies. In that way, the kinetic parameters for light water reactors could be validated. Finally, to respond to the needs of the industry, one perspective could be to validate the β_{eff} and the Inhour equation for UOx-MOX fuelled cores.

[8] *International Criticality Safety Benchmark Evaluation Project.*
[9] *Institut de Recherche sur les Phénomènes Hors Equilibre.*

Bibliography

[1] CAEN, Tools for Discovery. https://www.caen.it/products/v1724/. Accessed: 2019-03-07.

[2] Fission. https://cnx.org/contents/9zCw8Rtq@4/Fission. Accessed: 2019-06-18.

[3] National Nuclear Data Center, Chart of Nuclides. https://www.nndc.bnl.gov/nudat2/. Accessed: 2019-06-26.

[4] Nuclear Fission. https://www.euronuclear.org/info/encyclopedia/n/nuclear-fission.htm. Accessed: 2019-06-18.

[5] Wiener, Power Electronics. http://www.wiener-d.com/sc/powered-crates/nim/nim-compact-150w.html. Accessed: 2019-03-07.

[6] ENDF/B-VII.0: Next Generation Evaluated Nuclear Data Library for Nuclear Science and Technology. Technical Report UCRL-JRNL-225066, Lawrence Livermore National Laboratory, 10 2006.

[7] GEF Annual Performance Report 2008. Technical Report Evaluation Report No. 49, Global Enviroment Facility Evaluation Office, 10 2009.

[8] The JEFF-3.1/-3.1.1 radioactive decay data and fission yields sub-libraries. Technical Report ISBN 978-92-64-99087-6, OECD NEA, 2009.

[9] Digital Pulse Processing in Nuclear Physics. Technical Report WP2081, CAEN, Tools for Discovery, 08 2011.

[10] A. Santamarina. Validation of lwr reactivity versus reactor period. feedback on the delayed neutron data (β_i, λ_i). In *Proceedings of the PHYSOR 2018*, Cancun, Mexico, 2018.

[11] B. Habert, *et al.* Retroactive Generation of Covariance Matrix of Nuclear Model Parameters Using Marginalization Techniques. *Nuclear Science and Engineering*, 166:276–287, 2010.

[12] M.C. Brady. *Evaluation and Application of Delayed Neutron Precursor Data*. PhD thesis, Los Alamos National Laboratory, 04 1989.

[13] M.C. Brady and T.R. England. . Technical Report LAUR-89-3386(89), Los Alamos National Laboratory, 04 1989.

[14] C. De Saint Jean, *et al.* Status of conrad, a nuclear reaction analysis tool. In *International Conference on Nuclear Data for Science and Technology*, Nice, France, 2007.

[15] C. De Saint Jean, *et al.* A Monte Carlo Approach to Nuclear Model Parameter Uncertainties Propagation. *Nuclear Science and Engineering*, 161:363–370, 2009.

[16] C. De Saint Jean, *et al.* Evaluation of Neutron-induced Cross Sections and their Related Covariances with Physical Constraints. *Nuclear Data Sheets*, 148:383–419, 2018.

[17] C.B. Besant, *et al.* Absolute yields and group constants of delayed neutron in the fast fission of ^{235}U, ^{238}U and ^{239}Pu. *Journal of the British Nuclear Energy Society*, 16(2):161–176, 1977.

[18] D. Foligno *et al.* Summation calculation of delayed neutron yields for ^{235}U, ^{238}U and ^{239}Pu, based on various fission yield and neutron emission probability databases. *EPJ Web of Conferences*, 193(03004), 2018.

[19] D. Foligno *et al.* Uncertainty and covariances of the newly derived 8-groups delayed-neutrons abundances set. *EPJ Nuclear Science and Technology*, 4(31), 2018.

[20] H. Smith S. Kreiner D. Reilly, N. Ensslin. *Passive Nondestructive Assay of Nuclear Materials*. Nuclear Regulatory Commission, Washington DC, 1991.

[21] A. D'angelo and J. Rowlands. Conclusions concrning the delayed neutron data for the major actinides. *Progress in Nuclear Energy*, 41(1-4):391–412, 2002.

[22] A. Duranti E. Ivanov. SNEAK 7A and 7B Pu-fueled fast critical assemblies in the Karlsruhe fast critical facility. Technical Report NEA/NSC/DOC(2006)1, NEA, Nuclear Science Committee, 03 2011.

[23] T.R. England. . Technical Report LA-11151-MS(88), LA-11534T(89), LAUR-88-4118(89), Los Alamos National Laboratory, 03 1989.

[24] A. Chebboubi et al. Impact of fifrelin input parameters on fission observables. In *6th Workshop on Nuclear Fission and Spectroscopy of Neutron-Rich Nuclei*, Chamrousse, France, 2018.

[25] Ayazuddin S. K. et al. Reactor transfer function measurement at PARR by neutron noise analysis, year = 1984. Technical Report PINSTECH-105, PINSTECH, 3.

[26] D. Abriola et al. Beta-delayed neutron emission evaluation, year = 2011. Technical Report INDC(NDS)-0599, INDC International Nuclear Data Committee, 12.

[27] D.A. Brown et al. Endf/b-viii.0: The 8$^{\text{th}}$ major release of the nuclear reaction data library with cielo-project cross sections, new standards and thermal scattering data. *Nuclear Data Sheets*, 148:1–142, 2 2018.

[28] Henley E. J. et al. *Advances in Nuclear Science and Technology - volume 11*. Plenum Press, New York, 1979.

[29] I. Kodeli et al. Oecd/nea intercomparison of deterministic and monte carlo cross-section sensitivity codes using sneak-7 benchmarks. 05 2016.

[30] K. Skrable et al. A general equation for the kinetics of linear first order phenomena and suggested applications. *Health Physics*, 27(1):155–157, 1974.

[31] L. Mathieu et al. New neutron long-counter for delayed neutron investigations with the LOHENGRIN fission fragment separator. *Journal of Instrumentation,*, 7(8):P08029–P08029, 2012.

[32] Leconte P. et al. Reactor transfer function measurement at PARR by neutron noise analysis, year = 1984. Technical Report PINSTECH-105, PINSTECH, 3.

[33] M.B. Chadwick et al. Endf/b-vii.1 nuclear data for science and technology: Cross sections, covariances, fission product yields and decay data. *Nuclear Data Sheets*, 112:2887–2996, 10 2011.

[34] Santamarina A. et al. Calculation of lwr β_{eff} kinetic parameter. validation on the mistral experiments. *Annals of Nuclear Energy*, 48:51–59, 2012.

[35] V.M. Piksaikin et al. Energy Dependence of Relative Abundances and Periods of Delayed Neutrons from Neutron-Induced Fission of ^{235}U, ^{238}U, ^{239}Pu in 6- and 8-group model representation. *Progress in Nuclear Energy*, 41(1-4):203–222, 2002.

[36] W.B. Wilson et al. A manual for cinder'90 version 07.4 codes and data. Technical Report LA-UR-07-8412, Los Alamos National Laboratory, 2007.

[37] D. Foligno and J-F Lebrat. Bateman-solver validation with darwin. 5 2018.

[38] G. Rudstam, *et al.* Delayed Neutron Data for the Major Actinides. *NEA-WPEC-6*, 6, 2002.

[39] G.D. Spriggs. In-Pile Measurement of the Decay Constants and Relative Abundance of Delayed Neutrons. *Nuclear Science and Engineering*, 114(4):342–351, 1993.

[40] J.M. Campbell G.D.Spriggs and V.M.Piksaikin. An 8-group delayed neutron model based on a consistent set of half-lives. *Progress in Nuclear Energy*, 41(1-4):223–251, 2002.

[41] G.R. Keepin, *et al.* Delayed Neutrons from Fissionable Isotopes of Uranium, Plutonium, and Thorium. *Physical Review*, 107(4):1044–1049, 1957.

[42] Cross Section Evaluation Working Group. *Data Formats and Procedures for the Evaluated Nuclear Data File ENDF/B-VI and ENDF/B-VII.* Brookhaven National Laboratory, Upton, NY 11973-5000, 6 2009.

[43] J.K. Shultis, *et al. Fundamentals of Nuclear Science and Engineering Third Edition.* CRC press, 2016.

[44] K.-H.Schmidt. Energy Dependence of Fission Product Yields from ^{235}U, ^{238}U and ^{239}Pu for Incident Neutron Energies Between 0.5 and 14.8 MeV. *Nuclear Data Sheets*, 131:319–356, 2016.

[45] K.-H.Schmidt. General description of fission observables: GEF Model Code. *Nuclear Data Sheets*, 131:107–221, 2016.

[46] G. F. Knoll. *Radiation Detection and Measurement - Third Edition.* John Wiley & Sons, Michigan, 2000.

[47] K.S. Krane. *Introductory Nuclear Physics.* John Wiley & Sons, Singapore, 1988.

[48] W.R. Leo. *Techniques for Nuclear and Particle Physics Experiments. A How-to Approach*. Springer-Verlag, CH-1015 Lausanne, Switzerland, 1987.

[49] M.C. Brady and T.R. England. Delayed Neutrons Data and Group Parameters for 43 Fissioning Systems. *Nuclear Science and Engineering*, 103:129–149, 1989.

[50] R.W. Mills. *Fission Product Yield Evaluation*. PhD thesis, University of Birmingham, 3 1995.

[51] M.S. Krick & A.E. Evans. The Measurement of Total Delayed-Neutron Yields as a Function of the Energy of the Neutron Inducing Fission. *Nuclear Science and Engineering*, 47(3):311–318, 1972.

[52] A.L. Nichols. Nuclear data requirements for decay heat calculations. In *Workshop on Nuclear Reaction Data and Nuclear Reactors: Physics, Design and Safety*, page 64, Trieste, Italy, 2002.

[53] University Network of Excellence in Nuclear Engineering (UNENE). *The Essential CANDU, A Textbook on the CANDU Nuclear Power Plant Technology - Chapter 5 - Reactor Dynamics*. ISBN 0-9730040, 2016.

[54] P. Schillebeeckx et al. Determination of Resonance Parameters and their Covariances from Neutron Induced Reaction Cross Section Data. *Nuclear Data Sheets*, 113(12):3054–3100, 2012.

[55] Taylor J. R. *An introduction to Error Analysis. The study of uncertainties in physical measurements - second edition*. University Science Books, Sausalito, California, 1982.

[56] R.J. Tuttle. Review of delayed neutron yields in nuclear fission. In *Proceedings of the consultants' meeting on delayed neutron properties*, Vienna, Austria, 1979.

[57] E. Rossi. *Characterisation of the Spatial Resolution and the Gamma-ray Discrimination of Helium-3 Proportional Counters*. PhD thesis, Universita degli Studi di Milano-Bicocca, 2015.

[58] A. Patil S. Usman. Radiation detector deadtime and pile up: a review of the status of science. *Nuclear Engineering and Technology*, 50:1006–1016, 2018.

[59] L. San-Felice, R. Eschbach, and P. Bourdot. Experimental validation of the darwin2.3 package for fuel cycle applications. *Nuclear Technology*, 184(2):217–232, 2013.

[60] T. Williams. On the choice of delayed neutron parameters for the analysis of kinetics experiments in 235U systems. *Annals of Nuclear Energy*, 23(15):1261–1265, 1996.

[61] K.D. Talley. *Beta-Delayed Neutron Data and Models for SCALE*. PhD thesis, University of Tennessee, 12 2016.

[62] N. Terranova. *Covariance Evaluation for Nuclear Data of Interest to the Reactivity Loss Estimation of the Jules Horowitz Material Testing Reactor*. PhD thesis, Universita di Bologna, 2016.

[63] B. Pfeiffer *et al.* Status of delayed-neutron precursor data: half-lives and neutron emission probabilities. *Progress in Nuclear Energy*, 41(1-4):39–69, 2002.

[64] G. Audi *et al.* The nubase evaluation of nuclear and decay properties. *Nuclear Physics A*, 729(1):3–128, 2003.

[65] J. Katakura *et al.* Development of jendl fp decay data file 2000. *Journal of Nuclear Science and Technology*, 39(sup2):444–449, 2002.

[66] R. Capote *et al.* Ripl – reference input parameter library for calculation of nuclear reactions and nuclear data evaluations. *Nuclear Data Sheets*, 110(12):3107–3214, 2009.

[67] C. Tintori. Digital Pulse Processing for Physics Applications. https://www.caen.it/documents/News/32/DPPworkshop_UK_July2011.pdf. Accessed: 2019-06-19.

[68] A. Tobias. Decay heat. *Progress in Nuclear Energy*, 5:1–93, 1980.

[69] V.M. Piksaikin, *et al.* Measurements of periods, relative abundances and absolute total yields of delayed neutrons from fast neutron induced fission of ^{235}u and ^{237}np. In *International Conference on Nuclear Data for Science and Technology*, Trieste, Italy, 1998.

[70] V. Zammit-Averlant. *Validation Integrale des Estimations du Parametre Beta Effectif pour les Reacteurs MOX et Incinerateurs*. PhD thesis, Universite Aix-Marseille I, 1998.

Appendix A

WPEC-SG6 Recommendations

Table A.1: Origin of the kinetic parameters recommended by the WPEC.

Fiss. Sys.	Energy	Original Nb. Groups	Reference	Year
^{229}Th	thermal	5	Gudkov *et al.*	1989
^{232}Th	fast	6	Keepin *et al.*	1957
^{232}Th	high	5	Maksyutenko *et al.*	1958
^{231}Pa	fast	6	Anoussis *et al.*	1973
^{231}Pa	high	4	Brown *et al.*	1971
^{232}U	thermal	5	Waldo *et al.*	1981
^{233}U	thermal	6	Keepin *et al.*	1957
^{233}U	fast	6	Keepin *et al.*	1957
^{233}U	high	6	East *et al.*	1970
^{235}U	thermal	6	Keepin *et al.*	1957
^{235}U	fast	8	Piksaikin *et al.*	1997
^{235}U	high	6	East *et al.*	1970
^{236}U	high	6	Gudkov *et al.*	1989
^{238}U	fast	6	Keepin *et al.*	1957
^{238}U	high	6	East *et al.*	1970
^{237}Np	fast	8	Piksaikin *et al.*	1997
^{239}Pu	thermal	6	Waldo *et al.*	1981
^{239}Pu	fast	5	Benedetti *et al.*	1982
^{239}Pu	high	6	Maksyutenko *et al.*	1963
^{240}Pu	fast	6	Keepin *et al.*	1957
^{241}Pu	thermal	5	Cox *et al.*	1961
^{241}Pu	fast	6	Gudkov *et al.*	1989
^{242}Pu	fast	6	Waldo *et al.*	1981
^{242}Pu	high	6	Waldo *et al.*	1970
^{241}Am	thermal	5	Waldo *et al.*	1981
^{241}Am	fast	6	Gudkov *et al.*	1989
^{242m}Am	thermal	6	Waldo *et al.*	1981
^{243}Am	fast	7	Charlton *et al.*	1998
^{245}Cm	thermal	6	Waldo *et al.*	1981
^{249}Cf	thermal	4	Waldo *et al.*	1981
^{252}Cf	spontaneous	4	Chulick *et al.*	1969

Appendix B

Error Propagation

A result does not mean anything without its uncertainty. In this work every calculated or measured value is shown with its error.

B.1 Error propagation for the ν_d

In this part, the procedures used to derive and then verify the computed errors are presented. In the specific, the uncertainty analysis of the average delayed neutron yield has been performed by analytical error propagation. Afterwards, a stochastic method has been used to verify the correctness of the results.

B.1.1 Analytical method - Error propagation

Equation B.1 shows the formula used to compute the average delayed neutron yield.

$$\nu_d = \sum_i^N CY_i \; P_{n,i} \; x_i \qquad [\text{DN/fiss}], \tag{B.1}$$

Both CY_i and Pn, i are reported in the libraries with their uncertainty[1] (σ_{CY_i} and $\sigma_{P_{n,i}}$, respectively). To see the effects of these errors on the computed ν_d, the best way is to use the well-known error propagation formula in case of the independent variables[2]. Of course, this is a simplified formula, and a more rigourous calculation (with covariances) would be needed.

$$\begin{aligned} \sigma_{\nu_d} &= \sqrt{\sum_i^N \left(\left(\frac{\partial \nu_d}{\partial CY_i} \cdot \sigma_{CY_i} \right)^2 + \left(\frac{\partial \nu_d}{\partial P_{n,i}} \cdot \sigma_{P_{n,i}} \right)^2 \right)} \\ &= \sqrt{\sum_i^N \left(\left(P_{n,i} \cdot \sigma_{CY_i} \right)^2 + \left(CY_i \cdot \sigma_{P_{n,i}} \right)^2 \right)} \end{aligned} \tag{B.2}$$

Taking as an example the P_n from ENDF-B/VII.1 and the CY from JEFF-3.1.1, the error is 8E-4, corresponding to the 5.2% of the calculated ν_d (1.57E-02).

[1] The uncertainties are often missing, especially in the P_n-libraries. In case of missing error, the uncertainty has been considered null. In the following, when analysing the sensitivity of ν_d to the CY and/or to the P_n, the calculation has been performed again but this time setting the relative error to 100% when missing. The difference in the results when using one assumption or the other will be later highlighted.

[2] If the variables are independent of each others, then the cross-correlation term is null.

B.1.2 Stochastic method - Monte Carlo

A Monte Carlo simulation is a powerful tool to perform error analysis avoiding the struggle of solving cumbersome equations. The principle is very simple: rather than solving the equation with the *exact*[3] values reported in the libraries (CY and P_n), *perturbed* values are used (CY' and P'_n). The perturbation is performed by shifting the mean value by a fraction of the uncertainty reported in the library (σ_{CY_i} and $\sigma_{P_{n,i}}$).

$$CY_i^I = CY_i + \sigma_{CY_i} \cdot v^I \tag{B.3}$$

$$P_{n,i}^I = P_{n,i} + \sigma_{P_{n,i}} \cdot u^I \tag{B.4}$$

The fraction (v or u) is nothing but a normally distributed random number, with $\mu = 0$ and $\sigma = 1$. Note that each variable must be perturbed with a different vector of random numbers, in order for the variables to be considered independent of each other. For each sample, a new average delayed neutron fraction is calculated

$$\nu_d^I = \sum_i^N CY_i^I \cdot P_{n,i}^I \tag{B.5}$$

leading to a vector of normally distributed ν_d:

$$\nu_d = [\ \nu_d^I\ \nu_d^{II}\ \nu_d^{III} \cdots\ \nu_d^S\ ] \tag{B.6}$$

where S is the number of samples. Finally, an average of the vector values gives the best estimate of the $\overline{\nu}_d$ (1.57E-02), while its standard deviation gives the uncertainty of the best estimate of the $\overline{\nu}_d$ (8E-04). Obviously, the more the samples, the more the precision of the results. It's interesting to notice that less than 1000 samples are sufficient for the results to converge to the analytically calculated values.

B.2 Analytical error propagation for the a_i: simple equivalence

For the simple equivalence,

$$\begin{aligned} a_i = \frac{\nu_{d,i}}{\nu_d} &= \frac{\sum_{i=1}^{N_i} x_i\ CY_i\ P_{n,i}}{\sum_{k=1}^{8}\sum_{i=1}^{N_k} x_i\ CY_i\ P_{n,i}} = \frac{\sum_{i=1}^{N_i} x_i\ CY_i\ P_{n,i}}{\sum_{i=1}^{N_i} x_i\ CY_i\ P_{n,i} + \sum_{\substack{k=1\\k\neq i}}^{8}\sum_{j=1}^{N_k} x_j\ CY_j\ P_{n,j}} \\ &= \frac{x_{1,1}\ CY_{1,1}\ P_{n,1,1} + \cdots + x_{1,N_1}\ CY_{1,N_1}\ P_{n,1,N_1}}{x_{1,1}\ CY_{1,1}\ P_{n,1,1} + \cdots + x_{1,N_1}\ CY_{1,N_1}\ P_{n,1,N_1} + \sum_{\substack{k=1\\k\neq i}}^{8}\sum_{j=1}^{N_k} x_j\ CY_j\ P_{n,j}} \end{aligned} \tag{B.7}$$

and therefore

[3] The value reported in the library is not the exact one, but it can be considered the best estimate of the variable.

$$\begin{aligned}
\sigma_{a_i}^2 &= \left(\frac{\partial a_i}{\partial CY_{i,1}}\sigma_{CY_{i,1}}\right)^2 + \left(\frac{\partial a_i}{\partial P_{n,i,1}}\sigma_{P_{n,i,1}}\right)^2 + \cdots + \left(\frac{\partial a_i}{\partial CY_{i,N_1}}\sigma_{CY_{i,N_1}}\right)^2 + \left(\frac{\partial a_i}{\partial P_{n,i,N_1}}\sigma_{P_{n,i,N_1}}\right)^2 \\
&= \left[\left(\frac{P_{n,i,1}x_{i,1}\ \nu_d - \nu_{d,i}\ P_{n,i,1}x_{i,1}}{\nu_d^2}\right)\sigma_{CY_{i,1}}\right]^2 + \left[\left(\frac{CY_{i,1}x_{i,1}\ \nu_d - \nu_{d,i}\ CY_{i,1}x_{i,1}}{\nu_d^2}\right)\sigma_{P_{n,i,1}}\right]^2 + \cdots \\
&\cdots + \left[\left(\frac{P_{n,i,N_1}x_{i,N_1}\ \nu_d - \nu_{d,i}\ P_{n,i,N_1}x_{i,N_1}}{\nu_d^2}\right)\sigma_{CY_{i,N_1}}\right]^2 + \left[\left(\frac{CY_{i,N_1}x_{i,N_1}\ \nu_d - \nu_{d,i}\ CY_{i,N_1}x_{i,N_1}}{\nu_d^2}\right)\sigma_{P_{n,i,N_1}}\right]^2 \\
&= \left(\frac{1-a_i}{\nu_d}\right)^2\left[(x_{i,1}P_{n,i,1}\sigma_{CY_{i,1}})^2 + (x_{i,1}CY_{i,1}\sigma_{P_{n,i,1}})^2 + \cdots + (x_{i,N_1}P_{n,i,N_1}\sigma_{CY_{i,N_1}})^2 + (x_{i,N_1}CY_{i,N_1}\sigma_{P_{n,i,N_1}})^2\right] \\
&= \left(\frac{1-a_i}{\nu_d}\right)^2\sum_{i=1}^{N_i}\left[(x_iP_{n,i}\sigma_{CY_i})^2 + (x_iCY_i\sigma_{P_{n,i}})^2\right]
\end{aligned}$$

B.3 Analytical error propagation for the $\mathbf{a_i}$: exponential equivalence

In the exponential equivalence technique

$$a_i = \sum_{j=1}^{N} f_{i,j} \tag{B.8}$$

and therefore

$$\sigma_{a_i} = \sqrt{\sum_{j=1}^{N}\sigma_{f_{i,j}}^2}. \tag{B.9}$$

For groups 1 and 8:

$$f_{i,j} = \frac{\alpha_j\ \lambda_i}{\lambda_j} \tag{B.10}$$

and therefore

$$\sigma_{f_{i,j}} = \sqrt{\left(\frac{\lambda_i}{\lambda_j}\ \sigma_{\alpha_j}\right)^2 + \left(-\frac{\alpha_j\ \lambda_i}{\lambda_j^2}\ \sigma_{\lambda_j}\right)^2} \tag{B.11}$$

On the other hand, for the inner groups:

$$\begin{cases} f_{i+1,j} = \frac{\alpha_j\ \lambda_{i+1}}{\lambda_i - \lambda_{i+1}}\ (\frac{\lambda_i}{\lambda_j} - 1) \\ f_{i,j} = \alpha_j - f_{i+1,j} \end{cases} \tag{B.12}$$

and therefore:

$$\begin{cases} \sigma_{f_{i+1,j}}^2 = \left(\frac{\partial f_{i+1,j}}{\partial \alpha_j}\ \sigma_{\alpha_j}\right)^2 + \left(\frac{\partial f_{i+1,j}}{\partial \lambda_j}\ \sigma_{\lambda_j}\right)^2 \\ \sigma_{f_{i,j}}^2 = \sigma_{\alpha_j}^2 + \sigma_{f_{i+1,j}}^2 \end{cases} \tag{B.13}$$

where:

$$\frac{\partial f_{i+1,j}}{\partial \lambda_j} = -\frac{\lambda_i\ \lambda_{i+1}\ \alpha_j}{\lambda_j^2\ (\lambda_i - \lambda_{i+1})} \tag{B.14}$$

$$\frac{\partial f_{i+1,j}}{\partial \alpha_j} = \frac{\lambda_{i+1}}{\lambda_i - \lambda_{i+1}}\left(\frac{\lambda_i}{\lambda_j} - 1\right) \tag{B.15}$$

$$\sigma_{\alpha_j}^2 = \left(\frac{\partial \alpha_j}{\partial CY_j}\ \sigma_{CY_j}\right)^2 + \left(\frac{\partial \alpha_j}{\partial BR_j}\ \sigma_{BR_j}\right)^2 \tag{B.16}$$

$$\frac{\partial \alpha_j}{\partial CY_j} = \frac{BR_j\ x_j\ \nu_d - \nu_{d,j}\ BR_j\ x_j}{\nu_d^2} \tag{B.17}$$

$$\frac{\partial \alpha_j}{\partial BR_j} = \frac{CY_j\ x_j\ \nu_d - \nu_{d,j}\ CY_j\ x_j}{\nu_d^2} \tag{B.18}$$

B.4 Analytical error propagation for the $\overline{T_{1/2}}$

B.4.1 Direct summation

As shown for the average delayed-neutron yield, the uncertainty can be calculated both analytically and stochastically. Both methods have been used but only the analytical formulation will be shown here, since the Monte Carlo procedure is analogous to the $\overline{\nu_d}$-case.
In order to analytically estimate the uncertainty it is necessary to apply the error propagation. In the summation calculation

$$\begin{aligned}\overline{T_1/2} &= \frac{\sum_i^n P_{n,i} \cdot CY_i \cdot T_{1/2,i}}{\sum_i^n P_{n,i} \cdot CY_i} \\ &= \frac{P_{n,1} \cdot CY_1 \cdot T_{1/2,1} + P_{n,2} \cdot CY_2 \cdot T_{1/2,2} + \cdots + P_{n,n} \cdot CY_n \cdot T_{1/2,n}}{P_{n,1} \cdot CY_1 + P_{n,2} \cdot CY_2 + \cdots + P_{n,n} \cdot CY_n}\end{aligned} \tag{B.19}$$

and according to the error propagation law

$$\begin{aligned}\sigma^2_{\overline{T_1/2}} = &\left(\frac{\partial \overline{T_1/2}}{\partial P_{n,1}} \cdot \sigma_{P_{n,1}}\right)^2 + \left(\frac{\partial \overline{T_1/2}}{\partial CY_1} \cdot \sigma_{CY_1}\right)^2 + \left(\frac{\partial \overline{T_1/2}}{\partial T_{1/2,1}} \cdot \sigma_{T_{1/2,1}}\right)^2 \\ &+ \left(\frac{\partial \overline{T_1/2}}{\partial P_{n,2}} \cdot \sigma_{P_{n,2}}\right)^2 + \left(\frac{\partial \overline{T_1/2}}{\partial CY_2} \cdot \sigma_{CY_2}\right)^2 + \left(\frac{\partial \overline{T_1/2}}{\partial T_{1/2,2}} \cdot \sigma_{T_{1/2,2}}\right)^2 \\ &+ \quad \cdots \\ &+ \left(\frac{\partial \overline{T_1/2}}{\partial P_{n,n}} \cdot \sigma_{P_{n,n}}\right)^2 + \left(\frac{\partial \overline{T_1/2}}{\partial CY_n} \cdot \sigma_{CY_n}\right)^2 + \left(\frac{\partial \overline{T_1/2}}{\partial T_{1/2,n}} \cdot \sigma_{T_{1/2,n}}\right)^2 \\ &= \sum_i^n \left\{ \left(\frac{\partial \overline{T_1/2}}{\partial P_{n,i}} \cdot \sigma_{P_{n,i}}\right)^2 + \left(\frac{\partial \overline{T_1/2}}{\partial CY_i} \cdot \sigma_{CY_i}\right)^2 + \left(\frac{\partial \overline{T_1/2}}{\partial T_{1/2,i}} \cdot \sigma_{T_{1/2,i}}\right)^2 \right\}\end{aligned} \tag{B.20}$$

where

$$\frac{\partial \overline{T_1/2}}{\partial P_{n,i}} = \frac{(CY_i \cdot T_{1/2,i}) \cdot (\sum_i^n P_{n,i} \cdot CY_i) - (\sum_i^n P_{n,i} \cdot CY_i \cdot T_{1/2,i}) \cdot CY_i}{(\sum_i^n P_{n,i} \cdot CY_i)^2} \tag{B.21}$$

$$\frac{\partial \overline{T_1/2}}{\partial CY_i} = \frac{(P_{n,i} \cdot T_{1/2,i}) \cdot (\sum_i^n P_{n,i} \cdot CY_i) - (\sum_i^n P_{n,i} \cdot CY_i \cdot T_{1/2,i}) \cdot CY_i}{(\sum_i^n P_{n,i} \cdot P_{n,i})^2} \tag{B.22}$$

$$\frac{\partial \overline{T_1/2}}{\partial T_{1/2,i}} = \frac{P_{n,i} \cdot CY_i}{\sum_i^n P_{n,i} \cdot P_{n,i}} \tag{B.23}$$

B.4.2 Group model with correlations

$$\overline{T_{1/2}} = \frac{\sum\limits_{i=1}^{8} a_i T_{1/2,i}}{\sum\limits_{i=1}^{8} a_i} \tag{B.24}$$

$$\sigma_{\overline{T_{1/2}}} = \sqrt{\sum_{i=1}^{8}\sum_{j=1}^{8} \frac{\partial \overline{T_{1/2}}}{\partial a_i}\frac{\partial \overline{T_{1/2}}}{\partial a_j} corr(a_i, a_j)\sigma_{a_i}\sigma_{a_j}} \tag{B.25}$$

where

$$\frac{\partial \overline{T_{1/2}}}{\partial a_i} = \frac{T_{1/2,i}\sum\limits_{i=1}^{8} a_i - \sum\limits_{i=1}^{8}(a_i\, T_{1/2,i})}{\left(\sum\limits_{i=1}^{8} a_i\right)^2}\sigma_{a_i} \tag{B.26}$$

B.5 Analytical error propagation for the ρ

The Nordheim equation allows to compute the reactivity ρ from the measured reactor period τ and from other nuclear parameters

$$\rho = \omega\left(\Lambda + \sum_{i=1}^{G}\frac{\beta_{eff}\, a_i}{\lambda_i + \omega}\right), \tag{B.27}$$

and since $\omega = 1/\tau$,

$$\rho = \left(\frac{\Lambda}{\tau} + \beta_{eff}\sum_{i=1}^{G}\frac{a_i}{\lambda_i\tau + 1}\right), \tag{B.28}$$

The uncertainty associated with the reactivity expressed in dollars can be obtained by applying the well-known uncertainty propagation formula

$$\sigma_\rho = \sqrt{\left(\frac{\partial\rho}{\partial\Lambda}\sigma_\Lambda\right)^2 + \left(\frac{\partial\rho}{\partial\beta_{eff}}\sigma_{\beta_{eff}}\right)^2 + \sum_{i=1}^{8}\sum_{j=1}^{8}\frac{\partial\rho}{\partial a_i}\frac{\partial\rho}{\partial a_j}corr(a_i,a_j)\sigma_{a_i}\sigma_{a_j}} \tag{B.29}$$

where

$$\frac{\partial\rho}{\partial\Lambda} = \frac{1}{\tau} \tag{B.30}$$

$$\frac{\partial\rho}{\partial\beta_{eff}} = \sum_{i=1}^{G}\frac{a_i}{\lambda_i\tau + 1} \tag{B.31}$$

$$\frac{\partial\rho}{\partial a_i} = \frac{\beta_{eff}}{\lambda_i\tau + 1}. \tag{B.32}$$

The final expression for the uncertainty therefore becomes

$$\sigma_{\rho_x} = \sqrt{\left(\frac{\sigma_\Lambda}{\tau}\right)^2 + \left(\sigma_{\beta_{eff}}\sum_{i=1}^{G}\frac{a_i}{\lambda_i\tau+1}\right)^2 + \sum_{i=1}^{8}\sum_{j=1}^{8}\left(\frac{\beta_{eff}\sigma_{a_i}}{\lambda_i\tau+1}\right)\left(\frac{\beta_{eff}\sigma_{a_j}}{\lambda_j\tau+1}\right)corr(a_i,a_j)}. \tag{B.33}$$

Appendix C

Complete tables nud

C.1 ^{235}U thermal fission - Complete $\overline{\nu_d}$-table

Table C.1: $\overline{\nu_d}$ calculation by Summation Method - $^{235}U_{th}$.

$^{235}U_{th}$		FY			
		JEFF-3.1.1		FIFRELIN	
		CY	IY	CY	IY
P_n	RIPL-3	1.47E-02 -	1.36E-02 -	-	1.54E-02 -
	RIPL-3-2015	1.63E-02 -	1.49E-02 -	-	1.68E-02 -
	ENDF/B-VII.0	1.57E-02 5.2%	1.43E-02 7.2%	-	1.68E-02 1.2%
	ENDF/B-VII.1	1.57E-02 5.2%	1.43E-02 7.2%	-	1.68E-02 1.2%
	JENDL FPDD20	1.58E-02 5.6%	1.45E-02 7.5%	-	1.66E-02 2.6%
	JEFF-3.1.1	1.48E-02 5.3%	1.35E-02 7.4%	-	1.53E-02 1.3%
	NNDC	1.63E-02 5.6%	1.49E-02 7.5%	-	1.69E-02 2.6%
	Audi	1.55E-02 5.8%	1.41E-02 7.7%	-	1.66E-02 2.6%
	Pfeiffer	1.62E-02 5.5%	1.48E-02 7.3%	-	1.69E-02 2.5%
		ENDF/B-VII.0		GEFY-5.2	
		CY	IY	CY	IY
P_n	RIPL-3	1.56E-02 -	1.40E-02 -	1.67E-02 -	1.52E-02 -
	RIPL-3-2015	1.87E-02 -	1.54E-02 -	1.82E-02 -	1.65E-02 -
	ENDF/B-VII.0	1.90E-02 5.5%	1.65E-02 4.9%	1.80E-02 1.2%	1.62E-02 1.2%
	ENDF/B-VII.1	1.90E-02 5.5%	1.65E-02 4.9%	1.80E-02 1.2%	1.62E-02 1.2%
	JENDL FPDD20	1.85E-02 5.4%	1.60E-02 4.3%	1.80E-02 2.6%	1.62E-02 2.7%
	JEFF-3.1.1	1.73E-02 3.4%	1.41E-02 3.1%	1.69E-02 1.4%	1.51E-02 1.5%
	NNDC	1.90E-02 5.9%	1.54E-02 4.6%	1.84E-02 2.6%	1.66E-02 2.6%
	Audi	1.86E-02 6.1%	1.49E-02 4.6%	1.79E-02 2.6%	1.61E-02 2.7%
	Pfeiffer	1.84E-02 5.7%	1.51E-02 4.2%	1.86E-02 2.5%	1.69E-02 2.6%

C.2 Precursors' Importance - $^{235}U_{thermal}$

In the following, JEFF stands for JEFF-3.1.1, ENDF70 for ENDF/B-VII.0, and ENDF71 for ENDF/B-VII.1. For each precursor, the cumulative importance is reported. For example, ^{137}I accounts for 16.26% of the ν_d according to JEFF-ENDF71, while ^{137}I and ^{89}Br together account for 28.21%.

JEFF-ENDF71	ENDF70-ENDF71	JEFF-Pfeiffer

Z-A-I	Importance [%]	Z-A-I	Importance [%]	Z-A-I	Importance [%]
53 137 0	16.26	53 137 0	11.50	53 137 0	15.47
35 89 0	28.21	37 94 0	20.59	35 89 0	26.95
37 94 0	38.22	35 89 0	28.45	37 94 0	35.35
35 90 0	46.04	35 90 0	35.91	35 90 0	42.83
35 88 0	53.67	33 85 0	42.73	35 88 0	50.18
33 85 0	59.09	35 88 0	48.88	33 85 0	55.03
53 138 0	64.30	53 138 0	53.22	53 138 0	59.72
53 139 0	68.11	53 139 0	57.30	39 98 1	63.86
37 95 0	71.76	51 137 0	61.20	53 139 0	67.85
35 87 0	75.30	33 86 0	64.82	37 95 0	71.40
37 93 0	78.44	37 95 0	68.34	35 87 0	74.72
51 135 0	80.95	35 87 0	71.12	37 93 0	77.87
39 99 0	82.99	33 88 0	73.78	35 91 0	80.77
35 91 0	84.92	37 93 0	76.37	39 99 0	83.32
55 143 0	86.64	35 91 0	78.72	51 135 0	85.74
52 136 0	88.32	39 99 0	80.58	55 143 0	87.36
52 137 0	89.24	32 86 0	82.30	52 136 0	88.93
37 96 0	90.10	51 135 0	83.98	53 140 0	90
55 145 0	90.95	37 96 0	85.42	52 137 0	90.85
53 140 0	91.70	55 143 0	86.67	37 96 0	91.68
51 136 0	92.32	33 87 0	87.77	55 145 0	92.41
36 93 0	92.94	52 136 0	88.69	33 86 0	93.12
55 144 0	93.55	53 140 0	89.48	55 144 0	93.79
51 134 0	93.99	52 137 0	90.19	36 93 0	94.39
39 98 1	94.41	39 102 0	90.88	35 92 0	94.81
37 97 0	94.82	55 144 0	91.55	37 97 0	95.21
52 138 0	95.20	55 145 0	92.13	53 141 0	95.59
33 86 0	95.55	37 1 0	92.71	52 138 0	95.96
34 89 0	95.89	51 134 0	93.29	36 94 0	96.30
53 141 0	96.17	37 97 0	93.80	34 89 0	96.63
33 87 0	96.44	36 93 0	94.30	51 136 0	96.93
39 98 0	96.67	48 131 0	94.79	39 101 0	97.17
39 101 0	96.88	53 141 0	95.24	39 1 0	97.39
39 1 0	97.06	39 98 0	95.57	39 98 0	97.58
35 92 0	97.23	39 1 0	95.86	55 142 0	97.74
55 142 0	97.40	39 101 0	96.15	34 87 0	97.90
41 105 0	97.55	51 136 0	96.43	38 98 0	98.05
34 88 0	97.70	41 105 0	96.66	41 105 0	98.19
50 134 0	97.84	52 138 0	96.88	34 88 0	98.33
51 137 0	97.96	34 89 0	97.08	50 134 0	98.47
32 84 0	98.08	39 98 1	97.27	54 142 0	98.61
55 141 0	98.19	35 92 0	97.46	32 84 0	98.72
39 97 1	98.29	48 130 0	97.62	33 87 0	98.83
38 98 0	98.39	32 84 0	97.78	55 141 0	98.94
34 87 0	98.48	53 142 0	97.94	57 149 0	99.03
57 149 0	98.57	50 134 0	98.10	35 93 0	99.11
55 146 0	98.65	39 97 0	98.24	55 146 0	99.18
49 130 2	98.73	34 88 0	98.38	41 106 0	99.24

39 97 0	98.80	55 142 0	98.51	39 97 0	99.30
54 142 0	98.87	38 98 0	98.62	31 81 0	99.36
36 94 0	98.94	31 84 0	98.71	54 141 0	99.40
41 106 0	99	34 87 0	98.79	49 130 1	99.44
31 81 0	99.06	55 141 0	98.87	36 92 0	99.48
53 142 0	99.11	36 96 0	98.94	39 102 0	99.51
49 130 1	99.16	57 149 0	99	57 148 0	99.54
54 141 0	99.20	55 146 0	99.06	37 92 0	99.57
50 135 0	99.24	31 81 0	99.11	51 134 1	99.60
36 92 0	99.28	36 94 0	99.16	49 129 1	99.63
39 102 0	99.32	54 142 0	99.21	49 130 0	99.65
39 102 1	99.36	49 130 0	99.26	57 147 0	99.67
57 148 0	99.39	35 93 0	99.30	32 85 0	99.69
41 107 0	99.42	41 106 0	99.34	31 82 0	99.71
37 92 0	99.45	31 82 0	99.38	57 150 0	99.73
35 93 0	99.48	55 147 0	99.41	49 133 0	99.75
57 147 0	99.51	49 129 1	99.44	49 131 0	99.77
51 134 1	99.54	50 135 0	99.47	38 99 0	99.79
33 88 0	99.57	36 92 0	99.50	49 132 0	99.81
54 143 0	99.60	54 141 0	99.53	41 108 0	99.82
36 95 0	99.62	37 98 0	99.56	33 84 0	99.83
49 130 0	99.64	57 148 0	99.59	41 104 0	99.84
38 97 0	99.66	37 92 0	99.62	55 147 0	99.85
49 133 0	99.68	49 131 0	99.65	38 1 0	99.86
57 150 0	99.70	52 140 0	99.67	31 80 0	99.87
49 129 1	99.72	57 147 0	99.69	39 103 0	99.88
49 132 0	99.74	38 97 0	99.71	41 104 1	99.89
49 131 0	99.76	38 1 0	99.73	50 135 0	99.90
49 131 1	99.78	49 132 0	99.75	37 98 0	99.91
41 108 0	99.79	51 134 1	99.77	34 91 0	99.92
33 84 0	99.80	57 150 0	99.78	41 107 0	99.93
41 104 0	99.81	36 95 0	99.79	49 129 0	99.94
31 83 0	99.82	33 84 0	99.80	31 83 0	99.95
52 139 0	99.83	41 104 0	99.81	41 109 0	99.95
55 147 0	99.84	39 103 0	99.82	35 94 0	99.95
31 80 0	99.85	36 98 0	99.83	43 111 0	99.95
31 82 0	99.86	49 133 0	99.84	50 133 0	99.95
39 103 0	99.87	33 89 0	99.85	48 130 0	99.95
41 104 1	99.88	41 109 0	99.86	56 148 0	99.95
37 98 0	99.89	56 147 0	99.87	38 101 0	99.95
49 129 0	99.90	31 83 0	99.88	37 99 0	99.95
38 1 0	99.91	41 104 1	99.89	43 109 0	99.95
38 99 0	99.92	35 94 0	99.90	31 79 0	99.95
56 147 0	99.93	54 143 0	99.91	30 79 0	99.95
56 148 0	99.94	41 107 0	99.92	43 112 0	99.95
34 90 0	99.95	52 139 0	99.93	49 127 1	99.95
41 109 0	99.96	38 99 0	99.94	31 84 0	99.95
33 89 0	99.96	38 101 0	99.95	56 149 0	99.95
53 143 0	99.96	34 90 0	99.96	43 110 0	99.95

57 151 0	99.96	31 80 0	99.97	50 136 0	99.95

Table C.2: Precursors' importance for the thermal fission of ^{235}U.

C.3 Precursors' Importance - $^{235}\mathbf{U_{fast}}$

In the following, JEFF stands for JEFF-3.1.1, ENDF70 for ENDF/B-VII.0, and ENDF71 for ENDF/B-VII.1. For each precursor, the cumulative importance is reported. For example, ^{94}Rb accounts for 14.87% of the ν_d according to JEFF-ENDF71, while ^{94}Rb and ^{137}I together account for 28.08%.

JEFF-ENDF71		**ENDF70-ENDF71**		**JEFF-Pfeiffer**	
Z-A-I	**Importance [%]**	**Z-A-I**	**Importance [%]**	**Z-A-I**	**Importance [%]**
37 94 0	14.87	37 94 0	11.66	53 137 0	12.344
53 137 0	28.08	35 89 0	23	37 94 0	24.595
35 89 0	40.75	35 90 0	33.72	35 89 0	36.545
35 90 0	49.64	53 137 0	44.15	35 90 0	44.89
35 88 0	58.38	35 88 0	52.10	35 88 0	53.15
37 95 0	63.76	33 85 0	59.24	39 98 1	59.16
33 85 0	68.96	37 95 0	63.79	37 95 0	64.29
53 138 0	73.42	53 138 0	68.07	33 85 0	68.87
35 87 0	76.86	35 87 0	71.20	53 138 0	72.81
37 93 0	80.23	51 135 0	74.30	39 99 0	76.34
39 99 0	83.10	37 93 0	77.27	37 93 0	79.66
53 139 0	85.62	53 139 0	79.94	35 87 0	82.83
35 91 0	87.44	39 99 0	82.33	35 91 0	85.51
55 143 0	89.02	37 96 0	84.07	53 139 0	88.10
37 96 0	90.38	35 91 0	85.63	55 143 0	89.55
51 135 0	91.15	55 143 0	86.81	37 96 0	90.84
52 136 0	91.80	55 145 0	87.97	51 135 0	91.58
39 98 1	92.42	35 93 0	88.94	52 136 0	92.17
37 97 0	93.01	37 97 0	89.72	55 144 0	92.76
55 145 0	93.60	52 136 0	90.49	33 86 0	93.33
55 144 0	94.16	55 144 0	91.15	37 97 0	93.90
36 93 0	94.63	53 140 0	91.77	53 140 0	94.43
39 101 0	95.06	34 89 0	92.31	55 145 0	94.93
41 105 0	95.46	39 1 0	92.78	39 101 0	95.42
53 140 0	95.84	39 98 0	93.24	36 93 0	95.87
39 1 0	96.20	51 134 0	93.67	39 1 0	96.30
33 86 0	96.49	33 86 0	94.09	41 105 0	96.68
52 137 0	96.77	36 93 0	94.48	35 92 0	97.06
39 98 0	97.05	52 138 0	94.87	36 94 0	97.35
51 134 0	97.26	33 87 0	95.25	52 137 0	97.60
34 89 0	97.44	51 136 0	95.62	39 98 0	97.83
55 142 0	97.61	39 101 0	95.94	34 89 0	98
35 92 0	97.77	52 137 0	96.21	38 98 0	98.17
33 87 0	97.92	41 105 0	96.48	55 142 0	98.33
51 136 0	98.05	39 98 1	96.74	53 141 0	98.46
38 98 0	98.16	53 141 0	96.94	34 87 0	98.57

39 97 1	98.26	32 84 0	97.11	55 141 0	98.67
57 149 0	98.36	34 88 0	97.28	57 149 0	98.77
55 141 0	98.46	39 97 0	97.45	34 88 0	98.86
53 141 0	98.56	35 92 0	97.61	41 106 0	98.94
34 88 0	98.65	50 134 0	97.77	39 102 0	99.02
41 106 0	98.74	38 98 0	97.92	52 138 0	99.10
52 138 0	98.83	55 142 0	98.07	33 87 0	99.16
39 102 0	98.91	39 102 0	98.20	51 136 0	99.22
39 102 1	98.99	55 146 0	98.32	35 93 0	99.28
39 97 0	99.06	41 106 0	98.43	54 142 0	99.34
34 87 0	99.12	57 149 0	98.53	39 97 0	99.40
36 94 0	99.18	50 135 0	98.62	32 84 0	99.45
55 146 0	99.23	55 141 0	98.71	55 146 0	99.49
32 84 0	99.28	34 87 0	98.79	57 148 0	99.53
41 107 0	99.33	31 81 0	98.86	37 92 0	99.56
57 148 0	99.37	54 142 0	98.93	36 92 0	99.59
57 147 0	99.40	53 142 0	99	39 103 0	99.61
37 92 0	99.43	51 137 0	99.05	57 147 0	99.63
36 92 0	99.46	36 95 0	99.10	54 141 0	99.65
54 142 0	99.49	33 88 0	99.15	41 104 0	99.67
39 103 0	99.52	49 130 0	99.20	31 81 0	99.69
35 93 0	99.54	49 131 0	99.24	57 150 0	99.71
41 104 0	99.56	37 98 0	99.28	38 99 0	99.73
54 141 0	99.58	55 147 0	99.32	50 134 0	99.75
57 150 0	99.60	57 148 0	99.36	41 108 0	99.77
31 81 0	99.62	36 94 0	99.40	33 84 0	99.79
38 97 0	99.64	41 107 0	99.43	51 134 1	99.81
36 95 0	99.66	57 147 0	99.46	41 104 1	99.83
50 134 0	99.68	57 150 0	99.49	37 98 0	99.85
41 108 0	99.70	41 109 0	99.52	49 129 1	99.87
33 84 0	99.72	38 97 0	99.55	38 1 0	99.88
51 134 1	99.74	36 92 0	99.58	41 107 0	99.89
41 104 1	99.76	37 92 0	99.61	31 82 0	99.90
51 137 0	99.78	39 103 0	99.64	49 130 1	99.91
37 98 0	99.80	49 129 1	99.66	32 85 0	99.92
33 88 0	99.81	54 141 0	99.68	49 129 0	99.92
53 142 0	99.82	31 83 0	99.70	41 109 0	99.92
49 130 2	99.83	33 84 0	99.72	55 147 0	99.92
49 129 1	99.84	41 104 0	99.74	43 111 0	99.92
38 1 0	99.85	38 1 0	99.76	49 130 0	99.92
54 143 0	99.86	49 133 0	99.78	31 80 0	99.92
49 130 1	99.87	31 82 0	99.79	34 91 0	99.92
38 99 0	99.88	49 127 1	99.80	35 94 0	99.92
49 129 0	99.89	38 99 0	99.81	38 101 0	99.92
41 109 0	99.90	51 134 1	99.82	37 99 0	99.92
55 147 0	99.90	33 89 0	99.83	49 131 0	99.92
31 82 0	99.90	52 139 0	99.84	43 109 0	99.92
43 111 0	99.90	34 90 0	99.85	31 83 0	99.92
57 151 0	99.90	31 80 0	99.86	49 127 1	99.92

56 147 0	99.90	41 104 1	99.87	43 112 0	99.92
31 80 0	99.90	54 143 0	99.88	49 132 0	99.92
37 99 0	99.90	56 148 0	99.89	56 148 0	99.92
35 94 0	99.90	56 147 0	99.90	49 133 0	99.92
49 130 0	99.90	57 151 0	99.91	50 135 0	99.92
56 148 0	99.90	43 111 0	99.92	31 79 0	99.92
31 83 0	99.90	49 132 0	99.93	43 110 0	99.92

Table C.3: Precursors' importance for the fast fission of ^{235}U.

C.4 Precursors' Importance - $^{238}\mathbf{U_{fast}}$

In the following, JEFF stands for JEFF-3.1.1, ENDF70 for ENDF/B-VII.0, and ENDF71 for ENDF/B-VII.1. For each precursor, the cumulative importance is reported. For example, ^{137}I accounts for 8.89% of the ν_d according to JEFF-ENDF71, while ^{137}I and ^{94}Rb together account for 16.72%.

JEFF-ENDF71		**ENDF70-ENDF71**		**JEFF-Pfeiffer**	
Z-A-I	**Importance [%]**	**Z-A-I**	**Importance [%]**	**Z-A-I**	**Importance [%]**
53 137 0	8.89	53 137 0	8.67	53 137 0	8.69
37 94 0	16.72	35 90 0	17.28	37 94 0	15.44
35 90 0	23.43	37 94 0	25.34	35 90 0	22.03
35 89 0	29.87	35 89 0	31.69	35 89 0	28.39
51 135 0	35.51	33 85 0	37.35	53 139 0	34.45
53 139 0	41.15	51 135 0	42.77	51 135 0	40.06
33 85 0	46.49	53 139 0	47.90	35 91 0	45.18
53 138 0	51.43	53 138 0	52.70	33 85 0	50.10
37 95 0	55.68	37 96 0	56.49	53 138 0	54.66
35 91 0	59.00	35 91 0	60.15	37 95 0	58.90
51 136 0	62.26	37 95 0	63.68	53 140 0	62.00
35 88 0	65.04	51 136 0	66.33	35 88 0	64.75
55 145 0	67.75	35 88 0	68.63	55 145 0	67.15
37 96 0	69.89	53 140 0	70.68	39 99 0	69.45
53 140 0	72.00	55 145 0	72.66	53 141 0	71.75
37 97 0	73.95	39 99 0	74.57	37 96 0	73.88
39 99 0	75.74	37 93 0	75.92	37 97 0	75.85
53 141 0	77.37	55 144 0	77.25	39 98 1	77.82
37 93 0	78.79	53 141 0	78.54	51 136 0	79.43
55 143 0	80.06	52 136 0	79.69	37 93 0	80.89
51 137 0	81.29	52 137 0	80.82	35 92 0	82.29
52 136 0	82.49	55 143 0	81.92	55 143 0	83.51
52 137 0	83.60	51 134 0	82.92	52 136 0	84.66
52 138 0	84.56	35 87 0	83.87	33 86 0	85.76
55 144 0	85.52	51 137 0	84.78	55 144 0	86.84
35 87 0	86.43	52 138 0	85.61	52 137 0	87.89
41 105 0	87.22	41 105 0	86.42	52 138 0	88.85
33 87 0	87.90	35 92 0	87.18	35 87 0	89.72
50 134 0	88.57	50 134 0	87.92	41 105 0	90.50
39 101 0	89.23	39 1 0	88.62	39 101 0	91.27

55 146 0	89.88	39 101 0	89.31	36 94 0	91.99
41 106 0	90.52	33 86 0	90	50 134 0	92.66
36 93 0	91.11	36 93 0	90.68	41 106 0	93.30
35 92 0	91.68	41 106 0	91.31	55 146 0	93.91
53 142 0	92.24	34 89 0	91.93	35 93 0	94.51
33 86 0	92.77	39 102 0	92.54	36 93 0	95.09
51 134 0	93.28	37 97 0	93.08	34 89 0	95.59
34 89 0	93.78	53 142 0	93.60	39 1 0	95.98
50 135 0	94.25	33 87 0	94.07	33 87 0	96.28
39 1 0	94.56	50 135 0	94.51	57 149 0	96.56
57 149 0	94.83	55 146 0	94.91	39 102 0	96.81
49 133 0	95.08	35 93 0	95.23	49 133 0	97.03
35 93 0	95.33	39 98 0	95.53	39 103 0	97.24
39 102 0	95.57	37 98 0	95.81	55 147 0	97.44
39 102 1	95.81	39 103 0	96.06	38 98 0	97.62
41 107 0	96.05	57 149 0	96.30	39 98 0	97.79
39 103 0	96.26	32 84 0	96.51	57 150 0	97.95
55 147 0	96.47	41 107 0	96.72	54 142 0	98.11
39 98 1	96.66	36 94 0	96.92	41 109 0	98.25
39 98 0	96.85	49 133 0	97.09	32 84 0	98.37
57 150 0	97.01	53 143 0	97.25	50 135 0	98.48
41 109 0	97.15	33 88 0	97.41	34 88 0	98.58
36 94 0	97.29	35 94 0	97.57	37 98 0	98.68
33 88 0	97.43	57 150 0	97.71	49 132 0	98.78
53 143 0	97.55	38 98 0	97.85	55 142 0	98.87
32 84 0	97.67	39 98 1	97.97	41 108 0	98.95
38 98 0	97.79	37 99 0	98.08	34 87 0	99.02
34 88 0	97.90	36 95 0	98.19	35 94 0	99.08
37 98 0	98.00	55 147 0	98.29	38 1 0	99.14
36 95 0	98.10	34 88 0	98.38	41 107 0	99.20
49 132 0	98.20	55 142 0	98.46	57 148 0	99.26
55 142 0	98.29	33 89 0	98.54	34 91 0	99.32
35 94 0	98.37	49 132 0	98.62	49 131 0	99.37
41 108 0	98.45	54 142 0	98.70	32 85 0	99.42
54 142 0	98.53	39 97 0	98.77	55 141 0	99.47
57 151 0	98.60	31 83 0	98.84	38 99 0	99.51
54 143 0	98.66	57 151 0	98.90	37 99 0	99.55
52 139 0	98.72	52 139 0	98.96	31 81 0	99.59
37 99 0	98.78	38 1 0	99.02	54 141 0	99.62
57 148 0	98.84	57 148 0	99.07	51 134 1	99.65
33 89 0	98.89	31 81 0	99.11	41 104 0	99.68
49 131 0	98.94	55 141 0	99.15	39 97 0	99.71
49 131 1	98.99	34 87 0	99.19	31 82 0	99.74
55 141 0	99.04	49 129 1	99.23	38 101 0	99.76
38 1 0	99.08	41 104 0	99.26	49 130 1	99.78
49 133 1	99.12	50 136 0	99.29	36 92 0	99.80
34 87 0	99.16	54 141 0	99.32	31 83 0	99.82
50 136 0	99.20	36 96 0	99.35	57 147 0	99.84
39 97 0	99.24	31 82 0	99.38	41 104 1	99.86

31 81 0	99.27	54 143 0	99.41	55 148 0	99.88
31 83 0	99.30	38 101 0	99.44	41 110 0	99.89
48 131 0	99.33	51 134 1	99.47	37 92 0	99.90
51 134 1	99.36	41 108 0	99.50	50 136 0	99.91
54 141 0	99.39	56 148 0	99.52	49 130 0	99.92
41 104 0	99.42	38 99 0	99.54	49 129 1	99.93
49 130 2	99.45	57 147 0	99.56	56 149 0	99.94
56 148 0	99.48	54 144 0	99.58	43 111 0	99.95
39 97 1	99.51	36 92 0	99.60	56 148 0	99.96
54 144 0	99.53	34 90 0	99.62	33 84 0	99.97
51 138 0	99.55	39 104 0	99.64	43 112 0	99.98
57 147 0	99.57	51 138 0	99.66	50 133 0	99.99
49 130 1	99.59	41 104 1	99.68	38 102 0	100.00
38 101 0	99.61	49 130 0	99.70	31 84 0	100.00
36 92 0	99.63	38 97 0	99.71	49 129 0	100.00
36 96 0	99.65	55 148 0	99.72	43 109 0	100.00
38 99 0	99.67	49 131 0	99.73	31 80 0	100.00
41 104 1	99.69	43 111 0	99.74	48 132 0	100.00
38 97 0	99.70	56 147 0	99.75	49 134 0	100.00
31 82 0	99.71	33 84 0	99.76	37 1 0	100.00
39 104 0	99.72	41 109 0	99.77	49 127 1	100.00
55 148 0	99.73	57 152 0	99.78	43 113 0	100.00
34 90 0	99.74	37 92 0	99.79	48 131 0	100.00
57 152 0	99.75	52 140 0	99.80	56 150 0	100.00
56 147 0	99.76	32 85 0	99.81	43 110 0	100.00
52 140 0	99.77	37 1 0	99.82	30 79 0	100.00
54 145 0	99.78	43 112 0	99.83	47 123 0	100.00
37 92 0	99.79	54 145 0	99.84	29 77 0	100.00
43 111 0	99.80	39 105 0	99.85	30 81 0	100.00
49 130 0	99.81	57 153 0	99.86	43 114 0	100.00
51 139 0	99.82	38 102 0	99.87	37 101 0	100.00
57 153 0	99.83	32 86 0	99.88	47 121 0	100.00
35 95 0	99.84	51 139 0	99.89	31 79 0	100.00
33 84 0	99.85	41 111 0	99.90	30 80 0	100.00
49 134 0	99.86	49 134 0	99.91	47 122 0	100.00
49 129 1	99.87	49 127 1	99.92	29 78 0	100.00
41 110 0	99.88	34 91 0	99.93	29 75 0	100.00
43 112 0	99.89	52 141 0	99.94	29 79 0	100.00
50 133 0	99.90	56 149 0	99.94	48 130 0	100.00
38 102 0	99.91	43 109 0	99.94	29 76 0	100.00
37 1 0	99.92	50 133 0	99.94	55 150 0	100.00
32 85 0	99.93	43 114 0	99.94	47 124 0	100.00

Table C.4: Precursors' importance for the fast fission of ^{238}U.

C.5 Precursors' Importance - $^{239}\mathbf{Pu_{thermal}}$

In the following, JEFF stands for JEFF-3.1.1, ENDF70 for ENDF/B-VII.0, and ENDF71 for ENDF/B-VII.1. For each precursor, the cumulative importance is reported. For

example, ^{137}I accounts for 27.20% of the ν_d according to JEFF-ENDF71, while ^{137}I and ^{94}Rb together account for 39.34%.

JEFF-ENDF71		ENDF70-ENDF71		JEFF-Pfeiffer	
Z-A-I	**Importance [%]**	**Z-A-I**	**Importance [%]**	**Z-A-I**	**Importance [%]**
53 137 0	27.20	53 137 0	24.14	53 137 0	24.70
37 94 0	39.34	37 94 0	34.78	39 98 1	34.43
35 89 0	46.39	53 138 0	44.72	37 94 0	44.15
53 138 0	52.64	35 90 0	52.25	35 89 0	50.62
35 88 0	58.12	35 89 0	58.95	53 138 0	55.99
35 90 0	62.12	37 95 0	64.20	35 88 0	61.03
37 93 0	66.00	35 88 0	68.86	39 99 0	65.52
37 95 0	69.76	53 139 0	73.31	37 93 0	69.23
39 99 0	73.52	39 99 0	76.82	35 90 0	72.89
53 139 0	76.82	37 93 0	79.58	37 95 0	76.38
33 85 0	79.86	35 87 0	82.08	53 139 0	79.68
35 87 0	82.74	51 135 0	84.13	33 85 0	82.28
51 135 0	84.65	55 143 0	85.71	35 87 0	84.86
55 143 0	86.30	33 85 0	86.90	51 135 0	86.62
52 136 0	87.79	41 105 0	88.09	55 143 0	88.10
41 105 0	89.12	52 136 0	89.02	52 136 0	89.42
39 98 1	90.14	37 96 0	89.90	35 91 0	90.67
35 91 0	91.00	51 134 0	90.73	41 105 0	91.90
37 96 0	91.81	53 140 0	91.54	37 96 0	92.64
52 137 0	92.41	39 98 0	92.24	53 140 0	93.27
41 106 0	92.89	55 144 0	92.91	52 137 0	93.80
53 140 0	93.35	55 145 0	93.48	55 144 0	94.25
55 145 0	93.79	35 91 0	94.03	41 106 0	94.70
55 144 0	94.22	39 98 1	94.58	39 1 0	95.07
51 134 0	94.63	52 137 0	95.12	55 145 0	95.43
39 98 0	95.00	39 1 0	95.57	39 101 0	95.77
36 93 0	95.35	35 94 0	95.89	36 93 0	96.10
51 136 0	95.69	39 97 0	96.18	37 97 0	96.41
37 97 0	96.02	37 97 0	96.43	39 98 0	96.72
39 1 0	96.34	35 93 0	96.67	33 86 0	97.03
39 101 0	96.65	39 101 0	96.90	55 142 0	97.26
55 142 0	96.89	41 106 0	97.12	55 141 0	97.46
39 97 1	97.11	53 141 0	97.33	35 92 0	97.64
55 141 0	97.31	55 142 0	97.52	36 94 0	97.82
33 86 0	97.47	51 136 0	97.71	53 141 0	97.98
52 138 0	97.63	36 93 0	97.90	51 136 0	98.14
53 141 0	97.75	53 142 0	98.08	52 138 0	98.29
39 97 0	97.86	55 141 0	98.24	38 98 0	98.43
57 149 0	97.96	38 98 0	98.35	49 129 1	98.56
34 89 0	98.06	33 86 0	98.45	57 149 0	98.65
49 129 1	98.16	52 138 0	98.55	34 89 0	98.74
38 98 0	98.26	50 134 0	98.64	39 97 0	98.82
33 87 0	98.35	41 107 0	98.72	43 111 0	98.89
35 92 0	98.43	57 149 0	98.79	34 87 0	98.96

43 111 0	98.51	33 87 0	98.86	54 142 0	99.03
49 130 2	98.58	34 89 0	98.91	41 104 0	99.09
41 104 0	98.65	41 104 0	98.96	50 134 0	99.15
41 107 0	98.72	35 92 0	99.01	39 102 0	99.20
50 134 0	98.78	43 109 0	99.06	41 104 1	99.25
39 102 0	98.83	49 130 0	99.10	34 88 0	99.29
39 102 1	98.88	55 146 0	99.14	57 148 0	99.33
41 104 1	98.93	36 96 0	99.18	31 81 0	99.37
51 137 0	98.98	54 142 0	99.22	49 130 1	99.41
57 147 0	99.03	39 102 0	99.26	43 109 0	99.45
34 88 0	99.08	41 104 1	99.30	32 84 0	99.49
57 148 0	99.13	34 88 0	99.34	49 129 0	99.53
31 81 0	99.17	34 87 0	99.38	33 87 0	99.56
49 130 1	99.21	51 137 0	99.42	35 93 0	99.59
43 109 0	99.25	36 94 0	99.46	57 147 0	99.62
49 129 0	99.29	57 147 0	99.50	37 92 0	99.65
32 84 0	99.33	54 141 0	99.53	54 141 0	99.68
34 87 0	99.37	37 92 0	99.56	55 146 0	99.71
36 94 0	99.41	32 84 0	99.59	51 134 1	99.74
55 146 0	99.45	31 81 0	99.62	49 130 0	99.76
37 92 0	99.49	57 148 0	99.65	36 92 0	99.78
54 142 0	99.53	51 134 1	99.67	57 150 0	99.80
54 141 0	99.56	49 131 0	99.69	49 127 1	99.82
51 134 1	99.59	49 127 1	99.71	39 103 0	99.84
38 97 0	99.61	38 97 0	99.73	41 107 0	99.86
36 92 0	99.63	57 150 0	99.75	43 112 0	99.87
57 150 0	99.65	50 135 0	99.77	38 99 0	99.88
49 130 0	99.67	49 129 1	99.79	31 82 0	99.89
49 127 1	99.69	36 97 0	99.81	49 131 0	99.90
39 103 0	99.71	36 92 0	99.82	33 84 0	99.91
53 142 0	99.73	37 98 0	99.83	38 1 0	99.92
50 135 0	99.75	49 132 0	99.84	37 98 0	99.93
43 112 0	99.77	39 103 0	99.85	49 132 0	99.94
35 93 0	99.79	33 84 0	99.86	31 80 0	99.95
36 95 0	99.80	41 108 0	99.87	32 85 0	99.96
49 131 0	99.81	43 111 0	99.88	43 110 0	99.97
49 131 1	99.82	38 1 0	99.89	49 133 0	99.98
33 84 0	99.83	33 88 0	99.90	55 147 0	99.98
54 143 0	99.84	36 95 0	99.91	50 135 0	99.98
3 9 0	99.85	49 133 0	99.92	41 108 0	99.98
33 88 0	99.86	38 99 0	99.93	34 91 0	99.98
49 132 0	99.87	43 114 0	99.93	31 83 0	99.98
37 98 0	99.88	31 80 0	99.93	35 94 0	99.98
31 80 0	99.89	54 143 0	99.93	43 113 0	99.98
49 133 0	99.90	57 151 0	99.93	50 133 0	99.98
43 110 0	99.91	31 82 0	99.93	38 101 0	99.98
38 1 0	99.92	56 147 0	99.93	31 79 0	99.98
38 99 0	99.93	31 83 0	99.93	37 99 0	99.98
31 82 0	99.94	52 139 0	99.93	48 130 0	99.98

49 128 0	99.95	43 110 0	99.93	56 148 0	99.98
48 128 0	99.96	49 128 1	99.93	47 121 0	99.98

Table C.5: Precursors' importance for the thermal fission of ^{239}Pu.

C.6 Precursors' Importance - $^{239}\mathbf{Pu_{fast}}$

In the following, JEFF stands for JEFF-3.1.1, ENDF70 for ENDF/B-VII.0, and ENDF71 for ENDF/B-VII.1. For each precursor, the cumulative importance is reported. For example, ^{137}I accounts for 19.18% of the ν_d according to JEFF-ENDF71, while ^{137}I and ^{94}Rb together account for 35.07%.

JEFF-ENDF71		**ENDF70-ENDF71**		**JEFF-Pfeiffer**	
Z-A-I	**Importance [%]**	**Z-A-I**	**Importance [%]**	**Z-A-I**	**Importance [%]**
53 137 0	19.18	53 137 0	22.64	53 137 0	17.109
37 94 0	35.07	37 94 0	33.80	37 94 0	29.501
35 89 0	45.77	53 138 0	43.02	39 98 1	40.70
35 88 0	53.65	35 89 0	50.27	35 89 0	50.33
35 90 0	59.42	35 88 0	55.94	35 88 0	57.44
33 85 0	65.15	35 90 0	60.59	39 99 0	62.88
37 95 0	69.88	37 95 0	64.61	35 90 0	68.05
39 99 0	74.51	33 85 0	68.59	33 85 0	72.86
37 93 0	79.14	39 99 0	72.12	37 93 0	77.21
53 138 0	82.46	37 93 0	75.62	37 95 0	81.52
35 87 0	85.77	35 87 0	78.93	35 87 0	84.43
41 105 0	87.22	53 139 0	82.01	53 138 0	87.23
35 91 0	88.50	51 135 0	83.86	35 91 0	89.02
53 139 0	89.75	55 143 0	85.31	41 105 0	90.34
39 98 1	90.95	52 136 0	86.72	53 139 0	91.57
37 96 0	91.93	37 96 0	88.00	37 96 0	92.46
55 143 0	92.77	41 105 0	89.06	55 143 0	93.20
52 136 0	93.42	35 91 0	90.10	52 136 0	93.77
51 135 0	94.04	51 134 0	90.83	51 135 0	94.33
41 106 0	94.54	39 98 0	91.52	33 86 0	94.82
39 101 0	94.94	39 1 0	92.17	41 106 0	95.27
36 93 0	95.33	55 144 0	92.72	39 1 0	95.71
39 1 0	95.71	39 98 1	93.27	39 101 0	96.14
39 98 0	96.09	52 137 0	93.82	36 93 0	96.49
37 97 0	96.45	53 140 0	94.31	37 97 0	96.82
33 86 0	96.71	41 106 0	94.79	39 98 0	97.13
39 97 1	96.93	37 97 0	95.23	35 92 0	97.36
51 134 0	97.13	36 93 0	95.65	36 94 0	97.55
52 137 0	97.30	55 145 0	96.06	53 140 0	97.72
55 142 0	97.46	39 101 0	96.41	55 144 0	97.88
55 141 0	97.62	39 97 0	96.74	55 141 0	98.04
55 144 0	97.77	51 136 0	97.05	55 142 0	98.19
33 87 0	97.91	52 138 0	97.30	52 137 0	98.34
53 140 0	98.03	33 86 0	97.51	38 98 0	98.48
34 89 0	98.15	55 142 0	97.71	34 89 0	98.59

55 145 0	98.25	55 141 0	97.88	34 87 0	98.68
35 92 0	98.35	33 87 0	98.02	55 145 0	98.76
39 97 0	98.45	34 89 0	98.15	41 104 0	98.84
38 98 0	98.55	39 102 0	98.27	39 97 0	98.92
41 104 0	98.64	53 141 0	98.39	34 88 0	98.98
51 136 0	98.71	38 98 0	98.49	41 104 1	99.04
34 88 0	98.78	35 92 0	98.59	32 84 0	99.10
41 104 1	98.85	57 149 0	98.68	49 129 1	99.16
32 84 0	98.92	50 134 0	98.76	39 102 0	99.22
39 102 0	98.98	41 107 0	98.83	33 87 0	99.27
39 102 1	99.04	32 84 0	98.89	43 111 0	99.32
41 107 0	99.10	41 104 0	98.95	31 81 0	99.37
43 111 0	99.16	34 88 0	99.01	35 93 0	99.41
31 81 0	99.21	49 130 0	99.07	37 92 0	99.45
34 87 0	99.26	34 87 0	99.13	43 109 0	99.49
49 129 1	99.31	41 104 1	99.18	51 136 0	99.52
36 94 0	99.35	31 81 0	99.22	57 149 0	99.55
43 109 0	99.39	36 94 0	99.26	52 138 0	99.58
37 92 0	99.43	57 148 0	99.30	53 141 0	99.61
57 149 0	99.46	51 137 0	99.34	36 92 0	99.64
49 130 2	99.49	57 147 0	99.38	57 147 0	99.66
52 138 0	99.52	37 92 0	99.41	49 130 1	99.68
57 147 0	99.55	54 141 0	99.44	57 148 0	99.70
36 92 0	99.58	54 142 0	99.47	49 129 0	99.72
38 97 0	99.60	55 146 0	99.50	33 84 0	99.74
49 129 0	99.62	49 131 0	99.53	31 82 0	99.76
49 130 1	99.64	38 97 0	99.56	54 142 0	99.78
57 148 0	99.66	36 92 0	99.59	39 103 0	99.80
53 141 0	99.68	49 129 1	99.62	51 134 1	99.81
33 84 0	99.70	43 109 0	99.64	38 99 0	99.82
39 103 0	99.72	49 127 1	99.66	41 107 0	99.83
35 93 0	99.74	51 134 1	99.68	54 141 0	99.84
51 134 1	99.76	57 150 0	99.70	50 134 0	99.85
50 134 0	99.77	35 93 0	99.72	49 127 1	99.86
33 88 0	99.78	37 98 0	99.74	43 112 0	99.87
54 141 0	99.79	50 135 0	99.76	32 85 0	99.88
36 95 0	99.80	39 103 0	99.78	49 130 0	99.89
49 127 1	99.81	36 95 0	99.80	31 80 0	99.90
43 112 0	99.82	53 142 0	99.82	37 98 0	99.91
54 142 0	99.83	33 84 0	99.83	38 1 0	99.92
31 82 0	99.84	33 88 0	99.84	55 146 0	99.92
31 80 0	99.85	43 111 0	99.85	57 150 0	99.92
49 130 0	99.86	38 1 0	99.86	43 110 0	99.92
37 98 0	99.87	31 82 0	99.87	31 83 0	99.92
31 83 0	99.88	31 80 0	99.88	49 131 0	99.92
51 137 0	99.89	38 99 0	99.89	34 91 0	99.92
38 99 0	99.90	31 83 0	99.90	35 94 0	99.92
49 128 0	99.91	49 132 0	99.91	41 108 0	99.92
38 1 0	99.92	43 114 0	99.92	31 79 0	99.92

55 146 0	99.93	49 133 0	99.93	49 132 0	99.92

Table C.6: Precursors' importance for the fast fission of ^{239}Pu.

Appendix D

Bateman-solver validation with DARWIN

For the validation of the solver, the DARWIN-code is used.
For a physical system irradiated by a particle flux, the composition of the irradiated materials changes by both nuclear reactions and by radioactive decay. The differential equation describing the concentration as a function of time is

$$\frac{\mathrm{d}N_i(t)}{\mathrm{d}t} = \sum_{j=1}^{j=i-1} C_{i,j} \cdot N_j(t) - C_{i,i} \cdot N_i(t) \tag{D.1}$$

where $C_{i,j}$ is the transmutation rate of j in i after a radioactive decay or a nuclear reaction, while $C_{i,i}$ is the disappearance rate of a species i. Two methods are implemented in the evolution module PEPIN2: an analytical method, based on the development of the solution on the basis of exponential decay functions, and a numerical method (Runge-Kutta) of fourth order.

D.1 Analytical method

Equation D.1 can be written in the generalized case as

$$\frac{\mathrm{d}N_i(t)}{\mathrm{d}t} = b_i + \sum_{j=1}^{j=i-1} C_{i,j} \cdot N_j(t) - C_{i,i} \cdot N_i(t) \tag{D.2}$$

with b_i being a constant source of isotope i, and

$$\begin{cases} C_{i,j} & = BR_{j\to i} \cdot \lambda_j + BR'_{j\to i} \cdot \sigma_j^{capt} \cdot \phi \\ C_{i,i} & = C_{j,j} = \lambda_i + \sigma_i^{abs} \cdot \phi \end{cases} \tag{D.3}$$

where $BR_{k\to i}$ is the branching ratio of isotope k leading to isotope i, λ_k the decay constant of isotope k, ϕ the neutron flux and σ_k^{capt} and σ_i^{abs} the capture and absorption microscopic cross section of isotope k. In that case the solution would be

$$N_i(t) = N_i^S + \sum_{j=1}^{i} F_{i,j} \cdot e^{-C_{j,j} \cdot t} \tag{D.4}$$

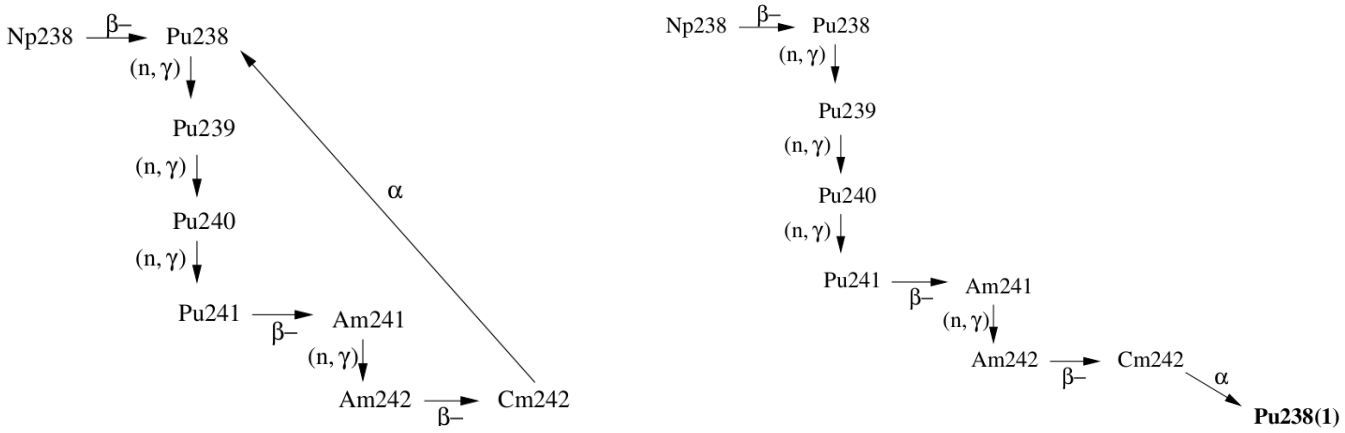

(a) From a close path ...

(b) ... to an open path.

Figure D.1: Example of a closed decay-chain treatment.

where $F_{i,j}$ and N_i^S have to be determined through D.2 by imposing $N_i(t=0) = N_i(0)$. With some substitutions, one obtains:

$$\begin{cases} N_i^S &= \frac{1}{C_{i,i}} \left[b_i + \sum_{k=1}^{i-1} C_{i,k} \cdot N_k^S \right] \qquad if\ C_{i,i} \neq 0 \\ F_{i,k} &= \frac{1}{C_{i,i} - C_{k,k}} \sum_{j=k}^{i-1} C_{i,j} \cdot F_{j,k} \qquad if\ C_{i,i} \neq C_{k,k}\ \ and\ \ 1 \leq k \leq i-1 \\ F_{i,i} &= N_i(0) - N_i(S) - \sum_{j=1}^{i-1} F_{i,j} \end{cases} \tag{D.5}$$

Note that in the particular case of $C_{i,i} = C_{k,k}$, $C_{i,i}$ is replaced by $\widetilde{C_{i,i}} = C_{i,i}(1+\epsilon)$, where ϵ is a real number much smaller than unity. The procedure described above does not work in case of a close decay-chain (see Fig. D.1a) This particular case is treated in a special way. The close decay-chain is first rewritten as an open chain (see Fig. D.1b), with the creation of an artificial twin isotope (^{238}Pu). The analytical method can, therefore, be applied, coupled with a temporal discretization of the irradiation phase in time meshes Δt. The analytical method is applied at each elementary Δt, at the end of which, the artificial isotope is emptied in the main one.

D.2 Numerical method

Bateman equation can also be written in matrix form

$$\frac{\mathrm{d}N_i(t)}{\mathrm{d}t} = S(t) + A(t) \cdot N(t) \tag{D.6}$$

where $S(t)$ is the source term, coming from fission, and $A(t)$ is the evolution matrix where the non-diagonal elements contain the feeding terms and the diagonal terms the disappearing terms. Explicitly,

$$\begin{cases} A_{i,i}(t) = -\lambda_i - \sigma_i^{disp} \cdot \phi(t) \\ A_{i,j}(t) = BR_{j \to i}^d \cdot \lambda_j + BR_{j \to i}^r \cdot \phi(t) \end{cases} \tag{D.7}$$

The $A(t)$ matrix depends almost entirely on time through the flux, which is known, due to the coupling of PEPIN2 with neutronics codes. The numerical scheme used is Runge-Kutta or fourth order, due to the good precision and the reasonable computing time. The irradiation phase is divided into irradiation intervals, over which the $A(t)$-matrix can be considered constant. Each interval is then discretized in elementary time-steps whose size depends on the isotopes having the largest decay-rate (τ_i).

$$\Delta t_i = \frac{\epsilon}{\tau_i} \tag{D.8}$$

An iterative procedure is repeated with the time-step Δt_i until the isotope i reaches its saturation concentration. After that, a new time-step is calculated for the following isotope and so on and so forth. For more information about the procedures implemented in the DARWIN-code, the authors recommend the official documentation [59].

D.2.1 DARWIN analytical resolution

This is the general equation

$$\frac{\mathrm{d}N_i(t)}{\mathrm{d}t} = \sum_{j=1}^{i-1} C_{i,j}\ Nj(t) - C_{i,i}\ Ni(t) \tag{D.9}$$

and I assume the solution to be in the form of

$$N_i(t) = N_i^S + \sum_{j=1}^{i} F_{i,j}\ e^{-C_{j,j}\ t} \tag{D.10}$$

with the BC (Boundary Condition)

$$N_i(t=0) = N_i(0) \tag{D.11}$$

Computing the derivative of Eq. D.10, one have

$$\frac{\mathrm{d}N_i(t)}{\mathrm{d}t} = -\sum_{j=1}^{i} C_{j,j}\ e^{-C_{j,j}\ t} \tag{D.12}$$

Finally, substituting Eq. D.12 and Eq. D.10 in Eq. D.9:

$$\begin{aligned}
-\sum_{j=1}^{i} C_{j,j}\ F_{i,j}\ e^{-C_{j,j}\ t} &= b_i + \sum_{j=1}^{i-1}\left[C_{i,j}\left(N_j^S + \sum_{k=1}^{j} F_{j,k}\ e^{-C_{k,k}\ t}\right)\right] - C_{i,i}\left(N_i^S + \sum_{j=1}^{i} F_{i,j}\ e^{-C_{j,j}\ t}\right) \\
0 &= b_i + \sum_{j=1}^{i-1}\left[C_{i,j}\left(N_j^S + \sum_{k=1}^{j} F_{j,k}\ e^{-C_{k,k}\ t}\right)\right] - C_{i,i}\left(N_i^S + \sum_{j=1}^{i} F_{i,j}\ e^{-C_{j,j}\ t}\right) + \sum_{j=1}^{i} C_{j,j}\ F_{i,j}\ e^{-C_{j,j}\ t} \\
0 &= b_i + \sum_{j=1}^{i-1} C_{i,j}\ N_j^S + \sum_{j=1}^{i-1} C_{i,j} \sum_{k=1}^{j} F_{j,k}\ e^{-C_{k,k}\ t} - C_{i,i}\ N_i^S - C_{i,i} \sum_{j=1}^{i} F_{i,j}\ e^{-C_{j,j}\ t} + \sum_{j=1}^{i} C_{j,j}\ F_{i,j}\ e^{-C_{j,j}\ t} \\
0 &= b_i + \sum_{j=1}^{i-1} C_{i,j}\ N_j^S - C_{i,i}\ N_i^S + \sum_{j=1}^{i}\left(C_{j,j} - C_{i,i}\right) F_{i,j}\ e^{-C_{j,j}\ t} + \sum_{j=1}^{i-1}\sum_{k=1}^{j} C_{i,j} F_{j,k}\ e^{-C_{k,k}\ t}
\end{aligned}$$

This equation should be valid independently of the time. Therefore for $t \to \infty$ and $t \to 0$ one has:

$$\begin{cases}
0 = b_i + \sum_{j=1}^{i-1} C_{i,j}\ N_j^S - C_{i,i}\ N_i^S & t \to \infty \\
0 = b_i + \sum_{j=1}^{i-1} C_{i,j}\ N_j^S - C_{i,i}\ N_i^S + \sum_{j=1}^{i}\left(C_{j,j} - C_{i,i}\right) F_{i,j} + \sum_{j=1}^{i-1}\sum_{k=1}^{j} C_{i,j} F_{j,k} & t \to 0
\end{cases} \tag{D.13}$$

from which:

$$\begin{cases} N_i^S &= \frac{1}{C_{i,i}} \left[b_i + \sum_{j=1}^{i-1} C_{i,j}\ N_j^S \right] \qquad if\ C_{i,i} \neq 0 \\ F_{i,j} &= \frac{\sum_{j=1}^{i-1} \sum_{k=1}^{j} C_{i,j} F_{j,k}}{C_{i,i} - C_{j,j}} \qquad if\ C_{i,i} \neq C_{j,j} \\ F_{i,i} &= N_i(0) - N_i^S - \sum_{j=1}^{i-1} F_{i,j} \end{cases} \tag{D.14}$$